

Diese Dissertation haben begutachtet:



DISSERTATION

Non-centrosymmetric superconductivity of intermetallic compounds in absence of strong correlations among electrons

ausgeführt zum Zwecke der Erlangung des akademischen Grades eines
Doktors der technischen Wissenschaften unter der Leitung von

Ao.Univ.Prof. Univ.Prof. Dipl.-Ing. Dr.techn. Ernst Bauer

E138

Institut für Festkörperphysik

eingereicht an der Technischen Universität Wien
Fakultät für Physik

von

Dipl.-Ing. Friedrich Kneidinger, BSc (WU)

Matrikelnummer: 0426652

Hardeggasse 55/6/24, 1220 Wien

Wien, am

Kurzfassung

Supraleitung beschreibt die Eigenschaft eines Materials, unterhalb einer Sprungtemperatur T_c einen verschwindenden elektrischen Widerstand aufzuweisen, sowie ein kleines äußeres magnetisches Feld ($\mu_0 H_{cth}$ bzw. $\mu_0 H_{c1}$) komplett zu verdrängen. Die mikroskopische Begründung wird durch die Kondensation von jeweils zwei Elektronen zu einem Cooper-Paar gegeben. Die einzelnen Cooper-Paare weisen eine Korrelation in Form einer einheitlichen Phase auf. Es entsteht somit eine makroskopische Wellenfunktion. Die genauen Paarungsmechanismen bzw. Voraussetzungen der Supraleitung sind bisher nicht vollständig erklärt. Spin-Triplet Paarung, sowie verschiedene ungewöhnliche Paarungskanäle haben das Interesse auf dem Weg zur Klärung des Phänomens Supraleitung weiter geweckt, um letztendlich Materialien und Strukturen zu finden, die Supraleitung bei höheren Temperaturen erlauben.

Diese Dissertation handelt von Supraleitern ohne Inversionszentrum und ohne schwere Fermionen. Polykristalline und einkristalline Materialien wurden dafür im Lichtbogen geschmolzen. Die Probenmaterialien konnten im Anschluss durch Röntgendiffraktometrie eindeutig einer Raumgruppe ohne Inversionszentrum zugeordnet werden. Mithilfe von EPMA (electron probe microanalysis) Messungen konnten zudem die stochiometrischen Zusammensetzungen verifiziert und die Primärphasen identifiziert werden. Hierfür werden die Proben mit Elektronen beschossen und angeregt. Die dabei emittierten Röntgenstrahlen sind für jedes Element charakteristisch. Die Materialien wurden im Anschluss weiter geschnitten und poliert. Im folgenden Schritt wurden die temperatur- und magnetfeldabhängigen physikalischen Eigenschaften, insbesondere der elektrische Widerstand, die spezifische Wärmekapazität und die magnetische Suszeptibilität, bestimmt. Vereinzelt wurde der elektrische Widerstand der Probenmaterialien unter dem Einfluss von äußerem hydrostatischen Druck untersucht. Hierbei konnten insgesamt fünf weitere Supraleiter ohne Inversionszentrum (SrNiSi_3 , SrPdSi_3 , SrPtSi_3 , HfRhGe und LaPtSi) sowie ein weiterer Supraleiter ($\text{La}_3\text{Pd}_4\text{Si}_4$) mit möglicherweise zwei Energielücken von unterschiedlicher Größe identifiziert und charakterisiert werden. Die supraleitenden Sprungtemperaturen befinden sich dabei zwischen 1 K und 3.6 K. Die experimentellen Daten wurden durch theoretische Berechnungen der Bandstrukturen unterstützt und zeigen zum Teil sehr starke \vec{k} abhängige Aufspaltungen der Spin- \uparrow als auch Spin- \downarrow Bänder, sowie mögliche Spin Triplet Paarungskanäle. Weitere Besonderheiten der Supraleiter ohne Inversionszentrum, wie die Unterschiede im oberen kritischen Magnetfeld ($\mu_0 H_{c2}$) bei unterschiedlichen physikalischen Messgrößen, wurden im Zusammenhang mit der Perkolationstheorie diskutiert. Die Kompositionen ohne Inversionszentrum zeigen hierbei vorwiegend eine vollständige, knotenlose Energielücke, sowie ein s -symmetrisches, konventionelles BCS Verhalten mit vernachlässigbarem Anteil an Triplet Cooper Paaren. Mikroskopische Überprüfungen der Singlet Paarungskanäle wurden durch μSR Messungen ermöglicht. Darüber hinaus konnte

die Materialklasse der E_pTX_3 ($E_p = \text{Sr, Ba}; T = \text{Ni, Pd, Pt}; X = \text{Si, Ge}$) Verbindungen vollständig in ihren physikalischen Charakteristiken analysiert werden.

Bei den Seltenen-Erden-Verbindungen wurden weitere Untersuchungen durchgeführt. So führt ein Austausch des La durch Ce zum möglichen Auftreten von magnetischen Phänomenen. In dieser Folge konnten interessante Effekte wie magnetische Ordnungen im Einfluss eines Kristallfeldes untersucht werden, sowie mögliches Auftreten eines Kondo Verhalten diskutiert werden.

Besonderer Dank gilt dem FWF Projekt 22295 für die Ermöglichung dieser Arbeit.

Abstract

Superconductivity describes the behavior of a material to show absolute zero electrical resistivity as well as an absolute expulsion of a small external magnetic field ($\mu_0 H_{c1}$ or $\mu_0 H_{c2}$) below a transition temperature T_c . This is microscopically based on the condensation of two electrons to one Cooper pair. Each single Cooper pair shows a correlation to each other by a single phase. Therefore, a macroscopic wave function emerges. The exact pairing mechanisms and preconditions for the existence of superconductivity are not fully clarified, yet. Spin triplet as well as other unconventional pairing channels have attracted much interest on the topic of superconductivity to further synthesize new materials and structures, allowing superconductivity at higher temperatures.

This doctoral thesis deals with superconductors lacking a center of inversion and strong correlations among Fermions. Polycrystalline and single crystalline materials were prepared by arc-melting. X-ray diffraction was used to precisely assign the samples to a certain point group without inversion center. With the help of EPMA (electron probe microanalysis) measurements, the stoichiometric composition and the primary phases could be proven and verified. Samples get bombarded by electrons and become excited. The X-rays subsequently emitted are characteristic for every specific element. Afterward, the specimen were further cut and polished. Furthermore, their physical properties in dependence of temperature and external magnetic fields, especially the electrical resistivity, specific heat and magnetic susceptibility were determined. On certain samples, electrical resistivity measurements were performed while exposed to external hydrostatic pressure. Here, five new superconductors lacking a center of inversion, i.e. SrNiSi₃, SrPdSi₃, SrPtSi₃, HfRhGe and LaPtSi, as well as a new superconductor (La₃Pd₄Si₄) with possible two gaps, were identified and characterized. The superconducting transition temperatures are between 1 K and 3.6 K. The experimental data were supported by theoretical calculations of the band structure and partly show strong \vec{k} -dependent splitting of the spin up and spin down bands and, therefore, possible spin triplet pairing channels. Further peculiarities of the non-centrosymmetric superconductors, i.e. the differences of the upper critical field ($\mu_0 H_{c2}$) of different physical properties, were discussed in the sense of the percolation theory. Predominately, the non-centrosymmetric compositions show a nodeless, full energy gap, and an *s*-wave, conventional BCS behavior with a negligible contribution of triplet Cooper pairing. Microscopical analysis of the singlet pairing channels were enabled by means of the μ SR measurement technique. Furthermore, the material class of EpTX₃ (Ep = Sr, Ba; T = Ni, Pd, Pt; X = Si, Ge) compounds could be fully examined.

The rare earth compounds were further investigated. An exchange of La by Ce can lead to a formation of magnetic phenomena. Therefore, interesting effects like magnetic ordering in the presence of crystalline electric field splitting were investigated and the possible

existence of Kondo behavior could be discussed.

My deepest gratitude to the FWF project 22295 for supporting this work.

Contents

List of Figures	viii
Nomenclature	xi
1 Introduction	1
2 Theoretical background	3
2.1 Symmetry aspects of crystals	6
2.2 Electrical resistivity	9
2.3 Specific heat	11
2.4 Muon spin relaxation spectroscopy (μ SR)	12
2.5 Superconductivity	14
2.5.1 Theories of superconductivity	15
2.5.2 Unconventional superconductivity	19
2.5.3 Transport phenomena in superconductors	21
2.5.4 Thermodynamical properties of superconductors	21
2.5.5 Percolation theory	25
3 Experimental	30
3.1 Preparation of the samples	30
3.1.1 Electrical resistivity	30
3.1.2 Specific heat	33
3.1.3 Magnetic susceptibility	33
3.2 Setup for electrical resistivity (ρ)	34
3.2.1 Measurement of ρ in the ^3He system	34

3.2.2	Measurement of ρ in the ^4He system	38
3.2.3	Measurement of electrical resistivity ρ in high pressure	38
3.3	Setup for specific heat capacity (C_p)	38
3.4	Setup for the magnetic susceptibility (χ)	40
3.5	Muon Spin Relaxation measurements (μSR)	41
4	1-1-1 compounds	44
4.1	LaPtSi	44
4.1.1	Experimental and computational details	45
4.1.2	Results and discussion	46
4.1.3	Vibrational Properties	59
4.2	LaIrSi and CeIrSi	63
4.2.1	Experimental details	64
4.2.2	Results and Discussion	64
4.2.3	LaIrSi	64
4.2.4	CeIrSi	66
4.3	HfRhGe	76
4.3.1	Experimental details	76
4.3.2	Results and Discussion	77
5	1-1-3 compounds (EpTX₃)	83
5.1	Introduction	83
5.2	Experimental Details	84
5.3	Crystallography	85
5.3.1	The BaAl ₄ family	85
5.3.2	Tetragonal BaAl ₄ derivative structure types	86
5.3.3	Orthorhombic BaAl ₄ derivative structure types	87
5.4	Superconductivity in the EpTX ₃ compounds with BaNiSn ₃ structure type .	88
5.5	Density functional theory (DFT) study for the EpTX ₃ compounds	95
5.5.1	Computational details	95
5.5.2	Structural details for the EpTX ₃ compounds as calculated by DFT	96

5.5.3	Electronic structure of the EpTX ₃ compounds as calculated by DFT	96
5.6	Listing of the samples analyzed	98
6	La₇Ir₃	106
6.1	Introduction	106
6.2	Results and discussion	108
7	La₃Pd₄Si₄ and Ce₃Pd₄Si₄	110
7.1	Introduction	110
7.2	Experimental	111
7.3	Results and Discussion	112
7.3.1	La ₃ Pd ₄ Si ₄	113
7.3.2	Ce ₃ Pd ₄ Si ₄	118
8	Summary	125
	Appendices	128
A	Programs and drafts	129
B	1-1-3 tables	147
C	Cleaning procedure of the ³He PPMS inset	155
	Bibliography	157

List of Figures

2.1	Cubic cell and how to count the atoms per unit cell.	5
2.2	Inversion symmetry operations.	7
2.3	Influences of the antisymmetric spin orbit coupling in the $E-\vec{k}$ plot.	9
2.4	Analysis of electrical resistivity in a superconductor.	22
2.5	Analysis of magnetic susceptibility in a superconductor.	23
2.6	Analysis of the temperature dependent heat capacity in a superconductor.	24
2.7	Random distribution of superconducting and normal conducting parts in the sense of percolation theory.	27
2.8	Percolation theory in electrical resistivity.	28
3.1	Theoretical and practical depiction of a proper 4-point connection technique.	31
3.2	Puck used for electrical resistivity measurements	33
3.3	Schematic plot of the ^3He bath cryostat.	36
3.4	3D plot of the FRITZ sample holder.	37
3.5	3D plot of the pressure cell with the single parts.	39
3.6	Schematic overview of the μSR experiment.	42
4.1	Structural details of LaPtSi.	47
4.2	Electrical resistivity of LaPtSi	48
4.3	First derivative of the electrical resistivity of LaPtSi	49
4.4	Temperature dependent specific heat measurements measurements of LaPtSi	51
4.5	Debye fit to LaPtSi.	52
4.6	Magnetic susceptibility measurements of LaPtSi.	53
4.7	Upper critical magnetic field $\mu_0 H_{c2}(T)$ of LaPtSi.	54
4.8	Entropy difference of SC and NC state in LaPtSi.	55

4.9	Density of states of LaPtSi.	56
4.10	Fermi Surfaces of LaPtSi (scalar relativistic and fully relativistic).	57
4.11	Spin directions of the Fermi surfaces of LaPtSi	58
4.12	Phonon dispersion and DOS for LaPtSi.	60
4.13	Experimental and theoretical heat capacity C_p of LaPtSi.	60
4.14	Junod model applied to LaPtSi.	61
4.15	The structure derivation of CeIrSi and LaIrSi.	63
4.16	Temperature dependent electrical resistivity and heat capacity measurements of LaIrSi.	65
4.17	Temperature dependent electrical resistivity and heat capacity of CeIrSi.	69
4.18	Comparison of $C_p(T)/T$ of LaIrSi and CeIrSi in zero field.	70
4.19	Magnetic susceptibility measurement in dependency of the temperature in CeIrSi.	71
4.20	Curie-Weiss fit to $1/\chi$ data of CeIrSi.	72
4.21	Arrott Plot of CeIrSi.	73
4.22	Phase diagram and comparison of physical properties of CeIrSi.	74
4.23	Magnetization measurements of CeIrSi.	75
4.24	Structure of HfRhGe.	76
4.25	The electrical resistivity measurement of HfRhGe in dependence of the temperature.	78
4.26	The first derivative of the temperature dependent electrical resistivity of HfRhGe.	79
4.27	Temperature dependent specific heat of HfRhGe.	80
4.28	Upper critical field of HfRhGe.	81
5.1	Group-subgroup relations for BaAl ₄ and several binary and ternary derivative structure types.	84
5.2	Graphical summary of all formed phases with all BaAl ₄ derivative structure type in the ternary systems Ep-T-X.	85
5.3	Group-subgroup relations for BaAl ₄ -BaNiSn ₃	86
5.4	Temperature dependent electrical resistivity $\rho(T)$ of various EpTX ₃	89
5.5	Upper critical field behavior $\mu_0 H_{c2}$ of SrPdGe ₃ with and without applied hydrostatic pressure.	91

5.6	Temperature dependent heat capacity C_p measurements of SrNiSi ₃ , BaPdSi ₃ , SrPdSi ₃ , SrPtSi ₃ , SrPdGe ₃ and SrPtGe ₃	92
5.7	Upper critical field $\mu_0 H_{c2}$ behavior of superconducting EpTX ₃ compounds.	93
5.8	Difference between 0.1K (blue, below T_c) and 3K (red, above T_c) in μ SR measurements.	94
5.9	Electronic band structure of SrTSi ₃ (T = Ni, Pd, Pt).	97
5.10	Specific heat measurements of BaPdSi ₃	98
5.11	Physical properties of SrNiSi ₃	100
5.12	Physical properties of SrPdSi ₃	101
5.13	Physical properties of SrPtSi ₃	102
5.14	Physical properties of SrPdGe ₃	103
5.15	Physical properties of SrPtGe ₃	104
5.16	SrNiGe ₃ , BaPdSn ₃ and BaPdGe ₃ do not show a superconducting transition.	105
6.1	Structure of La ₇ Ir ₃	106
6.2	The electrical resistivity measurement and the first derivative of the electrical resistivity measurement of La ₇ Ir ₃	107
6.3	Behavior of the upper critical field at different temperatures of La ₇ Ir ₃	108
7.1	X-ray powder pattern and Rietveld refinement of La ₃ Pd ₄ Si ₄	112
7.2	Temperature dependent electrical resistivity, ρ , of La ₃ Pd ₄ Si ₄	114
7.3	The first derivative of the electrical resistivity for La ₃ Pd ₄ Si ₄	115
7.4	Temperature dependent heat capacity, C_p , of La ₃ Pd ₄ Si ₄	116
7.5	Low temperature specific heat C_p of La ₃ Pd ₄ Si ₄	117
7.6	Temperature dependent resistivity ρ of La ₃ Pd ₄ Si ₄ and Ce ₃ Pd ₄ Si ₄	119
7.7	Low temperature electrical resistivity, ρ , of Ce ₃ Pd ₄ Si ₄	120
7.8	Temperature dependent magnetic susceptibility, χ of Ce ₃ Pd ₄ Si ₄	121
7.9	Temperature dependent specific heat C_p of Ce ₃ Pd ₄ Si ₄ plotted as C_p/T vs. $\ln T$	122
A.1	Drafts of the FRITZ sample holder (Top view).	143
A.2	Drafts of the FRITZ sample holder (Bottom view).	144
A.3	Drafts of the FRITZ sample holder (Lower part).	145
A.4	Drafts of the FRITZ sample holder (Feed through).	146

Nomenclature

α_M	Maki parameter	ρ'	first derivative of the electrical resistivity
α_R	Rashba constant	ρ_0	residual resistivity value
σ	Pauli matrices	θ_D	Debye temperature
χ	magnetic susceptibility	\vec{B}	magnetic field
Γ	center of the Brillouin zone	\vec{E}	electric field
γ	Sommerfeld value/ Sommerfeld coefficient	\vec{G}	lattice vector
\hat{H}	Hamiltonian	\vec{j}	current density
\hbar	reduced Planck's constant	\vec{m}	magnetic moment
λ_{so}	spin-orbit coupling strength	\vec{S}	spin
λ_{ep}	electron-phonon coupling constant	C	heat capacity
λ_{th}	thermal conductivity	E	energy
μSR	muon spin relaxation spectroscopy	e	electric charge
μ_c^*	Coulomb repulsion	e^+	hole
μ^\mp	muon/ antimuon	H_{Pauli}	Pauli limiting field
$\mu_0 H_{c,th}$	thermodynamical critical field	k_B	Boltzmann constant
$\mu_0 H_{c1}$	lower critical field	N_A	Avogadro's number
$\mu_0 H_{c2}$	upper critical field	N_r	atoms per formula unit
$\mu_0 H_{c3}$	third critical field	p	pressure
μ_0	permeability of free space	Q	heat
ω_L	Larmor precession	T	temperature
π^\pm	pion $^\pm$	T_c	transition temperature
ρ	electrical resistivity	U	inner energy
		V	potential

Z	atomic number	NFE	nearly free electron
Z_{eff}	effective atomic number	NMR	nuclear magnetic resonance
a.c.	alternating current	P	polarization
AFM	antiferromagnetic	PUC	primitive unit cell
ASOC	antisymmetric spin-orbit coupling	RRR	residual-resistivity-ratio
BCS	Bardeen, Schrieffer and Cooper	SC	superconductivity
CEF	crystalline electric field	Sec.	section
DFT	density functional theory	SEM	scanning electron microscopy
eDOS	electronic density of states	SNS	superconducting-normal-superconducting
EPMA	electron probe microanalysis	SOC	spin-orbit coupling
Eqn.	equation	SQUID	superconducting quantum interference device
FC	field cooling	TF	transversal field
Fig.	figure	TRS	time reversal symmetry
FM	ferromagnetic	V	volume
GL	Ginzburg and Landau	WHH	Werthamer, Helfand and Hohenberg
GLAG	Ginzburg-Landau-Abrikosov-Gor'kov	XRD	X-ray powder diffraction
LDA	local density approximation	ZFC	zero field cooling
LF	longitudinal field		

Chapter 1

Introduction

For more than 100 years, science has been aspiring to unveil and understand the underlying mechanisms of superconductivity. Many important steps were set, from the Meissner effect to the BCS theory in the late 50s. For almost 70 years, superconductivity had just been observed in spin singlet superconductors with electron-electron interaction mediated by phonons. Therefore, the evidence of superconductivity in heavy fermion compounds opened up new insights in the field of superconductivity by Steglich *et al.* [1]. Less than 10 years later, the discovery of high temperature superconductivity in the so called cuprates by Bednorz and Müller [2] further provoked a deeper understanding of the dependency of symmetry and crystallographic peculiarities. Additional pairing channels like spin triplet pairing were synthesized at the end of the last millennium in Sr_2RuO_4 [3]. In 2004, superconductivity was proven in the material CePt_3Si [4, 5] showing that spin triplet pairing can exist in a non-centrosymmetric (NCS) crystal structure, i.e. a crystal structure with no center of inversion along at least one direction.

The existence of spin triplet pairing has previously stated to be strictly dependent on the existence of spatial symmetry by Anderson's theorem. The NCS crystal structure is held responsible for the emergence of an internal electric field which gives rise to an antisymmetric spin-orbit coupling (ASOC). ASOC splits the Fermi surface in dependency to their \vec{k} direction. Therefore, parity is not a good quantum number anymore. In theory, a mixture of spin singlet and spin triplet states occurs in the respective superconducting state. CePt_3Si shows additional physical effects, e.g., magnetic ordering, partly covering the peculiarities of the occurring superconductivity. These overlapping effects make it hard to deduce the influences of ASOC on the superconducting state. The theoretical considerations of a superposition of singlet and triplet pairing have further encouraged the scientific community. The search for new simple intermetallic materials with a NCS crystal structure can provide a deeper insight in this phenomenon in absence of other effects, e.g., magnetism. In 2006, the measurement of the London penetration depth in $\text{Li}_2\text{Pt}_3\text{B}$ [6]

gave the first indication of an unconventional superconducting state. By contrast, $\text{Li}_2\text{Pd}_3\text{B}$ shows a simple BCS behavior. The strength of any kind of spin-orbit coupling is dependent on the square of the atomic number Z^2 . Therefore in this series, ASOC reveals a very strong influence on the Pt containing sample, whereas the Pd containing sample appears to be less influenced. Substitutions on this system show that T_c changes continuously but the deviations of BCS behavior occur at a ratio of $\text{Li}_2(\text{Pd}_{1-x}\text{Pt}_x)_3\text{B}$ of $x=0.8$ [7]. Another example of a possible spin triplet superconductor in a simple intermetallic compound is $\text{Mo}_3\text{Al}_2\text{C}$ [8].

After this brief introduction, the thesis is organized as follows:

The second chapter gives a brief introduction to a basic understanding of superconductivity, crystallography, symmetry effects as well as the behavior of physical quantities like electrical resistivity, specific heat and susceptibility. It provides a guideline to understand and analyze these properties, especially the deviations from the ideal theoretical behavior. Moreover, the μSR technique will be explained and applied to the question of time-reversal symmetry (TRS) breaking.

The third chapter deals with the experimental part and will describe the measurement devices in detail. The advantages and disadvantages of different techniques will be discussed. Furthermore, several advices and tricks on how to use certain measurement equipments and troubleshooting protocols will be provided.

The different samples are classified based on their stoichiometric composition. The fourth chapter treats of the 1-1-1 compounds, i.e. LaPtSi , LaIrSi , CeIrSi and HfRhGe with different non-centrosymmetric crystal structures. The fifth chapter, dealing with 1-1-3 compounds, represents the largest group of materials in this thesis. A structured analysis of all 24 EpTX_3 compounds ($\text{Ep} = \text{Sr}, \text{Ba}$; $\text{T} = \text{Ni}, \text{Pd}, \text{Pt}, \text{Cu}, \text{Ag}, \text{Au}$; $\text{X} = \text{Si}, \text{Ge}$) was performed and will be presented in detail. The sixth chapter gives a short overview of the NCS compound La_7Ir_3 . Due to the dominance of La inside the sample, the preparation and measurements were very crucial. The seventh chapter covers the $\text{La}_3\text{Pd}_4\text{Si}_4$ and $\text{Ce}_3\text{Pd}_4\text{Si}_4$. Both materials possess a centrosymmetric space group. However, one will find some intriguing arguments for unconventional superconductivity in the sense of two energy gaps in the former compound, as well as magnetic ordering and the influence of crystalline electric field and the Kondo effect for the corresponding Cerium compound.

Chapter 2

Theoretical background

Matter is observable in four different states, namely plasma, gas, liquid and solid state. Even though most of the matter in the universe exists in plasma state, the main focus will be on the three latter, which are also commonly known as the classical states of matter. Generally, a phase transition from one state to another is indicated by a change of an order parameter. Regarding the states of matter, this is not an easy definition. A thermodynamic phase transition is caused by a change of a natural variable like temperature T or pressure p . However, there is no single order parameter which can explain the transition from the solid to the liquid and, simultaneously, the transition from the liquid to the gaseous state. The phase transition of a liquid to its gaseous state can be well defined by a change of the density, i.e. volume constancy, although this might be misleading for the transition from the solid to the liquid state, e.g., water. Therefore, the resistance to deformation is a second parameter that describes the phase transition from the solid to the liquid state. As it is a general principle of nature, a system tries to increase its entropy. A high entropy comes along with a strong disorder. While gases do not possess any kind of ordering, liquids may exhibit short-range order. Some exotic liquids might even develop a hybrid behavior between solid and liquid as it holds true for the liquid crystals [9]. Materials in the solid state have either short-range or long-range order, where a fundamental structure is not disturbed over long distances. Short-range ordering means that the symmetry arrangement of a certain structure is limited to just a small distance from an arbitrary reference point. Long-range ordering prevails over a wide distance and long duration. At 0 K and ambient pressure, almost every matter becomes a solid. Thus two other parameters such as spatial periodicity and the range of the ordering can be identified to refine the states of matter. In general, matter tries to arrange its atoms in such a way that there is a long-range order and a high periodicity. However, this cannot be achieved by every material. A solid can be seen as amorphous, if just short-range ordering is dominant and any kind of periodicity is absent. Another class of solids, the quasicrystals, is also

worth mentioning, since it possesses long-range ordering but no periodicity [10]. Finally, a solid which can be described by its periodicity and its long-range ordering, is known as a crystalline solid or simply a crystal. A wide range of materials, which can be encountered in everyday life, e.g., metals or ceramics, are crystals. Long-range ordering as well as periodicity enormously reduce the complexity of the mathematical description of such a huge amount of atoms. A crystal lattice is a three-dimensional periodic arrangement of positions, called lattice points. These lattice points are mathematically described by three vectors with coefficients, i.e. Fourier coefficients.

$$\vec{R} = n_1 \cdot \vec{a}_1 + n_2 \cdot \vec{a}_2 + n_3 \cdot \vec{a}_3. \quad (2.1)$$

The three vectors \vec{a}_i with $i = 1, 2, 3$ span the lattice. Different scalar values for the vectors $|\vec{a}_i|$ and different values for the angles between the vectors ($\vec{a} \wedge \vec{b} = \gamma$, $\vec{a} \wedge \vec{c} = \beta$, $\vec{b} \wedge \vec{c} = \alpha$) thus lead to 14 different lattice systems. They are commonly known as the Bravais lattices. The simple idea behind a Bravais lattice is that one can apply the translational operation on every point, then set the center into the newly created point and apply the operation again and so on. A thorough discussion about the mathematics and a detailed overview on the different lattices can be found in literature [11, 12]. A primitive unit cell (PUC) is defined as the volume which fully contains exactly one lattice point (see Fig. 2.1). This comprises also two lattice points on a surface, or four points lying on the edge of two sides, or eight points which are in the corners of the spanned primitive unit cell and so on. This can be stated by the simple relation $n \cdot V = 1$, where n is the concentration of the lattice points and V the volume that is covered. There are many ways to define the PUC, the only restriction is that it has to fill the whole space of a Bravais Lattice. However, the symmetry of the primitive unit cells often veils an underlying symmetry on a larger scale. Therefore, conventional unit cells, or simply called unit cells, are constructed which possess the same symmetry like the Bravais Lattice and, therefore, allows to make use of all the underlying symmetry operations.

The next step from a lattice to a crystal contains the idea of a base. The base consists of one or more atoms which are arranged relative to a lattice point. The atom positions are defined by a vector $\vec{r} = \sum_{i=1}^3 b_i \cdot x_i$ where b_i are the Fourier coefficients and x_i are the x , y and z direction, respectively. So the lattice plus the base build up the crystal.

The atoms are bond together, either due to ionic, covalent, metallic, hydrogen, van der Waal's bonding or a superposition of these effects. In a metallic bond, the electrons are not localized on a certain lattice site but move freely inside the solid. The Heisenberg uncertainty relation allows to determine the exact momentum of a particle $\vec{p} = \hbar \vec{k}$ but losing all information about the exact position of it at the same moment. In 1933 Arnold Sommerfeld took the results from quantum mechanics and applied the Fermi-Dirac distribution $f(E)$ to this problem. He calculated the results of the Schrödinger equation for

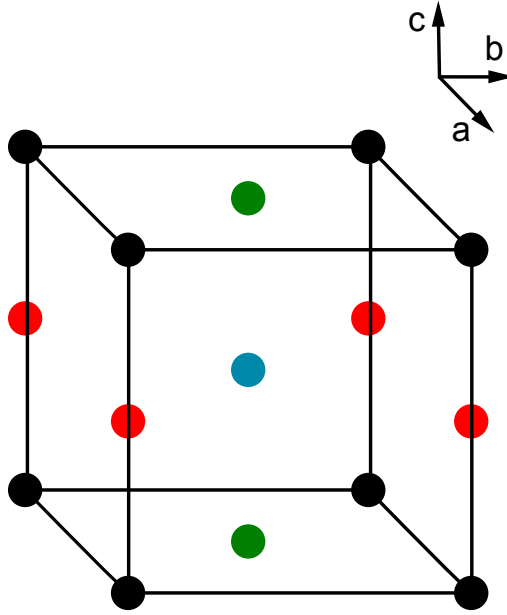


Figure 2.1: A schematic figure of a simple cubic unit cell and how to count the atoms inside the cell. Blue = 1, Green = 1/2, Red = 1/4 and Black = 1/8

an electron in an infinite potential. Those ideas gave rise to the concept of the density of states $D(E)$ which accounts for the number of possible quantum states in an energy shell ΔE :

$$D(E) = \frac{V}{2\pi^2} \frac{2m^{3/2}}{\hbar^2} \sqrt{E}. \quad (2.2)$$

As the kinetic energy is given by the relation

$$E = \frac{mv^2}{2} = \frac{\hbar^2 |\vec{k}|^2}{2m}, \quad (2.3)$$

one has a direct relation between energy and the wave vector \vec{k} with m , v and \hbar being the electron mass, the velocity of the electron and the reduced Planck's constant, respectively. The whole inner energy U , which is stored within the free Fermi gas, is then represented by

$$U = \int_{-\infty}^{\infty} f(E) D(E) E \, dE. \quad (2.4)$$

Furthermore, this new concept provided a valid explanation for the specific heat contribution of electrons in simple metals. Felix Bloch further extended the theory and interpreted the ion lattice as a periodic potential [13]. This led to the idea of bonded, static valence states and conduction bands, where electrons could move nearly free through the whole crystal, the nearly free electron model (NFE). The periodicity comes along with a Bragg reflection $\vec{k}' = \vec{k} + \vec{G}$ with a lattice vector \vec{G} between two lattice sites lifting the degen-

eracy and creating forbidden states. These energy gaps are responsible for the difference of conductors, semiconductors and insulators just as the electrons at the Fermi surface can participate in the charge carrier transport. Gaps in the band structure of electrons can further be the consequence of different physical effects, as e.g., the later discussion on superconductivity.

2.1 Symmetry aspects of crystals

Symmetry plays an extraordinary role in the physics of crystals and the search for the ground state of a system. There are four basic mathematical symmetry operations, which can further be combined. In detail, these are rotation, mirror, inversion and translation, which are shown in the Eqn. 2.5, 2.6, 2.7, 2.8. The matrices listed below are just examples of the more general types. In a point group there is one fixed point which is not changed under any of the former operations. This point is called center of inversion and is described by the symbol $\bar{1}$. The matrices Eqn. 2.5, 2.6, 2.7, 2.8 are examples of symmetry operations along the z-axis.

$$\begin{pmatrix} \sin(\theta) & \cos(\theta) & 0 \\ -\cos(\theta) & \sin(\theta) & 0 \\ 0 & 0 & 1 \end{pmatrix} \quad (2.5)$$

$$\begin{pmatrix} 1 & 0 & 0 \\ 0 & 1 & 0 \\ 0 & 0 & -1 \end{pmatrix} \quad (2.6)$$

$$\begin{pmatrix} -1 & 0 & 0 \\ 0 & -1 & 0 \\ 0 & 0 & -1 \end{pmatrix} \quad (2.7)$$

$$\begin{pmatrix} x & 0 & 0 \\ 0 & y & 0 \\ 0 & 0 & z \end{pmatrix} \quad (2.8)$$

The matrices 2.5, 2.6, 2.7 and 2.8 can be combined in any way and create new symmetry operations as well. Taking into account the translational operation, one can finally derive the 230 space groups.

Table 2.1: Combination of the four symmetry operations

	Rotation	Reflection	Inversion	Translation
Rotation		rotary reflection	rotary inversion	screw axes
Reflection			180° rotation	glide reflection
Inversion				inversion
Translation				

Symmetry considerations have shown that just rotations of 60°, 90°, 120°, 180° and 360°

are realized in nature¹. Those angles are symbolized by the numbers 6, 4, 3, 2 and 1 in the notation of crystallography, respectively. The combination of 180° rotation with the application of the inversion matrix thus gives the same result as applying the mirror matrix perpendicular to the respective axis. It can be represented either as $\bar{2}$ or simply m and is illustrated in Fig. 2.2.

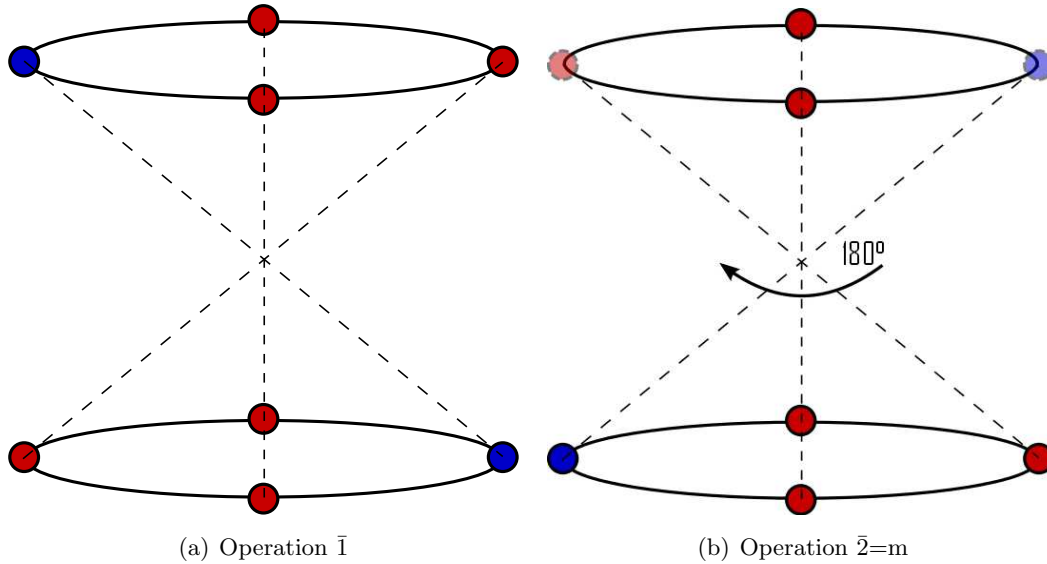


Figure 2.2: (a) The inversion symmetry for $360^\circ=\bar{1}$ (blue) and $90^\circ=\bar{4}$ (red). (b) For 2, 4 and 6 fold rotations, the inversion operation is equal to its mirror operation.

The center is indicated where the dashed lines cross. However, 21 of 32 possible point groups do not possess a center of inversion at all. These materials are referred to as non-centrosymmetric (NCS) materials. Generally, NCS materials can show some distinct intrinsic features, as e.g., the piezoelectric effect².

NCS materials possess an intrinsic electric potential V as a consequence of the absence of inversion symmetry. The gradient of a potential ∇V gives rise to an electric field \vec{E} with $\vec{E} = -\nabla V$. This electric field can be seen in the rest frame of the ionic lattice. For electrons, which are exposed to this electric field, it gives rise to an internal magnetic field \vec{B} . This can be understood in a relativistic sense, if one considers the rest frame of the electron, i.e.

$$\vec{B} = \frac{\vec{E} \times \vec{v}}{c^2}. \quad (2.9)$$

The further steps involve setting-up an appropriate Hamiltonian \hat{H} . The overall energy of a magnetic moment \vec{m} in a magnetic field is defined as $E = -\vec{m}\vec{B}$. Here, the magnetic moment of the electron will be constituted by its spin \vec{S} . If one adopts this idea one finally

¹besides the quasi-crystals mentioned above

²The point group 432 is one exception

gets

$$\hat{H} = c_1 \vec{S} \vec{B}, \quad (2.10)$$

with c_1 being a constant. With no loss of generality one can define the direction of the electric field gradient along the z-axis. This is indicated in Fig. 2.3(a). So an external magnetic field leads to a spin-orbit coupling (SOC). The Hamiltonian of the spin orbit interaction is represented by the Thomas term

$$\hat{H}_{SO} = -\frac{1}{2m^2 c^2 r} \frac{\partial V}{\partial \vec{r}} \vec{S} \vec{L}. \quad (2.11)$$

Inserting Eqn. 2.9 and Eqn. 2.10 in the above Eqn. 2.11 as well as considering that $\vec{L} = \vec{r} \times \hbar \vec{k}$ one derives

$$\hat{H}_{ASOC} = \alpha_R \cdot (\vec{\sigma} \times \vec{k}) \cdot \vec{e}_z \quad (2.12)$$

with $\vec{\sigma}$ representing the Pauli matrices. The α_R is the so-called Rashba constant, which includes the absolute value of the electric field $|\vec{E} = E_0|$. Rearranging the above equation finally gives

$$\hat{H}_R = \alpha_R \cdot (\vec{e}_z \times \vec{k}) \cdot \vec{S} = \alpha_R \cdot (k_y \cdot S_x - k_x \cdot S_y). \quad (2.13)$$

\hat{H}_R is known as the Rashba-type Hamiltonian [14]. The Rashba spin-orbit coupling is caused by a structural inversion asymmetry. A similar effect of the spin-orbit interaction, called Dresselhaus spin-orbit coupling, is caused by bulk inversion asymmetry or interface inversion asymmetry. The general term for both of these coupling mechanisms is the antisymmetric spin-orbit coupling (ASOC). The degeneration of the spin up \uparrow and spin down \downarrow energy band gets lifted. It is important to note that at $\vec{k} = 0$ the twofold spin degeneration prevails. Therefore, at the crystallographic Γ - point, i.e. the center of the Brillouin zone, the spin up and spin down bands are still degenerate as seen in 2.3.

Without an external magnetic field, the Hamiltonian, composed of the kinetic part in Eqn. 2.3 and the Rashba-type Hamiltonian in Eqn. 2.13, gives the dispersion relation

$$E^{\uparrow, \downarrow} = \frac{\hbar^2 k^2}{2m} \pm \alpha \vec{k}. \quad (2.14)$$

The spin orbit interaction is roughly dependent on the square of the atomic number, Z^2 . For a quasi hydrogen-like atom, the Z is set to Z_{eff} with Z_{eff} including the screening effect of the electrons. This can be seen as a rough proportionality but it enables new channels to trigger and tune spin-orbit effects, which will be later discussed in Sec. 5.

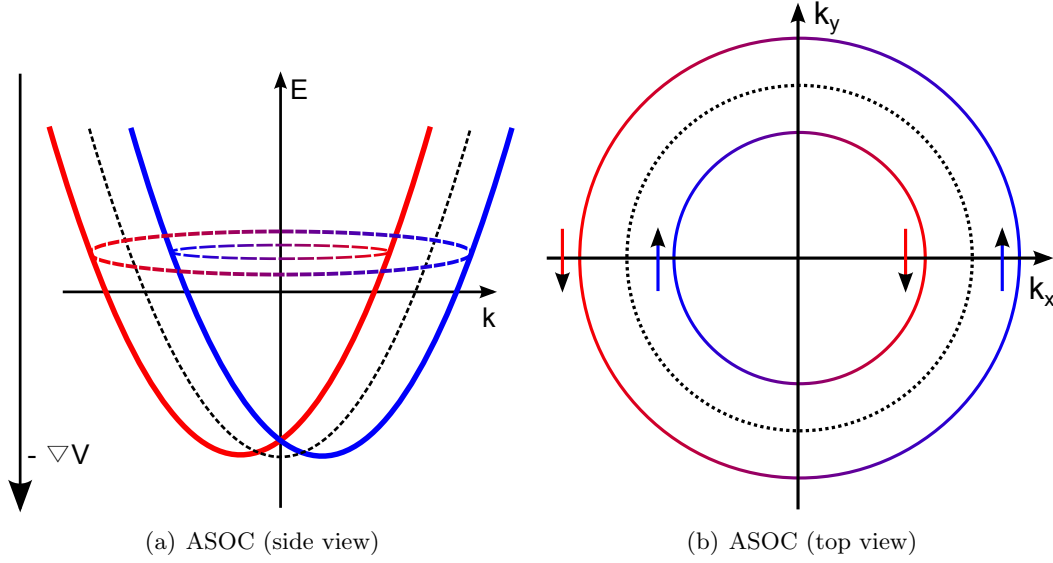


Figure 2.3: (a) The influence of an internal electric field on the dispersive bands relation of (free) electrons. The black dashed line indicates the unperturbed, degenerate state of the electrons. The resulting magnetic field splits the Fermi surface in the $k_x - k_y$ plane. This finally results in two different Fermi surfaces, where the spin itself is not a good quantum number anymore. (b) View from the top, directly on the $k_x - k_y$ plane. The colors represent the direction of the spin.

2.2 Electrical resistivity

Before the development of quantum physics, different approaches to describe the transport of electrons inside a conductor had been elaborated. One of the most famous models is the Drude model, which argues that an electron gets accelerated in an electric field and experiences collisions on the static ion lattice. With the current density \vec{j} , the density of the electrons n , the conductivity σ , the electric charge e , the time between two collisions τ and the electron mass m one gets the Drude form of Ohm's law.

$$\vec{j} = \left(\frac{ne^2\tau}{m} \right) \vec{E} = \sigma \vec{E}. \quad (2.15)$$

As an average result, a single electron loses all its energy in the scattering event and is accelerated again in the field, till the next collision occurs. This process is repeated as long as the electric field exposes a force on the electron itself. However, since the Drude model does not take into account any quantum mechanical effect, the electric force in this model affects all of the electrons and gives false results of the electric conductivity. However, it gives correct results for simple metals in terms of the Wiedemann-Franz law

$$\frac{\lambda_{th}}{\sigma} = LT \quad (2.16)$$

with λ_{th} , L and T being the thermal conductivity, the Lorenz number and the temperature, respectively. As the thermal conductivity is a transport phenomenon as well, the mistake cancels out and, therefore, the Drude model still has some meaning in modern physics. The simplicity of the Drude model is based on the phenomenon that for simple metals the electrons behave like free particles with just a modulation according to the periodic potential, as described above in the Bloch model. The main difference is that not all of the electrons contribute to the transport, but just a small amount of states localized around the Fermi level. Another important parameter in physics is the electric charge carrier mobility μ which can be derived from the simple Drude model,

$$\mu = \frac{|\vec{E}|}{|\vec{v}|}. \quad (2.17)$$

A comparison of Eqn. 2.18 and Eqn. 2.15 with $\vec{j} = -ne\vec{v}$ to the electrical resistivity ρ gives

$$\rho = -\frac{1}{ne\mu}. \quad (2.18)$$

In a real compound the charge carriers can be either electrons or holes. The idea is quite simple and will be briefly discussed. The state of an electron is fully described by five quantum numbers (n, l, m_l, s, m_s) . Given that there is a spherical Fermi surface, the electrons will occupy all states which are inside a sphere with a radius vector k_F . If just one position remains unoccupied, all the k-vectors opposed to each other cancel out. So just the state opposite to the unoccupied position persists. Instead of describing $n-1$ electrons, we can simplify this consideration by introducing one hole which moves in the opposite direction. Superconductivity in high temperature cuprates is often dominated by hole (e^+) pairing.

Nowadays, a sophisticated analysis of transport phenomena is conducted in the terms of the Boltzmann equation. The equation holds true for macroscopical as well as microscopical considerations if the free mean path is long in comparison to the average collision time. If this condition is not fulfilled, one has to make use of the Navier-Stokes equation. This equation describes how a collision of particles changes the density function $f(\vec{r}, \vec{p}, t)$ while exposed to changes according to time t , space \vec{r} and momentum \vec{p} . The four terms are usually written as

$$\left(\frac{\partial}{\partial t} + \frac{\vec{p}}{m} \nabla_{\vec{r}} + \vec{F} \nabla_{\vec{p}} \right) f(\vec{r}, \vec{p}, t) = \frac{\partial f}{\partial t}_{\text{coll}}. \quad (2.19)$$

Especially the colliding term $\frac{\partial f}{\partial t}_{\text{coll}}$ is often a rather complicated parameter and can just be calculated numerically. The common Bloch-Grüneisen law can be derived from the Boltzmann equation and sets the basis for a deeper insight and an overlap with additional effects, e.g., $s-d$ scattering effects.

2.3 Specific heat

Heat capacity (C) is the capability of a material to absorb or emit a certain amount of heat (δQ) while a temperature change of δT takes place. It can also be seen as the amount of heat ΔQ which is necessary to change the temperature of a material by ΔT . The general formulation is thus

$$C = \frac{\Delta Q}{\Delta T}. \quad (2.20)$$

With the first law of thermodynamics, $dU = \delta Q - pdV$, one can define the heat capacity at a constant volume V as

$$C_V = \left(\frac{\partial U}{\partial T} \right)_V. \quad (2.21)$$

In solid state physics it is experimentally easier to measure the heat capacity at a constant pressure p . With $H = U + pV$ one obtains for the heat capacity at constant p

$$C_p = \left(\frac{\partial H}{\partial T} \right)_p. \quad (2.22)$$

As the change of the volume is small while exposed to pressure, the following relation holds true in a solid $C_p \approx C_V$. Here, the main focus will be the heat capacity of a crystal. The next step is to build up the inner energy function $U(T)$. Every crystal has at least contributions from the ion lattice. The bonding between the ions can be visualized by springs. If the lattice gets excited, the ions start to vibrate. In other words, a phonon with the minimal excitation energy $E = \hbar\omega$ is created. Peter Debye applied a similar consideration of the Planck's law to the heat capacity of a solid. So there are quantized modes, the phonons (as equivalent to photons) which can be excited. Starting from the Debye model, it follows for the phononic contribution to the heat capacity a proportionality to T^3 with $C_{\text{ph}} = \beta T^3$ at lowest temperatures. The β factor is proportional to the Debye temperature θ_D . With the Boltzmann constant $k_B = 1.3806488 \times 10^{-23}$ J/K, the Avogadro's number $N_A = 6.02214129 \times 10^{23}$ 1/mol and N_r being the atoms per formula unit³ one obtains the following equation.

$$\theta_D = \sqrt[3]{\frac{N_A k_B N_r 12\pi^4}{5\beta}} \approx \sqrt[3]{\frac{N_r 1944}{\beta}}. \quad (2.23)$$

However, this model does not take into account optical modes. Optical phonons find consideration in the Einstein model, with just one single frequency ω_E [11]

$$C_p = \left(\frac{\partial U}{\partial T} \right)_{p=\text{const}} = \frac{3N}{k_B T^2} \frac{(\hbar\omega_E)^2}{\left[\exp\left(\frac{\hbar\omega_E}{k_B T}\right) - 1 \right]^2} \cdot \exp\left(\frac{\hbar\omega_E}{k_B T}\right). \quad (2.24)$$

³thus the number of atoms which are seen as one composition

The combination of both models is realized, e.g., in the so-called Junod model [15].

The density of states in a metal is finite at the Fermi energy. In the sense of the Sommerfeld model, the heat capacity of the electrons is proportional to the temperature T with $C_{\text{el}} = \gamma T$. The γ value is referred to as the Sommerfeld coefficient and is proportional to the density of states of electrons.

In the simple Debye model both contributions are taken into account at very low temperatures ($T < \frac{1}{50} \theta_D$) by the simple relation

$$C_p = \gamma T + \beta T^3. \quad (2.25)$$

Magnetic materials have further channels to absorb energy. Hence, a single excitation can be seen as a local magnetic moment which flips at a certain lattice site. A spin flip itself demands a higher energy and is thus separated from the oriented ground state by a certain energy gap. However, the magnetic moments can be dynamically coupled. Such an excitation is known as spin wave, and requires just a small amount of energy. In an analagon to the excitation of the lattice, those excitations are called magnons. Magnetic excitations, also known as magnons, contribute to the heat capacity proportional to $T^{3/2}$ or T^3 for ferromagnetic and anti-ferromagnetic materials, respectively. Other peculiarities of the heat capacity, e.g., crystal electric field splitting, will be discussed in the relevant sections.

2.4 Muon spin relaxation spectroscopy (μSR)

μSR is a proper tool to probe a bulk sample and analyze its internal magnetic structure, as it is very sensitive to inhomogeneous and small magnetic fields down to the order of 10^{-5} T within a sample. A muon μ is a metastable, elementary particle and belongs to the family of leptons. It has a negative (muon) or positive charge (antimuon), a spin of $1/2$, a mean lifetime of around $2.2 \mu\text{s}$ and a mass around 206.8 times the mass of an electron. As a spin $1/2$ particle it doesn't interact with a quadrupolar field, which is an advantage compared to other similar measurement methods like NMR. A muon is created by the decay of pions π .

$$\pi^+ \rightarrow \mu^+ + \nu_\mu \quad (2.26)$$

$$\pi^- \rightarrow \mu^- + \bar{\nu}_\mu. \quad (2.27)$$

In reality Eqn. 2.26 plays the major role for the μSR technique, as it can easily be experimentally achieved. The π^+ itself can be created in two different ways. One is via a proton-neutron interaction, the other way is via two protons colliding as given in the

following

$$p + n \rightarrow n + n + \pi^+ \quad (2.28)$$

$$p + p \rightarrow p + n + \pi^+. \quad (2.29)$$

The creation of a π^- , however, would require the use of antiprotons as colliding particles. The exact creation mechanism with common techniques will be discussed in Sec. 3.5. A fully polarized proton beam thus creates a fully polarized beam of μ^+ . The μ^+ further decays to a positron and two neutrinos via β^- decay. This is represented in the following

$$\mu^+ \rightarrow e^+ + \nu_e + \hat{\nu}_\mu. \quad (2.30)$$

The β^- decay violates the parity symmetry and is dependent on the spin direction. Therefore, the localization of the positrons unveil any change of the spin of the incident muons. The spatial distribution is thus given as

$$N_{e^+}(\theta) \propto 1 + P \cdot a \cdot \cos(\theta). \quad (2.31)$$

with P being the value of the polarization as an intrinsic asymmetry parameter and θ being the angle between the trajectory of the positron and the spin direction of the muon. If the positrons are just counted along the trajectory, the positron rate can be defined as

$$\frac{dN_{e^+}(t, \theta = 0)}{dt} = N(t = 0) \frac{1}{\tau_\mu} \left(1 + a \cdot P \underbrace{\frac{\vec{P}(t = 0) \cdot \vec{P}(t)}{\vec{P}(t = 0)^2}}_{G(t) = \frac{\langle \vec{s}(t) \cdot \vec{s}(0) \rangle}{\langle \vec{s}(0)^2 \rangle}} \right). \quad (2.32)$$

The positron rate is the amount of positrons N_{e^+} which can be counted in a time interval dt for a certain angle. There are several probing techniques for superconductors, mainly classified by the direction of the applied external magnetic field and the history of the cooling procedure, i.e. whether they are zero field cooled (ZFC) or field cooled (FC). The magnetic field can be either transversally (TF) or longitudinally (LF) aligned to the incident beam trajectory.

In a TF- μ SR technique, the muon is exposed to different magnetic fields, which can be summed up as a superposition like

$$\vec{B}_\mu = \mu_0 \vec{H}_{\text{ext}} + \vec{B}_{\text{dm}} + \left(\vec{B}_{\text{KS}} + \vec{B}_{\text{dip}} \right)_{\text{intrinsic}} + \dots \quad (2.33)$$

\vec{H}_{ext} is the external TF, \vec{B}_{dm} is the macroscopic demagnetization, \vec{B}_{KS} arises from the spin susceptibility and will be referred to as the Knight shift and \vec{B}_{dip} is the internal field from the microscopic dipole moments surrounding the muons. The field \vec{B}_μ leads to

a precession of the spin of the muon, which is known as the Larmor precession, $\omega_L = -\gamma_\mu \cdot B_\mu$. The technique allows samples to be probed for spin triplet pairing mechanism in a superconductor and, therefore, for a resulting spin susceptibility and internal dipole moments.

The LF method enables samples to be probed whether it breaks TRS or not by an additional spontaneous internal magnetic field below the SC transition. Therefore, the sample has to be investigated in ZFC and in FC. Both measurement curves are then compared. If the sample lacks additional magnetic phenomena, the polarized spin along the trajectory will show a proportionality $N_{e^+}(\theta) \propto 1 + P$. [16].

2.5 Superconductivity

This section gives an overview and comprises the basic knowledge of superconductivity (see also [17, 18, 19]). Since the discovery of superconductivity in 1911 by Heike Kamerlingh Onnes, more than one hundred years have passed. Even though superconductivity is one of the closest investigated phenomena in physics, especially in quantum physics, the basic mechanisms are not yet fully understood. Superconductivity is always realized as a coherent state of electrons or holons which are arranged pairwise as Cooper pairs. Conventional superconductivity originates as a result of electron phonon interaction with a symmetric gap in the electronic density of states (eDOS) at $E = E_F$. The term unconventional superconductivity comprises other pairing channels, either in terms of symmetry or in terms of the exchange particles.

At the beginning of the 20th century there were widespread speculations on the intrinsic behavior of electrical resistivity in the limit of absolute zero temperature. The expected scenarios varied from a continuous decrease to zero, to a saturation or even an increase at lowest temperatures. In a perfect crystal the resistivity would slowly decrease until the energy would be too low to excite phonons on which the electrons could scatter. If there was no scattering center left, the resistivity would be zero. One decisive development to find the answer to this question was the liquefaction of ^4He by Onnes in 1908, which was rewarded with the Nobel prize five years later. In 1911, while investigating the electrical resistivity of pure mercury, he observed a sharp drop to zero, which always happened at the same temperature. This was the first discovery of superconductivity (SC). However, the intrinsic mechanism of SC had remained unclear for more than twenty years, until Fritz Walther Meissner and Robert Ochsenfeld [20] found that superconductors can completely repel an external magnetic field. Since it does not matter whether a superconductor is first cooled down and afterwards exposed to an magnetic field (ZFC) or vice versa (FC), they were able to show that SC itself is more than just absolute zero electrical resistivity

$\rho = 0$ but also a perfect diamagnet $\chi = \frac{M}{H} = -1$ with χ being the magnetic susceptibility. Nevertheless, this result is just valid for small values of external magnetic fields. Generally, one distinguishes between a type I and a type II superconductor. Whereas for the former type it is energetically favorable to fully establish superconductivity inside the sample and expel the magnetic flux until the external field completely destroys the superconductivity, the latter favors a penetration of the magnetic field into the material.

2.5.1 Theories of superconductivity

London theory

In the 30s of the 20th century, Fritz and Heinz London were able to show that the repulsion of an external magnetic field was a logic consequence of a superconductor minimizing its free energy. The London equations allowed to provide a correct macroscopic picture of the superconducting behavior. From Ohm's law in Eqn. 2.15 one deduces the first London equation by applying the rotator on both sides

$$\nabla \times \vec{J} = -\frac{e^2 n}{mc} \vec{B}. \quad (2.34)$$

With $\nabla \times \vec{B} = \frac{4\pi}{c} \vec{J}$ and the Maxwell equation $\nabla \cdot \vec{B} = 0$ one easily calculates the second London equation

$$\begin{aligned} \Delta \vec{B}(x) &= \frac{1}{\lambda_L} \vec{B} \\ \vec{B}(x) &= \vec{B}_{\text{out}} e^{-x/\lambda_L}. \end{aligned} \quad (2.35)$$

λ_L is the London penetration depth equal to $\sqrt{\frac{mc^2}{4\pi e^2 n}}$ and \vec{B}_{out} being an external magnetic field. It is a measure of the distance at which the magnetic field inside the sample is e -times weaker.

Ginzburg-Landau theory

Continuing work, starting from London's results, was done by Ginzburg and Landau (GL) who developed a theory for the free energy. Within this theory, the free energy is dependent on an order parameter. In the sense of superconductivity, this parameter is realized by the wave function Ψ . Therefore, Ψ is 0 in the normal state and finite in the SC state.

$$F = F_{nc} + \alpha |\Psi|^2 + \beta |\Psi|^4 + \frac{1}{2m} \left| \left(-i\hbar + 2e\vec{A}\nabla \right) \Psi \right|^2 + \frac{\vec{B}^2}{2\mu_0}. \quad (2.36)$$

Minimization with respect to the vector potential A and Ψ gives the well-known Ginzburg-Landau equations [21].

$$\mu_0 \vec{J} = \frac{ie\hbar}{2m} (\Psi \nabla \Psi^* - \Psi^* \nabla \Psi) + \frac{2e^2}{m} |\Psi|^2 \vec{A} \quad (2.37)$$

$$0 = \alpha \Psi + \beta \Psi^3 + \frac{1}{2m} \left(-i\hbar + 2e\vec{A}\nabla \right)^2 \Psi. \quad (2.38)$$

It has to be noted that at the time when the GL theory was derived, it was not clarified that two electrons were involved in the formation.

If we now set the external field or rather the vector potential \vec{A} zero and normalize the order parameter $\Psi = \left(\frac{|\alpha|}{\beta} \right)^{1/2} f$ we can deduce from the first GL Eqn. 2.36 the following differential equation

$$\underbrace{\frac{\hbar^2}{2m|\alpha|}}_{\xi_{GL}} \frac{d^2 f}{dx^2} + f(1 - f^2) = 0. \quad (2.39)$$

The parameter ξ_{GL} as it is shown in the above Eqn. 2.39 thus emerges from the normalization of the GL equations. It is known as the coherence length and plays a very important role in the characterization of superconductors and we can finally clarify the meaning of the GL parameter κ . The connection between London penetration depth λ_L , GL parameter κ and GL coherence length ξ_{GL} and the critical magnetic fields are given in the following

$$\kappa = \frac{\lambda_L}{\xi_{GL}} \quad (2.40)$$

$$B_{c1} = \frac{\Phi_0 \ln \kappa}{4\pi \lambda_L^2} \quad (2.41)$$

$$B_{c2} = \frac{\Phi_0}{2\pi \xi_{GL}^2}. \quad (2.42)$$

Values of $\kappa \leq 1/\sqrt{2}$, $\kappa \geq 1/\sqrt{2}$ thus clearly discern between the type I and type II superconductors, respectively. However, the magnetic flux inside the type II superconductor is quantized which is then called a fluxoid $\Phi_0 = \frac{h}{2e}$. An increase of the external magnetic fields increases the number of fluxoids until the field reaches a critical value $\mu_0 H_{c2}$ where the superconducting states collapses. This result allowed superconductivity to be seen as a new thermodynamical state, where the transition without external magnetic field is from second order, i.e. without latent heat.

The Ginzburg-Landau theory is a phenomenological approach, derived from the basic laws of a thermodynamic transition of the second order type. Due to this reason the original theory made use of the general depiction of q instead of $-2e$ for the charge carriers. The theory mainly focused on the macroscopic properties of the superconducting wave function. However, the value of these equations had not been accounted for some years,

till the next milestone was developed and in 1960 Gorkov and Abrikosov were able to derive the GL equations from a microscopic point of view at temperatures close to the transition temperature T_c . Therefore, the Ginzburg-Landau theory was extended to the Ginzburg-Landau-Abrikosov-Gor'kov (GLAG) theory. Within it was shown that the GL theory could be derived from microscopic considerations of the so-called BCS theory from Bardeen, Schrieffer and Cooper, which will be presented in the following Section.

BCS theory and modern approaches to superconductivity

In 1950, Fröhlich showed that the electron-electron interaction can have an attractive component, if the energies of the electrons are very close together and their \vec{k} are orientated parallel or anti-parallel [22]. The same year Fröhlich theoretically predicted the isotope effect. The vibrational energy of a phonon is $\hbar\omega$. The frequency ω itself is dependent on the mass of the atom via the harmonic dispersion relation $\omega(k, M) = \sqrt{\frac{2c}{M} \cdot (1 - \cos(ka))}$. If an element has more than one isotope, the transition temperature has a negative proportionality with increasing mass $M^\alpha T_c = \text{const.}$ with an α close to 0.5. This effect was proven later that year and was especially analyzed in detail for tin and lead [23]. An important, but rarely mentioned side note is that the isotope effect has its limitation to the non transition elements [24]. In 1956 Cooper developed the fundamental idea that even a weak attractive potential $U(x-y)$ can cause an instability to the Fermi sea and leads to bound electron pairs [25]. This instability is caused by the indirect interaction of two electrons which can be realized by an exchanged Boson. In the original BCS theory those interacting particles were identified as the phonons. The small energy range, where electron-electron interaction is attractive, is approximately $2\hbar\omega_D$. However, the basic ideas can be also applied to other exchange particles. This considerations include the emission and absorption of virtual phonons. Starting from the ideas of Fröhlich and Cooper, a fundamental idea is the opposite spin and momentum directions of the two electrons, i.e.

$$\left| \hbar\vec{k}, \uparrow \right\rangle_1 \text{ and } \left| -\hbar\vec{k}, \downarrow \right\rangle_2, \quad (2.43)$$

because the pairing probability reaches its maximum. Those kind of pairs of electrons are known as Cooper pairs. Both electrons have the same energy $\frac{\hbar^2 k^2}{2m}$ in the initial state. If the electron emits a virtual phonon with a momentum $\hbar\vec{q}$, it reduces its momentum to $\hbar\vec{k}' = \hbar\vec{k} - \hbar\vec{q}$. The same virtual phonon gets absorbed by another electron with the opposite spin and momentum, thus the momentum changes to $-\hbar\vec{k}' = -\hbar\vec{k} + \hbar\vec{q}$.

In 1957 the BCS theory, named after its developers Bardeen, Cooper and Schrieffer [26], was invented. Starting from the superconducting pair function in real space $\Phi_{\alpha\beta}(x, y)$.

$$\Phi_{\alpha\beta}(x, y) = \left\langle \psi_\alpha^+ \psi_\beta^+ \right\rangle. \quad (2.44)$$

ψ_α^+ and ψ_β^+ create multi-fermion wave functions at different sites with spin direction α and β . In the disordered phase, the thermal integral in Eqn. 2.44 is 0, as the phases of each single electron function are not correlated among each other. Just the condensed BCS ground state, where the electrons form pairs, is a correlated function and the integral deviates from 0. The superconducting gap is introduced by

$$\Delta_{\alpha\beta}(x, y) = \Phi_{\alpha\beta}(x, y)U(x - y). \quad (2.45)$$

The basic idea was to identify the gap function as the order parameter of the superconducting state. It has to be noted that Φ in the BCS theory should not be mixed with the order parameter Ψ from the GL theory in Eqn. 2.36. However, as it is unveiled from Eqn. 2.45, the GL order parameter is proportional to the BCS pairing function. Generally, in solid state physics it is more favorable to depict the functions in the \vec{k} -space. Therefore, one has to apply a Fourier transformation on Eqn. 2.45. As with $V_{\vec{k}} = \frac{(2\pi)^3}{V_{\vec{r}}}$ being the volume in \vec{k} -space and $V_{\vec{r}} = \tilde{a}_1 * \tilde{a}_2 * \tilde{a}_3$ with the a_i are described in Eqn. 2.1, the gap in \vec{k} -space is then given by

$$\Delta(k) = \frac{1}{V_{\vec{k}}} \sum_p \Phi(k - p)U(p). \quad (2.46)$$

However, the simple picture of a regular Boson- particle gives a wrong impression in the vicinity of the superconducting gap function. The isotope effect manifests that phonons might be accounted as the interaction particles, mediating the attractive potential in the conventional frame of superconductivity. This can be also seen as a kind of polarization effect which screens the Coulomb repulsion of the electrons. The electron polarizes the ionic lattice and due to retardation effects the polarized lattice itself appears attractive to a second electron. The formation of Cooper pairs is thus strongly dependent on the strengths of the Coulomb repulsion in comparison to the attractive potential due to the exchange of bosonic particles. The remarkable conclusion is that materials with a very good conductivity, such as copper, gold and silver, do not become superconducting at ambient pressure and at temperatures, at least above 100 μ K. The electrical resistivity is strongly dependent on the charge carrier mobility as discussed in Eqn. 2.18 and Eqn. 2.17. Therefore, the velocity of the electrons plays a major role in the interplay of the repulsive and attractive forces. The velocity can be easily derived from the dispersion relation for the free electron gas approximation in Eqn. 2.3. The first derivative of the energy band thus gives the velocity

$$\frac{\partial E}{\hbar \partial \vec{k}} = \frac{\hbar \vec{k}}{m} = \vec{v}. \quad (2.47)$$

In the BCS theory the Coulomb repulsion μ_c^* is implicitly accounted by the term $V_0 D_n(0) =$

$\lambda_{ep} - \mu_c^*$. The critical temperature T_c is strongly dependent on this parameter, i.e. [26]

$$T_c = 1.13 \cdot \theta_D \exp\left(\frac{-1}{\lambda_{ep} - \mu_c^*}\right). \quad (2.48)$$

The electron-phonon coupling constant λ_{ep} is defined in more detail in the theory of Eliashberg [27]. It is also well known as the electron-phonon enhancement factor. The latter can be expressed by the density of states for the phonons $D_{ph}(\omega)$ and an $\alpha^2(\omega)$ -value which represents the strength of the electron-phonon coupling, thus gives

$$\lambda_{ep} = 2 \cdot \int_0^\infty \frac{\alpha^2(\omega) D_{ph}(\omega)}{\omega} d\omega. \quad (2.49)$$

Several other expressions for the relation of T_c , including the Coulomb repulsion and the electron-phonon coupling, can be found in literature. Later, the McMillan formula [28], which is a semi-empirical approach with the relation, will be used to analyze the samples.

$$T_c = \frac{\theta_D}{1.45} \exp\left(-\frac{1.04 (1 + \lambda_{ep})}{\lambda_{ep} - \mu_c^* (1 + 0.62\lambda_{ep})}\right). \quad (2.50)$$

In the McMillan formula, the Coulomb repulsion is often taken from literature values for comparable materials. However, it appears to be difficult to state a proper value, as the bare repulsion becomes screened due to the positive lattice atoms. With the proper application of band structure calculations of the phonon branches, λ_{ep} can be calculated and μ_c^* can be fitted to experimental results.

In 1962 Josephson found a new interpretation of the proximity effect in SNS (superconducting-normal-superconducting) contacts and predicted the Josephson current [29]. Within this theory, the superconducting current is sensitive to the phase difference of the macroscopic wave function. The Cooper pairs can tunnel through the thin normal-conducting barrier together. If the contacts are arranged in a loop, a change of the magnetic flux which flows through the loop will significantly change the phase of the resulting wave function. This principle gave rise to the development of superconducting quantum interference devices (SQUID).

2.5.2 Unconventional superconductivity

Generally, unconventional superconductivity covers all kind of superconductivity, which cannot be explained in terms of the BCS theory. Another, more sophisticated, definition can be found in the terms of the superconducting gap function. Therefore, an unconven-

tional superconductor fulfills the following condition

$$\sum_{\vec{k}} \Delta(\vec{k}) = 0. \quad (2.51)$$

As in 1979 Steglich *et al.* [1] discovered superconductivity in strongly correlated electron systems, new features of the SC state could be unveiled. In the bracket notation $|s, m_s\rangle$ with s being the spin and m_s being the magnetic spin quantum number, two electrons can pair either as a singlet

$$|0, 0\rangle = \frac{1}{2} (|\uparrow, \downarrow\rangle - |\downarrow, \uparrow\rangle) \quad (2.52)$$

or a triplet

$$\begin{aligned} |1, 0\rangle &= \frac{1}{2} (|\uparrow, \downarrow\rangle + |\downarrow, \uparrow\rangle) \\ |1, 1\rangle &= |\uparrow, \uparrow\rangle \\ |1, -1\rangle &= |\downarrow, \downarrow\rangle. \end{aligned} \quad (2.53)$$

Cooper pairing among electrons with the same spin direction leads to a boson-like state with spin equal 1. This has further impact on the symmetry of the spatial part of the wave function. A Slater determinant is a possibility to represent a multi-fermionic system. It is antisymmetric under the exchange of two particles. As the spin function of a triplet system is symmetric under exchange, the wave function itself has to be antisymmetric. This is a consequence of Eqn. 2.44. The pair function in \vec{k} -space is often written as $g_{k,\alpha,\beta}$ and has to fulfill the antisymmetry condition as mentioned above. Therefore, it follows $g_{-k,\alpha,\beta} = -g_{k,\beta,\alpha}$. In the classical BCS theory, superconductivity is explained in the limits of the singlet pairing. In 1994 Maeno *et al.* discovered triplet pairing in the Sr_2RuO_4 compound ([3], [30]) and was later found in other materials as well (e.g., [31], [32], [33], [34]).

However, this classification only makes sense if the parity is still a good quantum number. This is not the case for a non-centrosymmetric material and, therefore, Cooper pairing is neither of the pure singlet nor the pure triplet pairing, but a superposition of both. In Sec. 2.1 it was shown that a lack of center symmetry in a crystal gives rise to an additional Hamiltonian, which lifts the spin degeneracy. Sec. 2.5.1 deals with the pairing mechanism of the Cooper pairs. As the condition in Eqn. 2.43 has the highest pairing probability and different states, i.e. FFLO states, where the resulting vector $\vec{K} = \vec{k}_1 + \vec{k}_2 \neq 0$ is disparate from 0, are not yet being observed definitely, one has to analyze the influence of the additional Hamiltonian \hat{H}_R from Eqn. 2.13. The emerging superconducting gap thus becomes \vec{k} -dependent. In Sec. 2.1 it was shown that the strength of the splitting is Z_{eff} dependent.

For the analysis of a superconducting material it is important to understand and interpret the experimental data. However, the experimental results often deviate from the theoretical

predictions. Therefore, a proper discussion of the properties investigated helps to build up a deeper understanding on the underlying mechanisms of transport and thermodynamical properties.

2.5.3 Transport phenomena in superconductors

- **Electrical resistivity:** In the temperature dependent electrical resistivity measurements, the superconducting transition is generally indicated as a sharp drop to zero. However, there are several factors which can either broaden the transition width, or lowering the transition temperature of a superconductor and might lead to wrong interpretations of the measurement results. Several possible ways to define the superconducting transition temperature are listed in literature. From physical point of view, the onset is often defined as 90% of the residual resistivity value ρ_0 and refers to the change of the order parameter. At this point already some of the electrons condense to Cooper pairs and shorten the electronic path through the sample, whereas the other electrons remain unaffected. Other approaches make use of the 0% value, as this ensures the practical usage of the superconducting material. Other attempts to specify the transition temperature T_c take into account the first derivative of the electrical resistivity $\rho' = \frac{d\rho}{dT}$ and define the maximum as T_c .

2.5.4 Thermodynamical properties of superconductors

- **Magnetic susceptibility:** The results of magnetic susceptibility measurements in a type I superconductor as well as a type II superconductor in the Meissner state show a magnetic susceptibility of -1 as mentioned previously. In a type I superconductor there exists just one critical field, which is referred to as the thermodynamical critical field $\mu_0 H_{c,th}$. A type II superconductor has two different fields, the upper critical field $\mu_0 H_{c2}$ and the lower critical field $\mu_0 H_{c1}$. To calculate thermodynamical effects, one defines a thermodynamical field $\mu_0 H_{c,th}$ which holds as an analogous form of the $\mu_0 H_{c,th}$ for a type I SC. There are two distinguishable effects in a superconductor which leads to different considerations. If a perfect conductor is exposed to an external magnetic field, an electric current will emerge, following Lenz's law. As the current will persist for an infinite time, the resulting magnetic field would be opposite and from the same value as the external magnetic field. This effect is called flux exclusion and happens in a perfect conductor as well as in a superconductor. The main difference, and the main reason why superconductivity can be seen as a new thermodynamical phase, is the Meissner effect, which was already mentioned above. The Meissner effect is a flux expulsion effect. If a normal conducting material is exposed to an external magnetic field, the permeability in general will not be much

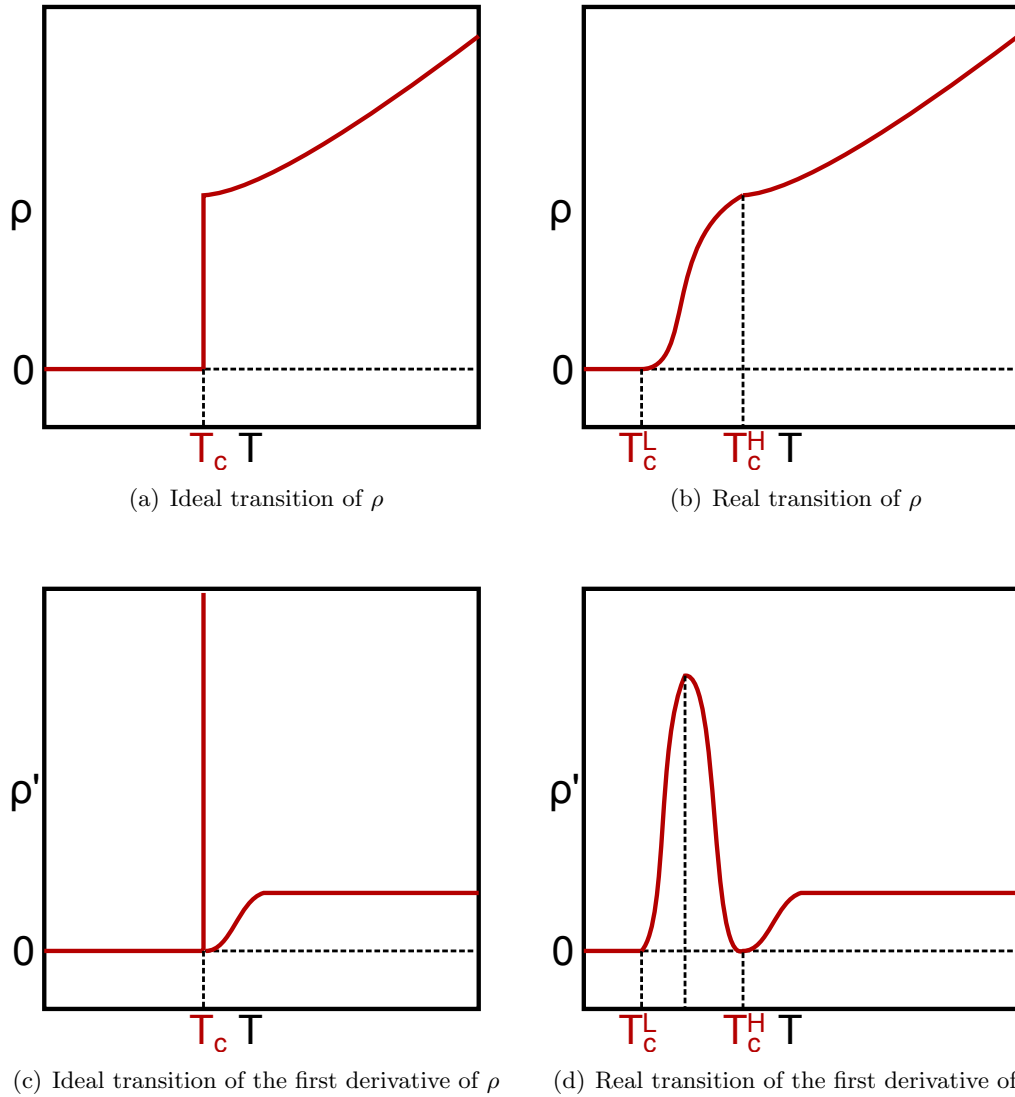


Figure 2.4: Different ways to identify the superconducting transition temperature T_c by the electrical resistivity and the first derivative data. (a) shows the ideal sharp superconducting transition at a temperature T_c . An analysis of ρ' in the ideal case (c) also shows a clear transition temperature. (b) schematically depicts a broadened transition. A clear identification of the superconducting transition seems to be difficult for the ρ as well as the ρ' data in (d). Though, several ways to define a transition temperature are listed in the text.

different to the vacuum value. If the material is then cooled down below $T_c(B_{\text{ext}})$ and the field is between 0 and either $\mu_0 H_{c,th}$ or $\mu_0 H_{c1}$ for a type I or a type II superconductor, respectively, a normal conductor and a superconductor will respond differently. In a perfect conductor, the field would persist, as there is no induction.

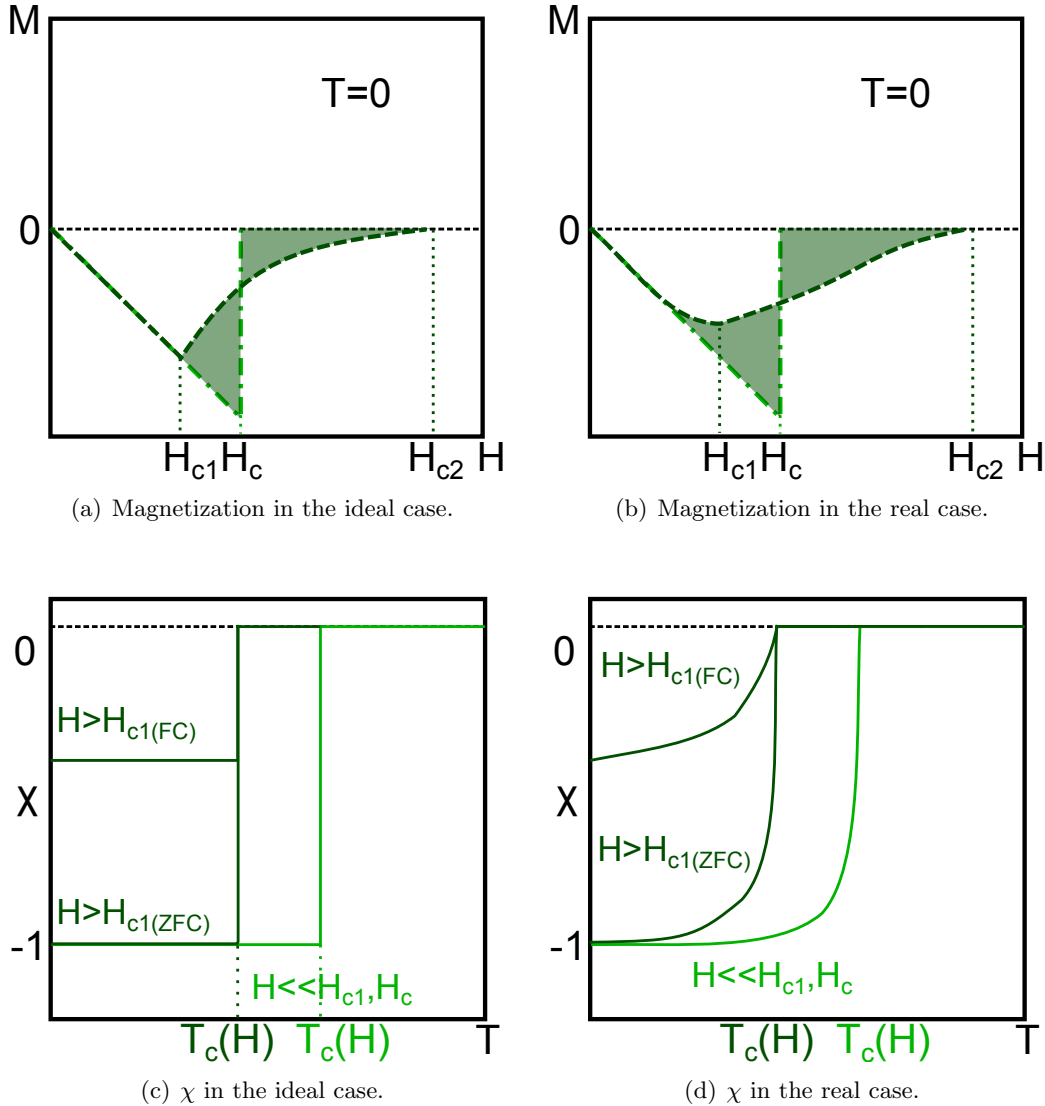
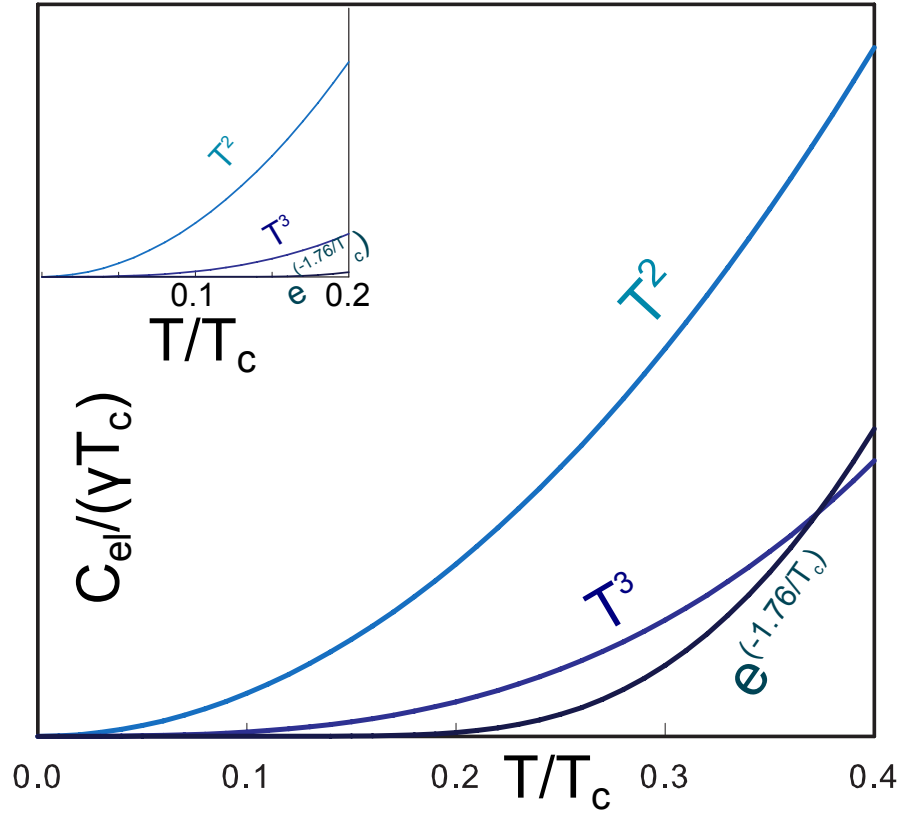
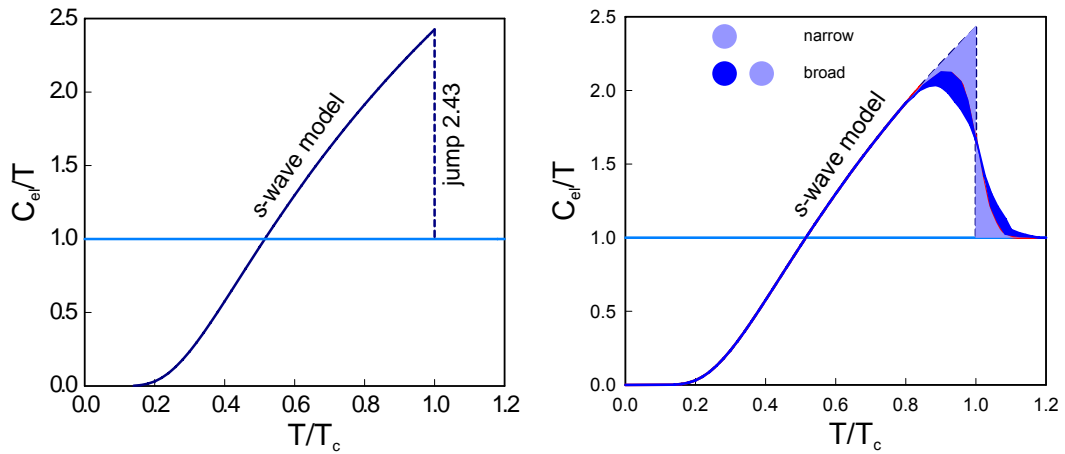


Figure 2.5: (a) shows the ideal superconducting transition for a type I (light green) and a type II (dark green) superconductor in the magnetization (M) measurements over the external field H. (b) the realistic behavior is shown, the transition becomes blurred. (c) and (d) schematically describe the transition in the magnetic susceptibility χ measurements. The differences of ZFC and FC are described in the text.

- Specific heat: Specific heat is an appropriate tool for investigating a superconducting transition. As a bulk property it is relatively stable against foreign phases. In a superconductor the electrons are condensed to Cooper pairs at the ground energy



(a) Different $C_p(T)$ behavior for gap functions with line nodes, point nodes and isotropic symmetry



(b) Ideal transition in $C_p(T)/T$ (Mühschlegel model)

(c) Real transition scenarios in $C_p(T)/T$

Figure 2.6: (a) shows different $C_p(T)$ behavior for gap functions with line nodes, point nodes and isotropic symmetry. (b) shows the BCS value in the s -wave model. The values were calculated by Mühschlegel [35]. T_c is identified at the jump position with a height of $2.43 \cdot C_n$. (c) shows transition of the heat capacity which are slightly broadened. Explanations can be found in the text. The colored areas left and right from the transition temperature should be equal.

level. The Cooper pair itself is not able to perform a transition to an excited state as the excitation leads to the decay of the pair itself. Therefore in a simple BCS superconductor, the amount of normal electrons decreases with lowering the temperature and the amount of possible energy excitations channels drops. BCS theory and thermodynamic considerations give different results. Thus it is not possible to formulate proper analytical solution for a conventional superconductor below T_c . However, at very low temperatures, below 40% of T_c , one can find a significant different behavior for conventional and unconventional superconductivity. The reason for this can be explained by the \vec{k} dependency of the energetic gap. For a conventional superconductor, the Fermi surfaces are supposed to be isotropic and, therefore, there are no nodes in the surface at all but a constant band gap Δ . For more complex forms of superconductivity, the gap is not isotropic anymore. Heat capacity is a thermodynamic property and thus gives in general an averaged value. The former remark holds true for polycrystalline samples, or single crystals without external magnetic fields. The distinct shapes of $C_p(T)$ below T_c are exponential, cubic and quadratic in temperature for BCS, node lines and point nodes, respectively. For many non-centrosymmetric superconductors, however, temperatures well below 40% of T_c are difficult to access. Furthermore, one needs a proper amount of measurement points to unequivocally derive a certain form of the gap structure. If the bulk sample consists of a large contribution of foreign phases, the specific heat will experience a reduced jump at $T = T_c$. The jump refers to the difference in C_p in the superconducting $C_{p,s}$ to the normal conducting state $C_{p,n}$, with $\Delta C_p = C_{p,s} - C_{p,n}$. These considerations do not apply to gapless superconductors [36].

2.5.5 Percolation theory

The main idea behind the percolation theory is based on the arbitrary distribution of a certain characteristic c inside an n -dimensional body and how this characteristic influences the transport of particles, which interact with the characteristic c . To provide a precise understanding of this general formulation, there are some reasonable examples given in the following. The origin of this theory is motivated by the question how a liquid will move through a porous material. An analysis of the tracks, i.e. an average minimum statistical distribution of ways through the sample, can be derived and bring light into this topic.

The principle ideas can be further applied to other questions and topics, i.e. normal conductors ([37], [38]), semiconductors and superconductors. First considerations regarding superconductivity were gathered in the sense of thin film superconductors. Focus of this thesis will be on the comparison of transport phenomena to bulk properties in a superconducting material, especially in the sense of conventional and unconventional or non-

centrosymmetric superconductors. In Sec. 2.5 the general transition behavior in transport and bulk properties was presented and will attract further attention especially in the analysis of the investigated samples.

One of the many peculiarities in a NCS material is the evident deviation of the $\mu_0 H_{c2}$ behavior in different physical properties. For a small Maki parameter α_M [39] it can be stated that bulk properties widely follow the conventional Werthamer or WHH model (after Werthamer, Helfand and Hohenberg) [40], whereas transport properties tend to follow a more linear behavior and thus exceed the usual upper critical field by far. Conventional BCS theory covers surface effects, also known as $\mu_0 H_{c3}$ behavior, which is linked to $\mu_0 H_{c2}$ via $H_{c3} \approx 1.695 H_{c2}$. However, several measurement results indicate a need for much higher external fields until superconductivity is completely suppressed. Early attempts of an explanation in terms of percolation superconductors were performed by Deutscher *et al.* [41]. There, a categorization of superconductors according to their resistivity values was performed and materials with a higher resistivity than $50 \mu\Omega\text{cm}$ were classified as percolation superconductors. This is based on the idea of a shorter mean free path limited by impurities. If the mean free path is shorter than the superconducting coherence length, those impurities become more or less invisible.

In NCS materials, a splitting of the Fermi surface for spin up and spin down electrons persists. Certain channels for spin singlet as well as spin triplet pairing open up and can be visualized theoretically by band structure calculations or experimentally by μSR measurements. A polycrystalline NCS material has a lot of different orientations within one bulk. If there is a negligible amount of spin triplet channels in a certain direction, the spin triplet pairing will not be influenced in the same way like a spin singlet pairing, while exposed to an external field. Therefore, spin triplet pairs might still be present inside the bulk, whereas the spin singlet pairs are already broken up.

High temperature SC, e.g., cuprates, show different $\mu_0 H_{c2}$ behavior in a single crystal along and perpendicular to the CuO layers. In addition, two-gap superconductors also show a different slope of $\mu_0 H_{c2}$ when T_c tends to zero as it is shown in Sec. 7. However, there is always a good agreement of the bulk as well as the transport phenomena. As it is discussed above, the main differences are the two discriminable Fermi surfaces, with a certain k-dependence. With the help of the percolation theory, one can show that the volume fraction of the superconductivity does not linearly correspond to the drop in the resistivity level. So even with a very small volume fraction, the material can still appear to be superconductive. As superconductivity still prevails in the temperature dependent electrical resistivity measurements even to very high external magnetic fields and the resistivity does not reach an intermediate ρ_0^* value, a foreign phase is unlikely to be hold responsible for this peculiarities. Therefore, the spin triplet channel might cause this effect. The flow of the electrical current is represented by Fig. 2.8.

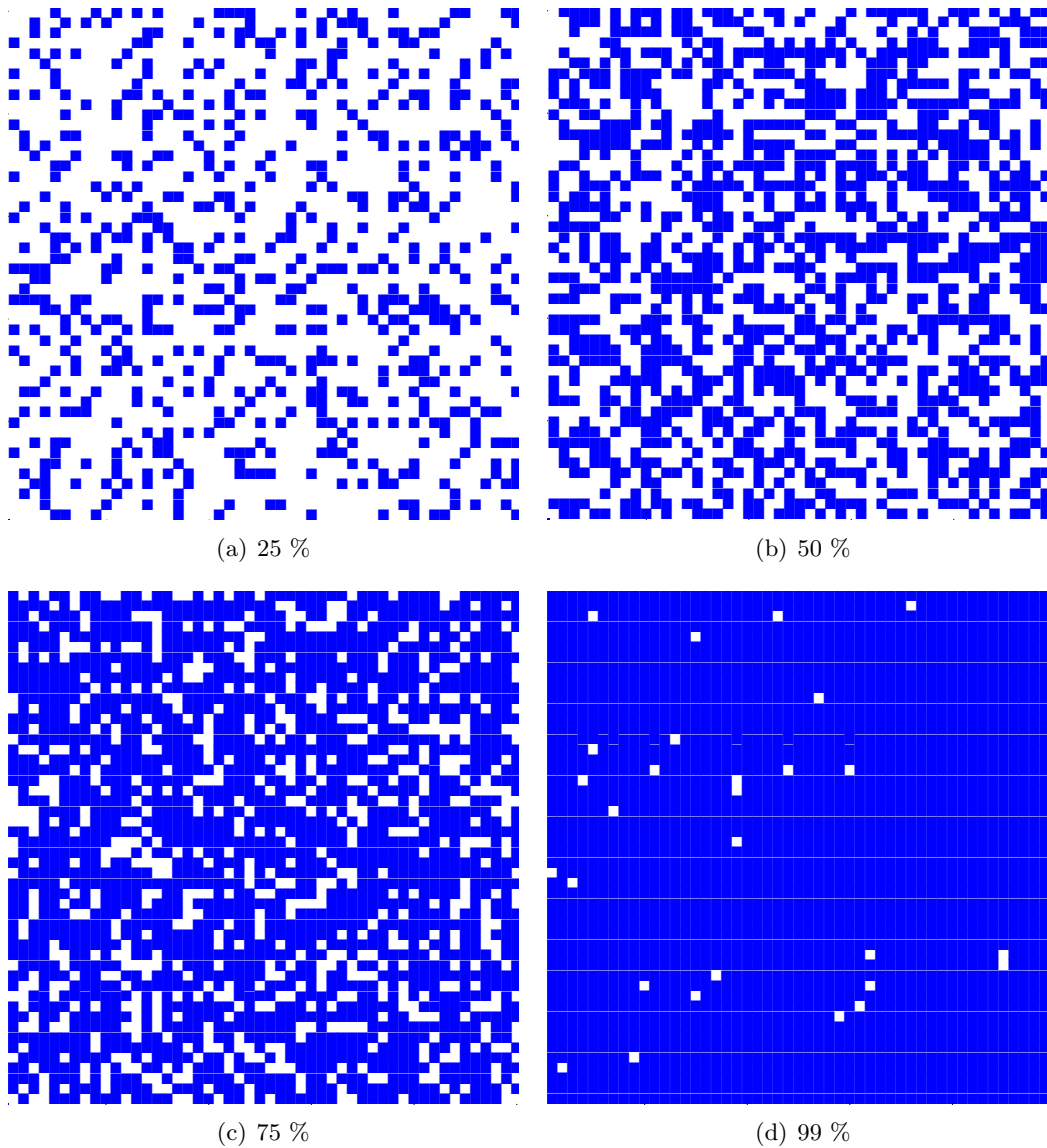


Figure 2.7: The figures show the principles of the percolation theory model for different probability states, e.g., a state of 1 % probability means, that superconductivity prevails in 1 % of the bulk. The figures depict different probability levels (a) 25 %, (b) 50 %, (c) 75 % and (d) 99 %.

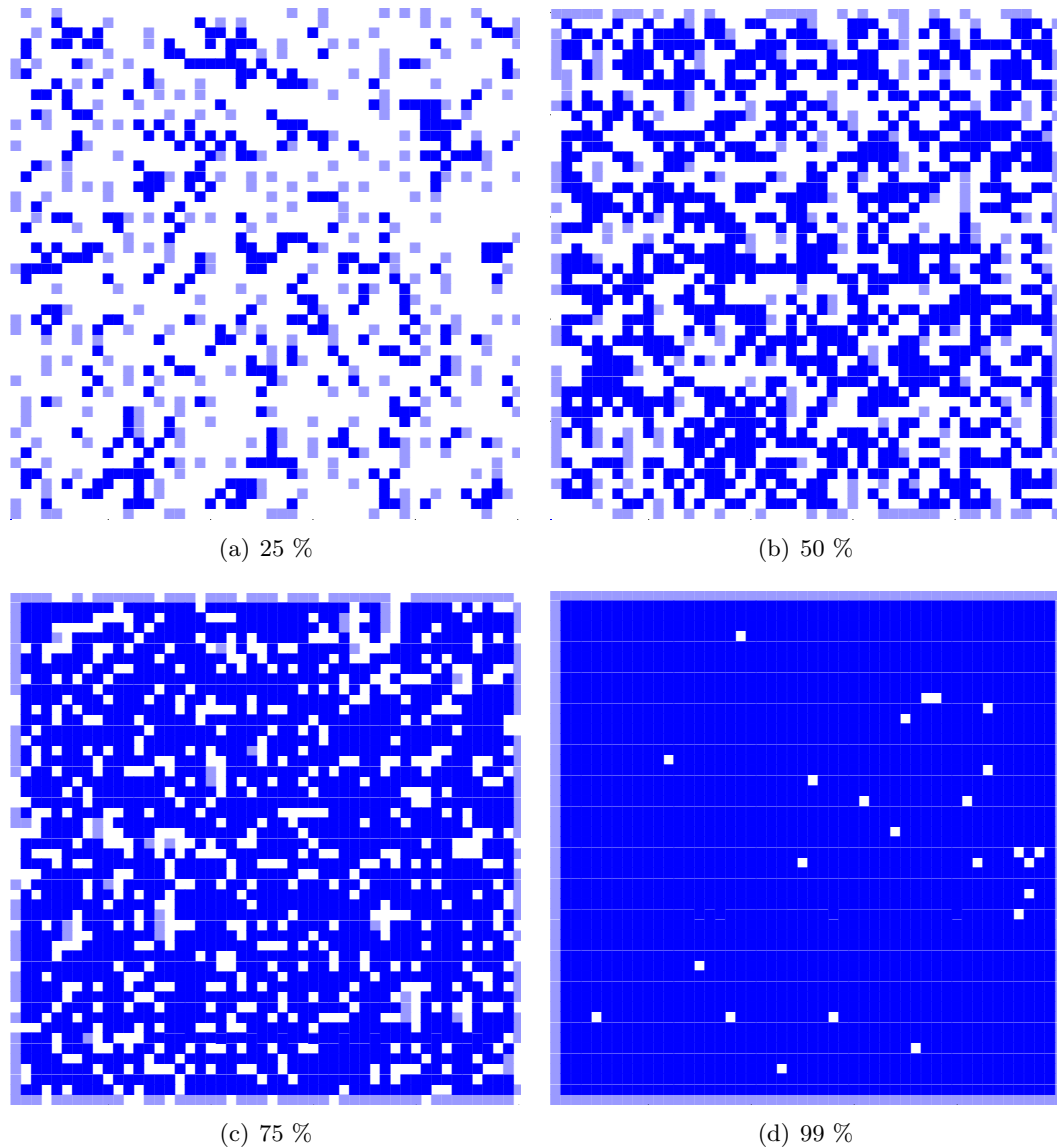


Figure 2.8: The highlight of the superconducting tracks through the sample. The current direction is from left to the right. The light blue tiles indicate a dead end. (a) At 25 % there are still some dead ends, the remaining resistivity deviates thus deviates from zero. (b) 50 % the amount of dead ends has already dramatically declined, the resistivity can already drop to zero, although the bulk is just 50 % superconducting. (c) 75 % and (d) 99 % show the influence of the percolation. There are many different tracks through the sample, which can host the superconducting current.

In the following chapters, the samples investigated tend to show some effects of percolation. It has to be emphasized that the effect of NCS superposition of spin triplet SC and spin singlet SC as well as simple SC and normal conducting parts both can be based on the percolation theory but show different effects. The former leads to a slower reduction of the electrical resistivity, whereas the latter shows clearly two distinct transitions. Further approaches to the topic of the unusual different behavior in $\mu_0 H_{c2}^{\text{res}}$ and $\mu_0 H_{c2}^{\text{C}_p}$ were also listed in [42].

Chapter 3

Experimental

3.1 Preparation of the samples

Polycrystalline samples were generally prepared by argon arc melting on a cooled copper hearth. They were further annealed for up to thirty days. A detailed description of the procedure as well as a statement on the purities and sources of the used elements will be given for each sample separately. The resulting lens-shaped samples were further cut by a wire saw with silicon-carbide powder dissolved in glycerol. A wire saw is in order with a high precision and, furthermore, reduces the loss of material as the thickness of a wire is just about 0.005 inch. Surfaces are further polished with silicon-carbide paper of different grain sizes. Highly polished surfaces were reached by using a 4000 paper. The geometric dimensions of the samples were investigated with a light optical microscope (Zeiss Stemi 2000-C). The sample masses were measured with a μg balance with a resolution down to 100 ng. Certain specimen were cut out of the sample material and had to be properly prepared for different kind of measurements. The different requirements are discussed in the following sections.

3.1.1 Electrical resistivity

As every transport phenomenon is strongly dependent on the geometry of the sample, samples for electrical resistivity measurement have to be prepared properly in order to meet these requirements. The theoretical electrical resistivity is defined by the following equation:

$$\rho = \frac{U}{I} \times \frac{A}{L}. \quad (3.1)$$

A is the area $A = H \times W$, with the height H and the width W , L is the length and U and I are the voltage and current, respectively. The samples have to be cut in long

bars. The length is in the best case much longer than the width and the height of the sample, i.e. the length L is longer than two times the square root of the area $L \geq 2 \cdot \sqrt{A}$. For sample measurements without pressure, the length should not exceed 8 mm as it would later not fit the puck platform, illustrated in Fig. 3.2(a). Samples, prepared for the pressure cell, should have a maximum length of 1 mm. The surfaces have to be parallel and should not indicate any sign of cracks, as a major crack, especially perpendicular to the current flow, locally narrows the area where the charge carriers flowing through the sample and thus increases the resistance. Transport properties are very sensitive to cracks or other deviations from an ideal shape. Especially thermodynamical cycling, caused by cooling and heating procedures, can give rise or aggravate mechanical stresses, leading to permanent deformations of the sample. Such an effect might be observed by an irreversible hysteresis. In this case the resistivity cannot be identified as an intrinsic value at all.

Electrical resistivity measurements were generally performed in the standard four probe technique. The advantages comprise the lack of influence of the feeding wires as well as canceling of the thermal voltages effect in the a.c. measurement method. In this probe technique, the contact points have to be arranged along a line as it is graphically depicted in Fig. 3.1. Another possibility is the so called Van der Pauw method [43], which allows to measure the electrical resistivity or the Hall coefficient of arbitrary arranged contact points as long as the thickness of the sample is constant. The contact wires are either made of gold or copper, with a diameter of 25 or 50 μm , respectively. The wires should have a length of at least 1 cm as seen in Fig. 3.2(b).

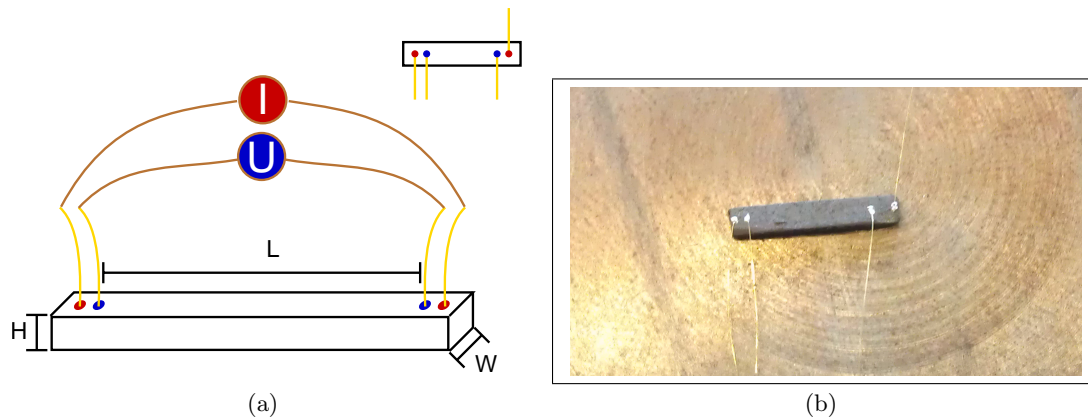


Figure 3.1: (a) Theoretical and (b) practical depiction of a proper 4-point connection technique.

Three commonly used methods for contacting samples are presented in the following:

- Spot-welding: It is strongly recommended to use spot welding for conductors. First, it dramatically reduces the size of the contact point. Second, it guarantees mechanical and electrical contact. In spot-welding technique a certain power flows through

the sample, locally heating the wire and the sample. The sample and the wire melt together and form the contact. The power supply of the spot-welding device has two different parameters for adjustment. These are the power and the time. Both parameters strongly depend on the resistance of the sample. Therefore, the sample thickness, i.e. the height of the sample, and the sample resistivity has to be considered in detail. If the sample is very sensitive to air or it is brittle, it is strongly recommended to carefully adjust the parameters step by step, otherwise the sample can be easily damaged or even destroyed.

- Silver glue: The Epotek H20E silver two-component glue can be chosen for semiconductors as well as conductors. As a general recommendation, the glue should be used just in addition to an already spot-welded conductor to enhance the mechanical stability of the contact. However, there are some disadvantages by using the glue. First, it cannot be perfectly set as a point. Additionally, the direct contact of the wire to the sample cannot be assured. Second, the contact resistance can be much larger than the required 2Ω . A high contact resistance comes along with a heating procedure during the measurement and gives an offset between the temperature measured by a temperature sensor and the actual temperature of the sample.
- Ultrasonic welding / Bonding: Bonding is the method for contacting semiconductors and conductors, where very small contact points are required. Therefore, a gold wire is locally heated by ultrasonic vibrations. The molten wire is then mechanically attached to the surface of the sample.

Within this thesis, the investigated samples were mainly spot-welded and additionally fixed with silver glue. The four wires connected to the sample were further lead to soldering pads. It has to be considered that gold and tin form an eutectic. The phase diagram of the Au-Sn eutectic shows liquefaction points at different concentrations at around $250 \text{ }^\circ\text{C}$, so special precautions have to be taken while using gold wires.

In the next step, the contacted samples are mounted on a puck. These pucks are designed to verify a good usability and allow to measure samples on different devices without any loss of contact quality. In general, the puck consists of twelve independent pins. However, for the electrical resistivity measurement, only four pins are used. Unfortunately, the remaining eight pins have to be cut off. Further attempts to unify the usage of the pucks are suggested but would require a complete reconstruction of the sample holders. The puck itself is 180° rotationally invariant and thus make it impossible to mix the current and voltage contacts, as they are arranged rotationally symmetrically.

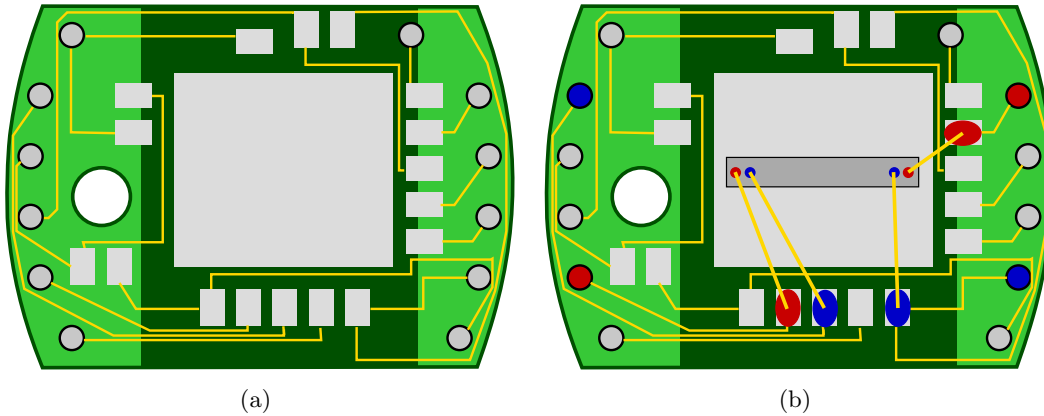


Figure 3.2: (a) Empty and (b) occupied illustration of the sample puck for the resistivity measurements in the ^3He as well as ^4He system. The red marks depict the current flow whereas the blue marks visualize the contacts to measure the voltage drop. These indications are in agreement with Fig. 3.1. It has to be noted that several soldering pads are connected to the same pin. Therefore, additional caution has to be taken to not shorten the contacts.

3.1.2 Specific heat

The sample preparation for specific heat is much easier in comparison. Specific heat is a bulk property and, therefore, in principle, independent of geometry. However, one has to consider the influence of the demagnetization factor, when a specimen is exposed to an external magnetic field. The major part of the samples were measured in the PPMS system. Specific heat measurements in the PPMS system should have a thin cuboid shape with a base of up to 2.5 mm times 2.5 mm. In general, a sample mass between 1 mg to 200 mg can be mounted on the sample stage. However, it is strongly recommended to adjust the sample mass in order to the Sommerfeld coefficient γ of the specific heat which is dominating at low temperatures. As a consequence, heavy fermion compounds should weight from 1.5 to 8 mg. In contrast, superconductors should have a mass of at least 25 mg. This holds true for superconductors with an existing superconducting gap, as the electronic contribution plays the major role at lowest temperature and a condensed electrons do not contribute to the specific heat anymore. A detailed explanation of the measurement process will be given in Sec. 3.3

3.1.3 Magnetic susceptibility

Magnetic susceptibility is another bulk property but the impact of demagnetization has to be taken even more seriously. Therefore, samples should have a bar-shape, in order to have a small demagnetization factor between 0.1 and 0.2. This requires the length being much larger than the thickness of the sample. In the case of a superconductor the mass should

not be too small, as the signal scales with the mass. Contrary, ferromagnetic samples of very small masses can also be measured.

3.2 Setup for electrical resistivity (ρ)

3.2.1 Measurement of ρ in the ^3He system

A glass fiber aluminum ^3He top-loading bath cryostat (CRYOGENIC) measurement system was used to investigate electrical resistance. Temperatures down to 300 mK were accessed. The measurement system is separated in two parts, i.e. the cryostat itself and the top loading probe. The former is connected via a supply line with an external ^3He dump which is also equipped with an external Sorb to extract the complete ^3He out of the cryostat system. The dump has a volume of 40 liters with a filling charge of 25 liters of gaseous ^3He . A pressure below ambient pressure is generally used in such kind of system to prevent the immediate loss of very expensive ^3He due to small leaks. The ^3He itself fulfills two distinct functions. On the one hand it works as the exchange gas which surrounds directly the inset and the samples themselves. On the other hand it is needed as cooling gas. The cryostat system is of cylindrical shape with an outer diameter of 1.02 m, a height of 1.35 m. The inside of the system is built up like an onion. The outer part contains a multilayer high purity aluminum radiation shield and a super-insulation blanket of alternative layers of reflective aluminized mylar and nylon netting. These layers reduce the effect of thermal radiation from the environment. An additional LN_2 reservoir with approximately 30 liters acts as a second shielding and decreases the more expensive ^4He usage. A second multilayer builds up a second barrier. On the one hand it separates the LN_2 reservoir from an inner ^4He reservoir which catches approximately 40 liters. On the other hand it also separates the ^4He from the measurement chamber. The ^4He dump itself contains a superconducting coil system. These coils are constructed as a hybrid system of NbSn_3 and NbTi which generates magnetic fields up to $\mu_0 H = 12$ T. An external power supply provides the current via a superconducting switch. The magnetic field reaches its maximum in the center of the measurement chamber. The variation of the magnetic field along the z -axis in a +5 cm and -5cm distance to the center is accountable for an error of around 9 %. With the help of a lambda stage, the magnet can be reach even higher magnetic fields. Therefore, ^4He at the bottom of the reservoir will be further cooled. Due to the low thermal conductivity, the warmer ^4He at the top and the cold ^4He at the bottom do not mix so easily. The cooling is realized by an external rotary pump directly connected to the lambda stage. A needle valve allows to adjust the pressure. With the lambda stage below 2.2 K and a pressure of around 100 mbar, magnetic fields up to $\mu_0 H = 14$ T can be reached.

The center of the cryostat system is the measurement chamber. On the top of it there is a NW40KF main gate which is either covered by a blind flange or the top loading probe. The regulation of the temperature inside the measurement chamber is possible by pumping liquid ^3He . Therefore, one needs a position close to the bottom, where the ^3He is liquified and an internal or external pump, which reduces the boiling pressure and thus decreases the boiling temperature by removing the vaporization heat. In the system used this is realized by a 1K-pot and an internal Sorb pump, respectively. The former is localized approximately 350 mm above the bottom of the measurement chamber, while the later is mounted in a height of approximately 550 mm. Both have a ^4He and a ^3He site with a strong thermal connection between them. Two independent capillary tubes connect the ^4He reservoir to the Sorb and 1K stage. External pumps are connected to the system through a small impedance, where the flow can be driven by two independent needle valves to cool the Sorb and the 1K stage. Manometers are connected to the pumping site and monitor the vapor-pressure. The normal operating pressures are 22 mbar and 8 mbar for Sorb and 1K, respectively. The Sorb is known as a hybrid of adsorption and absorption and acts as cryo-pump. It is a bulk of charcoal with a large surface and thus allows to cool down an immense amount of cold gas. The purpose of the 1K stage is to liquify the ^3He at temperatures below 3.19 K. As it is close to the bottom of the measurement chamber, i.e., where the samples are positioned during measurement, the samples are fully covered with liquid ^3He if all the ^3He is condensed. The measurement chamber itself has a diameter of around 29.8 mm. The system has two permanent temperature sensors at the bottom and at the lambda plate stage, respectively, as well as three CERNOX sensors mounted at Sorb, 1K and the bottom of the measurement chamber.

The top loading probe consists of two main parts. The first is a stainless steel tube which will be referred to as tube. It has two valves and one connection flange for pumping either the inner part of the tube or the sealing part. The sealing part has two viper seals and holds or guides the second part. The later is a stainless steel rod which will be referred to as sample rod or sample holder. On the measurement-site, the sample holder provides different set ups, e.g., a holder for the pressure cell or for PPMS-pucks (FRITZ). Twenty independent pins are available where four of them are reserved for a CERNOX temperature sensor. On the top site there are two Fisher plugs with 18 and 11 pins for the electrical connection, respectively. The sample rod is moveable along the z-axis guided by the viper seals, preventing a loss of ^3He , while the rod itself still remains moveable.

Resistance measurements are performed with a Lakeshore a.c. resistance bridge with an internal source providing an a.c. with a frequency of 13.7 Hz. There are two advantages of a low frequency source. First, it is possible to detect phase shifts of the current to the voltage signal. Second, the influences interfering high frequency noises are small in comparison to high frequencies. There are four channels reserved for each sample. A low

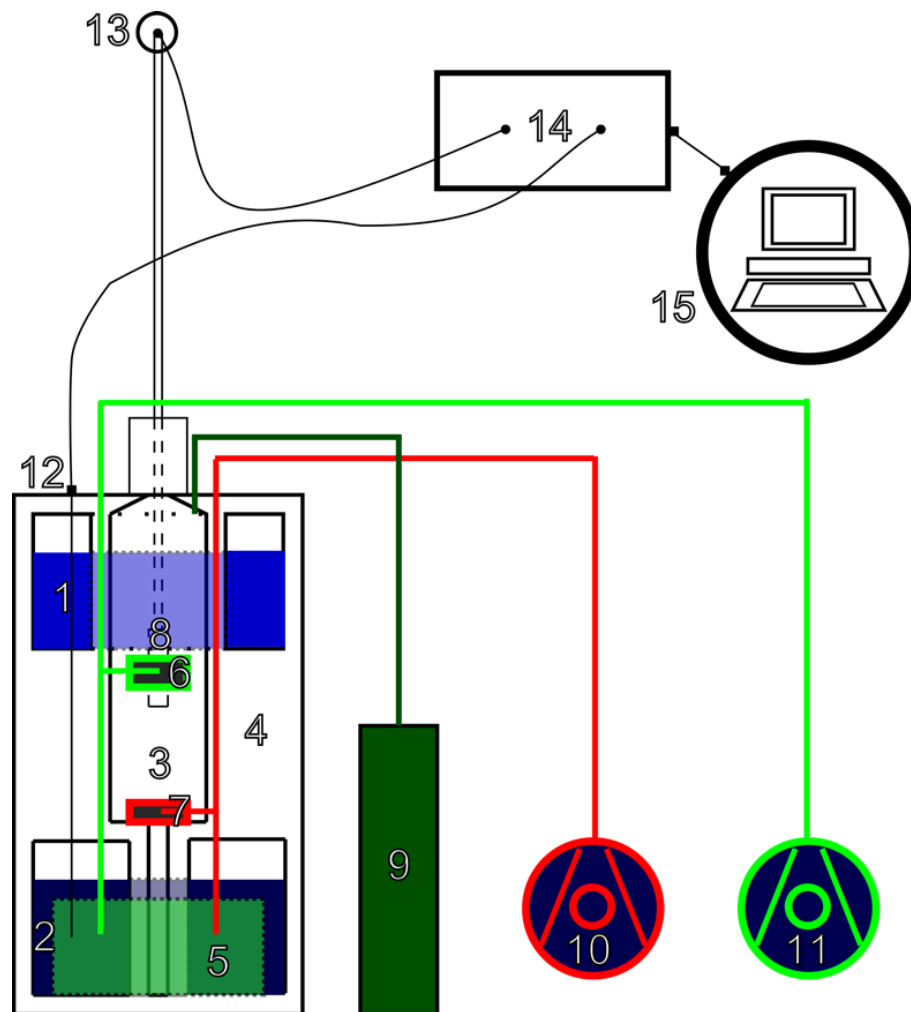


Figure 3.3: Schematic plot of the ^3He bath cryostat. The operating mechanism is described in the text. 1.) LN₂ reservoir 2.) ^4He reservoir 3.) Measurement chamber in ^3He atmosphere 4.) Super-insulation 5.) Superconducting hybrid magnet 6.) Sorb 7.) 1-K Stage 8.) Sample rod and sample platform 9.) ^3He dump 10.) External 1-K pump 11.) External Sorb pump 12.) Power supply connection of the magnet 13.) Fischer connectors 14.) Power supply/temperature controllers/ Lakeshore bridge/ pressure gauge 15.) Computer

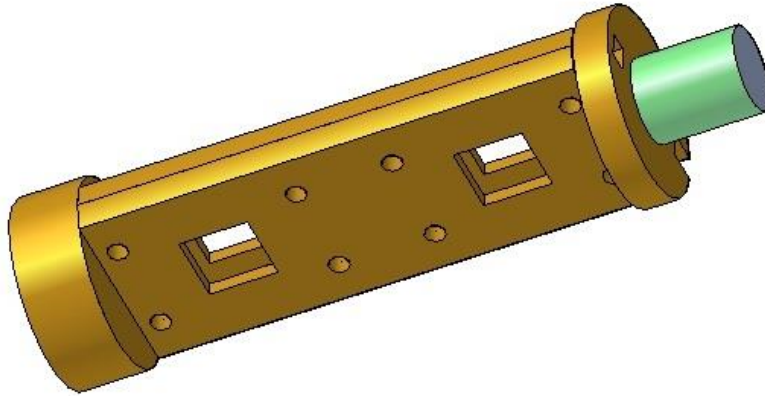


Figure 3.4: 3D plot of the FRITZ sample holder. A detailed building plan is presented in the Appendix.

resistance scanner allows to resolve very low resistance of intermetallic compounds. A Lakeshore temperature controller monitors the temperatures at Sorb, 1 K, Bottom and the sample itself. The data are collected from a master computer via a conventional GPIB (IEEE488) Bus. A GUI graphs the data points and states the relevant information. An overview is given in Fig. 3.2.1.

The FRITZ sample holder provides four measurement positions, i.e. two on the front and two on the back side, for measuring the electrical resistivity in the sense of the four probe technique. The holder can be fixed on the ^3He top loading system via a M12 metric fine thread. For a clear diversification, the current pins are marked with white color. Additionally, the numbers for each measurement position are also noted on the black shrinking tubes stabilizing the connection pins. Since the a.c. measurement method is used, there is no difference in the connections of I^+ and I^- or U^+ and U^- as already mentioned above.

The sample holder is made of brass which has a low heat capacity as well as a good thermal linking to the samples and the temperature sensor at low temperatures. The 1/10 inch plugs are connected via copper wires to the mounting stage of the top loading probe and are fed through a small hole in the sample holder to provide a mechanical stability, i.e. a cable anchorage, against stress and strains on the wires.

Sample pucks, very similar to the PPMS types, were used to enable a proper connection and allow a fast switch between the ^3He and the ^4He systems. The samples have to be contacted by gold wires and soldered to the pucks in the same manner as shown above in Fig. 3.2(a) and Fig. 3.2(b).

3.2.2 Measurement of ρ in the ^4He system

Two different sample holders were used in the ^4He system. First, the LuBer system, acting as an archetype for the FRITZ sample holder. Second, the Gundi device. The first works with the same pucks as the FRITZ holder, with the discussed advantages above. The second provides four independent contact pins, which are arranged in one line. The single pins are fully elastic and can contact samples of at least 5 mm just by mechanical contact. This method faces some problems for brittle samples and materials which tend to exhibit small oxide layers on the surface. Both sample holders have their own sample rod and are connected via two Oxford connectors. The measurements are performed inside a small ^4He bath cryostat. The electrical set up is similar as given in Sec. 3.2.1. The main difference is the measurement of the temperature. In the ^3He system, the temperature and the resistance are measured at the same time. In contrast, the samples as well as the temperature sensors are measured in series in the ^4He system. This could pose some problems at very fast drift speeds and could cause slightly blurred measurement results especially around the strong change of the heat capacity of ^4He between 10 K and 40 K. Therefore a cap, increasing the heat capacity and lowering the drift speed, can be used.

3.2.3 Measurement of electrical resistivity ρ in high pressure

As discussed above, the application of high pressure can modify the crystallographic properties of a solid. The effort of measuring physical properties in high pressure is strongly linked to the difficulties of the sample preparation. It is very important to use a material lacking the influence of magnetic contribution or shielding effects. Therefore, a mixture of copper and beryllium, in short CuBe or also referred to as beryllium copper, is used. Around 0.5 % to 3.0 % of beryllium is dissolved in copper. CuBe is known as the mechanically most stable and highest strength copper alloy. The application varies from special tools to parts which are exposed to strong forces. As beryllium compounds tend to exhibit high toxicity it should be handled with certain precautions. Generally, when in solid state it has no toxic side-effects but it should be avoided to grind, weld, polish or drill a CuBe part.

3.3 Setup for specific heat capacity (C_p)

Specific heat measurements were carried out in a conventional PPMS from Quantum Design. Heat capacity is measured by making use of the relaxation time method and the relation $C_p = (dQ/dT)_p$. The sample is mounted on a platform which is connected by four and eight wires for the ^3He and ^4He puck, respectively. A certain amount of heat Q is fed to

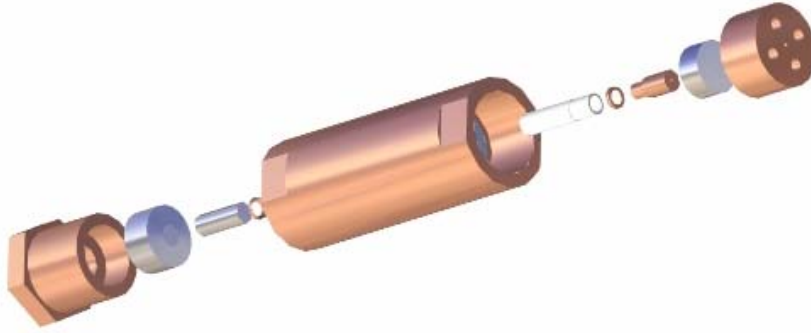


Figure 3.5: 3D plot of the pressure cell with the single parts. Further information on pressure cell measurements as well as detailed instructions of the preparation of a cell can be found in the theses of Khan [44] and Ackerl [45].

the sample via the heater on the platform stage. The temperature as well as the time t_{heat} are permanently monitored. If the temperature reaches a certain percentage of the base temperature, the system will stop the heating procedure and records the cooling period with the same time t_{heat} for the sample. This time is strongly dependent on the mass and the temperature dependence of the samples. The system is controlled by the Model 6000, which works as a voltage and current source, as well as providing the functionality of a lock-in amplifier and a bridge. It provides two different kinds of sample holders. One is used for ^4He measurements, while the other is used along with the ^3He measurement inset. The general build-up of the sample holders comprises a sapphire platform with a thermometer and a heater attached to the backside. The platform has a quadratic base with dimensions of 2.5 mm times 2.5 mm. The electrical connections to the heater and the thermometer are provided by 4 and 8 very thin gold wires of around 25 μm for the ^3He and ^4He puck, respectively. Those are used to minimize the thermal connection to the sample stage.

The ^4He puck comprises the measurement platform and the complete thermal and electrical connection to the PPMS system. It has thermal contact fingers on the outer side for the thermal contact and pins on the lower side to provide the electrical connection. The PPMS system can cool down to 1.8 K which also denotes the lowest accessible temperature for the ^4He puck. The main advantage of using the ^4He puck is its small mass. This allows a very fast cooling and stabilization procedure. For temperatures above 10 K to room temperature and even to 400 K the usage of the ^4He puck is strongly recommended and preferred over the ^3He system.

The ^3He puck has 8 contact fingers on the lower side and has to be fixed on a special ^3He inset rod. The inset rod is stored outside the PPMS system and has an additional ^3He tank fixed on the rag. The ^3He must be cleaned after some measurements or when the

system was not in use for a while. A peculiarity of the running system (internal name: PPMS-2) is that the impedance tends to get stuck very easily. One explanation can be hold responsible for this event to occur: As it is impossible to perfectly seal a system and due to the fact that the ^3He cycle is operated below ambient pressure, some air can contaminate the system. The containing water steam can freeze, while the system is getting cooled down. If this occurs in the small capillary of the impedance, the system might not be able to condense ^3He anymore. As a precaution, it is strongly recommended to apply external heat (i.e. with a heat gun) at the position, where the impedance is located during the ^3He cleaning procedure with the external LN_2 trap. Generally, this avoids a stuck impedance. As a last option, one can secure and store ^3He in the dump and then pump from both sides with a turbo pump, while the system is at room temperature. This can be realized with an external pump with a Swagelok connector attached to the exhaust line pumping against the internal pump. The detailed procedure is explained step by step in the appendix Sec. C. The impedance can also be partly stuck. In this case the system can operate below 1.8 K but cannot reach the base temperature anymore. In the equilibrium state, the partly permeable impedance is liquefying as much ^3He as pumped down via the turbo pump.

For temperatures in the range between 300 mK and 300 K, Apiezon N grease is used for attaching the sample via adhesive forces to the platform. The sample must not exceed the dimensions of the sample platform. ^3He measurements are mainly performed to measure temperature regions between 300 mK and 20 K. In this temperature region the contribution of the phonons is usually very small. A good indicator is the Debye temperature θ_D . At temperatures below $\theta_D/50$, the phononic part can be estimated by the low temperature Debye fit. If the sample mass is too large, it takes a longer time to transfer the energy from the heater to the sample. This time is defined as t_{heat} . A high t_{heat} might cause a non negligible loss of heat due to radiation and thermal linking effects and can cause major errors. These deviations cannot be resolved by the system or considered by calculation afterwards.

3.4 Setup for the magnetic susceptibility (χ)

Magnetic susceptibility was measured in a superconducting quantum interference device (SQUID) which works on the basis of the Josephson effect [29]. Furthermore, a current in a superconducting conductor loop can just be induced in quantized values. The susceptibility can be measured in a ^4He system as well as with a ^3He inset to reach temperatures down to 300 mK. Overlaps of both measurement methods give a good comparison of the quality of the measurement. Additionally, a CuBe pressure cell provides the possibility of investigating magnetic responses while exposed to hydrostatic pressure. Hydrostatic

pressure is mediated by Daphne oil and can reach up to 10 kbar. In this measurement setup, the pressure is not metered by an additional manometer. It is just gauged by the number of turns of the sealing plug. Therefore, the amount of Daphne oil has to be very precise.

Regardless of an additional applied pressure, the sample itself is mounted on a thin SiO_4 (quartz)- tube which itself possess no magnetic momentum and realizes good mechanical usability at high and low temperatures. The samples are fixed with super glue. To simplify the assembling procedure, the facing surfaces should be parallelly aligned.

3.5 Muon Spin Relaxation measurements (μSR)

The first μSR measurements were conducted at TRIUMF (Canada's national laboratory for particle and nuclear physics) in 1979 [46] to proof the theoretical predictions and calculations from Kubo and Toyabe in 1966 (M.S. thesis, unpublished). Different samples, e.g., MnSi, were mounted in an arrangement schematically depicted in Fig. 3.6. The principle underlying methods for μSR measurements have not changed so far. The Rutherford Appleton Laboratory (RAL) is a research facility with around 1200 scientists in Oxfordshire, UK [47]. RAL provides several sites for muons and neutron experiments, with one of them being the so called ISIS project. ISIS is a 800 MeV proton synchrotron with a cycling frequency of 50 Hz. It produces an overall beam power of around 160 kW to 200 kW. At first a H^- ion is accelerated to an energy of around 70 MeV in a linear accelerator (linac). The beam is then feed to the main acceleration stage where the H- beam is stripped of its electrons by a $0.3 \mu\text{m}$ thick aluminum oxide stripping foil. The resulting protons are accelerated in bunches for several times in a synchrotron. The resulting proton beam produces neutrons, acting as a so called spallation neutron source, as well as muons on different target sites. For the former, the target is tungsten. By contrast, a proton beam which hits a thin carbon target produces the muon beam. Around 26 independent measurement sites exist and can be operated at the same time. The detailed decay mechanisms from the initial proton beam to the resulting muon beam are highlighted in Sec. 2.4. The final muon beam is further distributed to seven different experimental facilities, with μSR station.

The samples for the μSR probe technique have to be powdered in advance. The powder is then fixed by GE-Vanish on a silver sample holder while fully covered by a thin silver foil. Silver has no magnetic dipole moment, can be produced in very thin foils and is, therefore, practically invisible for the muon-spin interaction. The sample itself can be assembled on different instruments. The temperature ranges vary between 40 mK up to 1000 K. For the lowest temperature regions, the measurements are conducted in a ^3He - ^4He dilution refrigerator.

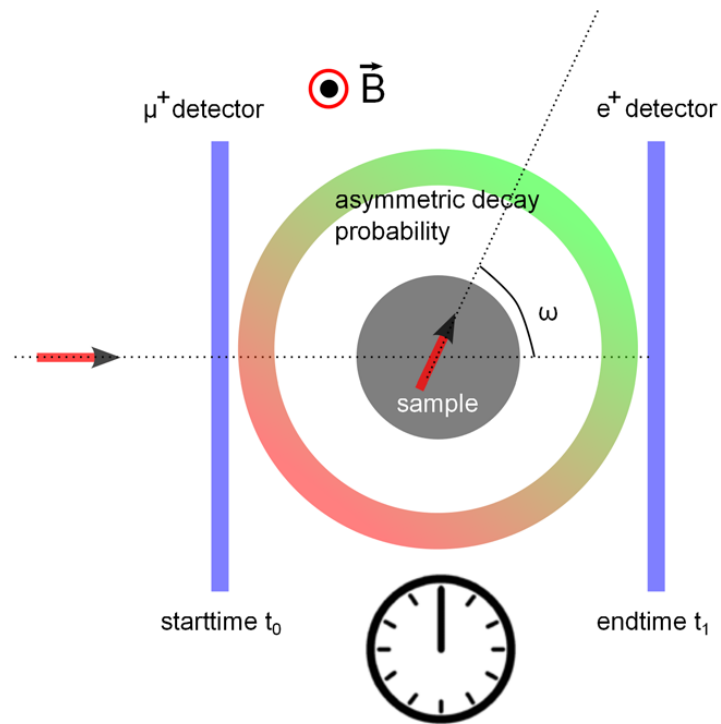


Figure 3.6: Schematic principles of the μ SR experiment. The arrows indicate the spin polarization of the incident μ^+ - beam. When the spin interacts with the external field \vec{B} and a possible internal field arising from the sample, the μ^+ starts to precess with the Larmor frequency ω_L . The decay direction underlies the probability of the β -decay. The highest probability is along the spin direction. In the figure a higher probability is indicated by the green region, whereas less probable direction are colored in red. The μ^+ detector acts as a starting time and the e^+ detector counts the positron as well as the end time. With the statistical distribution of the e^+ one can derive the polarization. From the polarization the Larmor frequency and therefore the unknown field as defined in Eqn. 2.33 can be calculated.

External magnetic fields can be applied transversally as in Eqn. 2.33 up to 600 G or longitudinally up to 2500 G. The field is created by a pair of Helmholtz coils. The low fields are on the one hand due to technical complexity of properly supplying a homogeneous field with a superconductor over a larger volume. On the other hand, a high external magnetic field can already rearrange the internal magnetic dipole moments. Therefore, it would contradict the idea of the superposition as discussed in Eqn. 2.33. The μ^+ detector is rotatable up to 90° to meet the requirements of the LF and TF measurements [48].

Chapter 4

1-1-1 compounds

This and the following chapters deal with the sample preparation, the physical property measurements and the theoretical calculations regarding non-centrosymmetric compounds and unconventional superconductors. The sample preparations were performed in cooperation with the Institute of Physical Chemistry of the University of Vienna. Physical properties were measured in the Institute of Solid State Physics of the Vienna University of Technology and in the Rutherford Appleton Laboratory in Oxfordshire. Theoretical band structure calculations were performed in cooperation with the Institute of Physical Chemistry, University of Vienna and Center for Computational Materials Science. The cooperation was enabled by the FWF Project 22295.

4.1 LaPtSi

This section deals with the intermetallic compound LaPtSi. It includes major parts of the author's published paper on the LaPtSi system [49].

The present study aims at a further check of materials, whether or not strong electron correlations are the primary cause of unconventional superconductivity occurring in materials without inversion symmetry. LaPtSi is selected for this goal, because the heavy element Pt promotes a significant spin-orbit coupling, lifting the two-fold spin-degeneracy of electronic bands.

The crystal structure of ternary non-centrosymmetric LaPtSi has already been described by Klepp and Parthe [50] from single crystal investigations. Evers *et al.* [51] reported superconductivity in LaPtSi with a superconducting transition temperature of 3.3 K. Ramakrishnan and coworkers [52] studied the superconducting properties of LaPtSi in some detail, revealing $T_c = 3.8$ K from resistivity, specific heat, and susceptibility measurements.

Additionally, magnetic pair breaking was studied by these authors from substituting La by Ce and Nd. However, no investigations have been made concerning the absence of inversion symmetry. The space group of LaPtSi is of the non-centrosymmetric $I4_1md$ chiral type. The isotopic compound CePtSi has been classified by Lee and Shelton [53] as a heavy fermion and coherent dense Kondo lattice system without a magnetic or superconducting transition down to 70 mK.

The aims of the present study are to investigate the superconducting compound concerning the lack of inversion symmetry in its crystal structure and to understand the superconducting properties in combination with density functional theory (DFT) calculations.

4.1.1 Experimental and computational details

Polycrystalline samples were prepared by arc melting the stoichiometric amounts of pure metal ingots under Ti-gettered argon. To ensure homogeneity of the samples, they were turned over and remelted several times. All samples were sealed in quartz ampoules under vacuum and annealed at 800°C for one week. For sample characterization X-ray powder diffraction (XRD), scanning electron microscopy (SEM), and electron probe microanalysis (EPMA) have been used. Details on characterization techniques are summarized in Ref. [54]. Resistivity measurements were performed in a cryogenic ^3He set-up from 350 mK to room temperature at magnetic fields up to 12 Tesla. Samples were prepared as thin bars and mounted parallel to the magnetic field. Four gold wires were connected by spot welding. The electrical resistivity was measured by an a.c. resistance bridge as was described in Sec. 3.2.1. For the specific heat measurements a conventional Quantum Design PPMS with a ^3He inset down to 400 mK on a relaxation-time calorimeter with heat pulses of around 2% and a 9 T magnet was used. Flat, highly polished, quadratic samples of around 40 mg were fixed with Apiezon N grease on the $\alpha\text{-Al}_2\text{O}_3$ measurement platform. Magnetization was measured employing a Cryogenic SQUID magnetometer (S700X) at temperatures from 1.8 K to 5 K. The sample used was cylindrical with an aspect ratio of 1:2 (diameter to length) and was mounted parallel to the applied field.

The density functional theory (DFT) calculations were done using the Vienna *ab initio* simulation package (VASP) [55, 56] utilizing the pseudopotential construction according to the projector augmented wave method [57]. For the exchange-correlation functional the local density approximation (LDA) as parametrized by Ceperley and Alder [58] was chosen. The size of the basis set was defined by an energy cutoff of 245.7 eV. The Brillouin-zone integration for the computation of total energies was made using a Gaussian smearing with $\sigma = 0.2\text{ eV}$ on a $11 \times 11 \times 11$ Monkhorst and Pack [59] \vec{k} -point mesh.

The vibrational properties were calculated within the harmonic approximation by making use of the direct force-constant method as implemented in the program package fPHON

(full-symmetry PHON), which is based on the package PHON [60]. To derive the force constants atomic displacements of 0.02 \AA were chosen. Before applying such displacements the structural parameters (i.e., the volume and shape of the unit cell as well as the positions of the atoms within the unit cell) were relaxed until the residual forces were less than 10^{-4} eV/\AA and furthermore a suitable supercell was constructed. Because LaPtSi, as a ternary derivative of the α -ThSi₂-type, has a body-centered tetragonal primitive crystal structure containing six atoms in the asymmetric unit cell, a supercell that contains 48 atoms was constructed.

4.1.2 Results and discussion

Structural Details

Ternary LaPtSi (space group $I4_1md$) belongs to an ordered ternary derivative structure type of the α -ThSi₂-type (space group $I4_1/amd$; $a = 0.4126 \text{ nm}$, $c = 1.4346 \text{ nm}$) [50]. The corresponding group-subgroup relation in form of a Bärnighausen tree [61, 62] is shown in Fig. 4.1(a). Note that in this case, a non-standardized setting is used. The space group of LaPtSi is of a chiral type. In the chiral type, no combination of the the rotation matrix in Eqn. 2.5 and mirroring matrix in Eqn. 2.7 can map the mirror image. This can be identified as the rotary reflection as listed in Tab. 2.1. A Rietveld refinement of the X-ray pattern observed for LaPtSi at room temperature is shown in Fig. 4.1(b). Corresponding crystallographic data are summarized in Tab. 4.1. The lattice parameters obtained in this work are in excellent agreement with data reported previously in Ref. [50].

The inset in Fig. 4.1(b) shows the 3-dimensional Si-Pt framework formed by two sets of perpendicular Si-Pt zig-zag chains. Intra- and interchain distances are rather homogeneous. Also, the Pt-Si-Pt bond angles are almost identical, with only a slight deviation from 120° . This reflects the fact that LaPtSi is an ordered representative of the α -ThSi₂-type structure, which in turn is a shift variant of the hexagonal AlB₂-type.

A comparison of the calculated (DFT) structural parameters to the experimental values in Tab. 4.1 shows both in excellent agreement, the Wyckoff positions and the c/a -ratio of 3.42 are almost identical. Regarding the lattice parameters a slight underestimation of about 1% by the DFT-LDA as compared to experiment is noticeable.

Physical properties

As reported in Refs. [51, 52, 53, 63] LaPtSi exhibits superconductivity. The values of the superconducting transition temperatures reported in literature scatter between 3.18 K and 3.8 K [63, 51, 53, 52] agreeing well with $T_c = 3.35 \text{ K}$ from the present specific heat

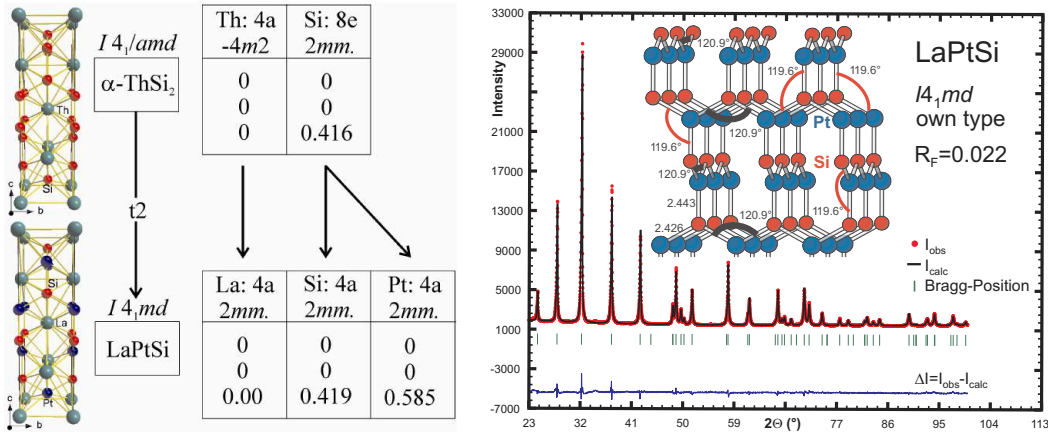


Figure 4.1: The inset shows structural details of LaPtSi. Group-subgroup relations for ThSi_2 – LaPtSi and the unit cells of these compounds. 4.1(b) Rietveld refinement for LaPtSi (standardized setting).

Table 4.1: Structural parameters and Wyckoff positions of LaPtSi.

	Exp.	DFT
lattice parameter a :	0.42502(1) nm	0.420 nm
lattice parameter c :	1.4525(5) nm	1.436 nm
La on 4a	z : 0.5805(4)	0.5804
Pt* on 4a	z : 0.1670(3)	0.1680
Si* on 4a	z : 0.0	0.0
crystal structure:	ternary derivative of $\alpha\text{-ThSi}_2$	
space group:	109 or $I4_1md$	

measurement.

Electrical resistivity (ρ) measurements on polycrystalline LaPtSi were carried out from 350 mK to room temperature, with $\rho_{300\text{K}} = 230 \mu\Omega\text{cm}$ (data below 80 K are displayed in Fig. 4.2). The respective residual-resistivity-ratio $\text{RRR} \approx 9$, together with the relatively small width of the superconducting phase transition temperature refer to fairly good sample quality.

Below 3.65 K the electrical resistivity of LaPtSi drops from around $25 \mu\Omega\text{cm}$ to zero (see inset, Fig. 4.2), indicating a second order phase transition into the superconducting state. The transition temperature was identified at 10% of the residual resistivity at 3.42 K.

The first derivative of the electrical resistivity is shown in Fig. 4.3. The transition broadened up while exposed to external fields, which generally indicates a poor sample quality. However, the transition at zero field is almost ideal and the RRR is of sufficient high value of around 9. The shape of the transition in resistivity should not change, while exposed to

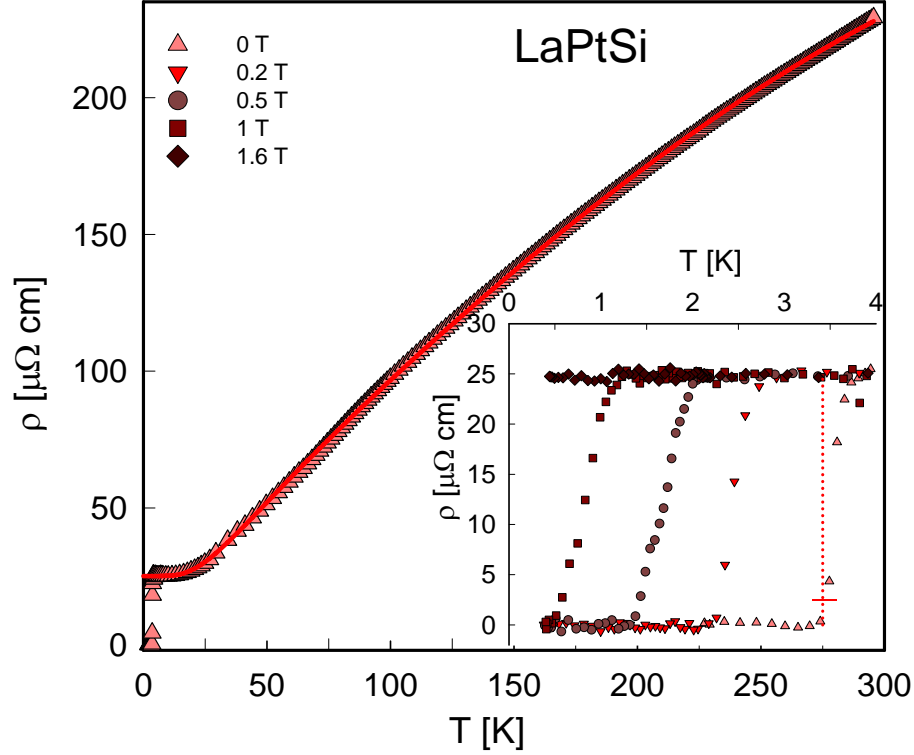


Figure 4.2: Temperature dependent electrical resistivity $\rho(T)$ of LaPtSi. The solid line is a least squares fit as explained in the text. The inset shows the magnetic field dependence of the resistive superconducting transition. The dotted line indicates the phase transition temperature at $\mu_0 H = 0$ T.

an external field because electrical resistivity represents a transport phenomenon. Therefore, this broadening might fortify the theory of percolation effects, where the bulk itself is not superconducting as a whole, but a conductible track through the sample persists for much higher fields.

The resistivity curve above T_c follows a metallic behavior and can be accounted for in terms of the Bloch-Wilson model [64] which, in addition to the standard Bloch-Grüneisen law, incorporates phonon assisted s - d scattering. The latter originates a T^3 temperature component for low temperatures, being appropriate to account for the experimental data of LaPtSi with d -states resulting from Pt and La. A least squares fit of this model, i.e.,

$$\rho(T) = A \left(\frac{T}{\theta_D} \right)^5 \int_0^{\theta_D/T} \frac{z^5 dz}{(\exp(z) - 1)(1 - \exp(-z))} + B \left(\frac{T}{\theta_D} \right)^3 \int_{\theta_{min}/T}^{\theta_D/T} \frac{z^3 dz}{(\exp(z) - 1)(1 - \exp(-z))}, \quad (4.1)$$

to the experimental data (solid line, Fig. 4.2) reveals a Debye temperature $\theta_D = 152$ K, as well as a minimum phonon energy $k_B \theta_{min} = \hbar \omega_{min}$, with $\theta_{min} = 77$ K. Here, ω_{min}

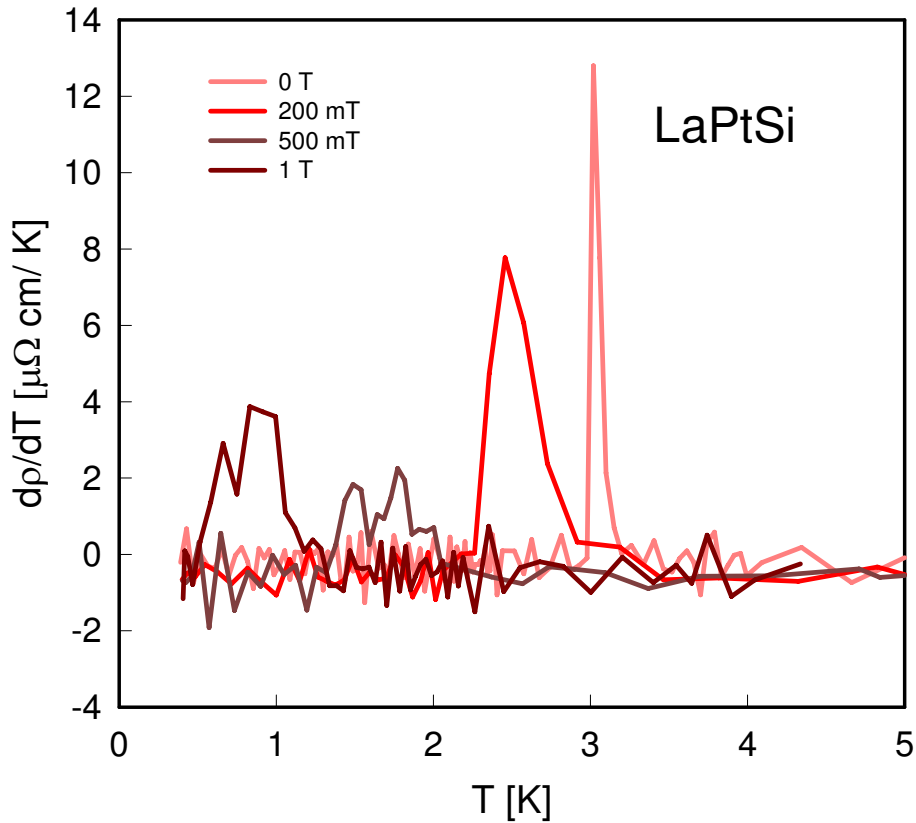


Figure 4.3: First derivative of the electrical resistivity regarding the temperature $\rho'(T) = \frac{d\rho(T)}{dT}$ at different external magnetic fields (0, 200, 500 and 1000 mT). The clear transition at 0 field is comparable with the ideal SC transition as shown in Fig. 2.4(c) whereas the transition of LaPtSi becomes blurred while exposed to external fields as indicated in Fig. 2.4(d).

is the frequency corresponding to the minimum \vec{q} value to excite the s - d transitions [64]. $A = 230 \mu\Omega\text{cm}$ and $B = 160 \mu\Omega\text{cm}$ are material dependent constants. A description in terms of the parallel resistance model of LaPtSi, as was also executed by Ramakrishnan *et al.*, [52] generates for the present resistivity data-set a Debye temperature of 169 K. Both values assessed are well below the Debye temperature derived from the specific heat measurement ($\theta_D^{LT} = 245$ K, see below).

Discrepancies in the absolute numbers of the Debye temperatures between resistivity and specific heat analyses are frequently observed for intermetallic compounds. The primary cause for this fact might be the difference in the temperature ranges considered: while heat capacity data are usually analyzed only in a narrow temperature range (below about 10 K and thus sensing low- \vec{q} acoustic phonon excitations only), $\rho(T)$ analyses extend over the entire measured range up to 300 K where thermal excitations involve the whole phonon spectrum. Consequently, the discrepancy between the values of the Debye temperature extracted from specific heat and resistivity refer to a significant difference between the

actual phonon DOS and that of the simple Debye model (see the ab-initio calculation of the phonon DOS in section 4.1.3). Differences are in general substantial if strongly curved $\rho(T)$ data-sets are taken into consideration, where, e.g., Mott-Jones type scattering [65] processes cause at high temperatures strong deviations from the T -linear dependence of simple metallic systems.

A comparison of the present $\rho(T)$ data to those of Ramakrishnan *et al.* [52], evidences a much smaller room temperature value but a slightly larger residual resistivity of the present sample, resulting in a larger RRR value for the material used in Ref. [52]. These differences might be an implication of some preferred orientation of grains in the polycrystalline sample. Given that LaPtSi is rather anisotropic ($c/a \approx 3.45$) a preferred orientation can favor either basal plane or c -axis components arranged in the electrical current direction at the $\rho(T)$ measurement. Consequently, a substantial variation of $\rho(T)$ data of samples with comparable quality is possible.

As indicated in Table 4.1, there is X-ray evidence for a non-negligible site-interchange of Si and Pt on the $4a$ -sites in the crystalline unit cell. The resulting partial disorder can then be made responsible for the somewhat larger residual resistivity of the sample studied, rather than impurity phases. The latter is backed from the absence of any traces of impurities in the X-ray pattern (Fig. 4.1(b)) and the excellent agreement with model calculations (solid line, Fig. 4.1(b)) employing the LaPtSi phase only.

The inset of Fig. 4.2 demonstrates the suppression of superconductivity in LaPtSi upon the application of external magnetic fields. The $\mu_0 H = 1.6$ T run does not reveal any indication of superconductivity above 350 mK. As displayed in the inset, the width of the transition increases with the applied field. Such a behavior has been found in various non-centrosymmetric superconductors like $\text{Li}_2\text{Pd}_3\text{B}$ [66], $\text{Mg}_{10}\text{Ir}_{19}\text{B}_{16}$ [67], BaPtSi_3 [68], or YNiGe_3 [69], just to mention a few.

Bulk superconductivity at 3.35 K is proven by measurements of the specific heat (Fig. 4.4). Entropy balance was used as constraint to determine the superconducting transition temperature, i.e., comparing the values where the entropy in the SC state and the entropy in the field suppressed state are equal. The transition appears to be slightly broadened due to the applied heat pulses of around 2% of the absolute temperature. The application of an external magnetic field leads to a suppression of the superconducting transition at $H_{c2}^{C_p} \approx 0.45$ T in heat capacity measurements. From a low temperature fit of the specific heat according to $C_p = \gamma T + \beta T^3$ at $\mu_0 H = 1.6$ T, the Sommerfeld value $\gamma = 6.5$ mJ/molK² and $\beta = 0.39$ mJ/molK⁴ were determined, yielding a Debye temperature θ_D^{LT} of 245 K which are in close agreement with the values calculated in Ref. [52]. The values for γ and β can be easily unveiled by plotting C_p/T over T^2 as shown in Fig. 4.5. The offset of the y -axis gives the γ value, while the slope of the curve gives the β value.

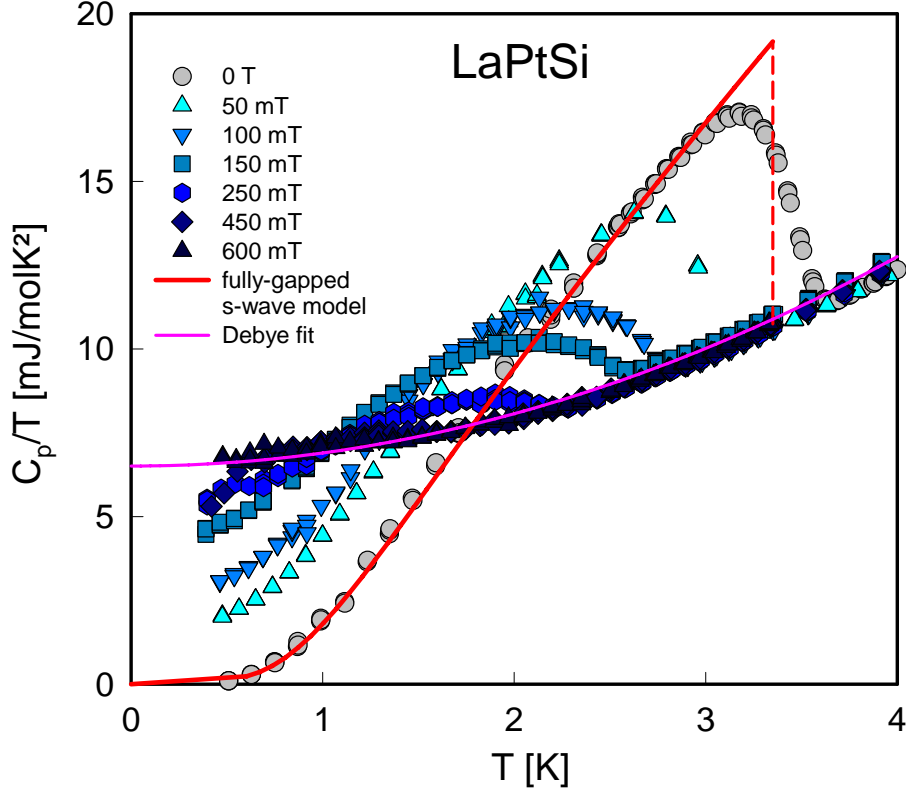


Figure 4.4: Temperature dependent specific heat measurements of LaPtSi for various values of applied magnetic fields plotted as $C_p(T)/T$ vs. T . The red dashed line refers to the ideal superconducting transition at $T = 3.35$ K, while the solid line is the temperature dependent heat capacity of a fully gapped s -wave BCS superconductor. The pink line refers to a low temperature extrapolation of the heat capacity data in the normal state.

The jump of the specific heat $(C_{es} - C_{en})/(\gamma T_c)$ at the superconducting transition reveals a value of 1.37 which is in rather good agreement with the BCS ratio of 1.43, reflecting weak coupling. As demonstrated in Fig. 4.4 the numerical values of the BCS theory as calculated by Mühlischlegel [35] are close to the experimental results and, therefore, indicate conventional Cooper pairing with an exponential decay of $C_p(T)$ at low temperatures. This, in general, characterizes a fully gapped s -wave superconductor.

Low temperature magnetization measurements on LaPtSi have been carried out in a field cooling (FC) and zero field cooling (ZFC) mode at various externally applied magnetic fields (see Fig. 4.6). The rapid drop of the ZFC data below 3.15 K denotes the onset of superconductivity, in fair agreement with resistivity and heat capacity results. Given that the demagnetization factor of the sample lies between 0.2 and 0.1, the ZFC results indicate that the shielding of the superconducting volume in LaPtSi covers a fraction between 89 % and 100 % ($\chi = -1$) of the sample, respectively.

In the case of FC measurements, flux pinning centers tend to trap magnetic flux. As

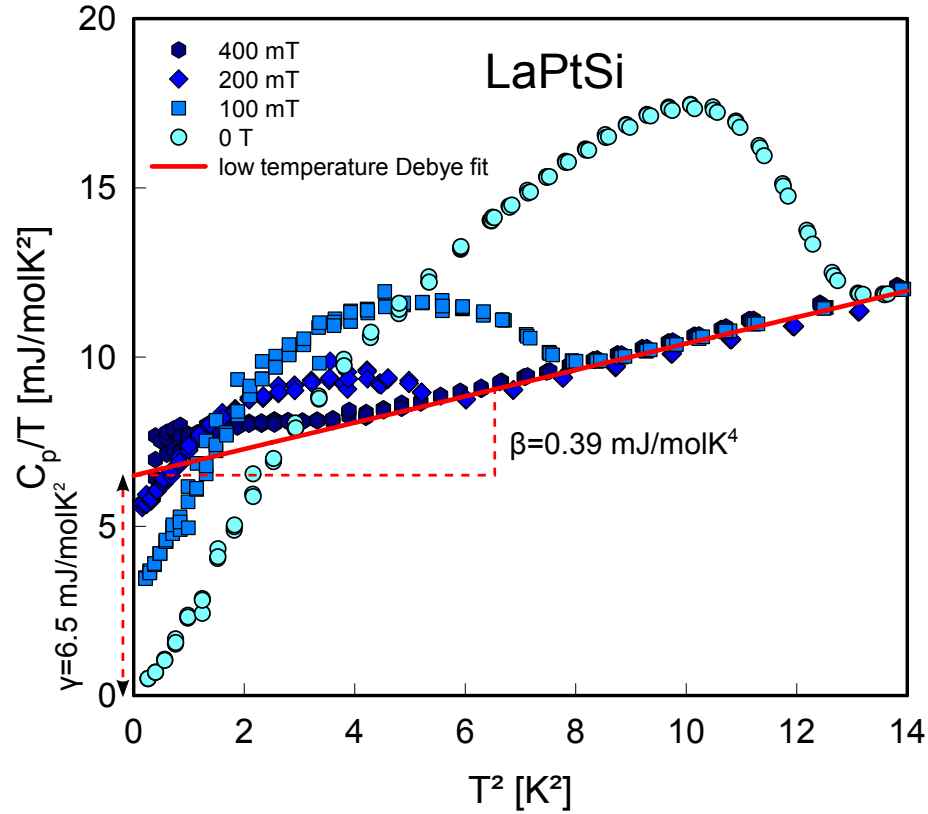


Figure 4.5: Plot of the temperature dependent heat capacity divided by T over T^2 to visualize the low temperature coefficients of the Debye model.

a result, the susceptibility in the superconducting state keeps small. Thus, the distinct differences in both the ZFC and the FC case validate type-II bulk superconductivity below 3.15 K in LaPtSi.

The upper critical magnetic field $\mu_0 H_{c2}(T)$ of LaPtSi as derived from both resistivity and heat capacity data is plotted in Fig. 4.7. While at low fields both quantities agree well, the superconducting transition temperatures are quite different in the high field limit. Predominantly three mechanisms are known to account for this observation, i) anisotropy of the upper critical magnetic field; ii) surface effects, which give rise to $\mu_0 H_{c3}$ or iii) filamentary effects as was discussed in detail, e.g., for non-centrosymmetric $\text{Mg}_{10}\text{Ir}_{19}\text{B}_{16}$ by Klimczuk *et al.* [67]. Here, the much stronger scattering of electrons at grain boundaries causes a reduced electronic mean free path, which in turn governs the superconducting coherence length, thus rising $\mu_0 H_{c2}$ above the intrinsic values. Taking into account the bulk data as derived from heat capacity measurements, $\mu_0 H_{c2}$ extrapolates to ≈ 0.4 T for $T = 0$ with an initial slope $\mu_0 H'_{c2} = -0.17$ T/K. The Werthamer-Helfand-Hohenberg (WHH) theory [40] describes the upper critical magnetic field by taking into account orbital pair breaking as well as Pauli limiting, employing two parameters, the Maki parameter α_M [39] and the spin-orbit coupling strength λ_{so} . While $\alpha_M = 0.11$ can be calculated

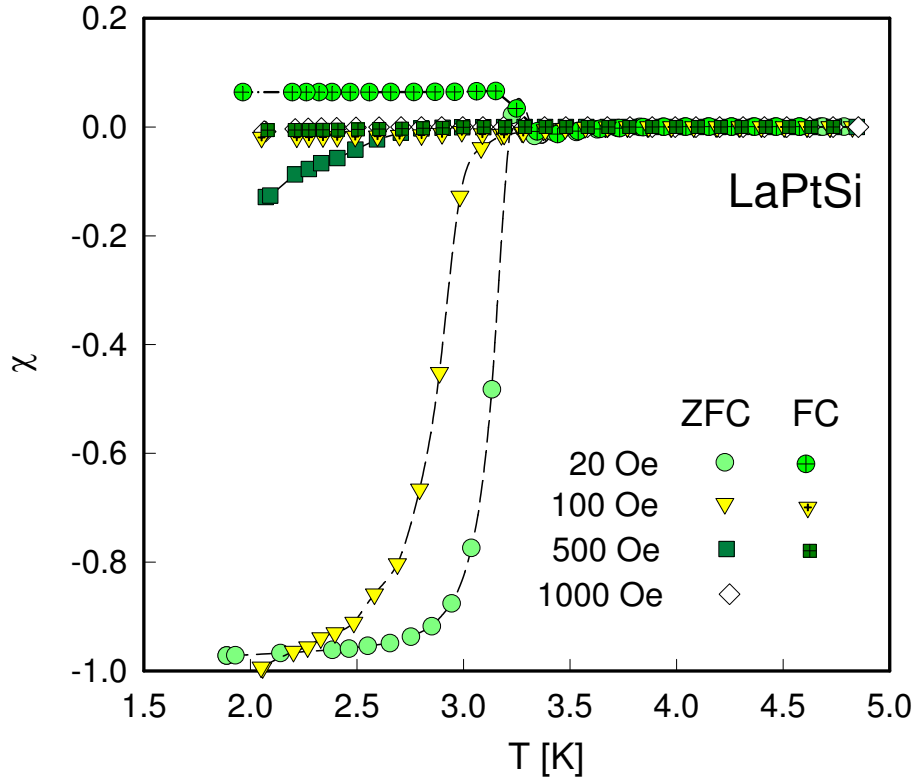


Figure 4.6: Low temperature (1.8 to 5K) magnetic susceptibility (χ) of LaPtSi taken at various fields for zero field cooling and field cooling.

from the knowledge of the residual resistivity ρ_0 and the Sommerfeld constant γ , λ_{so} is a fit parameter. Note that while a finite value of α_M reduces $\mu_0 H_{c2}(0)$, an increasing value of λ_{so} recovers the $\alpha_M = 0$ scenario. Setting $\lambda_{so} = 10$, reveals a convincing fit to the experimental data (solid line, Fig. 4.7). Since, however, λ_{so} does not significantly change $\mu_0 H_{c2}(T)$ if α_M is small, a modeling of the experimental $\mu_0 H_{c2}(T)$ data with $\lambda_{so} = 0$ does not reveal noticeable changes (small diamonds, Fig. 4.7).

The rather small value of the Maki parameter hints to the absence of Pauli limiting. A simplified expression of the Pauli limiting field [70], i.e., $\mu_0 H_{\text{Pauli}} \approx 1.84 \text{T/K} \cdot T_c$ yields 6.2 T, far above the experimental value. Thus the upper critical magnetic field of LaPtSi is limited almost entirely by orbital pair breaking.

As already mentioned above, the significant c/a crystal anisotropy may cause a substantial anisotropy of the upper critical field. Moreover, preferred orientation of grains can influence a simple polycrystalline average of the upper critical field ($\mu_0 H_{c2}^{\text{poly}} = (2/3)\mu_0 H_{c2}^{a,b} + (1/3)\mu_0 H_{c2}^c$) such that in resistivity measurements a certain crystallographic direction is favored on cost of the other. Additionally, anisotropy can contribute to a moderate broadening of the superconducting transition upon increasing external magnetic field as indeed is observed for both the resistive as well as heat capacity anomalies. From the

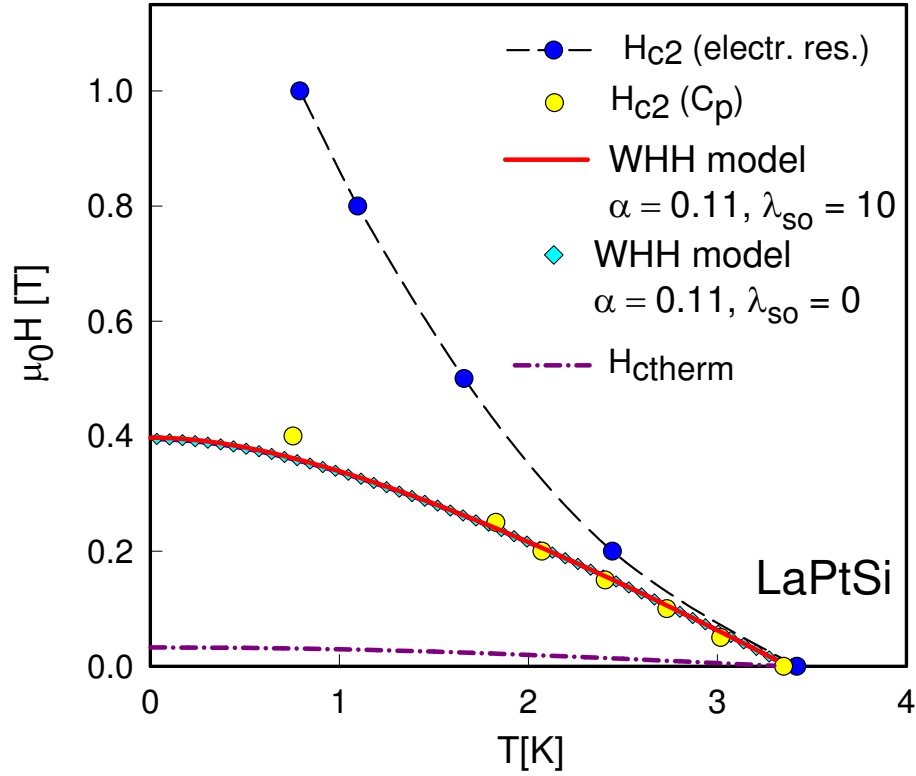


Figure 4.7: Upper critical magnetic field $\mu_0 H_{c2}(T)$ of LaPtSi as derived from resistivity and heat capacity data. The solid line and the small diamonds are fits according to the WHH model and the dashed-dotted line displays the temperature dependent thermodynamic critical field $\mu_0 H_c$. The dashed line is a guide for the eyes.

latter one can evaluate an upper limit for the anisotropy of the upper critical field slopes of about 30 %.

The integration of the entropy difference from the superconducting and the normal state as shown in Fig. 4.8 gives the difference in the free energy. The difference in the free energy $\Delta F = F_n - F_s$, is being proportional to the thermodynamical critical field, i.e.,

$$\Delta F(T) = \frac{\mu_0 H_c^2(T)}{2} = \int_{T_c}^T \int_{T_c}^{T'} \frac{C_s - C_n}{(T'')} dT'' dT' \quad (4.2)$$

revealing $\mu_0 H_c = 33$ mT when extrapolating towards $T = 0$ (dashed-dotted line, Fig. 4.7).

The knowledge of the thermodynamical critical field allows to evaluate a value for the dimensionless Ginzburg-Landau parameter $\kappa_{GL} = H_{c2}(0)/(\sqrt{2}H_c) \simeq 8.7$, where the WHH value for $H_{c2}(0) = 0.41$ T has been used. The coherence length ξ_0 for $T \rightarrow 0$ can be obtained from $\mu_0 H_{c2} = \Phi_0/(2\pi\xi_0^2)$, yielding $\xi_0 \simeq 2.83 \times 10^{-8}$ m. Combining the Ginzburg-Landau parameter with the coherence length, the London penetration depth can be obtained as $\lambda_L(T \rightarrow 0) \simeq 2.5 \times 10^{-7}$ m. It should be noted that these values deviate slightly

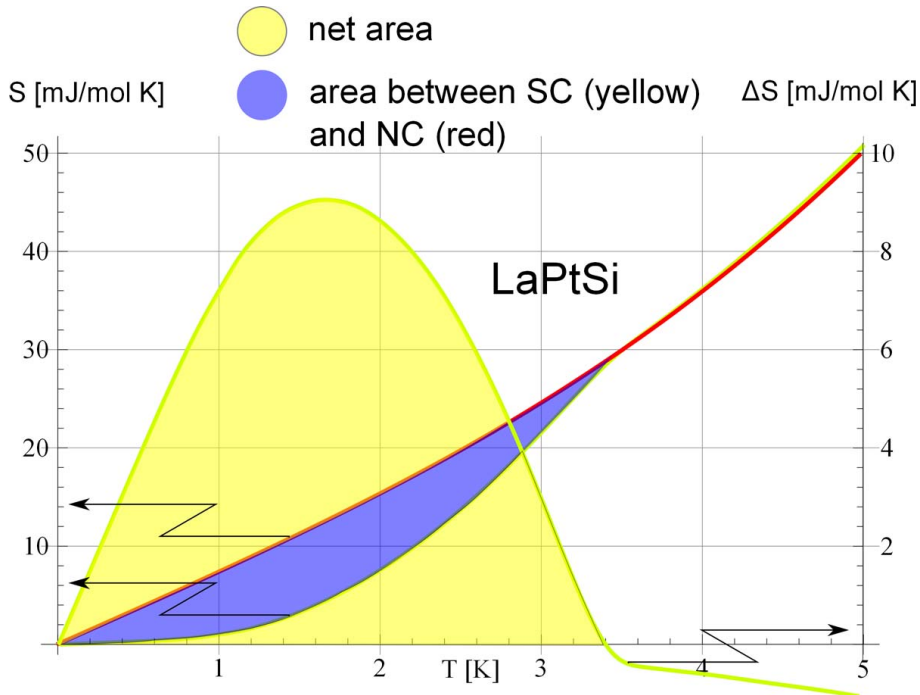


Figure 4.8: Temperature dependencies of the entropy in the superconducting and normal conducting state are depicted in this figure. The calculation of the difference of both states, ΔS , is a fundamental parameter. The yellow and the blue areas are the same (Note the different y-axis). The superconducting state is highly ordered, so the entropy becomes smaller in the SC state.

from the parameters as reported in Ref. [52]. This reflects the discrepancy in the values of H_{c2}^{Cp} and H_{c2}^{res} , since the data in Ref. [52] are taken from resistivity measurements only.

Based on $l_{tr}/\xi \approx 0.92$ LaPtSi can be classified as a superconductor in the dirty limit (l_{tr} is the total elastic mean free path). l_{tr} represents the length of the path from one scattering process to the next one. There are several possible ways to determine the total elastic mean free path. Within a first approximation of a spherical Fermi surface F_{sphere} , one can derive $l_{tr} = 1.533 \cdot 10^6 / (\rho_0 \cdot F_{\text{sphere}})$.

Electronic Structure

In Fig. 4.9(a) the electronic band structure and density of states (DOS) and in Fig. 4.9(b) the Fermi surfaces are shown calculated both in a scalar relativistic approximation, omitting spin-orbit coupling, and fully relativistically, including spin-orbit coupling, as implemented in VASP, in a self-consistent and parameter-free manner [71]. The preciseness of spin-orbit coupling in the projector augmented wave method has been verified by comparing the VASP results to calculations using the all electron full-potential linearized augmented plane-wave method [72, 73] in Ref. [74] and also cross-checked for LaPtSi.

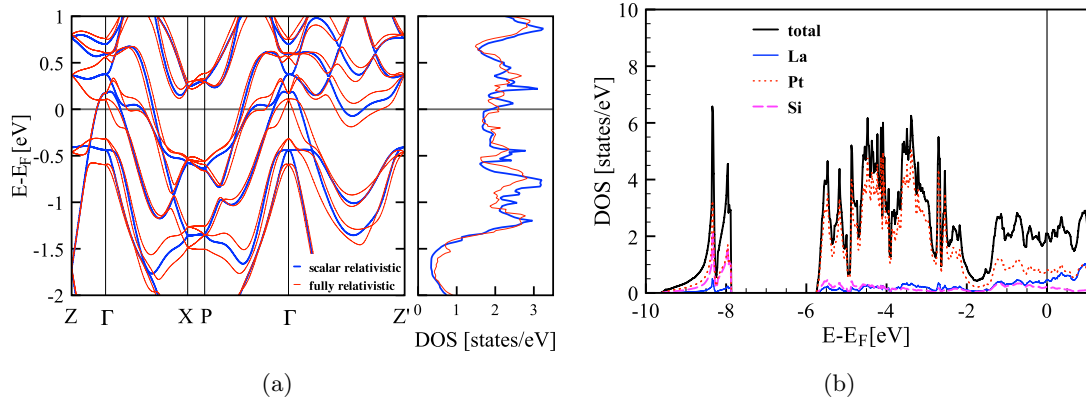


Figure 4.9: (a) Electronic band structure and DOS per formula unit of LaPtSi calculated scalar relativistically (blue lines) and fully relativistically including spin-orbit coupling (red lines). The energy scale is defined relative to the Fermi energy. (b) Total and atomic-projected electronic DOS per formula unit of LaPtSi calculated fully relativistically including spin-orbit coupling. The energy scale is defined relative to the Fermi energy.

The band structure in Fig. 4.9(a) (left panel) shows that some of the degeneracies at the high-symmetry points are lifted by taking the spin-orbit coupling into account. E.g., at Γ a spin-orbit splitting of ~ 275 meV below the Fermi energy and of ~ 455 meV above the Fermi energy is obvious.

The lack of inversion symmetry in the crystal structure of LaPtSi gives rise to an anti-symmetric spin-orbit coupling (ASOC) [75, 76, 6, 68], i.e., the double (spin) degeneracy of the bands is lost due to spin-orbit coupling in non-centrosymmetric compounds. In LaPtSi the inversion center is destroyed solely by the arrangement of the atoms along the c -axis. Therefore, the two-fold degeneracy of the bands along Γ - Z is still pertained, since the ASOC occurs only perpendicular to the directions that break inversion symmetry as revealed by the electronic band structure in Fig. 4.9(a). With the exception of the Γ - Z direction an ASOC of varying size is found, for example for the spin-orbit split band originating at Γ at ~ 170 meV (second eigenvalue including spin-orbit coupling above the Fermi energy at Γ) the vertical ASOC splitting of the bands is ~ 130 meV along both Γ - X and Γ - P and ~ 255 meV along Γ - Z' .

Concerning superconductivity of a non-centrosymmetric compound, the horizontal ASOC splitting of the bands at the Fermi energy is of prime importance. Such a horizontal ASOC splitting can be easily seen by looking at the Fermi surfaces (Fig. 4.10).

Omitting spin-orbit coupling, the Fermi surfaces of LaPtSi consist of three sheets: a closed hole Fermi surface around Γ , an irregular open hole tube around Γ - Z , and a twisted electron pillar along X - X' . Taking spin-orbit coupling into account the ASOC gives rise to a substantial splitting of these Fermi surfaces. Along Γ - Z' no doubling of the tube Fermi

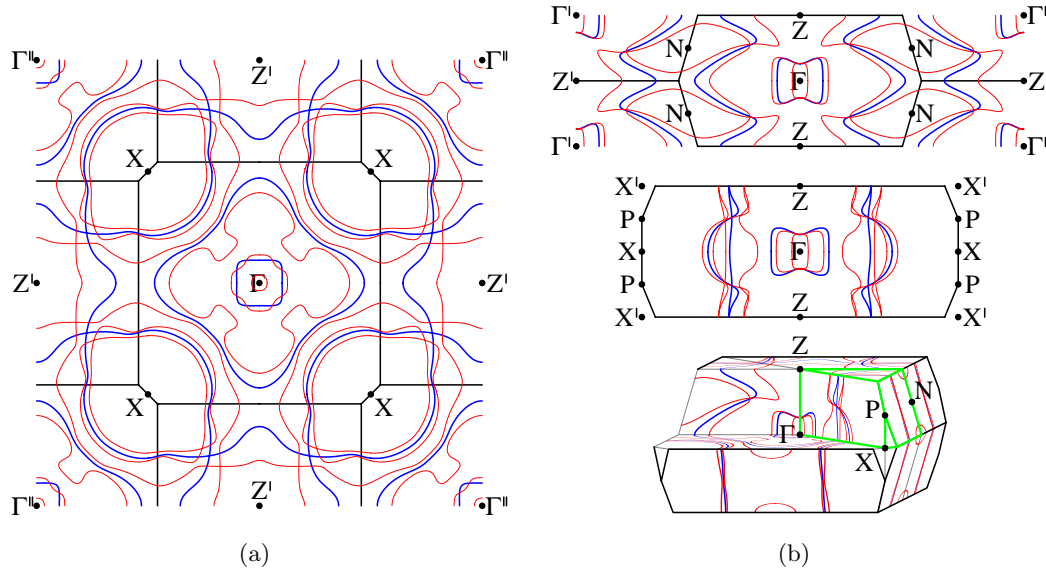


Figure 4.10: Fermi surfaces of LaPtSi calculated scalar relativistically (blue lines) and fully relativistically including spin-orbit coupling (red lines) and the Brillouin zone of the body-centered tetragonal lattice for $c > a$ from top (a) and side (b) view.

surface sheet is observed, as one of the split bands moves completely above the Fermi surface (see Fig. 4.9(a)). As discussed there is no ASOC splitting along Γ - Z , therefore the ASOC split Fermi surfaces touch along Γ - Z .

Regarding Fig. 4.11 it becomes obvious that electrons on the ASOC split Fermi surfaces do not have strictly opposite spin directions. This is due to a rather strong interband spin-orbit coupling in LaPtSi. However, as expected the spin directions rotate along each Fermi surface sheet.

Fig. 4.9(b) shows the electronic density of states (DOS) obtained from a fully relativistic calculation including spin-orbit coupling. In the range -6 to -2 eV below the Fermi energy the Pt- d -band can be identified with some hybridization of La- d and Si- p . At the Fermi energy the contribution of Pt is dominant, but the contributions of both La and Si cannot be neglected. The most dominant contributions are Pt- d , La- d , Pt- p , and Si- p . The DOS at the Fermi energy is mainly of d character whereby the Pt- d contribution is by a factor of 1.7 larger than the La- d contribution. The Pt- p is about 90% of the La- d , and the Si- p is about 75% of the Pt- p . The electronic DOS per formula unit of LaPtSi at the Fermi energy is 2.076 states/eV when spin-orbit coupling is included compared to 1.898 states/eV omitting spin-orbit coupling (see also Fig. 4.9(a)), corresponding to a calculated electronic Sommerfeld value $\gamma_e = DOS(E_F) \cdot k_B^2 \pi^2 / 3$ of 4.89 mJ/molK² for the former and 4.47 mJ/molK² for the latter.

A comparison of the experimental Sommerfeld value, γ , with the electronic one γ_e deter-

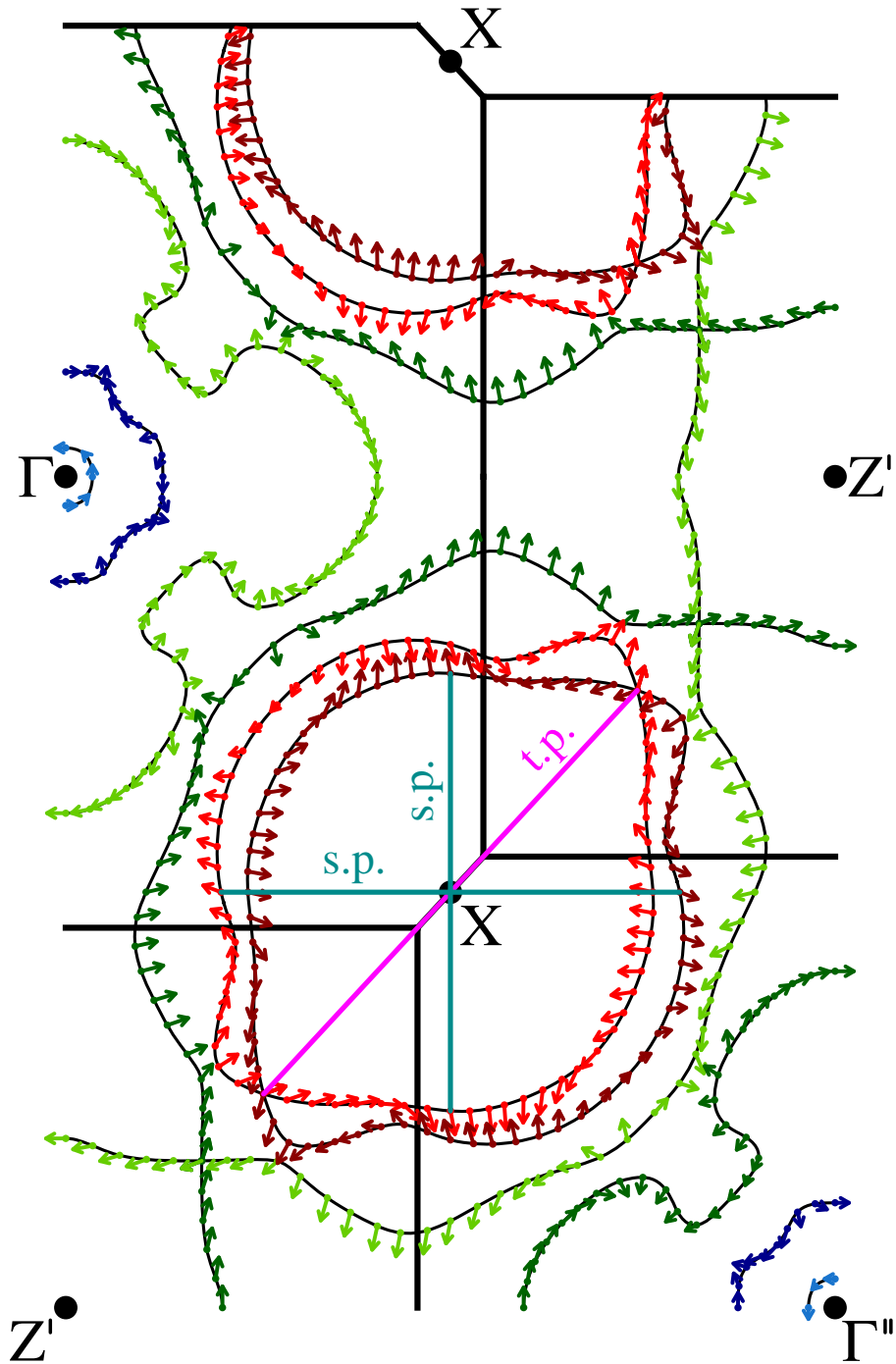


Figure 4.11: Spin directions on the Fermi surfaces of LaPtSi calculated in a fully relativistic scheme. The arrows indicate the direction and the magnitude of the spins. Note that in the plane shown the spins have no out-of-plane components. Examples for spin singlet pairing (s.p.) and simultaneous spin singlet and spin triplet pairing (t.p.) are also indicated.

mined from the electronic structure calculation reveals an electron-phonon enhancement factor λ_{ep} via

$$\gamma = \gamma_e(1 + \lambda_{ep}) \quad (4.3)$$

as $\lambda_{ep} = 0.33$ and 0.45 , respectively. Both parameters point to a weakly coupled superconducting state in LaPtSi.

Employing the semi-empirical McMillan's formula from Eqn. 2.50 [28] with the experimental value of $T_c = 3.35$ K, θ_D in the range 152–245 K, and the Coulomb repulsion strength μ_c^* generally lying within 0.09–0.18, the resulting values for $\lambda_{ep} = 0.5$ – 0.8 also suggest weak coupling. The rather high DOS at the Fermi energy accounts for the lower values of λ_{ep} as extracted from Sommerfeld values compared to the values extracted from McMillan's formula.

4.1.3 Vibrational Properties

Considering the phonon dispersion in Fig. 4.12(a) one can find that LaPtSi (see Table 4.1 for its crystal structure) is dynamically stable. About half-way along Γ - Z' (at $\vec{q}_{\text{soft}} \simeq 0.5\overline{\Gamma Z'}$) a distinct phonon softening can be identified. This phonon softening at \vec{q}_{soft} comes along with a Fermi surface nesting as seen from Figs. 4.10 and 4.11. Frequently, such a coexistence of phonon softening and Fermi surface nesting in the normal state favors superconductivity.

Studying the normalized phonon DOS in Fig. 4.12(a) one can observe that, as expected, Si as the lightest element in the compound dominates at the higher frequencies. Specifically the range of 4.7–6.1 THz and 9.7–10.7 THz with a very pronounced peak around 10.5 THz is attributed almost entirely to Si. While Pt, as the heaviest element, dominates the lower frequencies in the range of 0–2.5 THz. The contribution of La to the phonon modes is strongest between 2.5–4.0 THz. In the whole range of 0–4 THz a strong La–Pt hybridization can be seen. Further, a much smaller Si contribution has been observed in this lower frequency range of 0–4 THz and some La and Pt contributions can be seen in the higher frequency ranges of 4.7–6.1 THz and 9.7–10.7 THz.

From the DFT derived phonon DOS, $D_{ph}(\omega)$, the heat capacity is calculated using

$$C_p(T) = R \int D_{ph}(\omega) \frac{\left(\frac{1}{2} \frac{h\omega}{k_B T}\right)^2}{\sinh^2\left(\frac{1}{2} \frac{h\omega}{k_B T}\right)} d\omega \quad , \quad (4.4)$$

where ω is the phonon frequency, k_B the Boltzmann constant, h the Planck constant, and R the gas constant. Regarding the accuracy of the DFT derived phonon DOS $D_{ph}(\omega)$ the

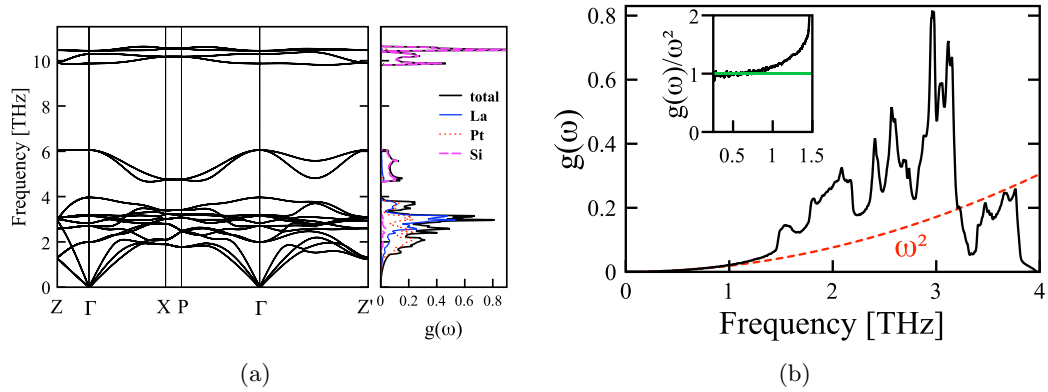


Figure 4.12: (a) Phonon dispersion and DOS ($D_{ph}(\omega)=g(\omega)$) for LaPtSi. The phonon DOS is split into the contributions of the modes attributed to La, Pt, and Si. (b) Phonon DOS ($D_{ph}(\omega)$) up to 4 THz (solid black line) compared to a Debye-like ω^2 behavior (red dashed line). The inset shows $D_{ph}(\omega)/\omega^2$ versus frequency highlighting the deviations of $D_{ph}(\omega)$ from a Debye-like ω^2 behavior.

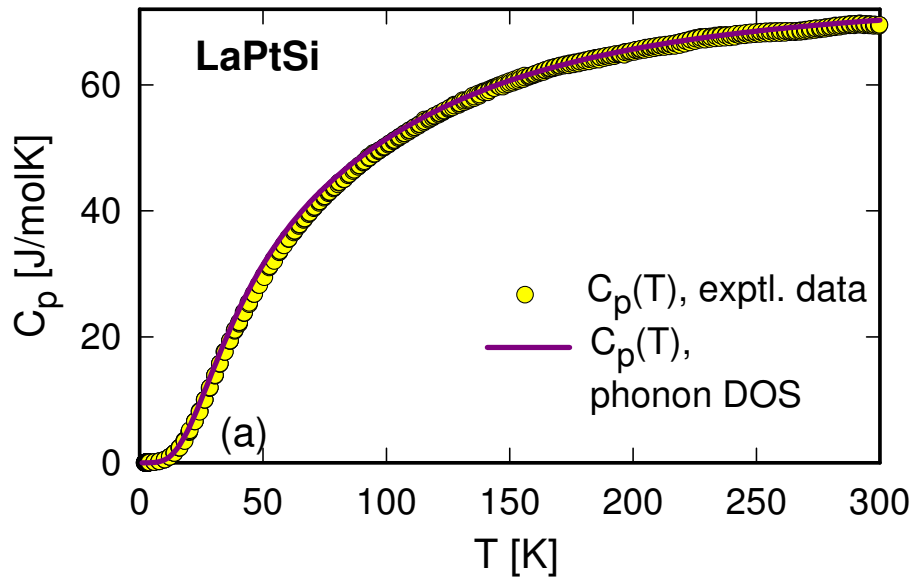


Figure 4.13: Experimental and theoretical heat capacity C_p of LaPtSi.

specific heat capacity $C_p(T)$ (Eq. 4.4) is compared to the experimental results in Fig. 4.14. Perfect agreement is revealed, with an exception for temperatures in the range from 50 to 100 K where the experimental data are slightly below the DFT ones.

An estimation of relevant phonon branches can be derived from the specific heat data analyzed in terms of a model suggested by Junod *et al.* [77, 15]. In this model, the temperature dependent quantity $(C_p - \gamma T)/T^3$ allows for a straightforward inspection of deviations from the simple Debye model. The approximated phonon spectrum consists of a Debye spectrum overlaid by Einstein branches with finite spectral widths. The experimental data for

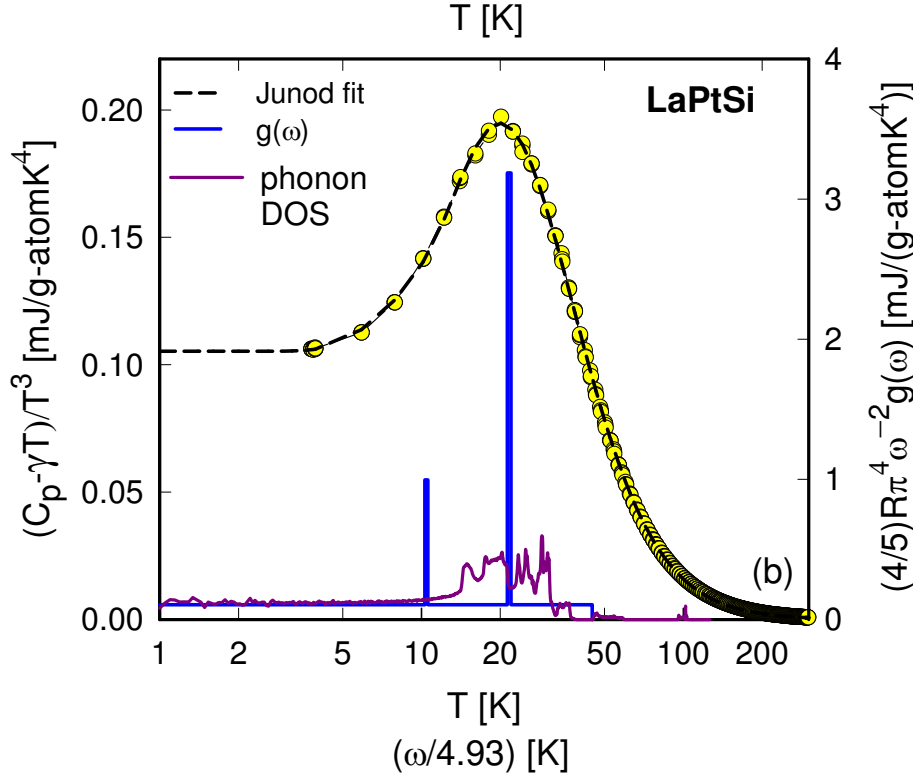


Figure 4.14: A plot of $(C_p - \gamma T)/T^3$ vs. $\ln T$ of LaPtSi. The dashed line is a least squares fit of the experimental data using the model described in the text. The essential parameters of the model used to construct the spectral function $D(\omega)$ (solid lines, right axis), are $\theta_D = 216$ K, $\omega_{E1} = 51.4$ K with a width of 1.5 K, and $\omega_{E2} = 106.6$ K with a width of 3.5 K.

LaPtSi are shown in Fig. 4.14, referring to the left axis of this graph. Besides a Debye-like background, at least two Einstein branches are needed to account for the experimental findings. A least squares fit according to Junod's model returns a Debye temperature $\theta_D = 216$ K, as well as the Einstein modes $\omega_{E1} = 51.4$ K and $\omega_{E2} = 106.6$ K with frequency widths $\Delta\omega$ of 1.5 K and 3.5 K, respectively. The slightly lower Einstein branches derived from this fit compared to the pronounced $D(\omega)$ features of the DFT calculation might be suspected to be due to the slightly smaller DFT unit cell parameters. However, this is not the case because the lower Einstein branches remain practically unchanged for small variations of the unit cell parameters.

From Fig. 4.12(a) one would assume that the Debye-like ω^2 behavior of the phonon DOS ends with the onset of the first Einstein mode at ~ 1.5 THz. However, from Fig. 4.12(b) and especially from the inset it is seen that the phonon DOS starts to deviate from a Debye-like ω^2 behavior already at a much lower frequency of ~ 0.7 THz. These deviations are attributed to a slight phonon softening that is also visible in the phonon dispersion along Γ -Z (Fig. 4.12(a)). Such a specific feature, in combination with the large spectral weight at 1.5 - 2.2 THz, is expected to account for the disagreement between the Debye

temperatures derived from specific heat and resistivity data.

By comparing the phonons from Figs. 4.12(a) and 4.12(b) to the Fermi surfaces shown in Figs. 4.10 and 4.11 one can identify unusual and important phonon modes that might play a crucial role for superconductivity. Electronic states with \vec{k}_F on the closed hole Fermi surface around Γ can be paired by phonons \vec{q} (via $\vec{k}_F + \vec{q} = -\vec{k}_F$) with frequencies of the lowest acoustic mode smaller than 1.2 THz, i.e., the range where the phonon DOS does not show a distinct peak but deviations from Debye-like ω^2 behavior are already obvious. Electronic states with \vec{k}_F on the remaining open tubes and pillar-like Fermi surfaces can be connected by phonons \vec{q} with frequencies of the lowest acoustic mode ~ 1.5 THz (first Einstein mode) and ~ 2 THz, both corresponding to pronounced peaks in the phonon DOS.

The moderate height of these peaks, however, might be the reason for the low superconducting transition temperature. Such a correlation has recently been shown for ternary APt_3P superconductors ($A = \text{Ca, Sr, La}$) where the height of the low energy phonon DOS peak was in-line with the respective value of T_c [78].

Concerning a possible unconventional behavior of LaPtSi , the above described pairing results predominately in spin singlets since the spin directions rotate concomitantly along the Fermi surface sheets with the electronic states at \vec{k}_F and $-\vec{k}_F$ having opposite spins, as can be seen from Fig. 4.11. In this figure examples for spin singlet pairing and simultaneous spin singlet and spin triplet pairing are also indicated. Spin singlets (total spin of the Cooper pair $S = 0$) are possible everywhere on the Fermi surface. Spin triplets ($S \neq 0$), although in principle allowed to coexist with spin singlets due to the ASOC for non-centrosymmetric systems, are of much lesser importance for LaPtSi as they may only occur at Fermi surface intersections. This is completely in-line with the experimental observations.

4.2 LaIrSi and CeIrSi

This section deals with the ternary NCS compounds LaIrSi and CeIrSi. LaIrSi raised particular interest because possible superconductivity had been reported previously in [51] and [79]. A superconducting state of the whole bulk was not identified but some features, e.g. a drop in electrical resistivity data and a small kink in specific heat measurements, might indicate a foreign phase being responsible for the proclamation of superconductivity. CeIrSi, as many intermetallic compounds containing Ce, shows interesting features such as magnetic ordering in the presence of a cubical symmetric crystalline electric field (CEF) splitting. A comparison to LaIrSi allows further discussions leading to a deeper understanding of the possible ground state.

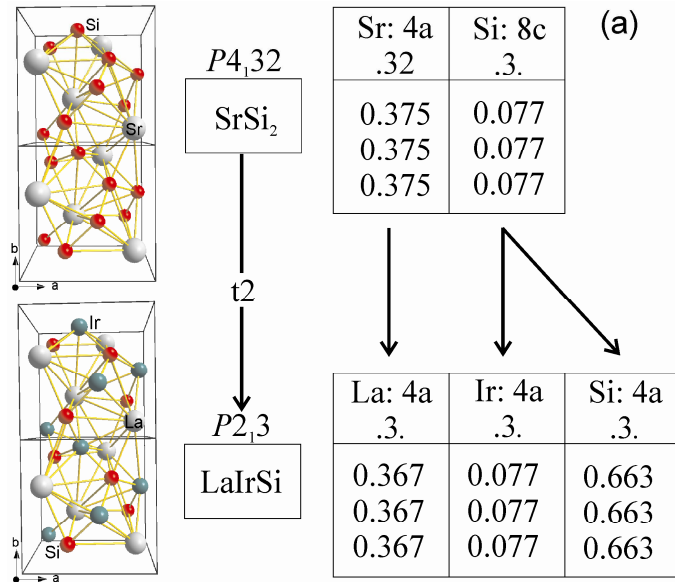


Figure 4.15: The structure derivation of CeIrSi and LaIrSi. The graph also includes the site positions.

Table 4.2: Structure and parameters of LaIrSi and CeIrSi

	LaIrSi	CeIrSi
Space group	$P2_13$	$P2_13$
a (nm)	0.63766(3)	0.62951(1)
RE 4a (x=y=z)	0.36714(6)	0.3683(2)
Ir 4a (x=y=z)	0.07740(5)	0.0830(2)
Si 4a (x=y=z)	0.6635(2)	0.6693(6)
RF	0.028	0.062
EPMA (at.%)		
RE; Ir; Si	33.4; 34.7; 31.9	34.3; 32.7; 33.0

4.2.1 Experimental details

Samples of polycrystalline LaIrSi and CeIrSi were molten from pure ingots in the arc furnace. The ingots were weighted in proper stoichiometric composition and melted in argon atmosphere with Ti acting as getter material to absorb unpleasant remaining gas particles. Several remelting processes were conducted to assure homogeneity. Subsequently, the samples were sealed in quartz tubes and annealed for one week. X-ray powder diffraction (XRD), scanning electron microscopy (SEM) and electron probe micro analysis (EPMA) were used for the characterization of the samples. The compounds LaIrSi and CeIrSi crystallize in the primitive cubic ZrSiSi structure type ($P2_13$) with a lattice parameter $a = 0.5881(2)$. This structure type is a derivative of the also non-centrosymmetric SrSi₂-type (space group $P4_132$; $a = 0.6515$ nm) and identified by Klepp *et al.* [50].

4.2.2 Results and Discussion

The unit cell of both compounds and the group-subgroup relations in form of a Bärnighausen tree [61, 62] are shown in Fig. 4.15. The results received from Rietveld refinement using the FullProf program [80] and from EPMA are summarized in Tab. 4.2. The LaIrSi sample contains small amounts (<2%) of LaIr₂Si₂ as an impurity phase and the CeIrSi contains also about 2% of CeIr₂Si₂, CeSi_{1.7} and small amounts of cerium oxide as impurities.

4.2.3 LaIrSi

Superconductivity in LaIrSi was reported in several papers with a varying critical temperature between 1.5 K and 2.3 K in [51] and [79], respectively. Evers *et al.* already discussed the question of superconductivity as a bulk property of LaIrSi. Within this thesis, superconductivity was not fortified as a property of this specific sample. Electrical resistivity measurements have been performed in a ³He bath cryostat as well described in Sec. 3.2.1 from 400 mK up to 120 K.

At higher temperatures, the data points can be perfectly described with the Bloch-Grüneisen law as depicted in Fig. 4.16(a). At lowest temperatures, a residual resistivity of around 82 $\mu\Omega\text{cm}$ was estimated. Without an external magnetic field one can identify a rather small decrease of the electrical resistivity already at 1.25 K and then a larger drop of around 50% to 43 $\mu\Omega\text{cm}$ at 0.8 K. Here, the electrical resistivity never reaches absolute zero. An elaborate consideration of the influence of magnetic fields on the samples unveils at least a small decrease of the resistivity even at external fields of $\mu_0 H = 1$ T.

Specific heat measurements show an almost perfect simple metallic behavior without any

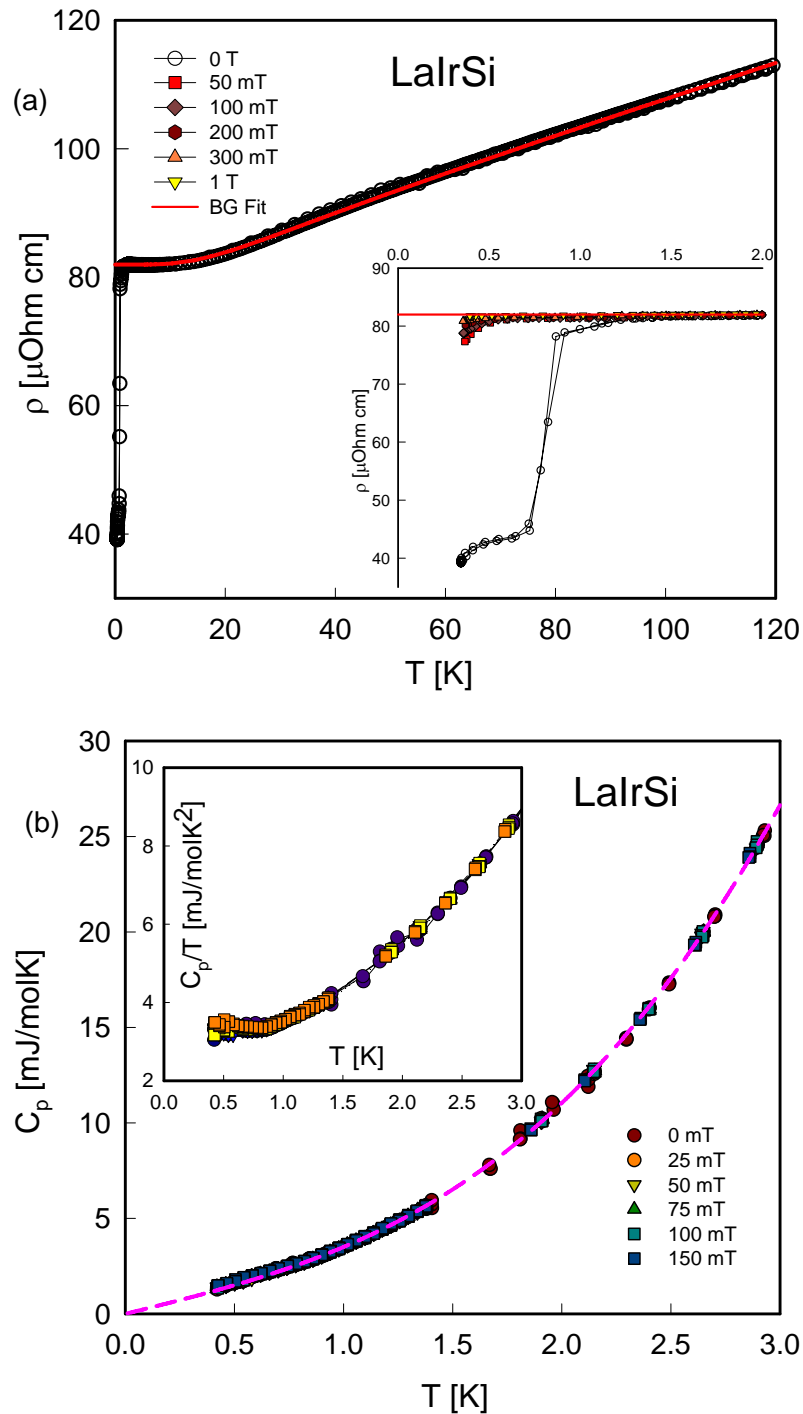


Figure 4.16: (a) The temperature dependent electrical resistivity measurement of LaIrSi. The red line is the Bloch-Grüneisen fit. (b) Temperature dependent specific heat of LaIrSi. The pink line is a low temperature Debye-fit. The inset shows the specific heat divided by the temperature.

significant evidence of a phase transition. Therefore, superconductivity was not identified as a bulk property within this sample. However, the inset of Fig. 4.16(b) shows a rather small bump at very low temperatures. The onset of a superconducting transition from the electrical resistivity measurements and the small bump in C_p/T might bolster up the theory of either the influence of a foreign phase, or some other effects like grain boundary superconductivity.

Even at higher external magnetic fields, the bump gets not fully suppressed. A Debye law was used to fit the low temperature values of C_p . With Eqn. 2.25 one can deduce $\gamma = 2.8$ mJ/mol K² and $\beta = 0.6723$ mJ/mol K⁴ (or $\Theta_D = 205$ K).

4.2.4 CeIrSi

Intermetallic Ce compounds often come along with an interesting ground state which usually triggers widespread interest in the scientific community. Within this chapter, a variety of the physical properties, i.e. the electrical resistivity, the heat capacity and the magnetic susceptibility are discussed and analyzed in detail. A comparison to the non-magnetic composition LaIrSi allows to derive the magnetic contribution. Possible overlapping effects of foreign phases will be discussed as well. Three different features at around 2 K, 5.5 K and 11 K can be identified and attract most of the attention in the following.

Generally, a Hamiltonian which describes a system of N f-electrons is composed of four independent parts $\hat{H}_{\text{total}} = \hat{H}_0 + \hat{H}_1 + \hat{H}_{SO} + \hat{H}_{\text{CEF}}$. \hat{H}_0 comprises a kinetic term, \hat{H}_1 a screened Coulomb term, \hat{H}_{SO} a SO interaction like in Eqn. 2.11 and the CEF splitting contribution

$$\hat{H}_{\text{CEF}} = \sum_i^N V_{\text{CEF}}(\vec{r}_i). \quad (4.5)$$

The CEF potential strongly depends on the surrounding ions. Assuming that the f-shells do not overlap with their neighbors, one can perform a series expansion. A detailed form of this procedure can be found in [11, 81]. Finally, one obtains

$$\hat{H}_{\text{CEF}} = \sum_{l,m} B_l^m O_l^m. \quad (4.6)$$

O_l^m are known as the Stevens operators and B_l^m are the crystal field parameters. The symmetry of the crystal and the magnetic moment \mathbf{J} have a crucial influence on O_l^m and B_l^m .

In a 4f-shell element, the SO interaction is by far stronger than the CEF splitting. Especially the NCS has an interesting effect as ASOC prevails. Ce, in general, can be found in the 2+, 3+ and 4+ oxidation state. The 2+ state is rarely realized in nature and will

not be considered in detail. The 3+ state is the magnetic state of Ce and has a magnetic moment of $J = |L + S| = |-3 + 1/2| = 5/2$. The 4+ state is non-magnetic. A possibility to change the 3+ state to the 4+ state is the application of hydrostatic pressure as it was discussed in detail in Sec. 3.2.3. There are also materials known with a mixed or intermediate valence state of Ce [82]. Ce in the 5/2 state is a Kramer's ion. A half-integer value for j implies an odd number of electrons and thus two possible orientations. Therefore, the CEF levels of Ce^{3+} are at least two-fold degenerated. One has to note that Kramer's theorem is just valid in a system with time reversal symmetry. The structure of CeIrSi is from the primitive cubic type as seen in Fig. 4.15. In a first approximation the crystal structure can be also seen as symmetry of the crystal electric field. This symmetry condition involves to identify the ground state as a doublet and a quartet as the excited state or vice versa. One has to note that the CEF levels were calculated for a symmetric potential which is not valid in this sample. To this day, a fully covering theory has yet to be elaborated for \hat{H}_{CEF} splitting in a NCS material. Nevertheless, a Hamiltonian for a centrosymmetric cubic potential for a Ce^{3+} ion is given by

$$\hat{H}_{\text{CEF}} = B_4^0(O_4^0 + 5O_4^4). \quad (4.7)$$

The electrical resistivity of CeIrSi shows an almost constant value over large temperature ranges and is depicted in Fig. 4.17(a). It shows a value of $305 \mu\Omega \text{ cm}$ at room temperature and slowly declines to $302 \mu\Omega \text{ cm}$ at around 100 K. From 100 K to 15 K the absolute value further decreases to $288 \mu\Omega$. The electrical resistivity in these regimes is dominated by phonon scattering and spin-disorder scattering. The latter contribution can be accounted by the following equation as derived by De Gennes *et al.* [83],

$$\rho_{\text{spd}} \propto (g_L - 1)^2 \cdot J(J + 1). \quad (4.8)$$

Additional effects, which distinguish between the ground state and excited states are neglected within this approximation. In a CEF, the contribution of ρ_{spd} becomes temperature dependent. This is explained in detail, e.g., in Ref. [84].

A first indication of a magnetic phase transition from electrical resistivity measurements can be seen at around 10.2 K. The change in the first derivative of ρ is rather small, which might already indicate a foreign phase and, therefore, just a small volume contribution. This will be further discussed in other physical property measurement. At fields above 7 T the transition appears to be fully suppressed.

With decreasing temperature, the system undergoes a second phase transition. This is indicated by the small kink at around 2.3 K. With an increasing field the spins get aligned along the external field axis and reduce the electrical resistivity. The magnetoresistance at lowest temperatures shows an almost linear dependency with a small slope of $\frac{d\rho}{dB} =$

0.7 $\mu\Omega\text{cm}/\text{T}$. At temperatures above 60 K the influence of external magnetic fields up to 9 T appears to be negligible. The external field seems to move the phase transition to higher temperatures. This will be later bolstered up by specific heat measurements.

Specific heat measurements provide a deeper insight on the energetic ground state of CeIrSi. Zero field measurements were performed in an adiabatic calorimeter from 1.9 K up to 80 K and are shown in the inset of Fig. 4.18. Results at higher temperatures will be discussed later in terms of the entropy. $C_p(T)$ measurements in an external magnetic field were carried out in a PPMS with the ^3He inset down to 400 mK; results are shown in Fig. 4.17(b). The transition at 10.2 K from the resistivity measurements cannot be seen in these data. However, at around 5.6 K one can see a small kink in the heat capacity. This kink is evident in the adiabatic measurements as well as in the results obtained from the relaxation time method even though a mass of around 1 g and 1.5 mg were used, respectively. This is a strong hint for an intrinsic effect. At 1.7 K a maximum is visible indicating a magnetic phase transition. The identification as a lambda like transition can be difficult in the relaxation time method, as the transition usually gets smeared out. The maximum lies below 1.9 K and, therefore, could not be accessed by the adiabatic method.

External magnetic fields from 0.5 T up to 9 T were applied. The temperature of the first transition shifts to higher temperatures. This can be seen from Fig. 4.17(b). The temperatures of the maxima are emphasized by the colored lines. A magnetic transition becoming shifted to higher temperatures while exposed to an external field usually strengthens the idea of a ferromagnetic transition. The difference of the heat capacity of CeIrSi to LaIrSi can be attributed to the magnetic contribution. From this difference, the magnetic entropy $S_{mag}(T)$ can be calculated and is indicated in Fig. 4.18. At low temperatures, below 20 K, S_{mag} gives a value of $R \cdot \ln 2$. This is in agreement with a two-fold degenerate ground state. The solutions to the Hamiltonian are presented in the base of J_z , giving the doublet ground state

$$|\Gamma_7\rangle = \alpha |\pm 5/2\rangle - \beta |\mp 3/2\rangle \quad (4.9)$$

and the excited quartet state

$$|\Gamma_8\rangle = \begin{cases} \beta |\pm \frac{5}{2}\rangle + \alpha |\mp \frac{3}{2}\rangle \\ |\pm \frac{1}{2}\rangle \end{cases} . \quad (4.10)$$

α and β are the mixing coefficients and are $\sqrt{1/6}$ and $\sqrt{5/6}$, respectively [85]. With the knowledge of the ground state, one can calculate the magnetization of this state.

$$M_{\text{Ce}^{3+}} = g_L \mu_B \cdot \langle \Gamma_7 | J_z | \Gamma_7 \rangle = 6/7 \mu_B (1/6 \cdot -5/2 + 5/6 \cdot 3/2) = 0.71428 \mu_B \quad (4.11)$$

At 20 K the value of the entropy seem to be rather constant, with just a small slope.

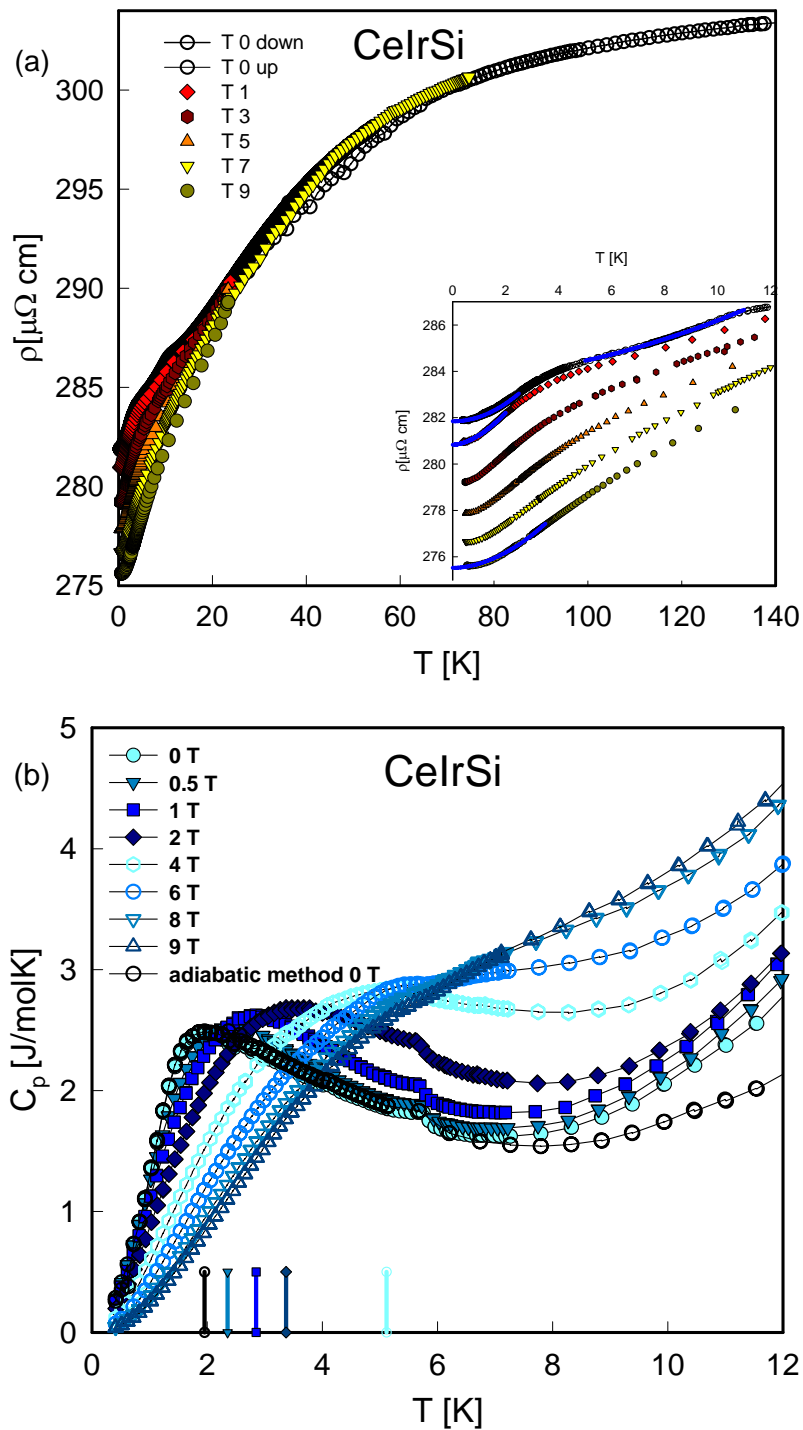


Figure 4.17: (a) Temperature dependent electrical resistivity measurements of CeIrSi. The insets show the temperature range from 0 K to 12 K and unveils two transitions. (b) Specific heat in dependency of the temperature of CeIrSi in different fields up to the maximum of 9 T.

Generally, this counts as an evidence for a larger energy between the ground state and the further excited states. The kink at 5.6 K prevails up to 4 T. Even at higher fields, a small anomaly seems to persist. Several attempts to resolve the origin of this kink, i.e. quadrupolar ordering, were disproved by an analysis of the entropy.

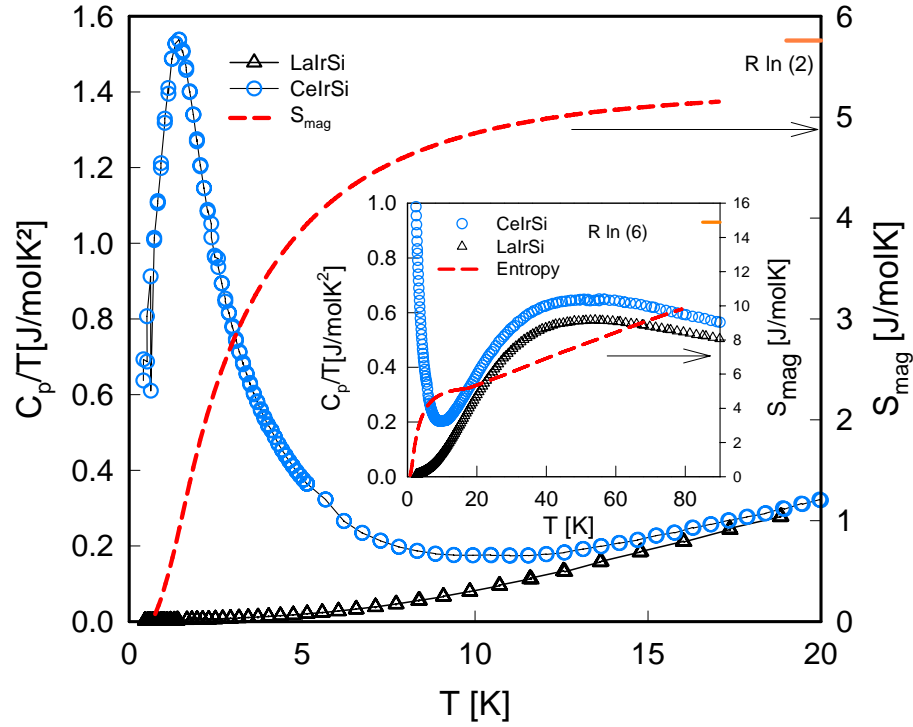


Figure 4.18: Comparison of $C_p(T)/T$ of LaIrSi and CeIrSi in zero field. The magnetic entropy was derived from the difference of both values and integration over T . A possible ground state value of the entropy $S_{mag} = R \cdot \ln(2)$ is drawn in the chart.

Magnetic susceptibility measurements χ on CeIrSi were performed in different external magnetic fields from 5 mT to 9 T at a temperature drift from 300 mK to 2 K in the ³He inset and from 2 K to 300 K in the ⁴He system. Fig. 4.19 depicts the magnetization measurements from 300 mK to 20 K. The maximum of the susceptibility at 5 mT is located at 1.2 K with 0.85 emu/mol Oe. Below this temperature the susceptibility reduces to 0.61 emu/mol Oe. This is a good indicator of an antiferromagnetic (AFM) transition with a Neel temperature of $T_N = 1.2$ K. However, a polycrystalline sample with randomly arranged unit cells generally causes a decrease of χ by a factor of 1/3. Possible explanations can be a deviation of randomly orientated unit cells or additional effects which overlap with the AFM transition. The latter aspect might be an effective approach to discuss further peculiarities found in the sample. The application of higher fields still shows the magnetic ordering, but the drop of χ becomes smaller and smaller. At 1 T the drop is completely suppressed, while the sample still shows a magnetically ordered phase, because the curves

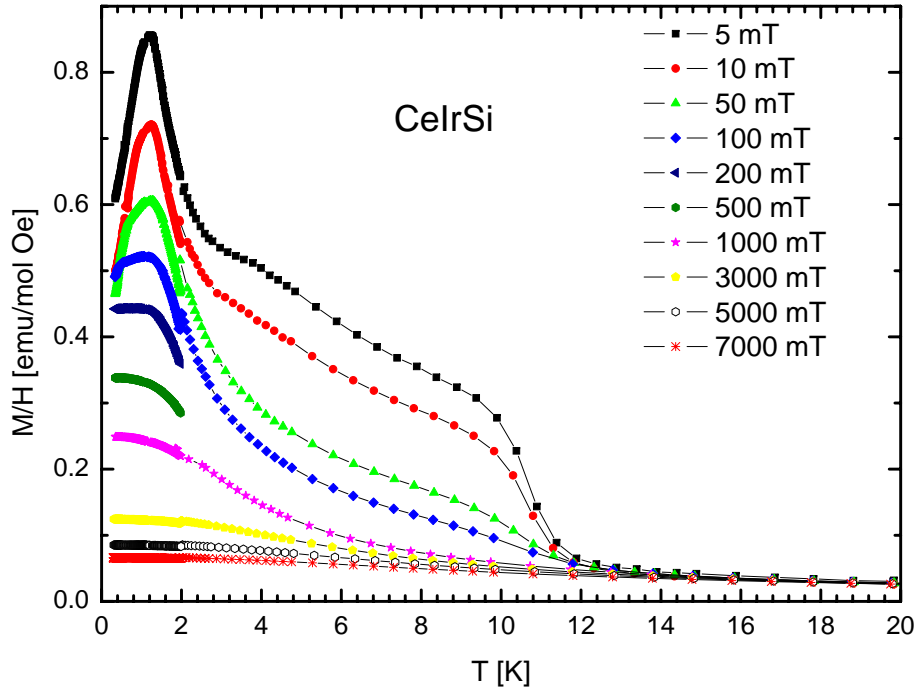


Figure 4.19: Magnetic susceptibility measurement in dependency of the temperature in CeIrSi. A detailed explanation of the visible transitions are given in the text.

from 1 T to 7 T do not overlap as it would be expected from a simple paramagnetic phase. At around 4.5 K the susceptibility measurements indicates a tiny kink, which might be correlated to the kink observed in specific heat measurements at 5.6 K. However, small fields of 50 mT upwards are sufficient to make the kink disappear which contradicts the results from electrical resistivity measurements. At around 11 K, a ferromagnetic (FM) transition occurs. This is in a fairly good agreement with the transition one has noted in the electrical resistivity measurements at 10.2 K. As there is no such transition visible in the heat capacity measurements, the idea of a foreign FM phase superimposing the magnetic behavior of the primary phase, is further bolstered up by these results.

Additionally, field ramps at constant temperatures were performed from around 0.5 K to 50 K. The Curie-Weiss law

$$\chi = \chi_0 + \frac{C}{T - \theta_p} \quad (4.12)$$

allows to analyze the behavior of the inverse of the magnetic susceptibility $1/\chi$ in the paramagnetic regime. The least squares fit ($T > 100$ K) according to the Eqn. (4.12) is shown as a solid line in Fig. 4.20, revealing an effective magnetic moment $\mu_{\text{eff}} = 2.64 \mu_B$ which is slightly larger than $\mu_{\text{eff}} = 2.53 \mu_B$ of a free Ce^{3+} ion. Iridium containing materials are well known to have interesting influence on the magnetic behavior of a compound. One possible explanation, therefore, interprets this increase based on the Ir influence. The

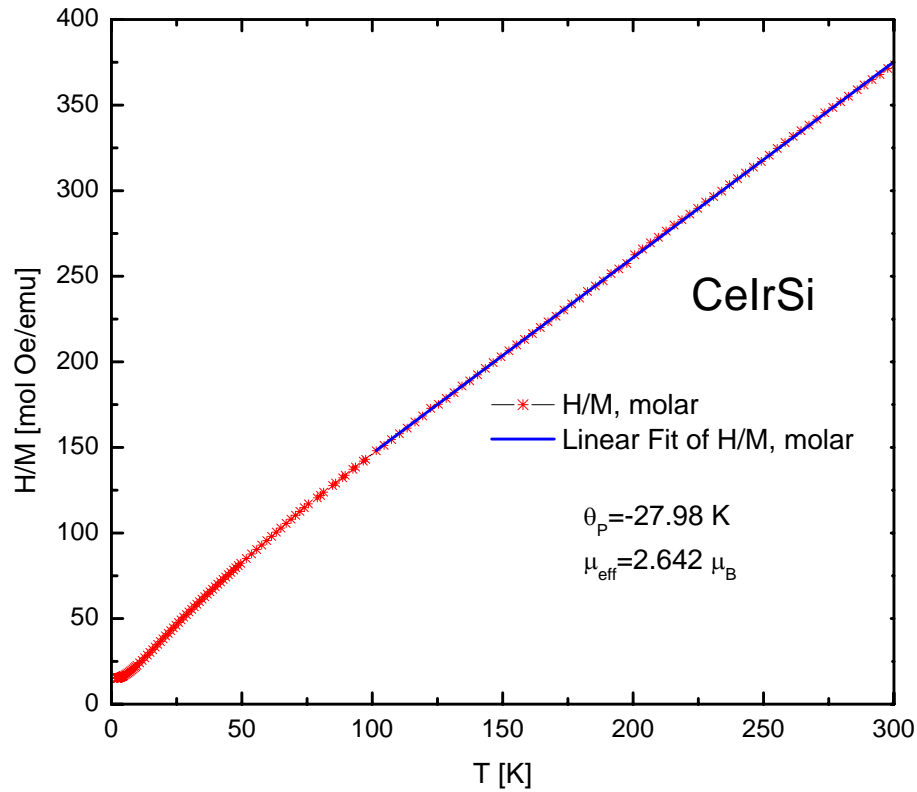


Figure 4.20: The Curie-Weiss fit to the data. A negative paramagnetic ordering temperature was derived fortifying an AFM transition.

paramagnetic Curie temperature was estimated to $\theta_p = -28 \text{ K}$. A negative paramagnetic Curie temperatures indicates an AFM interaction among the Ce^{3+} ions.

The Landau theory of a magnetic phase transition is given by the following equation

$$F_{\text{mag}}(M) = -HM + a(T - T_c)M^2 + b(T - T_c)M^4 + \dots \quad (4.13)$$

This equation is best represented by plotting M^2 over H/M . This is called Arrott plot [86]. Thus the assumption of an AFM transition is further bolstered up by Fig. 4.21. In a simple model, the Arrott plot will show just a linear dependency, if the factor $b(T - T_c)$ is zero. The more complex form indicates that terms of higher order contribute to the shape of the plot. In a FM system, lines below the Curie temperature T_C will have a value greater than 0 at $H/M = 0$. With increasing temperatures, the lines shift to the right. The distance between the lines should scale with the temperature difference. In an AFM system, lines below the Neel temperature T_N shift at first to the left with increasing temperature. At temperatures above T_N , this trend turns and the lines shift to the right with increasing temperature. In Fig. 4.21, the curves at 0.5 K and 2.15 K almost overlap and finally meet at higher fields. These two measurements show different slopes. A comparison of the

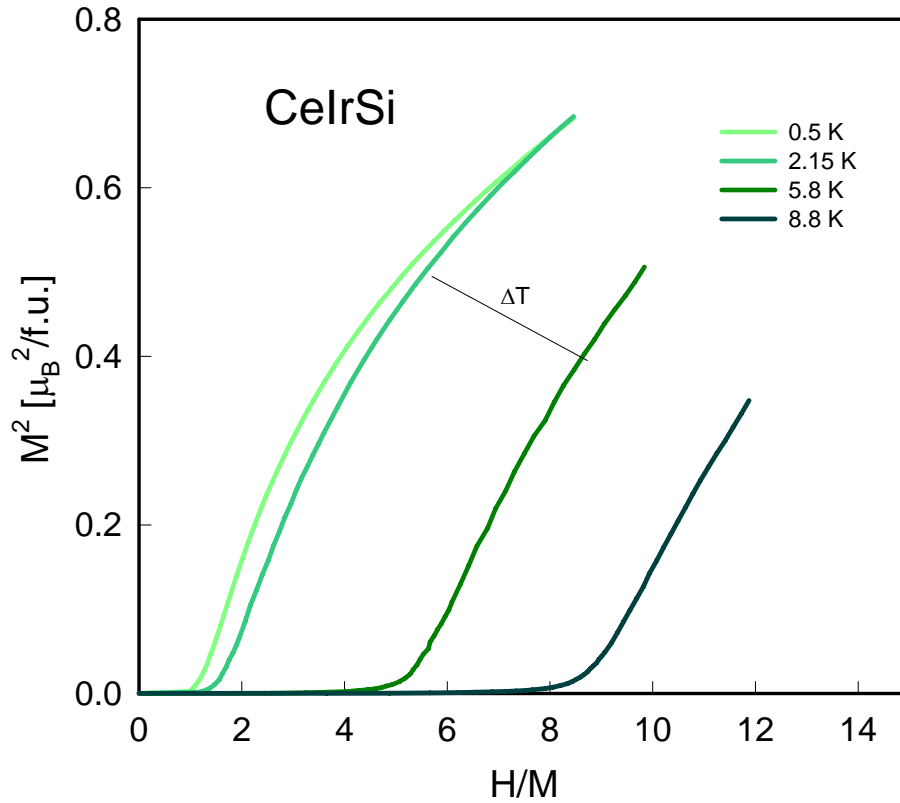


Figure 4.21: Arrott Plot of CeIrSi. A discussion is provided in the text.

2.15 K, 5.8 K and 8.8 K depicts a similar behavior of these three curves.

Yashima *et al.* [87] and Sato *et al.* [88] studied in detail CeSi_x compounds which crystallize in the centrosymmetric $\alpha\text{-ThSi}_2$ structure with varying x from 1.55 to 2. They showed that in a single crystal of $\text{CeSi}_{1.7}$ two distinct transition occur at 12.4 K and 13.7 K, respectively. However, in a polycrystalline sample, the two independent transition appear to merge to a single FM transition at temperature of 10.9 K. This value might correspond to the FM transition, observable in the measurement data of CeIrSi, especially in the ρ and χ data. Additionally, $\text{CeSi}_{1.7}$ is close to FM instability which can cause a small shift of the transition temperature.

The red dashed circle in Fig. 4.23 highlights an initial magnetization of CeIrSi of $0.01 \mu_B$ per Ce atom without an external field. At temperatures above the FM transition, i.e. above ≈ 12 K, one can see that the initial magnetization is absent. The magnetic moment of CeIrSi is seen in the inset of Fig. 4.23 with a value of $0.82 \mu_B$ at 7 T. From the analytical calculation of the ground state magnetization in Eqn. 4.11 the a value of $0.71 \mu_B$ was derived. This difference can be again explained with the contribution of the Ir atoms, which boost the magnetic moment of the bare Ce^{3+} ion. Another interesting effect can be

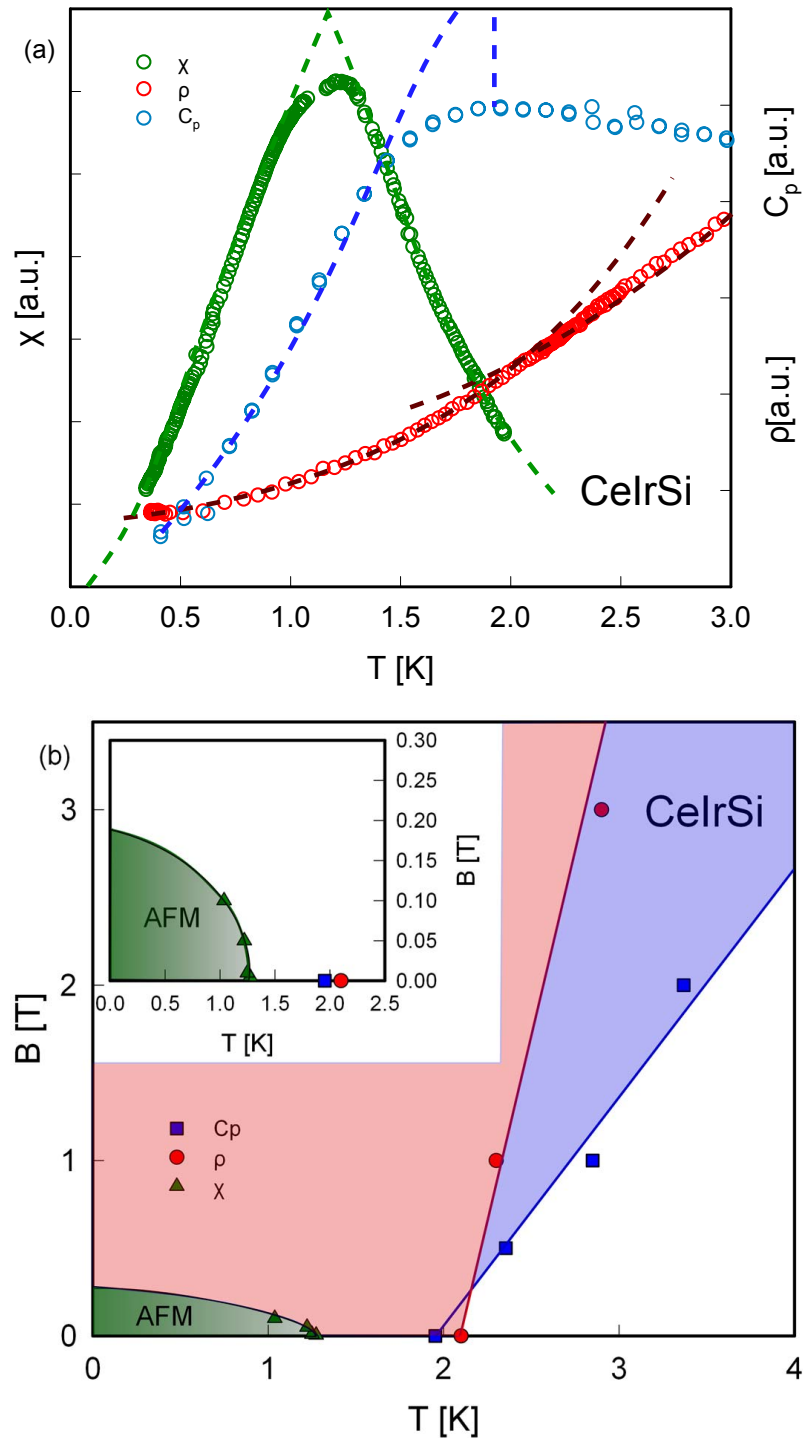


Figure 4.22: (a) A comparison of the measured physical properties of CeIrSi. The ideal forms of the transitions are highlighted by the colored dashed lines. The susceptibility data show the kink due to the AFM transition, heat capacity data unveils a smeared lambda-anomaly and electrical resistivity data exhibit a change in the slope. (b) Phase diagram of CeIrSi. Results from magnetization measurements show a clear transition to the AFM state. Contrary, ρ and C_p are much more influenced which is also visible from Fig. 4.17.

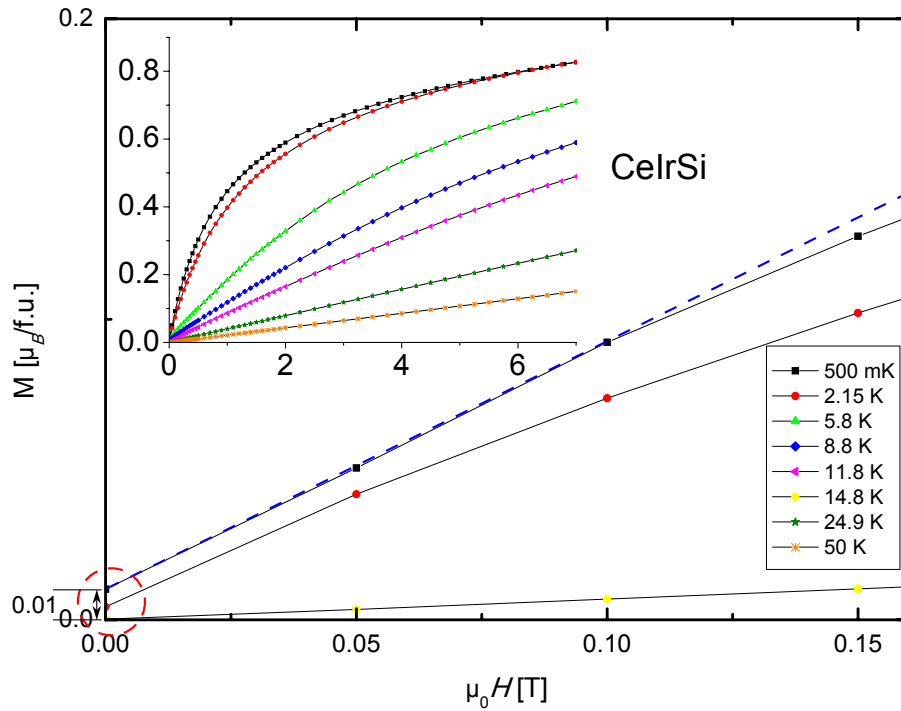


Figure 4.23: Magnetization measurements of CeIrSi. The blue dashed line extrapolates the initial behavior. The susceptibility as the derivative dM/dH increases for small temperatures and small external fields, as it is also observed from Fig. 4.19. Additionally, a small initial magnetization of $0.01 \mu_B$ is visible, fortifying the assumption of a foreign phase contribution.

derived from the initial slope of $M(H)$ which is highlighted in Fig. 4.23 by the blue dashed line. From 0 to 200 mT the increase of M just slightly deviates from a linear behavior and shows a rather small s-like shape. With the persistent non-zero initial magnetization an overlapping effect of the FM foreign phase can be identified as good explanation for various deviations from an unperturbed AFM ordering.

4.3 HfRhGe

This chapter covers experimental details of the superconductor HfRhGe which crystallizes in the non-centrosymmetric ZrNiAl-type structure (space group $P\bar{6}2m$). The phase transition occurs at critical temperatures T_c of 1.69 K and 1.66 K in electrical resistivity and specific heat measurements, respectively. HfRhGe has not been studied up to now and can be seen as a new example of a NCS SC. The present study of HfRhGe is supposed to examine superconductivity in a non-centrosymmetric hexagonal structure in order to obtain a deeper understanding of the physical properties and the influence of the crystal structure on the pairing mechanisms. A main focus is also set on the unusual strong discrepancy of bulk and transport properties obtained for the upper critical field H_{c2} and H_{c2}^{res} .

4.3.1 Experimental details

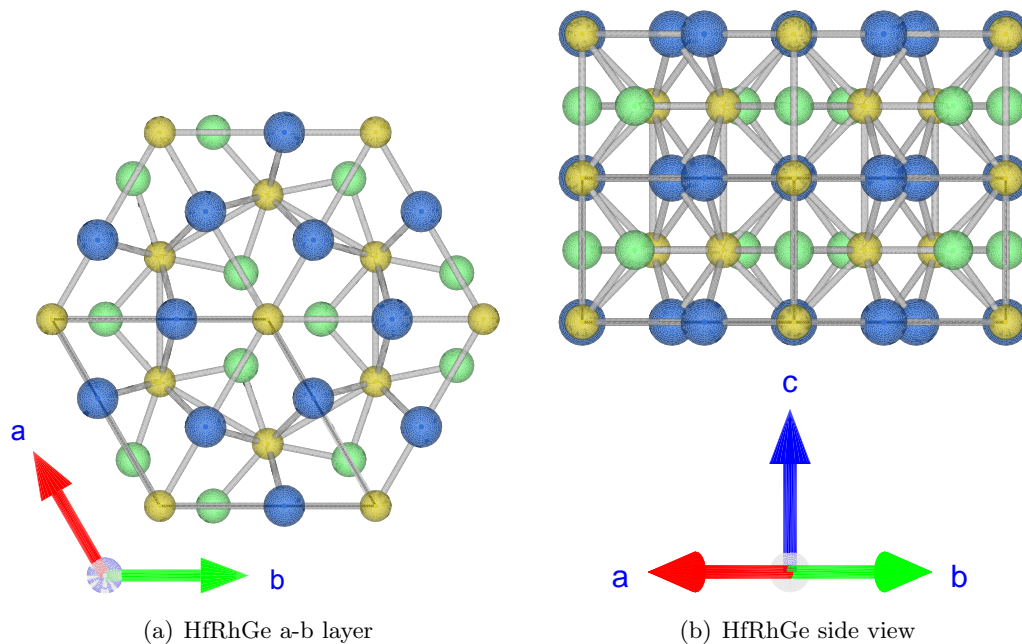


Figure 4.24: Structure of HfRhGe. The absence of an inversion symmetry is unveiled in the a-b plane. Blue, green and yellow atoms indicate the positions of the Hf, Rh and Ge, respectively.

A bulk sample of HfRhGe was prepared in the pure stoichiometric composition of 1-1-1 by arc melting in a sealed argon atmosphere with an additional Ti getter. The raw ingots were melt together and further turned and remolten several times to ensure a proper homogenous stoichiometric composition throughout the whole sample volume. The samples were further cut. A small amount was powdered for XRD analysis and further

Table 4.3: Structural parameters and Wyckoff positions of HfRhGe.

		Exp.
lattice parameter	<i>a</i> :	0.659126(8) nm
lattice parameter	<i>c</i> :	0.388219(5) nm
Hf on 3f	(<i>x</i> , 0, 0):	0.57643(9)
Rh on 3g	(<i>x</i> , 0, 1/2):	0.2479(1)
Ge1 on 1a	(0, 0, 0):	
Ge2 on 2d	(1/3, 2/3, 1/2):	
crystal structure:	ternary derivative of Fe ₂ P	
space group:	189 or <i>P6̄2m</i>	

characterized by Structure Tidy in Ref. [80]. After the arc-melting procedure, the HfRhGe specimen formed already larger single crystals. All measurements have been performed on the single crystals. The crystal was not orientated. The single crystals themselves were very brittle which might have an influence on the absolute values of the electrical resistivity.

4.3.2 Results and Discussion

XRD measurements indicate that the stoichiometric composition 1-1-1 as HfRhGe is the main phase with just a small contribution of foreign phases. HfRhGe crystallizes in the non-centrosymmetric hexagonal *P6̄2m* space group in the ZrNiAl (see Fig. 4.24(a)) structure which is an ordered ternary derivative of the Fe₂P type.

The electrical resistivity in Fig. 4.25 shows a rather simple metallic behavior which can be accounted for in term of the BG formula and an additional *s-d* scattering term (T^3), as described in the following equation.

$$\rho(T) = \rho_0 + c_0 \left(\frac{T}{\theta_D} \right)^5 \int_0^{\frac{\theta_D}{T}} \frac{x^5 dx}{(e^x - 1)(1 - e^{-x})} + c_1 T^3 \quad (4.14)$$

Below the critical temperature $T_c = 1.69$ K a sharp drop of the residual resistivity $\rho_0 \approx 275 \mu\Omega\text{cm}$ to zero indicates the superconducting transition. From Eqn. 4.14, a Debye temperature $\theta_D = 387$ K can be identified. The absolute values of the electrical resistivity, especially ρ_0 , appear to be rather high. A possible renormalization of the electrical resistivity values will be discussed later on. The RRR (ρ_{290K}/ρ_0) is 3.5 indicating a fairly good sample quality. External magnetic fields up to $\mu_0 H = 2$ T were applied by a superconducting magnet. Even at 2 T a declining tendency of the electrical resistivity was not suppressed. To identify the superconducting transition, the maxima of the transition in the first derivative of the electrical resistivity for each external applied field were analyzed as

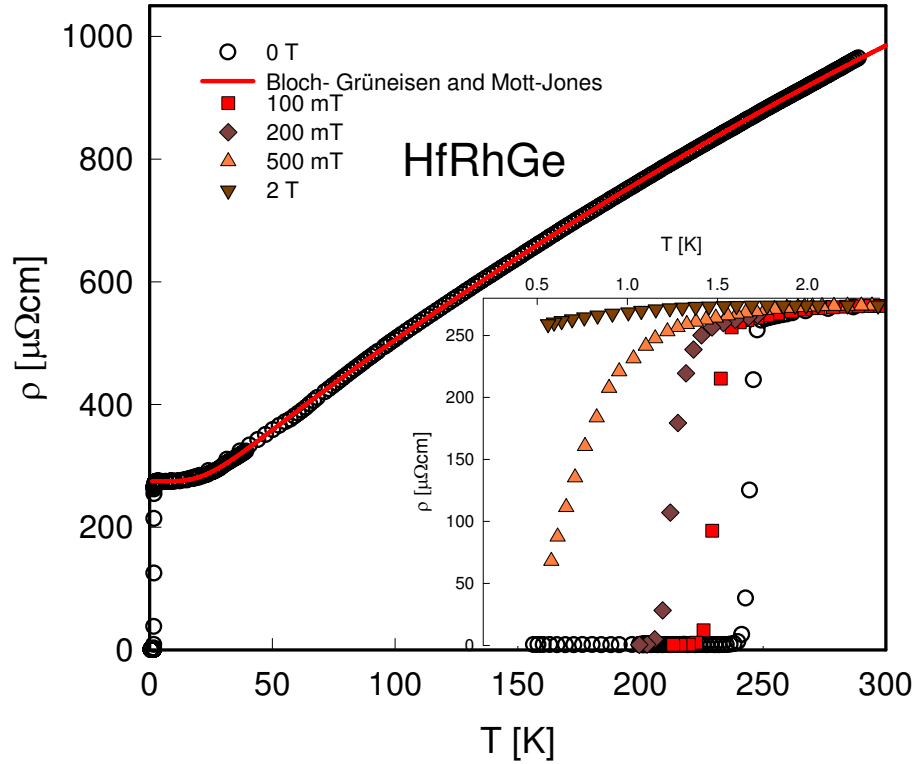


Figure 4.25: The electrical resistivity measurement of HfRhGe in dependence of the temperature. The red line is the Bloch-Grüneisen fit with an additional Mott-Jones term

shown in Fig. 4.26. The peaks of $d\rho/dT$ are rather sharp for low fields but further broadens up. At 2 T, a small declining tendency is visible. Here, along small tracks throughout the sample, Cooper pairs are still be formed in an non negligible amount.

The specific heat measurements reveal a phase transition at 1.66 K (see Fig. 4.27). External magnetic fields up to 1 T were applied. There is a rather small bump visible at highest fields, which might be due to a stabilization problem. The Sommerfeld value γ was analyzed from the 1 T measurements via the relation $\frac{C_p}{T}(T^2) = \gamma + \beta T^2$. This gives a value of $\gamma = 6.93$ mJ/molK². From the β -value of 0.196 mJ/mol K⁴ taking three atoms per formula unit, the Debye temperature was calculated via Eqn. 2.23 as 310 K. This value is slightly lower than the value obtained from the electrical resistivity measurements. The elaboration of the jump height in C_p shows an unusual small value of $\frac{C_s - C_n}{\gamma T_c} = 1.12$. The simple BCS model predicts a value of $\frac{C_s - C_n}{\gamma T_c} = 1.43$. This is a quite common technical problem in this temperature range for two coupled, but otherwise independently regulated ³He and ⁴He cooling cycles.

A closer look at the behavior below 40% of T_c (≈ 0.7 K) unveils a rather good agreement with the BCS theory, depicting an exponentially decreasing characteristics. The numerical values were provided by Mühlischlegel [35].

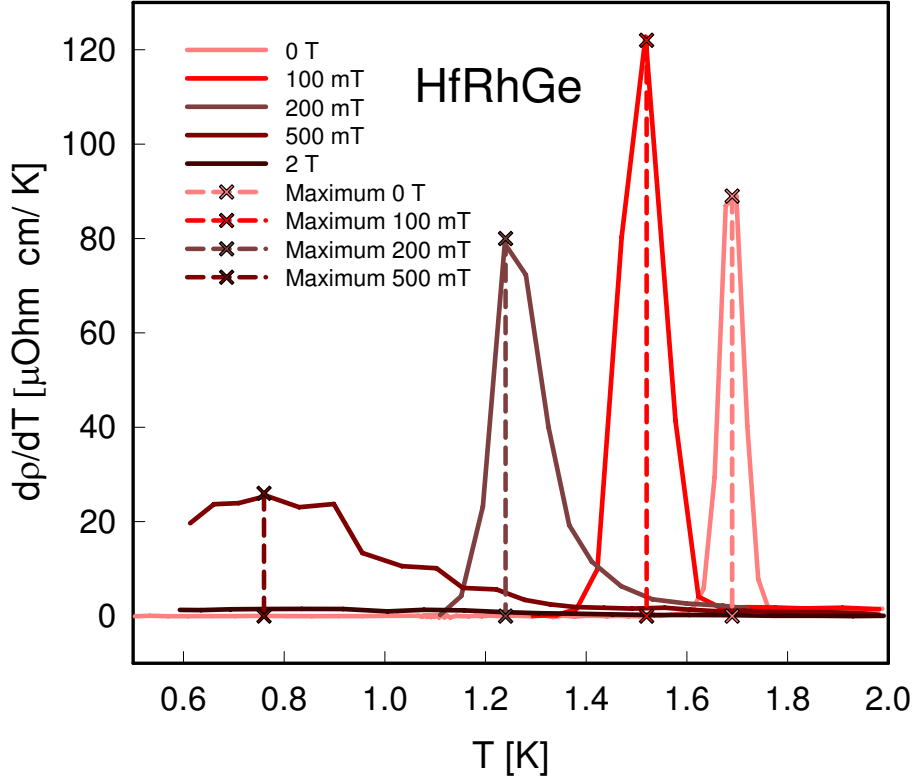


Figure 4.26: The first derivative of the temperature dependent electrical resistivity. The maxima of the transitions are highlighted.

The superconducting behavior can be further analyzed in terms of the BCS theory. The initial slope of the H_{c2} behavior for C_p data is $\mu_0 \frac{dH_{c2}}{dT} = -0.33$ T/K. The behavior of $\mu_0 H_{c2}$ is mainly influenced by the residual resistivity ρ_0 and γ . This is indicated by the following expressions for the Maki parameter α_M [39],

$$\alpha_M = \frac{3e^2 \hbar \gamma \rho_0}{2m_0 \pi^2 k_b}. \quad (4.15)$$

Another expression is given by

$$\alpha_M = 5.35 * 10^{-1} * \frac{dH_{c2}}{dT} \quad (4.16)$$

Both ways usually give comparable results. In the HfRhGe compound we find a strong deviation. While Eqn. 4.15 gives an $\alpha_M = 1.25394$, Eqn. 4.16 leads to $\alpha_M = 0.1712$. As it is discussed above, ρ_0 appears to be rather large. The resistivity is strongly dependent on the geometry of the sample material. If there are cracks or holes inside the sample, which cannot be resolved, the electrical resistivity values can be much larger as a wrong cross section is used in the calculation (compare to Eqn. 3.1). As both values are separated by a

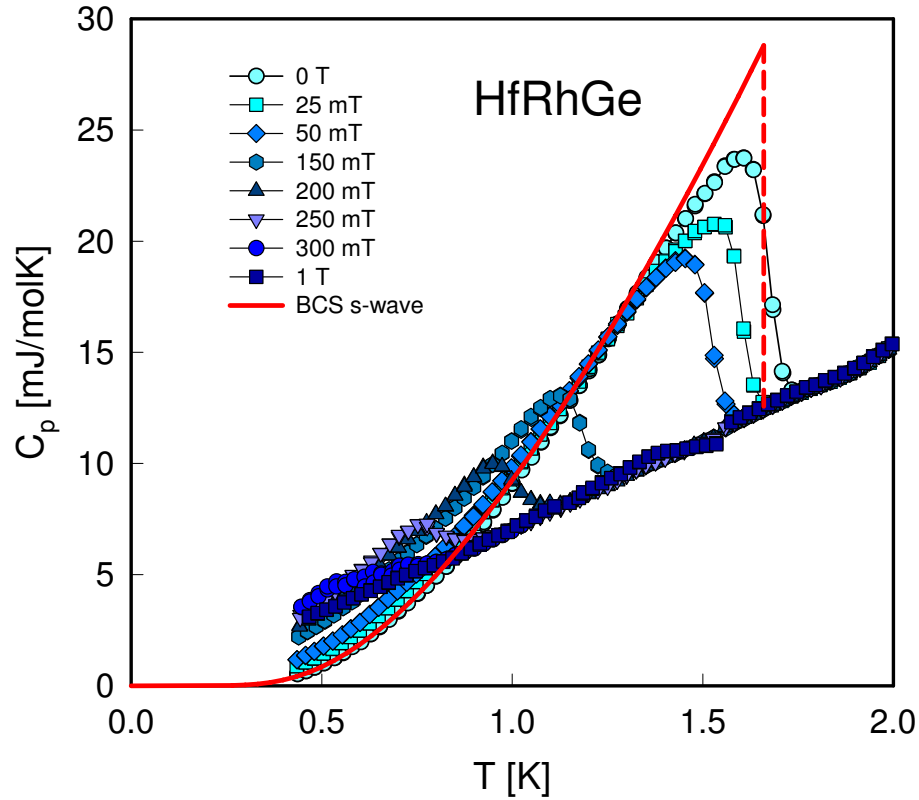


Figure 4.27: Temperature dependent specific heat of HfRhGe. The simple s -wave BCS model is indicated by the red line. It is evident that the jump height is much less in reality than expected from the BCS theory.

factor of around 7.3, one can choose this factor to normalize the resistivity values as well. For the further analysis, the Maki parameter was set to be $\alpha_M = 0.1712$. With the model of Werthamer *et al.* one finds a very good agreement with the experimental data. The respective λ_{so} value, known as the spin-orbit coupling strength, holds as a fit parameter to the model. A small Maki parameter has a small influence on the shape of $\mu_0 H_{c2}$. Therefore, the fit parameter λ_{so} can vary between 0 and 10 with just a minor influence on $\mu_0 H_{c2}$. In contradiction, the value of the Maki parameter calculated by using Eqn. 4.15 is rather large. There, the difference between $\lambda_{so} = 0$ and $\lambda_{so} = 10$ changes the value of $\mu_0 H_{c2}$ by more than 30 %. A proper WHH fit estimates the upper critical field $\mu_0 H_{c2}$ to be 380 mT which is far below the Pauli limiting field of $\mu_0 H_{\text{Pauli}} \approx 1.84 \text{ T/K} \cdot T_c = 1.84 \cdot 1.66 \text{ T} = 3.05 \text{ T}$. The formula of McMillan in Eqn. 2.50 is a possibility to calculate the electron-phonon enhancement factor λ_{ep} of this material. This value is linked to the phonon density of states, which was clarified by the Eliashberg theory in Eqn. 2.49. λ_{ep} is calculated to be ≈ 0.49 , which is an intermediate coupled superconductor, i.e. between weakly and strongly coupled.

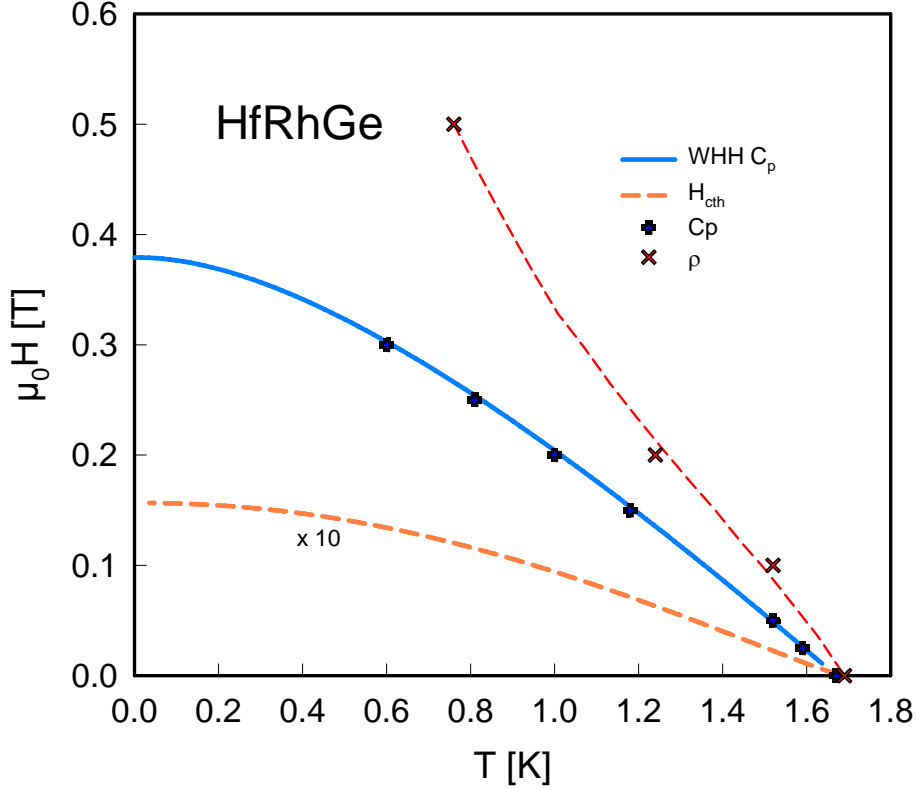


Figure 4.28: An analysis of the upper critical field for HfRhGe. The WHH model (light blue dashed) perfectly fits the experimental data obtained from $C_p(T)$ data. A Maki parameter of $\alpha = 0.1712$ and a $\lambda_{so} = 1$ were used. The difference to $\lambda_{so} = 10$ is negligible. The red short-dashed line is a guideline to the eyes and unveils a rather large slope $\frac{dH_{c2}^{res}}{dT}$. The orange dashed line is the thermodynamical critical field. The value was scaled by a factor of 10 to make it visible on the larger scale.

Deducing the upper critical field from resistivity data H_{c2}^{res} reveals a much higher field being necessary to completely suppress superconductivity. The initial slope is $\mu_0 \frac{dH_{c2}^{res}}{dT} = 0.59$ T/K. Whereas bulk superconductivity is estimated to be suppressed at 380 mT as seen in Fig. 4.28.

Table 4.4: Properties of HfRhGe at a glance

	T_c [K]	RRR	γ [mJ/(mol K ²)]	κ	λ_L [nm]	ξ_{GL} [nm]	θ_D [K]
HfRhGe	1.66	3.5	6.93	17.1	159.54	9.31	310

A mathematical analysis of the specific heat in terms of Eqn. 4.2 allows to derive a value for the thermodynamical critical field H_{cth} of 15.6 mT. comparison to $\mu_0 H_{c2}$ gives a GL parameter κ of 17.1. This value is rather large and characterizes HfRhGe as a type II superconductor. As it was already emphasized, the jump in $C_p(T)$ is also rather small and makes the area below the $C_p(T)$ curve even smaller. From Eqn. 2.42 one can determine

the GL coherence length as 9.31 nm and, subsequently, the London penetration depth by making use of Eqn. 2.40. The relevant parameters of HfRhGe are summarized in Tab. 4.4.

Chapter 5

1-1-3 compounds (EpTX_3)

5.1 Introduction

This chapter comprises the large range of 1-1-3 compounds. The EpTX_3 compounds ($\text{Ep} = \text{Sr, Ba}; \text{T} = \text{Ni, Pd, Pt, Cu, Ag, Au}; \text{X} = \text{Si, Ge, Sn}$) investigated in this work are isotypic to the NCS BaNiSn_3 structure type, which belongs to the BaAl_4 family. The structural relation of BaNiSn_3 and many other derivative structure types to BaAl_4 have been shown by Kußmann *et al.* in form of a Bärnighausen tree [89]. The BaNiSn_3 structure type has been reported first by Dörrscheidt and Schäfer [90] in 1978 together with the isotypic compounds SrNiSn_3 and BaPtSn_3 . Since that time a large number of EpTX_3 compounds have been found, where Ep is an alkaline earth or rare earth element, T is a transition element and X is an element from the 3rd or 4th main group of the periodic table.

Although Fujii *et al.* [91] reported the absence of superconductivity above 1.8 K (DC magnetization measurements) for SrMGe_3 ($\text{M} = \text{Rh, Ir, Ni, Pd, Pt}$), superconductivity has been found in SrPdGe_3 and SrPtGe_3 by Miliyanchuk *et al.* [92] at ambient pressure at 1.49 and 1.0 K, respectively. BaPtSi_3 also exhibits superconductivity at 2.25 K and the experimental results of these compounds are accompanied by density functional theory (DFT) calculations [93, 94]. The compounds SrNiSi_3 [95], BaPdGe_3 [96], BaPdSi_3 , BaPtGe_3 [97], BaAuGe_3 [98], SrPdSn_3 and BaPdSn_3 [99] have already been reported in literature but without any information on physical properties. The aim of the present work is to provide complete information on the existence of EpTX_3 and $\text{EpT}_x\text{X}_{4-x}$ compounds with $\text{Ep} = \text{Sr, Ba}; \text{T} = \text{Ni, Pd, Pt, Cu, Ag, Au}$ and $\text{X} = \text{Si, Ge, Sn}$ including structural details and physical properties (resistivity, heat capacity).

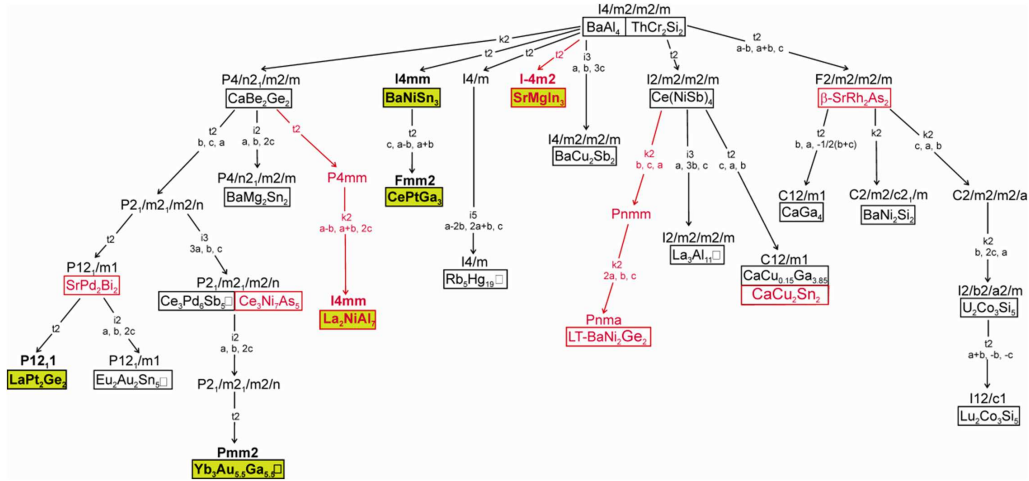


Figure 5.1: Group-subgroup relations for BaAl_4 and several binary and ternary derivative structure types in form of a Barnighausen tree. The original tree from Kußmann *et al.* [89] is shown in black, new branches or structure types are shown in red and non-centrosymmetric structure types are shown bold and in a green box.

5.2 Experimental Details

Polycrystalline samples were prepared by arc melting the stoichiometric mixtures of the pure elements under Ti-gettered argon atmosphere. Afterwards the regulii were sealed into quartz tubes under vacuum and annealed at 800 or 900°C for one week. A detailed description of the various characterization techniques employed, like scanning electron microscopy (SEM, EPMA (electron probe microanalysis) on a Zeiss Supra 55 VP operated at 20 kV and 60 μA using EDX quantitative analysis), crystal structure (X-ray powder diffraction (XPD) and single crystal diffraction (XSCD)) can be found in our previous publications [100, 101].

Electrical resistivity measurements with a standard 4-probe technique employing an a.c. bridge, and specific heat measurements with the relaxation time method were performed from 350 mK to room temperature at magnetic fields up to 12 T and 9 T, respectively. For the former, the specimen was mounted parallel to the magnetic field in a conventional He-3 bath system. Specific heat was measured in a conventional PPMS (Quantum Design) with a ^3He inset and a heat pulse of 2 % in zero field cooling (ZFC). Samples with quadratic and highly polished basal area and a mass of around 20 to 40 mg were attached to the measurement stage using Apiezon N grease.

T	Ba-T-Si	Ba-T-Ge	Ba-T-Sn	Sr-T-Si	Sr-T-Ge	Sr-T-Sn
Ni						
Pd						
Pt						
Cu						
Ag						
Au						

EpTX ₃ forms with BaNiSn ₃ type	EpT _x X _{4-x} forms with ThCr ₂ Si ₂ type
EpT _x X _{4-x} forms with BaNi ₂ Si ₂ type	EpT _x X _{4-x} forms with BaNi ₂ Ge ₂ type
EpT _x X _{4-x} forms with CaBe ₂ Ge ₂ type	No phase with any of the BaAl ₄ derivative structure type is known
EpT _x X _{4-x} forms with CaCu ₂ Sn ₂ type	EpT _x X _{4-x} forms with BaCu ₂ Sb ₂ type

Figure 5.2: Graphical summary of all formed phases with any BaAl₄ derivative structure type in the ternary systems Ep-T-X (Ep = Sr, Ba; T = Ni, Pd, Pt, Cu, Ag, Au; X = Si, Ge, Sn)

5.3 Crystallography

5.3.1 The BaAl₄ family

The group-subgroup relations in form of a Bärnighausen tree [61, 62] have been shown for BaAl₄ and its binary and ternary derivative structure types by Kußmann *et al.* [89]. Several new structure types, which have been reported in literature since that time are added in red color to the original tree (black) in Fig. 5.1. The crystal structure of Ce₃Ni₇As₅ has been reported by Babizheztzsky *et al.* [102], that of La₂NiAl₇ by Gout *et al.* [103], of SrMgIn₃ by Bin and Corbett [104] and of SrPd₂Bi₂ by Frik *et al.* [105]. Details concerning group-subgroup relations and on other derivative structure types can be found in Ref. [89, 61, 62]. Six of the 21 shown derivative structure types of BaAl₄ are non-centrosymmetric and are marked with green color in Fig. 5.1.

In the next two sections the BaNiSn₃ structure type and other tetragonal or orthorhombic BaAl₄ derivative structure types, which appear in the investigated ternary systems Ep-T-X (Ep = Sr, Ba; T = Ni, Pd, Pt, Cu, Ag, Au; X = Si, Ge, Sn) will be discussed in more details. Fig. 5.2 shows a graphical summary of all the formed phases with any BaAl₄ derivative structure type appearing in these ternary systems.

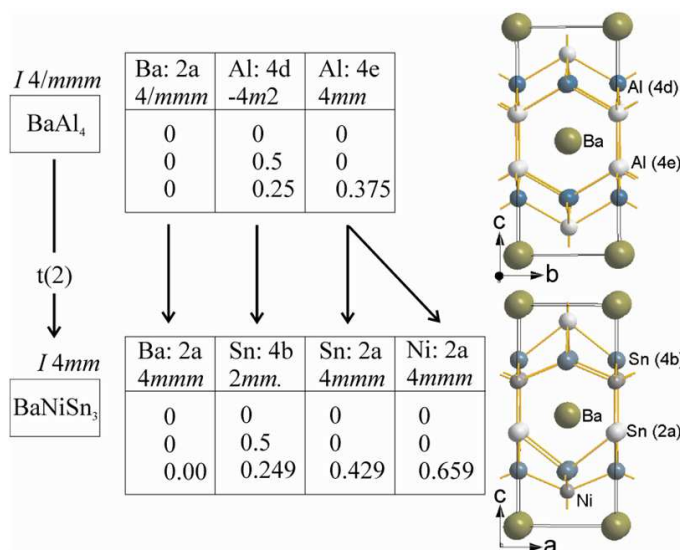


Figure 5.3: Group-subgroup relations for BaAl₄-BaNiSn₃ including the unit cells for both compounds

5.3.2 Tetragonal BaAl₄ derivative structure types

EpTX₃ compounds with BaNiSn₃ structure type

The ternary systems Ep-T-X (Ep = Sr, Ba; T = Ni, Pd, Pt, Cu, Ag, Au; X = Si, Ge, Sn) have been investigated systematically concerning the appearance of EpTX₃ compounds with BaNiSn₃ structure type in as cast state (after arc melting) and after annealing at 800 or 900°C. Tab. B summarizes these investigations, together with data taken from literature. All the crystallographic data were standardized with the program Structure Tidy [105]. As can be seen from Fig. 5.3, the transition BaAl₄ → BaNiSn₃ is translationengleich of index 2 and leads to a symmetry reduction from the centrosymmetric space group *I4/mmm* to the non-centrosymmetric *I4mm* due to the loss of the mirror plane perpendicular to the *c*-axis. The barium and nickel atoms occupy the crystallographic site 2a (0,0,*z*) and the tin atoms the 2a and 4b (0,1/2,*z*) sites.

EpT_xX_{4-x} compounds with ThCr₂Si₂ structure type

For the ternary systems considered here, a large number of phases have been reported in literature, crystallize in the ThCr₂Si₂ structure type [106] (see Table B). The ThCr₂Si₂ structure type is the ordered ternary substitution variant of BaAl₄, where Th occupies the 2a (0,0,0) site, Cr the 4d (0,1/2,1/4) and Si the 4e (0,0,*z*) site (Fig. 5.2). In several of these phases, a rather large homogeneity region has been obtained, e. g., for SrCu_xSi_{4-x}

[95], BaAg_xGe_{4-x} [107] or SrAu_xSn_{4-x} [99]. A mixed occupancy of Au and Sn at sites 4d and 4e has been observed by Tkachuk and Mar [99] for SrAu_{1.4}Sn_{1.6} from single crystal investigations, whereas for BaAg_xGe_{4-x} a mixed occupancy of Ag and Ge occurs only at the 4d sites [107].

EpT_xX_{4-x} compounds with CaBe₂Ge₂ structure type

A klassengleiche symmetry reduction of index 2 (k2) leads from the body centered tetragonal unit cell of BaAl₄ to the primitive cell of CaBe₂Ge₂ (space group P4/nmm; $a = 0.402(2)$, $c = 0.992(2)$ nm [108]) (Fig. 5.1). Calcium occupies the crystallographic site 2c (1/4,1/4,z), beryllium the crystallographic sites 2a (3/4,1/4,0) and 2c and germanium the sites 2b (3/4,1/4,1/2) and 2c. The crystal structure of SrAu_{1.6}Ge_{2.4} has been solved with direct methods and has been found to be isotypic with CaBe₂Ge₂. The refinement showed a mixed occupancy of Au and Ge in both Be and both Ge sites. For details see Tab. B.

EpT_xX_{4-x} compounds with BaCu₂Sb₂ structure type

The crystal structure of BaCu₂Sb₂ (space group I4/mmm; $a = 0.4655(1)$, $c = 3.2709(6)$ nm [109]) is built of blocks of CaBe₂Ge₂ and ThCr₂Si₂ at the ratio of 2:1 in *c*-direction (isomorphic symmetry reduction (i3); $c\text{BaCu}_2\text{Sb}_2 = 3c\text{BaAl}_4$). Barium occupies the crystallographic sites 2a (0,0,0) and 4e (0,0,z), *Cu* the 4e and 8g (0,1/2,z) sites and *Sb* the crystallographic sites 4d (0,1/2,1/4) and 2 times site 4e. As superstructure reflections were observed in the X-ray powder diffraction pattern of a sample with nominal composition SrAu₂Ge₂ annealed at 900 °C, we selected a single crystal and found isotypism with the BaCu₂Sb₂ structure type. The refinement of the occupancies of all Wyckoff sites showed full ordering of strontium in the sites 2a and 4e, of gold in one 4e site and of germanium in the 4d site. A mixed occupancy of Au and Ge has been found in the sites 8g and in the other two 4e sites leading to the composition SrAu_{1.9}Ge_{2.1} for the single crystal. Details of the crystal structure refinement can be found in Tab. B.

5.3.3 Orthorhombic BaAl₄ derivative structure types

Different site occupations and slight distortions in the crystal lattice cause symmetry reductions and lead to many different orthorhombic or even monoclinic BaAl₄ derivative structure types. A translationengleiche symmetry reduction of index 2 (t2) leads from the body centered tetragonal unit cell of BaAl₄ either to a body centered orthorhombic unit cell of Ce(Ni, Sb)₄ (space group *Immm*; $a = 0.4312(3)$, $b = 0.4285(3)$, $c = 1.00205(7)$ nm) or to a face centered orthorhombic cell of β-SrRh₂As₂ (space group *Fmmm*; $a = 0.5760(3)$

, $b = 0.6067(4)$, $c = 1.1264(5)$ nm [110]). In the Ce(Ni, Sb)₄ structure type, cerium occupies the Wyckoff position 2a (0,0,0) and Ni and Sb the sites 4j (1/2,0,z) and 4i (0,0,z). In our previous work [98], BaAu₂Ge₂ has been found to be isotypic with Ce(Ni, Sb)₄ (see Tab. B) from X-ray single crystal investigations. Two lower symmetry structure types deriving from the Ce(Ni, Sb)₄ structure type (see Fig. 5.1) have been reported in literature concerning our ternary systems, namely the low temperature BaNi₂Ge₂ and the CaCu₂Sn₂ structure type. In the low temperature modification of BaNi₂Ge₂ (space group Pnma; $a = 0.83852(4)$, $b = 1.13174(8)$, $c = 0.42902(9)$ nm [111]), the Ba atoms are located on the Wyckoff position 4c (x,1/4,z) and the Ni and Ge atoms on the 8d (x,y,z) sites. Pani *et al.* [112] reported isotypism for SrCu₂Sn₂ (see Tab. B) with the CaCu₂Sn₂ structure type (space group C2/m; $a = 1.0943(3)$, $b = 0.4222(1)$, $c = 0.4834(1)$ nm, $\beta = 107.94(1)^\circ$ [113]), where Ca is occupying the 2a (0,0,0) site and Cu and Sn the sites 4i (x,0,z). Concerning the second orthorhombic branch of the Bärnighausen tree in Fig. 5.1, a klassengleiche symmetry reduction of index 2 leads from a face centered orthorhombic unit cell of β -SrRh₂As₂ to a C-centered one of BaNi₂Si₂ (space group Cmc; $a = 0.650(1)$, $b = 0.535(1)$, $c = 1.133(2)$ nm) reported by Dörrscheidt and Schäfer [114]. In this structure type, Ba is located in the crystallographic site 4c (0,y,1/4), Ni in 8e (x,0,0) and Si in the 8f (0,y,z) site.

5.4 Superconductivity in the EpTX₃ compounds with BaNiSn₃ structure type

As stated in Tab. B, not every composition exhibits a stable phase. Proper investigations were carried out on stable and single-phase, polycrystalline samples. In the following we summarize the experimental results obtained from the stable members of this family. Type II superconductivity was observed in the compounds listed in Tab. 5.1 and was proven by electrical resistivity and specific heat as a transport and bulk quantity, respectively.

Collected in Fig. 5.4 are exemplified resistivity data of EpTX₃ compounds, exhibiting clear hints for a superconducting phase transition at low temperatures (compare Tab. 5.1). Above T_c all investigated non-centrosymmetric EpTX₃ BaNiSn₃ structure type specimen represent a class of intermetallic compounds like BaPtSi₃ [94]. In electrical resistivity measurements simple metals can often be described with the help of the Bloch and Grüneisen law. Within this model the resistance is described by a temperature dependent scattering of the electrons on lattice vibrations (phonons) and a temperature independent scattering on lattice defects, causing the residual resistivity ρ_0 . Electron-electron interaction, in general, plays a negligible role for simple metals where the electrons are described in terms of a free electron gas. Nevertheless, for narrow d -bands close to the Fermi surface an interaction of the electrons proportional to T^3 has to be taken into account by the theory

of Mott and Jones [65]. The Bloch-Grüneisen law with the Mott-Jones term was already discussed in detail in Sec. 4.1.2. Since f-shell electrons are missing, there are no strong correlations among electrons, which might enhance many other physical effects as it can be seen in the pressure-induced superconductors CeIrSi₃ [115] and CeRhSi₃ [116].

In electrical resistivity the superconducting transition is indicated by a sharp drop to zero at the transition temperature T_c . The application of an external magnetic field further

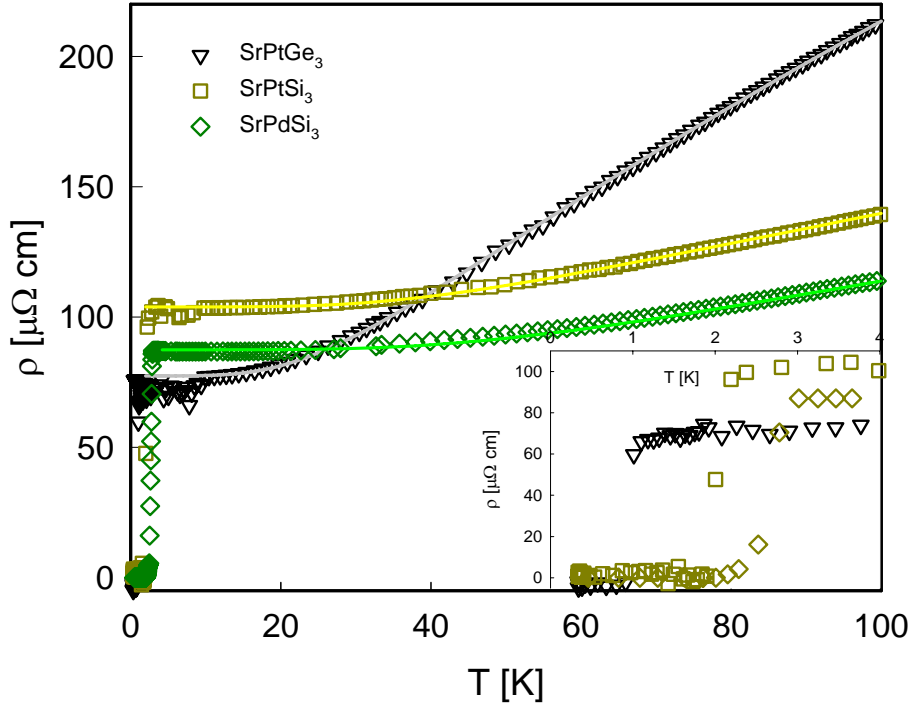


Figure 5.4: Temperature dependent electrical resistivity $\rho(T)$ of various EpTX₃.

reduces the transition temperature and at a certain magnetic field, which in Type II superconductors is known as the upper magnetic field H_{c2} , the superconducting transition is eventually suppressed. The phase transition might broaden with higher fields, exacerbating the determination of the transition temperature. Since there are many different definitions of fixing the superconducting transition temperature, the transition was defined by 50% within this chapter. This was done in order to state consistent values, which was not possible from ρ' data, as peculiarities like double peaks persist, e.g., in Fig. 5.11(b). As it is widely discussed in literature, the transition itself may not be perfectly sharp but slightly broadened. Different physical explanations are held responsible for this and are discussed in Sec. 2.5.5 Usually, the width of the superconducting transitions is increased in samples of poor quality or large fractions of impurities. Therefore, besides the residual-resistance-ratio (RRR), which is the ratio of the resistivity at room temperature to ρ_0 , EPMA (electron probe microscopy) provides another tool to state the sample quality. In

this series of compounds the sample quality does not seem to have a strong impact on the width of the transition and the RRR varies from 2.2 to 10.5 as stated in Tab. 5.1. High pressure studies were performed in a CuBe cell with Daphne oil as hydrostatic medium as explained in Sec. 3.2.3 on SrPdGe₃. Electrical resistivity measurements were performed in the temperature drift mode from 300 mK up to 5 K while exposed now to two different external parameters, i.e. magnetic fields and hydrostatic pressure. The former ranged from 0 to 0.1 T while the later ranged from ambient pressure (0.1 MPa) to a maximum of 1.85 GPa. The absolute values of residual resistivity ρ_0 remained almost constant in different magnetic fields and hydrostatic pressures. However, the application of both external parameters tend to decrease the transition temperature T_c . While the magnetic field directly acts on the Cooper pairs, triggering orbital and paramagnetic depairing, the influence of hydrostatic pressure has also two distinct effects. This can be understood by taking a closer look at Eqn. 2.2 and Eqn. 2.48. First, the density of states is dependent on the volume. So a decrease in the volume also decreases the density of states. Second, the pressure acts on the lattice parameters and can influence the Debye temperature θ_D and the electron-phonon coupling constant. A reduction of the density of states while θ_D remains almost constant, leading to a decrease of the superconducting transition temperature. As a consequence, hydrostatic pressure reduces T_c in many simple elements [117] and intermetallic compounds which can be described by the BCS theory [118]. By contrast, the application of hydrostatic pressure can drive cuprates to higher transition temperatures [119]. An analysis of $\mu_0 H_{c2}$ obtained from the electrical resistivity data is presented in Fig. 5.5 for SrPdGe₃. The transition temperatures are reduced due to the pressure and show an initial drop of $\partial T/\partial p = -0.19$ K/GPa which is comparable to the value of BaPtSi₃ [68]. The behavior of $\mu_0 H_{c2}(p)$ is almost linear dependent over the whole range. The superconducting transition could not be suppressed at 1.85 GPa. A linear extrapolation of this tendency would result in a hydrostatic pressure of more than 8.4 GPa being necessary to completely suppress superconductivity. The slope of $\mu_0 H_{c2}$ remains undisturbed at $\mu_0 dH_{c2}/dT = 0.15$ for different pressures. Additionally, the behavior of $\mu_0 H_{c2}$ differs among physical properties, which is a still ongoing discussion in literature and can be seen in the detailed listings in Sec. 5.6 with Fig. 5.7. The slope of $\mu_0 H_{c2}(T)$ for electrical resistivity measurements turns out to be much stronger than obtained from specific heat data [92] and can even exceed the conventional BCS value of the third critical field $\mu_0 H_{c3}$ ($H_{c3}/H_{c2} \sim 1.695$ in BCS).

Specific heat measurements provide a deep insight in the thermodynamic behavior of a superconductor and allow the calculation of the free energy and, furthermore, the critical magnetic fields like in Eqn. 4.2. Above the transition temperature, simple metals usually follow the simple Debye law, which is given by Eqn. 2.25. Taking into account the condensation of a fraction of the electrons into Cooper pairs causes the formation of an energy gap, which is revealed by a jump of the specific heat. The size of this jump for BCS su-

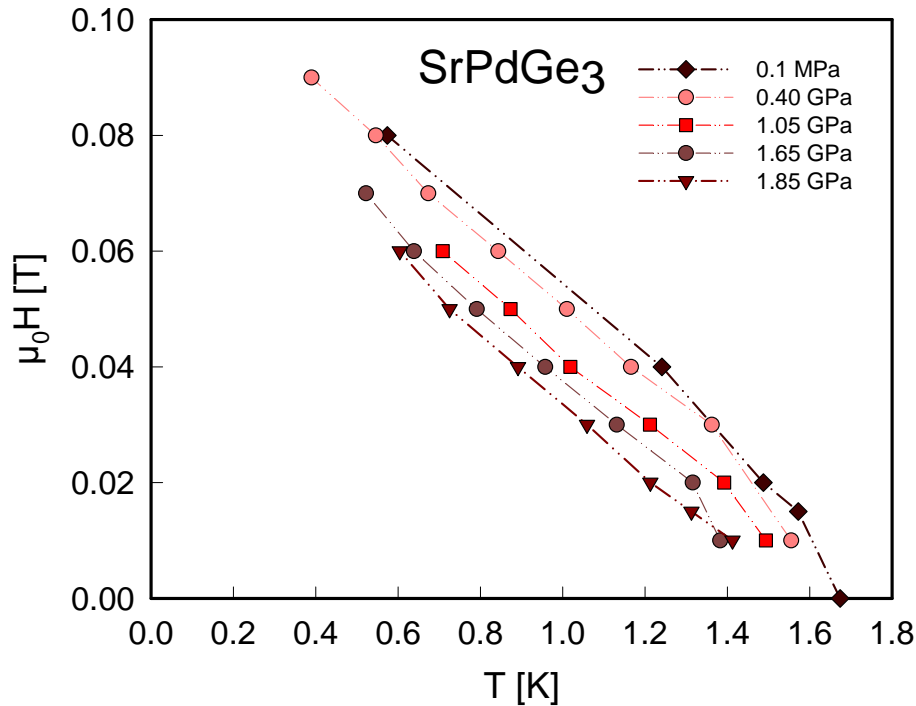


Figure 5.5: [Upper critical field behavior $\mu_0 H_{c2}$ of SrPdGe₃ with and without applied hydrostatic pressure.

perconductors in the weak coupling limit is $\Delta C_p/\gamma T_c = 1.43$. ΔC_p is the difference of the specific heat in the superconducting and the normal conducting state, as it was described in Sec. 2.5.4. Therefore, a larger value of $\Delta C_p/\gamma T_c$ might refer to a stronger coupling, whereas a smaller value can show that the bulk is either not completely superconducting or giving a first hint to a non-isotropic gap function.

The numerical BCS values of the temperature dependent specific heat were first calculated by Mühlshlegel [35] in terms of the weak coupling limit. While the model itself is normalized to T_c and the γ value, it is independent of other parameters. Therefore, a comparison of the specific heat data obtained can already point out deviations from con-

Table 5.1: List of superconducting EpTX₃ compounds

	T_c [K]	RRR	γ [mJ/(mol K ²)]	κ	λ_L [nm]	ξ_{GL} [nm]	θ_D [K]
SrNiSi ₃	1.1	3.4	5.3	3.3	307	93	458
SrPdSi ₃	3.0	2.4	4.5	4.1	187	46	359
SrPdGe ₃	1.5	10.5	5.0	2.7	215	80	268
SrPtSi ₃	2.0	2.3	3.9	5.2	227	44	343
SrPtGe ₃	1.0	6.4	4.0	2.8	292	105	271
BaPdSi ₃	2.8	2.7	4.9	2.3	131	57	344
BaPtSi ₃	2.3	6.1	5.8	2.2	188	72	370

ventional superconducting behavior. In standard BCS theory, below 40% of T_c to lowest temperatures one can find an exponential decay of the electronic specific heat of the form $C_{p,e}(T) = c_1 e^{-1.76 T_c/T}$ where c_1 is a material dependent constant. However, point nodes and line nodes in the gap function generate a T^3 and a T^2 dependence, respectively. This general behavior can be also seen in Fig. 2.6(a). As in the BCS theory the gap function is linked to the superconducting wave function, an isotropic gap comes along with spatial symmetry. The measurements of the specific heat are presented in Fig. 5.6 and are analyzed in the sense of the BCS theory.

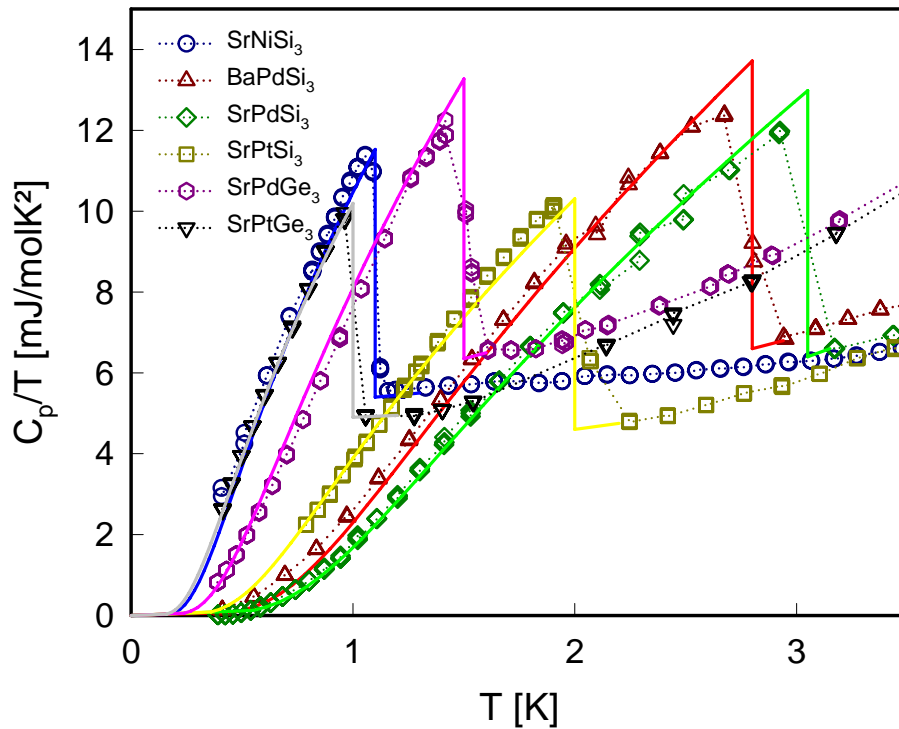


Figure 5.6: Temperature dependent heat capacity C_p measurements of SrNiSi₃, BaPdSi₃, SrPdSi₃, SrPtSi₃, SrPdGe₃ and SrPtGe₃ plotted as C_p/T vs T . The full lines are the numerical fit in the sense of an s -wave BCS analysis, agreeing well to the measured data.

Since in a conventional superconductor the electrons are paired anti-parallel, an external field tends to break up the Cooper pairs as it flips the spin of the electron with the spin anti-parallel to the applied field which is generally described in terms of the Pauli-Clogston model [70]. For conventional superconductors, the Pauli-Clogston limit reveals $\mu_0 H_{\text{Pauli}}(0\text{K}) \approx 1.84 \text{ T/K } T_c$. In conventional superconductors, the value of the upper critical field H_{c2} is usually much lower. Therefore, the depairing mechanism is mainly provoked by the orbital depairing effects, where the fluxoids tend to overlap and the superconducting wave function collapses at a distance of the Ginzburg Landau coherence length ξ_{GL} . However, in NCS superconductors the distinction between spin singlet and spin triplet pairing becomes blurred and can be seen as a quantum mechanical superpo-

sition. Therefore, the temperature dependence of the upper critical magnetic field gives good insight of the nature and dominance of the superconducting pairs. Thus the slope $\mu_0 \frac{dH_{c2}(T)}{dT} = H'$ of the derived function can demonstrate singlet or triplet contributions. The model of Werthamer, Helfand and Hohenberg [40] expresses $\mu_0 H_{c2}(T)$ in terms of the orbital pair breaking and the Pauli limiting.

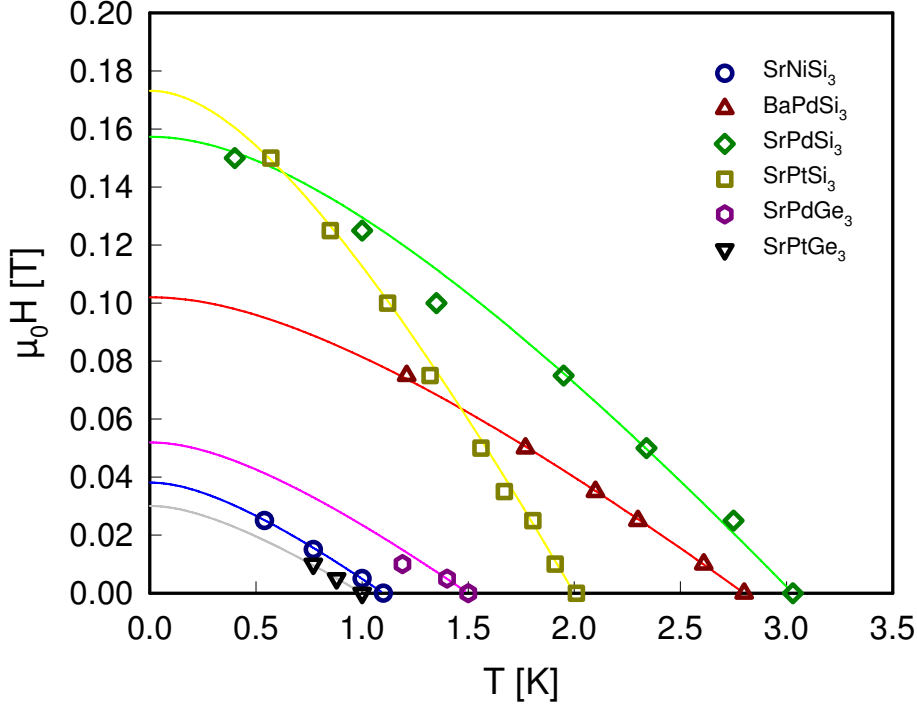


Figure 5.7: Upper critical field $\mu_0 H_{c2}$ behavior of superconducting EpTX₃ compounds.

An analysis of all samples employing the WHH model shows good agreement (compare Fig. 5.7) with the experimental results and thus indicates mainly *s*-wave Cooper pairing (from very low values of the Maki-parameter) with negligible participation of spin triplet pairing. Therefore, Muon Spin Relaxation (μ SR) was used to probe BaPtSi₃. A detailed analysis of the asymmetry evolution of the muon decay which unveils the London penetration depth as well as the upper critical field H_{c2} has been performed and as presented by Miliyanchuk *et al.* in [92]. To clarify the type of Cooper pairing, the sample has to be probed in the sense of time reversal symmetry breaking. An internal magnetic field, which could arise from a spin triplet pairing mechanism, would break this symmetry. A polarised muon beam interacts with the sample material in a longitudinal magnetic field. The time evolution of the asymmetry factor is monitored. The measurement is performed once below T_c and once at a temperature above T_c . If there is no deviation of both asymmetry evolutions, it indicates that there is no internal magnetic field present and thus the pairing mechanism is mainly due to spin singlet pairing. The results are shown in Fig. 5.8. A detailed theoretical background is given in Sec. 2.4

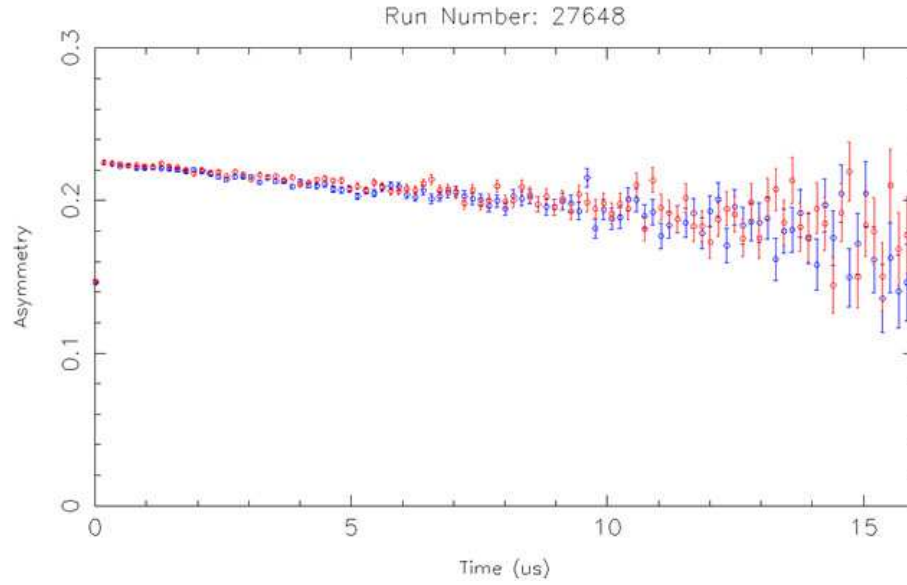


Figure 5.8: Difference between 0.1K (blue, below T_c) and 3K (red, above T_c). The 0.1 K run was cooled in the instrument (truly ZFC). Both measurement curves are in a good agreement and thus indicate spin singlet pairing mechanism dominate in BaPtSi₃.

Even though the samples have different T_c and $\mu_0 H_{c2}(0)$, the behavior of the materials show similarities. For SrPtSi₃, however, a distinctly larger critical field is observed. As mentioned earlier, the RRR of this sample was found to be around 2.2 with a high residual resistivity of around 104 $\mu\Omega\text{cm}$. From the relation [120]

$$\mu_0 H'_{c2} = 4490 \times \rho_0 \times \gamma \quad (5.1)$$

with γ given in $J/m^3 K^2$, ρ_0 in $\mu\Omega\text{cm}$ and $\mu_0 H'_{c2}$ in T/K , one can calculate the theoretical slope of the critical field. Therefore, materials with a higher residual resistivity usually tend to have a higher upper critical field. In general, a higher resistivity at lower temperatures indicates a higher density of lattice defects. The magnetic flux lines tend to pin to these defects and thus reduce the influence of the orbital pair breaking. By contrast, the γ value represents a bulk property which, in general, is independent of lattice defects and, besides the influence of foreign phases, gives no such raise for H' caused by a lower sample quality. Considering the experimental results derived for these samples, Eqn. 5.1 yields too high values for $\mu_0 H'_{c2}$. Additionally, brittle samples or small cracks, which might not be detected, can have a strong impact on the true value of ρ_0 as it can reduce the cross section of the current and thus sophisticates the proper geometry factor of the specimen. Therefore, one can derive the intrinsic resistivity values if Eqn. 5.1 holds true.

With the $\mu_0 H'_{c2}$ as shown in Fig. 5.7 and the corresponding γ value one ends up with a theoretical ρ_0 of 16.4 $\mu\Omega\text{cm}$ in the case of SrPtSi₃ which is far below the experimental

determined value. However, this consideration can only be applied in the sense of the BCS theory.

From Tab. 5.1 one can deduce the influence of the ASOC on T_c . In Sec. 2.1 it was shown that the spin-orbit interaction is dependent on Z^2 . The exchange of Si with Ge in the SrPdX₃ and SrPtX₃ gives a reduction of T_c by a factor of 2. In the BaPtX₃ compounds the exchange of Si with Ge just gives a slightly smaller reduction of T_c by a factor of 1.2. The exchange of Pd with Pt in SrTSi₃ and SrTGe₃ is exactly a factor of 1.5 in both cases. This is a remarkable result and clearly shows the possibility of tuning this effect.

Superconductivity can be found in various of the investigated EpMX₃ compositions, which gives the possibility to interpret the tuning effects and influences on the energy bands due to the strong dependency of the ASOC.

We already reported on the calculated density of states for SrPdGe₃ and SrPtGe₃ [92], where the \vec{k} -depending splitting of the spin up and spin down band around the Fermi level appeared to be rather small.

5.5 Density functional theory (DFT) study for the EpTX₃ compounds

5.5.1 Computational details

The DFT calculations were done using the Vienna *ab initio* simulation package (VASP) [55, 56] utilizing the pseudopotential construction according to the projector augmented wave method. [57] For the exchange-correlation functional the local density approximation (LDA) as parametrized by Ceperley and Alder [58] was chosen. The VASP calculations were done in a rather standard way in high precision, the settings used with the atomic potentials involved can be read off from Table B.6. The size of the basis set was defined by an energy cutoff determined by the maximum value of ENCUT for each compound. The Brillouin-zone integration for the computation of total energies was made using a Gaussian smearing with $\sigma = 0.2$ eV on a $11 \times 11 \times 11$ Monkhorst and Pack [59] \vec{k} -point mesh.

The electronic structure calculations were done starting from a scalar relativistic approximation, omitting spin-orbit coupling, and then continued in a fully relativistic manner, including spin-orbit coupling, as implemented in VASP, in a self-consistent and parameter-free manner [71]. All values and figures shown in this paper refer to the fully relativistic calculations including spin-orbit coupling.

The vibrational properties were calculated within the harmonic approximation by making

use of the direct force-constant method as implemented in our program package fPHON (full-symmetry PHON), which is based on the package PHON [60]. Atomic displacements of 0.02 Å were chosen to derive the force constants. Before applying such displacements the structural parameters (i.e., the volume and shape of the unit cell as well as the positions of the atoms within the unit cell) were relaxed until the residual forces were less than 10^{-4} eV/Å and, furthermore, a suitable supercell was constructed.

5.5.2 Structural details for the EpTX₃ compounds as calculated by DFT

DFT calculations were done for the seven superconducting EpTX₃ compounds with BaNiSn₃-structure-type (see Table B), plus for SrNiGe₃ (that was not found to be superconducting experimentally) and for BaNiSi₃ (that did not form a stable phase in the BaNiSn₃-structure-type experimentally; see Fig. 5.2).

The structural parameters in the BaNiSn₃-structure-type were relaxed (i.e., the volume and shape of the unit cell as well as the positions of the atoms within the unit cell were allowed to change) to find the stable total-energy minimum structure. The calculated (DFT) structural details are listed in Table B. It should be noted that all of these structures are dynamically stable (i.e., there are no imaginary phonon modes;), even though BaNiSi₃ did not form a stable phase in the BaNiSn₃-structure-type experimentally (see Fig. 5.2).

A comparison of our calculated (Table B) to our experimental (Table B) values shows an excellent agreement. For the superconducting EpTX₃ compounds the main difference is a slight underestimation of the lattice parameters by the DFT-LDA as compared to experiment, in all cases of less than 2%, for the c/a ratio and for the Wyckoff positions the agreement between DFT calculations and crystallographic measurements is even much better. For non-superconducting SrNiGe₃ the agreement between DFT calculation and experimental values is worse (the difference is 3.9% for a and 4.9% for c).

5.5.3 Electronic structure of the EpTX₃ compounds as calculated by DFT

The electronic structures of all nine EpTX₃ compounds calculated are very similar, indeed. The differences are due to the different atomic numbers of the atomic constituents involved, which is a consequence of the different strength of the spin-orbit coupling. In Fig. 5.9 the electronic band structures for the series SrT₂Si₃ (T = Ni, Pd, Pt) around the Fermi level are shown as examples, the band structures of SrPtGe₃ and BaPtSi₃ are published in [92] and [94], respectively.

The effect of spin-orbit coupling onto the band structures is twofold: First, some of the

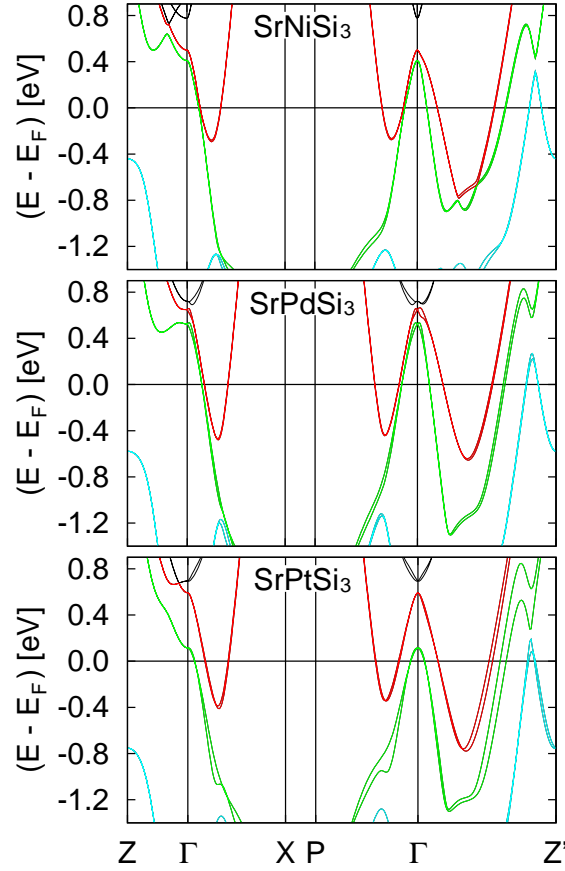


Figure 5.9: Electronic band structure of SrTSi₃ (T = Ni, Pd, Pt). The energy scale is defined relative to the Fermi energy.

degeneracies (i.e., the four- and six-fold degenerate states) at the high-symmetry points that would be observed in a non or scalar relativistic approximation (omitting spin-orbit coupling) are lifted by taking spin-orbit coupling into account. This spin-orbit coupling (SOC) effect is found for all crystal structures independent of the existence of a center of inversion in the crystal structure or not. In Fig. 5.9 it can be identified, e.g., at Γ above the Fermi level as the difference between the red and the green bands.

Second, an effect that only occurs in compounds with NSC crystal structures. The lack of inversion symmetry in the crystal structure gives rise to an ASOC [76, 6, 75] effect, i.e., the double (spin) degeneracy of the bands is lifted, that occurs perpendicular to the directions that break inversion symmetry. As in the BaNiSn₃-structure-type the inversion center is destroyed solely by the arrangement of the atoms along the c axis, a two-fold degeneracy of the bands along Γ -Z is pertained. In Fig. 5.9 the ASOC effect can be seen as the characteristic splitting into double bands away from the high-symmetry points. However, in real systems the ASOC has both an intra-band and an inter-band contribution, and because of this inter-band contribution it is not always easy to identify spin-split partners.

Obviously the strength of the spin-orbit coupling effects (SOC and ASOC) depend on the atomic numbers of the atomic constituents involved. This can easily be seen directly from Fig. 5.9 and was already discussed in Sec. 2.1.

One should keep in mind that the *spd*- and site-projected results are qualitative, since there is no unambiguous way to determine the location of an electron and hence these results depend on the setting of the Wigner-Seitz radius (RWIGS in Table B.6) used. What can be derived from the partial DOS is the typical character of a peak in the DOS. However, the comparison between the different compounds should be done with special care.

5.6 Listing of the samples analyzed

In the following, a comprehensive listing of the data analyzed, as well as brief discussions on certain peculiarities of the specific samples will be presented.

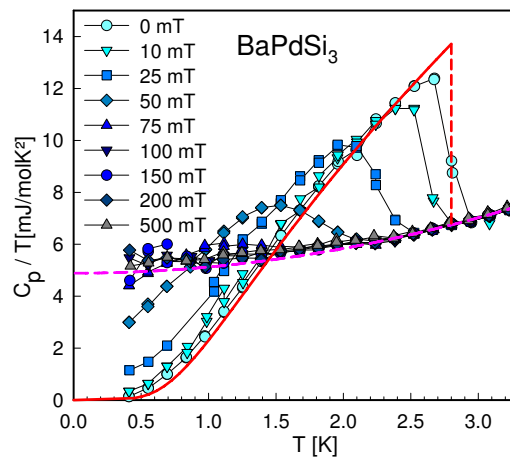


Figure 5.10: Temperature dependent specific heat measurements of BaPdSi_3 . The pink line is the low temperature Debye fit below 3 K. Just minor deviations from a regular *s*-wave BCS behavior (red line) at temperatures close to T_c are visible.

BaPdSi_3 , apart from BaPtSi_3 [68], is one of two EpTX_3 compositions containing Ba, having a stable structure and becomes superconducting above 350 mK. Specific heat data were analyzed and show a clear superconducting transition at 2.8 K. The common *s*-wave solution slightly deviates from the measurement results. However, other models, including different gap symmetries, have a worse overlap. Especially at lower temperatures, the match with the simple model is in a rather good agreement.

SrNiSi_3 as shown in Fig. 5.11 has the second lowest transition temperature in the whole series as deducible from Tab. 5.1. This fact seems to be very interesting, both from the theoretical point of view as well as the measurement results. Due to the Debye temperature

θ_D , Eqn. 2.48 reveals an implicit dependency of T_c on the mass of the ion lattice, $T_c \propto \frac{1}{\sqrt{m}}$. Ceteris paribus, compositions with small masses should have a higher transition temperature. Nevertheless, since the transition temperature is very sensitive to the density of states, a closer look at the band structure and the influence of ASOC might reveal the reason for a smaller transition temperature. Since the influence of the spin-orbit interaction is proportional to the effective atomic number Z_{eff}^2 , the overall influence on SrNiSi₃ is small within the EpTX₃ class. Temperature dependent electrical resistivity measurements show a second transition, which is believed to be due to a foreign phase.

The percolation theory, which was introduced in Sec. 2.5.5 can be hold as an explanation for this phenomenon. Just a small track through the sample can be sufficient to provide superconductivity. In this case one can see that the track through the sample is partly of a superconducting contribution and the normal contribution, which holds responsible for the remaining resistivity ρ_0^* of around $6 \mu\Omega\text{cm}$ after the first transition. The peak width of the first derivative, seen in Fig. 5.11(b), is rather sharp for the superconducting transition to zero, whereas the declining behavior of the resistivity is still visible even at an external magnetic field of 1 T.

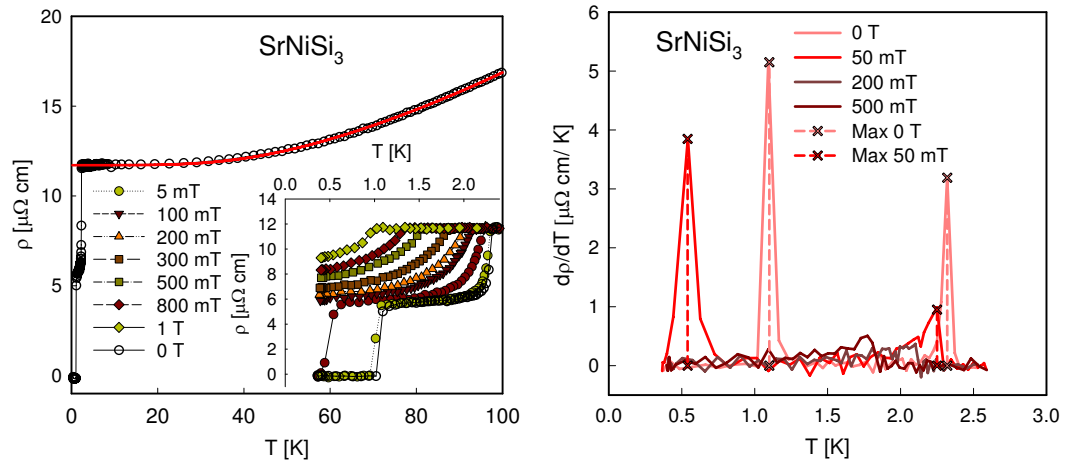
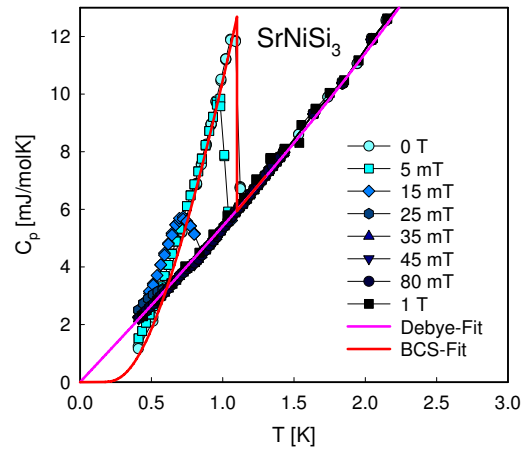
(a) SrNiSi₃ $\rho(T)$ (b) SrNiSi₃ $\rho'(T)$ (c) SrNiSi₃ $C_p(T)$

Figure 5.11: (a) Temperature dependent electrical resistivity of SrNiSi₃. The red line is a fit to the Bloch-Grüneisen law with additional *s-d* electron scattering. (b) First derivative calculations on the temperature dependent electrical resistivity of SrNiSi₃. The two peaks in zero field measurements are clearly visible. (c) The temperature dependent specific heat measurements on SrNiSi₃. The pink line is the low temperature Debye fit below 5 K. Further explanation can be found in the text.

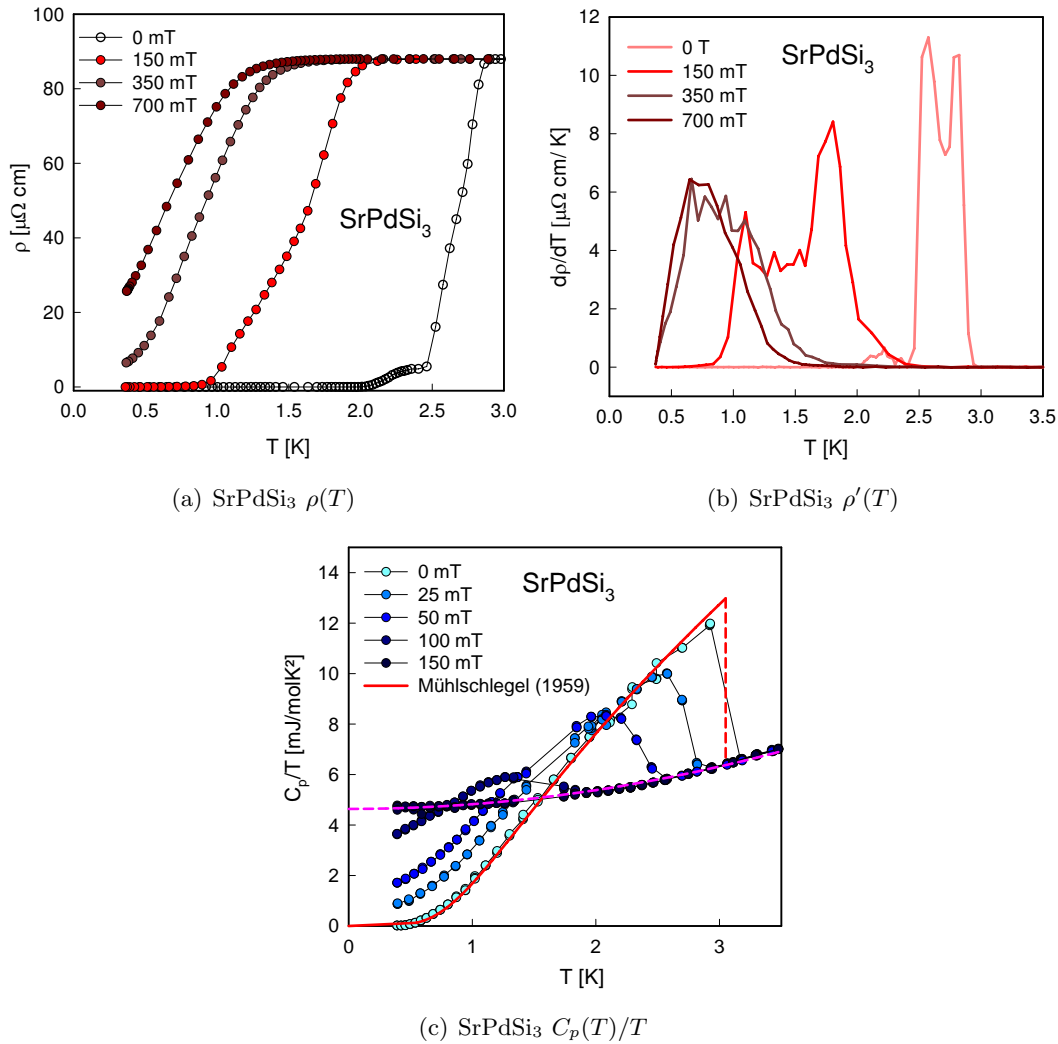


Figure 5.12: (a) Temperature dependent electrical resistivity of SrPdSi₃. An analysis in form of the Bloch-Grüneisen law was performed in Fig. 5.4. (b) The first derivative of the temperature dependent electrical resistivity performed on SrPdSi₃. The peculiarities are discussed in the text. (c) The specific heat measurements on SrPdSi₃ plotted as C_p/T vs T . The pink line is the low temperature Debye fit below 5 K. The red line shows the Mühlischlegel model.

SrPdSi₃ exhibits the highest T_c of all the EpTX₃ materials at around 3 K. A detailed representation of the obtained data points are shown in Fig. 5.12. A proper analysis of the first derivative of the electrical resistivity unveils a kind of double-peak situation seen in Fig. 5.12(b). This double-peak just appears in ZF and becomes blurred already at 150 mT. This might be some effect of small contributions of foreign phases. The heat capacity measurements show a very clear picture of a simple *s*-wave BCS superconductor as stated in Fig. 5.12(c).

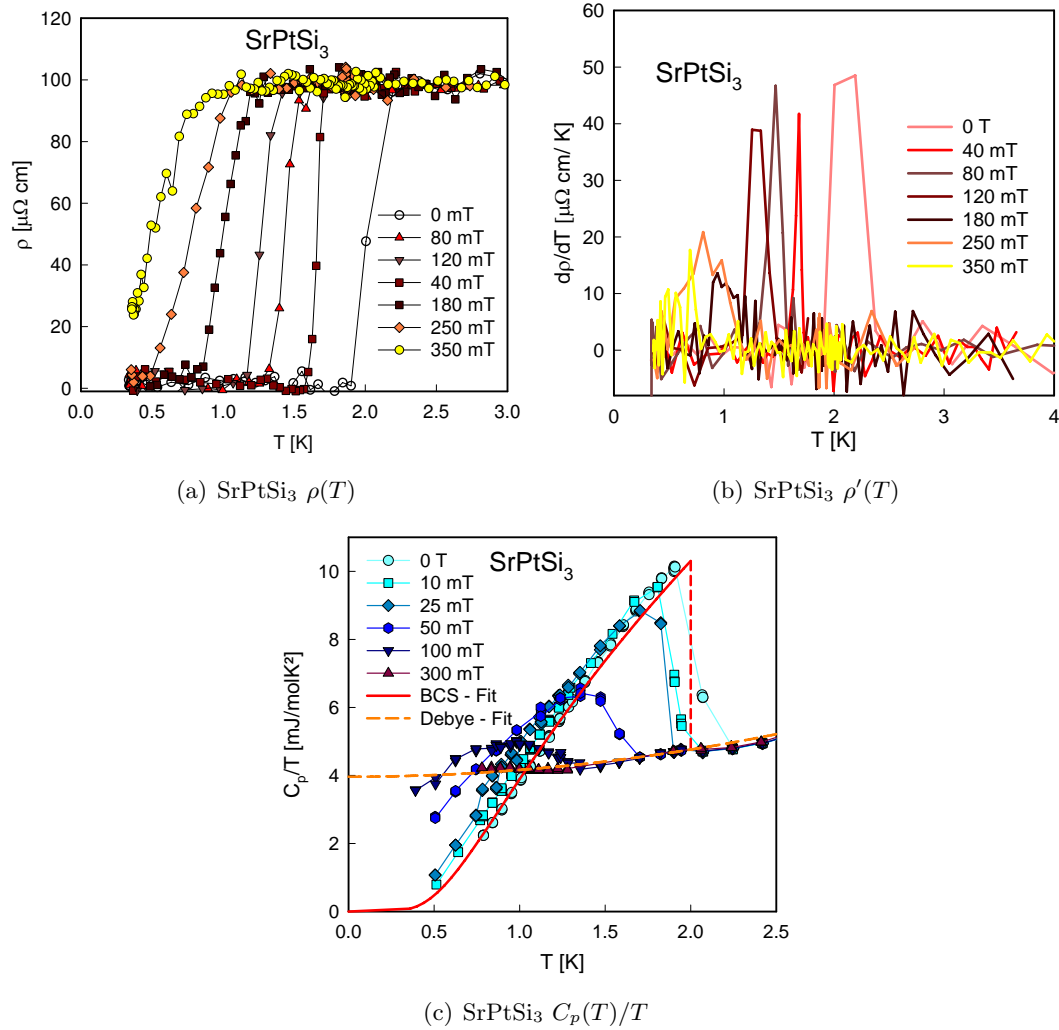


Figure 5.13: (a) Temperature dependent electrical resistivity of SrPtSi₃. An analysis in form of the simple Bloch-Grüneisen law was performed in Fig. 5.4. (b) First derivative calculations on the temperature dependent electrical resistivity data of SrPtSi₃. A very strong scattering is indicated. This is based on the very small used currents of 100 μ A. Additionally, new wiring and new shielding were installed after that. (c) The specific heat measurements in dependency on the temperature depicted as C_p/T versus T of SrPtSi₃. The orange line is the low temperature Debye fit below 5 K, whereas the red line fits to conventional BCS s -wave calculations.

SrPtSi₃ has the highest value of ρ_0 and shows the strongest increase of $\mu_0 H_{c2}$ as it was already discussed above and is shown in Fig. 5.13. It has the highest upper critical field of the EpTX₃ compounds. The upper critical field of the electrical resistivity is even more than two times larger than obtained from heat capacity measurements. Despite the large scattering amplitude, the transition width appears to be relatively small. Details are summarized in Fig. 5.13.

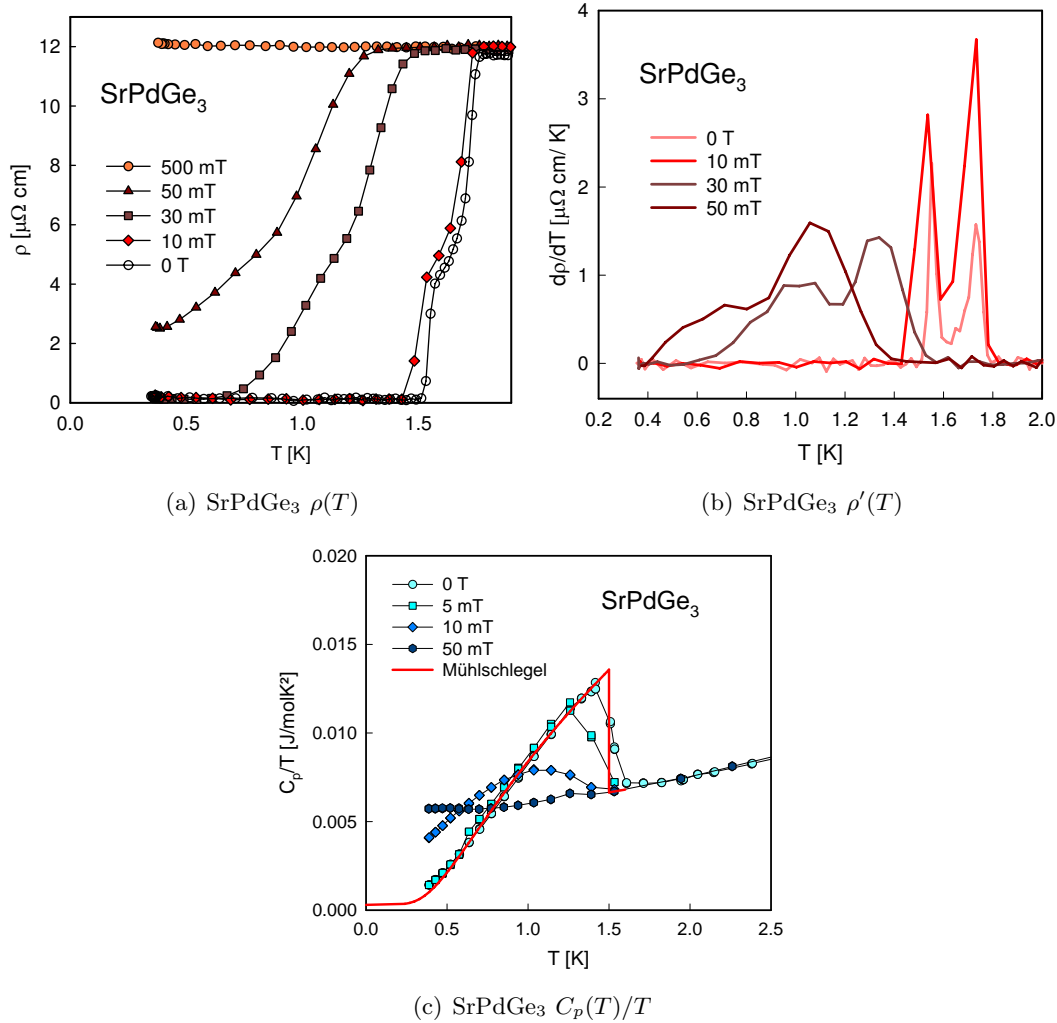


Figure 5.14: (a) Electrical resistivity of SrPdGe₃ in dependence of the temperature T . (b) First derivative calculations of the temperature dependent resistivity results of SrPdGe₃. A similar effect like in SrPdSi₃ with the double peak is indicated. (c) The red line shows the fit to the model of Mühlischlegel. A slight offset of zero heat capacity at lowest temperatures is visible. Those effects have been discussed in [92] and might come from a discrepancy of the addenda calibration data for the first measurements.

SrPdGe₃ has the highest RRR. Some of the data are already shown in [92]. A double peak in the first derivative of the temperature dependent electrical resistivity can be seen. Especially very low fields show this kind of behavior but even at higher fields of more than 30 mT there is still a double peak visible which just slowly gets suppressed above 50 mT. Temperature dependent specific heat data perfectly match the well known theories. However, a slightly deranged heat capacity calibration can be hold responsible for the offset of around 0.5 mJ/mol K².

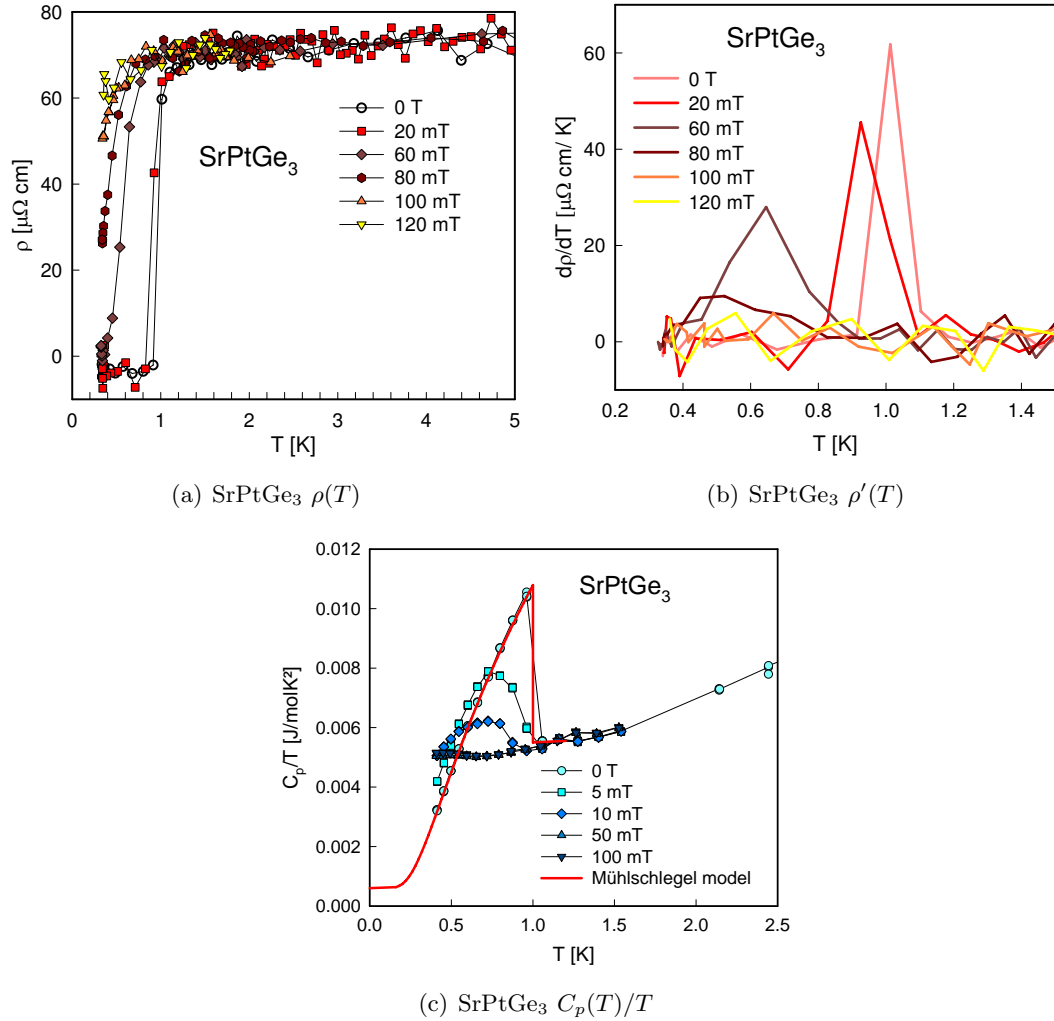


Figure 5.15: (a) Temperature dependent electrical resistivity of SrPtGe₃. An analysis in form of the Bloch-Grüneisen law was performed in Fig. 5.4. (b) The first derivative of $\rho(T)$ for SrPtGe₃. Small current values very used, which generally produces a larger scattering but also a sharper transition width. (c) The temperature dependent specific heat measurements on SrPtGe₃. Similar offsets like in SrPdGe₃ can be identified.

SrPtGe₃ has the lowest transition temperature just slightly below SrNiSi₃ at least at accessible temperatures of above 350 mK. The detailed plots are presented in Fig. 5.15. As the transition temperature is so small, measurement data below 40% of T_c are rather difficult to access. In the accessible regions, the shape of the heat capacity curve in ZF perfectly matches the values derived from the paper of Mühlischlegel [35].

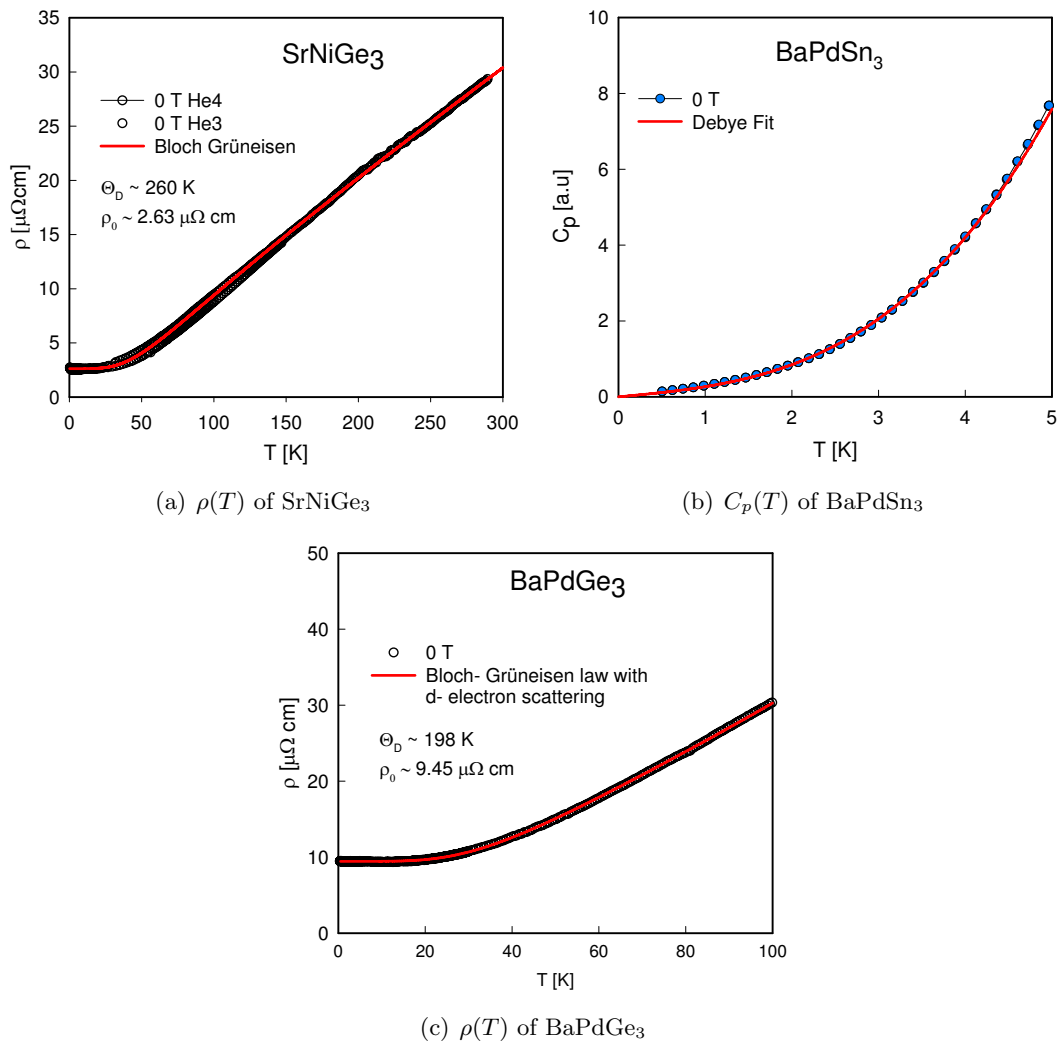


Figure 5.16: The figures show the investigated samples SrNiGe₃, BaPdSn₃ and BaPdGe₃ which do not show a superconducting transition above 350 mK neither in temperature dependent electrical resistivity measurements $\rho(T)$ (SrNiGe₃, BaPdGe₃) nor temperature dependent heat capacity $C_p(T)$ (BaPdSn₃).

SrNiGe₃, BaPdSn₃ and BaPdGe₃ do not show any sign of superconductivity at temperatures above 350 mK as presented in Fig. 5.16.

Chapter 6

La₇Ir₃

6.1 Introduction

The non-centrosymmetric compound La₇Ir₃ is analyzed in this chapter. It crystallizes in the Fe₃Th₇-type structure, with a NCS $P6_3mc$ space group (see Fig. 6.1). Superconductivity was first reported in [121] at around 2.33 K with no major focus on the crystallographic structure. The compound is highly reactive in atmosphere and has to be treated with proper precaution.

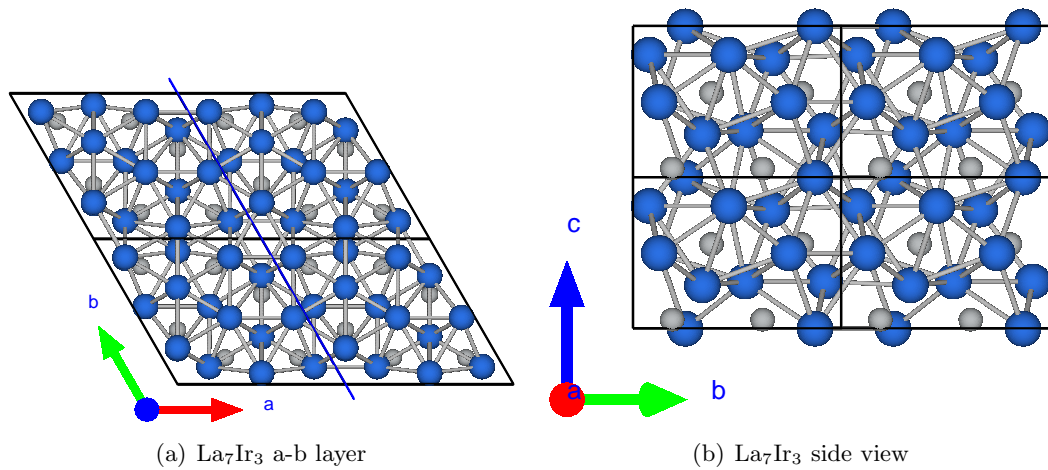


Figure 6.1: Structure of La₇Ir₃. The absence of an inversion symmetry is unveiled in the side view. Blue and light blue atoms indicate the positions of the La and Ir, respectively.

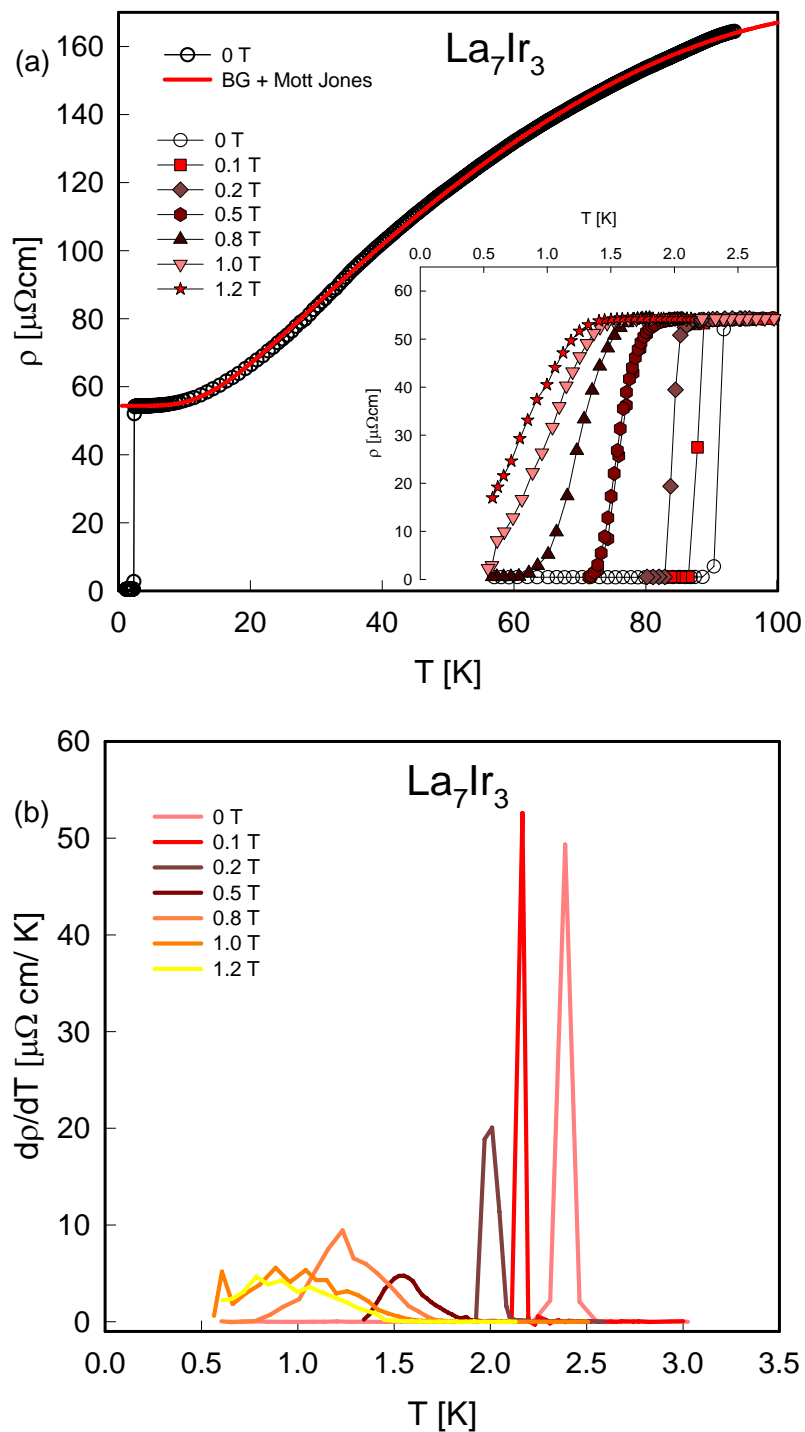


Figure 6.2: (a) The electrical resistivity measurement of La_7Ir_3 . The red line is the Bloch-Grüneisen fit with an additional Mott-Jones term. (b) The first derivative of the electrical resistivity measurement of La_7Ir_3 . The maxima show a sharp transition at low fields and broadens at higher fields.

6.2 Results and discussion

For resistivity measurements, the samples were at first cut with the wire saw and subsequently polished. The gold wires were attached to the surface with spot welding. The advantage is to ensure the wires will be not just mechanically fixed but electrical conductive, which is very important in this sample, as already small oxide layers can be sufficient to act as an insulator. To protect the sample from further oxidization, the samples were at first coated with super glue. However, during the measurements, when the sample got cooled down, the super glue showed a different thermal extension behavior. Some contacts broke or were mechanically stresses and the measurements show irregularities in the respective curves. Therefore, the coating material was exchanged to GE-Vanish, which turned out to work perfectly fine.

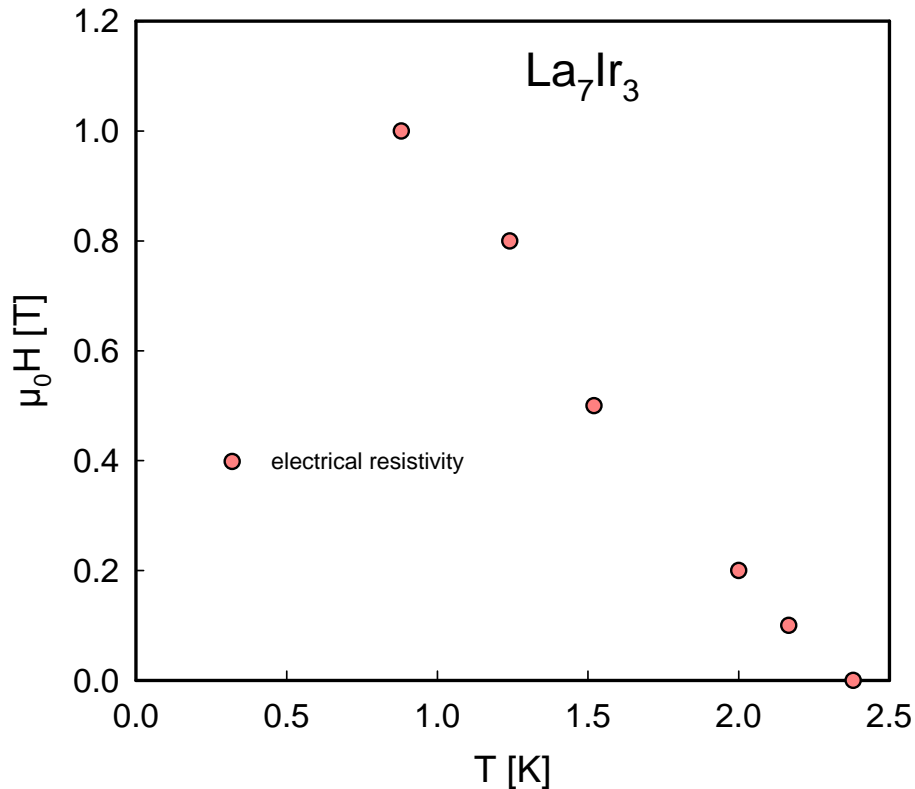


Figure 6.3: Behavior of the upper critical field at different temperatures of La_7Ir_3 . The transition temperatures were determined from $\frac{d\rho}{dT}$ maxima.

Electrical resistivity measurements ρ were performed from 400 mK up to 277 K. The residual resistivity was determined to $\rho_0 = 54.4 \mu\Omega\text{cm}$ at 2.4 K. At 277 K the resistivity data show a value of $248.9 \mu\Omega\text{cm}$. The residual resistivity ratio (RRR) was calculated to be 4.58. This generally indicates a relatively good sample quality. The behavior of $\rho(T)$ is shown from 500 mK to 90 K in Fig. 6.2(a). Above 2.4 K, it was analyzed in terms of the

T^5 Bloch-Grüneisen law with contributions of s - d scattering on Ir atoms. Below 2.38 K a sharp drop to zero is visible, indicating the transition to the superconducting state. This is in a very good agreement to the results from [121].

The behavior of the upper critical field $\mu_0 H_{c2}$ is presented in Fig. 6.3. The initial slope $\mu_0 \frac{dH_{c2}}{dT} = 0.47$ T/K. With a T_c of 2.38 K this value is far below the Pauli limiting field of 4.38 T.

Chapter 7

La₃Pd₄Si₄ and Ce₃Pd₄Si₄

7.1 Introduction

This chapter deals with the intermetallic compounds with a composition of RE₃T₄X₄ (RE = rare earth, T = transition metal, X = Si, Ge, Sn). It includes major parts of the author's published paper on the RE₃T₄X₄ system [122]. This class became subject of intense research, partly because of the variety of magnetic structures [123, 124, 125, 126, 127] and partly because of superconductivity occurring in four members of this series with RE = La, T = Ni, , Pd and X = Si, , Ge [128, 129, 130, 131, 132]. Transport and magnetic properties of the compounds containing magnetic rare earth elements are governed by the RKKY interaction in presence of strong crystalline electric field effects. While the compounds with heavy rare earth elements and X = Ge and Sn crystallize in the Gd₃Cu₄Ge₄ type of structure [123, 124, 125], Ge based ternary compounds seem not to exist for the light rare earth based metals [125]. Sn compounds with Pr and Nd, however, do exist [126].

Ternary La-based systems with T = Pd and Ni and X = Si and Ge have been reported to crystallize in the orthorhombic U₃Ni₄Si₄ type of structure and superconductivity was observed for each member of this family, with T_c ranging from $T_c = 2.5$ K (La₃Pd₄Ge₄) to $T_c = 0.76$ K (La₃Ni₄Ge₄) [131]. Fuji *et al.* [128] reported type II superconductivity for La₃Pd₄Si₄, with $T_c = 2.15$ K from resistivity and magnetic susceptibility measurements. Ce₃Ni₄Si₄ and Ce₃Rh₄Si₄ were found to crystallize in the U₃Ni₄Si₄ structure, too [133].

In the previous work on the system Ce-Pd-Si [134] it was reported on the existence of Ce₃Pd₄Si₄ with U₃Ni₄Si₄ type observed from both X-ray powder and single crystal diffraction data, as well as from scanning electron microscopy (SEM). The crystal structure of the compound was solved from single crystal data: space group *Immm*; a = 0.41618(1), b = 0.42640(1), c = 2.45744(7) nm [134]. The structure of U₃Ni₄Si₄ can be explained as a combination of AlB₂-type and BaAl₄-type layers [135]. The unit cell and crystal structure

packing of $\text{Ce}_3\text{Pd}_4\text{Si}_4$ is shown in the inset of Fig. 7.1. Layers of the ordered derivative from the BaAl_4 -type, i.e., the ThCr_2Si_2 -type was used as better choice for illustrating the ternary compound.

This chapter deals with the results of field and temperature dependent electrical resistivity, magnetic susceptibility and specific heat measurements of $\text{Ce}_3\text{Pd}_4\text{Si}_4$ at low temperatures in order to derive information about the ground state properties of this novel ternary compound. Data were analyzed in comparison with isostructural $\text{La}_3\text{Pd}_4\text{Si}_4$, representing the non-magnetic background of this material, revealing clear signatures of a non-Fermi liquid state in terms of the spin fluctuation theory by Moriya and Takimoto [136]. In addition, $\text{La}_3\text{Pd}_4\text{Si}_4$ was studied in some detail to evaluate the superconducting properties of this compound. Interestingly, the heat capacity and the upper critical magnetic field do not follow the predictions of a fully gapped s -wave state; rather, a two gap model is better suited to describe the temperature dependent specific heat, in line with a pronounced positive curvature of the upper critical magnetic field.

7.2 Experimental

Polycrystalline samples with stoichiometric composition $\text{RE}_3\text{Pd}_4\text{Si}_4$ ($\text{RE} = \text{La}, \text{Ce}$), each of a weight of 1 g, were prepared by argon arc-melting from high-purity elements (99.9 mass % rare-earth elements, 99.999% mass Si and 99.99 mass % Pd), on a water-cooled copper hearth. The melting was repeated several times with the button turned over between each melting. The weight loss was less than 0.5 mass %. After melting, the alloys were vacuum-sealed in a quartz tube and annealed at 800°C for 30 days before being quenched in cold water. Both samples were examined by X-ray powder diffraction (XRD). Data were collected at room temperature employing a STOE STADI P diffractometer with a linear PSD and $\text{CuK}_{\alpha 1}$ radiation. Quantitative Rietveld refinement of the X-ray was performed with the program FULLPROF [137, 138], employing internal tables for X-ray atomic form factors. Lattice parameters were calculated using program STOE-WinXpow [139].

A superconducting quantum interference device (SQUID) magnetometer was used to study magnetic properties from 2.5 K up to 300 K in fields up to 6 T using polycrystalline specimens of about 20 mg. Specific heat measurements on about 1 g of polycrystalline $\text{Ce}_3\text{Pd}_4\text{Si}_4$ were performed at temperatures ranging from 2.5 K up to 100 K by means of an adiabatic step heating method. Additionally, specific heat measurements in the temperature range between 350 mK and 20 K were carried on $\text{La}_3\text{Pd}_4\text{Si}_4$ and $\text{Ce}_3\text{Pd}_4\text{Si}_4$ samples with a commercial Quantum design PPMS ^3He relaxation calorimeter in fields up to 1 T with a mass of 29 mg and 1.7 mg, respectively. The lower mass for the Ce compound was chosen to optimize the relaxation times as discussed in Sec. 3.1.2. Electrical resistivity measurements

were carried out in a ^3He bath top-loading cryostat with a maximum magnetic field of 12.5 T and for temperatures from 350 mK up to 300 K. Resistivity was measured with the electrical current flowing parallel to the applied magnetic field via a four-probe technique using an a.c. bridge (Lakeshore 370). The measurement devices were described in detail in Sec. 3.2.1, 3.3 and 3.4.

7.3 Results and Discussion

The XRD analyses indicate that $\text{RE}_3\text{Pd}_4\text{Si}_4$ phases with La and Ce as rare earth element are present as a major phase with a minor amount of impurity phases. The XRD pattern of $\text{La}_3\text{Pd}_4\text{Si}_4$ together with the corresponding Rietveld refinement are shown in Fig. 7.1, revealing $a = 0.42358(1)$ nm, $b = 0.42900(1)$ nm and $c = 2.45400(7)$ nm. Some small extra XRD peaks could be indexed on the basis of a $\text{La}_2\text{Pd}_3\text{Si}_3$ phase. The content of impurities is estimated to be a few percents in each sample. In the case of $\text{Ce}_3\text{Pd}_4\text{Si}_4$ these small impurity phases were identified as $\text{Ce}_2\text{Pd}_3\text{Si}_3$ ($\text{Ce}_2\text{Rh}_{1.35}\text{Ge}_{4.65}$ -type) and CePd_2Si_2 (ThCr_2Si_2 -type) in agreement with the Ce-Pd-Si phase diagram where these two phases were reported as neighboring phases.

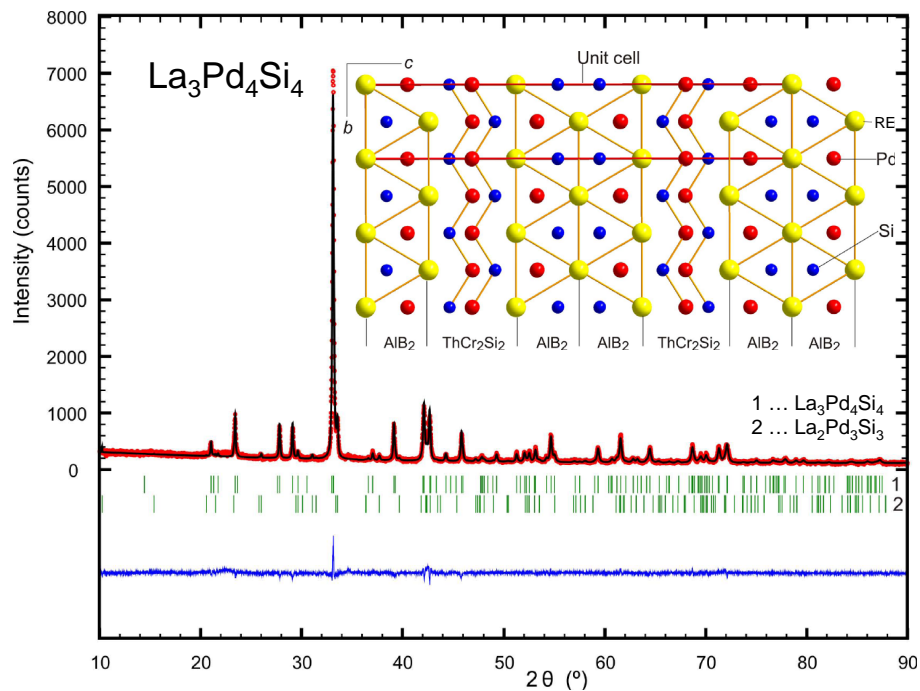


Figure 7.1: X-ray powder pattern and Rietveld refinement of $\text{La}_3\text{Pd}_4\text{Si}_4$. The inset is a sketch of the crystal structure in projection along $[100]$.

7.3.1 $\text{La}_3\text{Pd}_4\text{Si}_4$

Both resistivity and heat capacity measurements carried out on $\text{La}_3\text{Pd}_4\text{Si}_4$ evidence bulk superconductivity below 2 K. Shown in Fig. 7.3.1 is the temperature dependent electrical resistivity, ρ , of $\text{La}_3\text{Pd}_3\text{Si}_4$ at zero field (main panel) and at various externally applied magnetic fields. Clearly visible is a superconducting transition being located slightly above 2 K. This transition temperature is in good coincidence with data reported in Ref. [128, 129] derived from measurements of the electrical resistivity and magnetic susceptibility. Metallic behavior and the importance of s - d scattering in $\text{La}_3\text{Pd}_3\text{Si}_4$ is quantitatively revealed from the applicability of the Bloch-Wilson model [64], i.e.,

$$\begin{aligned} \rho(T) = & A \left(\frac{T}{\theta_D} \right)^5 \int_0^{\theta_D/T} \frac{z^5 dz}{(\exp(z) - 1)(1 - \exp(-z))} \\ & + B \left(\frac{T}{\theta_D} \right)^3 \int_{\theta_{min}/T}^{\theta_D/T} \frac{z^3 dz}{(\exp(z) - 1)(1 - \exp(-z))} - \kappa T^3. \end{aligned} \quad (7.1)$$

The Mott-Jones term κT^3 accounts for scattering of conduction electrons on a narrow d -band (e.g., Pd- $4d$ or La- $5d$ in $\text{La}_3\text{Pd}_3\text{Si}_4$) near to the Fermi energy [140] and explains the negative curvature in $\rho(T)$ at higher temperatures. A least squares fit of this model to the experimental data (solid line, Fig. 7.3.1) reveals a Debye temperature $\theta_D = 155$ K, and $\kappa \approx 10^{-7} \mu\Omega\text{cmK}^{-3}$ as well as a minimum phonon energy $k_B\theta_{min} = \hbar\omega_{min}$, with $\theta_{min} = 98$ K. Here, ω_{min} is the frequency corresponding to the minimum \vec{q} value to excite the s - d transitions [64]. $A = 54 \mu\Omega\text{cm}$ and $B = 8.6 \mu\Omega\text{cm}$ are material dependent constants (compare Fig. 7.6, too).

The superconducting phase transition is relatively sharp, evidencing good sample quality. The application of magnetic fields (inset, Fig. 7.3.1) consecutively suppresses superconductivity and magnetic fields of the order of 1 T are sufficient to entirely eliminate the superconducting state. This suppression is accompanied by a slight increase of the width of the phase transition. The Debye temperature as derived from resistivity data is significantly lower than that derived from the specific heat measurements (see below). This might be a result of non-negligible electron-electron scattering superimposed to electron-phonon scattering.

To proof whether superconductivity in $\text{La}_3\text{Pd}_4\text{Si}_4$ is of bulk nature and does not refer to an impurity phase, heat capacity measurements, $C_p(T)$, have been carried out for temperatures down to 350 mK and for magnetic fields up to 0.4 T. Results are displayed in Fig. 7.3.1. Bulk superconductivity is obvious from the distinct anomaly of C_p/T around 2 K. An accurate determination of the superconducting transition temperature can be made from an idealized jump of the heat capacity anomaly (solid line, Fig. 7.3.1) by a balance of entropy, yielding $T_c = 1.98$ K, in good agreement with the resistivity data. The ideal

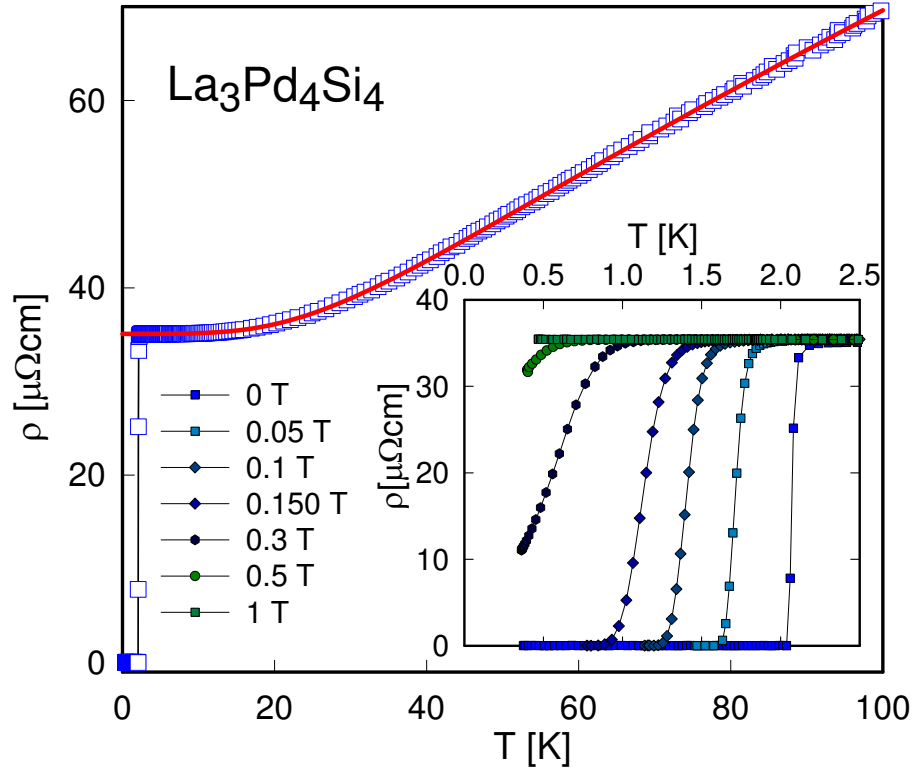


Figure 7.2: Temperature dependent electrical resistivity, ρ , of $\text{La}_3\text{Pd}_4\text{Si}_4$. The solid line is a least squares fit as explained in the text. The inset shows $\rho(T)$ of $\text{La}_3\text{Pd}_4\text{Si}_4$ at various externally applied magnetic fields.

peak height of the SC anomaly would then be 27 mJ/molK^2 .

Fig. 7.3.1 shows $\frac{d\rho'}{dT}$ over the temperature. In the zero field measurement, the transition is sharp similar to LaPtSi and is in a good agreement with the theoretically predicted behavior as illustrated in Fig. 2.4(c). With increasing field the transition width gets broader. This is in a good agreement with a two gap model for superconductivity which will be discussed later.

An estimation of the normal state Sommerfeld value γ_n within the temperature range between 2 and 5 K, reveals 26 mJ/molK^2 , and, additionally, $\theta_D = 280 \text{ K}$. A similar γ -value is obtained if field measurements (e.g., $\mu_0 H = 0.4 \text{ T}$) are considered, resulting in $\gamma_n = 28 \text{ mJ/molK}^2$. The latter, however, is derived within a much smaller range of extrapolation.

From the jump of the specific heat $\Delta C_p/T(T = T_c) \approx 27 \text{ mJ/molK}^2$, one calculates the parameter $\Delta C_p/(\gamma_n T_c) \approx 1.03$, which is below the figure expected from BCS theory, $\Delta C_p/(\gamma T_c) \approx 1.43$.

Deviations from a standard BCS behavior are also evident from the temperature depen-

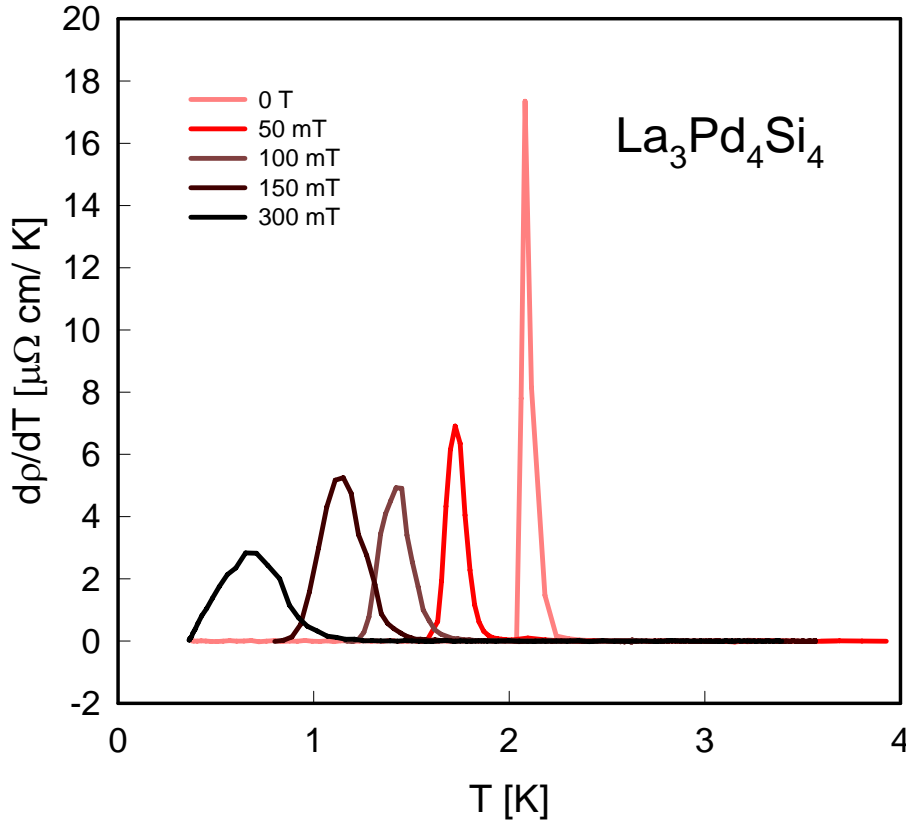


Figure 7.3: The first derivative of the electrical resistivity over the temperature. The measurement shows a clear behavior and seems to be more stable than the LaPtSi compound shown in Fig. 4.3 while exposed to external fields.

dent specific heat. Compared in Fig. 7.5(a) are the experimental heat capacity data of $\text{La}_3\text{Pd}_4\text{Si}_4$, plotted in a normalized representation $C_p/(\gamma_n T_c)$, together with the heat capacity of a fully gapped s -wave superconductor as tabulated by Mühlischlegel [35] (solid line, Fig. 7.5(a)) and a simple power law $C_p \propto T^3$ (dashed - double-dotted line, Fig. 7.5(a)). The latter would indicate point-nodes in the superconducting gap. Obviously, both models do not properly account for the experimental data, specifically in the low temperature range.

A further model calculation is based on a two gap scenario employing the so-called α -model developed by Padamsee *et al.* [141] with only one adjustable parameter $\alpha = \Delta(0)/(k_B T_c)$. Note, the value $\alpha = 1.764$ corresponds to the weak coupling BCS limit. The heat capacity in the superconducting state is then a sum of individual contributions of both gaps $\Delta_i(0)$, together with the ratio γ_1/γ_2 , with the partial specific heat contributions $\gamma_1 + \gamma_2 = \gamma_n$. Such calculations have been successfully applied to MgB_2 [142], to borocarbide superconductors [143], or recently, to the ternary iron-silicide $\text{Lu}_2\text{Fe}_3\text{Si}_5$ [144]. Employing this model to $\text{La}_3\text{Pd}_4\text{Si}_4$ with $\alpha_1 = 1.95$, $\alpha_2 = 1.1$ and $\gamma_1/\gamma_2 = 0.7/0.3$ (dashed line, Fig. 7.5(a)) reveals convincing agreement with the experimental data in an extended temperature range. Such

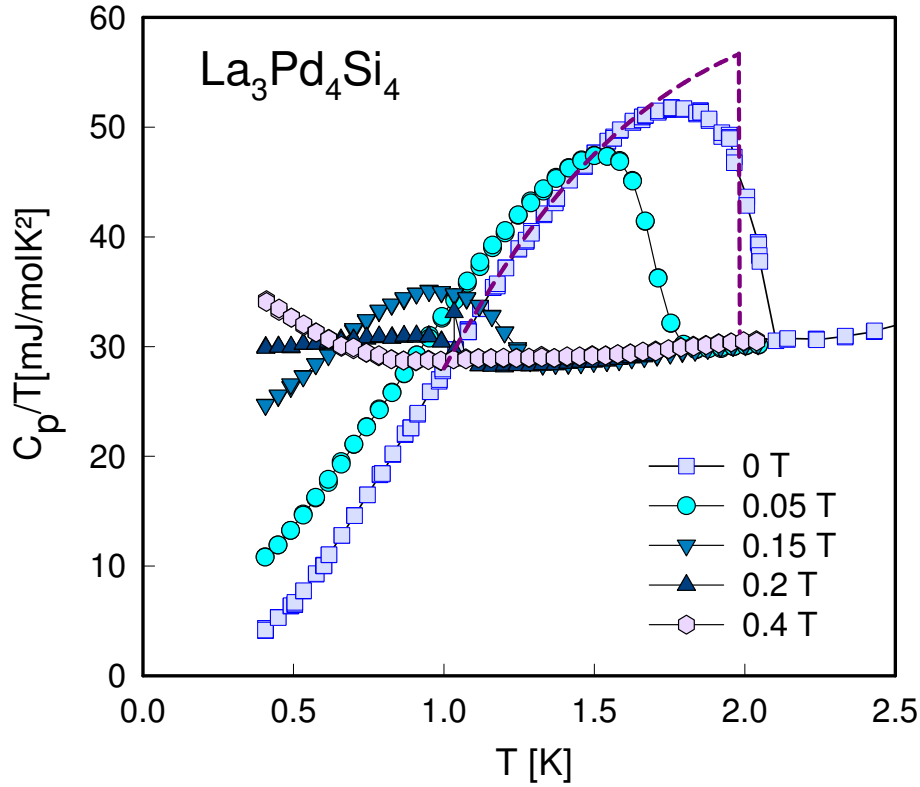


Figure 7.4: Temperature dependent heat capacity, C_p , of $\text{La}_3\text{Pd}_4\text{Si}_4$ plotted as C_p/T vs. T for various externally applied magnetic fields. The dashed line represents an ideal superconducting transition with $T_c = 1.98 \text{ K}$.

a two gap model would also be in line with the pronounced positive curvature found for the upper critical field of $\text{La}_3\text{Pd}_4\text{Si}_4$ (see below). The temperature dependent difference between the experimental data and the three theoretical models are shown in Fig. 7.5(b), clearly demonstrating the superior agreement of the two gap scenario over a fully gapped s -wave model or the simple power law.

As shown in Fig. 7.3.1, both the transition temperature and the jump of the specific heat at T_c become suppressed with increasing externally applied magnetic fields. This field dependent lowering of T_c is outlined in Fig. 7.5(b), where both resistivity and heat capacity data are summarized. As it is obvious from this figure, $T_c(\mu_0 H)$ shows a super-linear dependence, reaching an upper critical field at zero temperature, $\mu_0 H_{c2}(0)$, of about 0.6 T. A typical BCS superconductor, however, would exhibit a sub-linear temperature dependence $\mu_0 H_{c2}(T)$. In absence of low temperature measurements, Fujii [128, 129] estimated an upper critical field $\mu_0 H_{c2} \approx 0.33 \text{ T}$ from a simple extrapolation of susceptibility results.

The unusual temperature dependence of the upper critical field of $\text{La}_3\text{Pd}_4\text{Si}_4$ can have different microscopic origins: i) the existence of more than one Fermi surface sheet with energy gaps of different magnitudes as reported e.g., for binary MgB_2 or ii) strong anisotropies

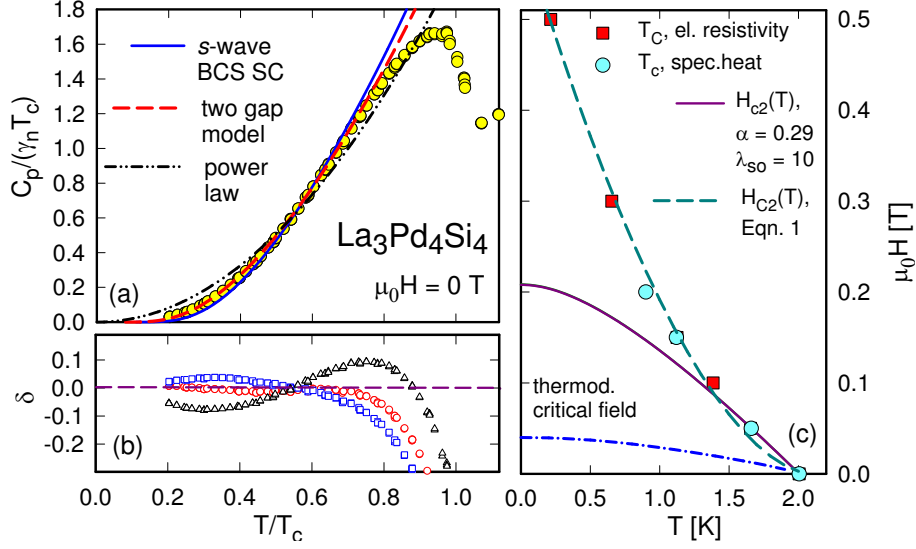


Figure 7.5: (a) Low temperature specific heat C_p of $\text{La}_3\text{Pd}_4\text{Si}_4$ plotted in a normalized representation $C_p/(\gamma_n T_c)$ vs. T/T_c . γ_n is the Sommerfeld constant in the normal state region of $\text{La}_3\text{Pd}_4\text{Si}_4$. The solid line is the heat capacity of a fully gapped BCS superconductor whereas the dashed line represents a model with two different superconducting gaps. For details see the text. The dashed - double-dotted line is a power law, $C_p \propto T^3$. (b) Temperature dependent difference δ of experimental and theoretical heat capacity data $C_p/(\gamma_n T_c)$ below T_c . The colors refer to panel (a). (c) Upper critical magnetic field $\mu_0 H_{c2}$ of $\text{La}_3\text{Pd}_4\text{Si}_4$ as derived from resistivity (50% criterion) and specific heat data (thermodynamic mean value of the transition). The dashed line is a least squares fit employing Eqn. 1 and the solid line is a fit based on the WHH model (see text). The dashed-dotted line is the thermodynamic critical field.

of the superconducting order parameter residing on a single Fermi surface sheet.

Positive curvatures of $\mu_0 H_{c2}(T)$ have been observed e.g., for the non-magnetic rare-earth nickel borocarbides $\text{RNi}_2\text{B}_2\text{C}$ ($\text{R} = \text{Y}, \text{Lu}$) and were explained theoretically employing effective two-band models [145, 146]. Phenomenologically, $\mu_0 H_{c2}(T)$ of borocarbides and MgB_2 were accounted for in a wide temperature range using the simple expression [147]

$$\mu_0 H_{c2} = \frac{\mu_0 H_{c2}^*}{(1 - T/T_c)^{1+\beta}} \quad (7.2)$$

where $\mu_0 H_{c2}^*$ and β are fitting parameters. Similar to the borocarbide case and MgB_2 , $\mu_0 H_{c2}(T)$ of $\text{La}_3\text{Pd}_4\text{Si}_4$, as displayed in Fig. 7.5(b) can be described on the basis of Eqn. 7.2. A least squares fit is shown in Fig. 7.5(b) as dashed line revealing $H_{c2}^* = 0.6$ and $\beta = 0.77$. Exponents of a similar order were derived for borocarbides and MgB_2 , too.

Werthamer *et al.* [40] derived an expression (abbreviated as *WHH model*) for the upper critical field $\mu_0 H_{c2}$ in terms of orbital pair-breaking, including the effect of Pauli spin

paramagnetism and spin-orbit scattering. The WHH model is ruled by two parameters, namely α_M , the Pauli paramagnetic limitation (= Maki parameter, [39]), and λ_{so} , describing spin-orbit scattering. While the value of α_M allows a rough discrimination between orbital pair breaking and Pauli limiting, λ_{so} becomes non-negligible for heavier atoms.

The Maki parameter α_M can be estimated [40] from the Sommerfeld value γ and the residual resistivity ρ_0 as $\alpha_M = 0.23$. The reasonably low value of α_M indicates that orbital pair-breaking in $\text{La}_3\text{Pd}_4\text{Si}_4$ is the essential mechanism, limiting the upper critical field. The overall temperature dependence of $\mu_0 H_{c2}$ as derived from the WHH model is displayed as a solid line in Fig. 7.5(b), revealing $\mu_0 H_{c2}(0) = 0.21$ T, which is more than two times smaller than the experimentally observed data.

The thermodynamic critical field is calculated from the free energy difference between the superconducting and normal state, given by Eqn. 4.2. The quantity $C_s(T)$ is obtained from the zero field specific heat measurement whereas $C_n(T)$ is obtained from the data corresponding to the 0.4 T run. The values derived are displayed in Fig. 7.5(b) as dashed-dotted line; an extrapolation to $T \rightarrow 0$ yields $\mu_0 H_c(0) \approx 0.04$ T. This allows to evaluate a value for the dimensionless Ginzburg Landau parameter $\kappa_{GL} = H_{c2}(0)/(\sqrt{2}H_c) \simeq 9.8$, where the experimentally determined $H_{c2}(0) = 0.55$ T has been used. The coherence length ξ_0 for $T \rightarrow 0$ can be obtained from $\mu_0 H_{c2} = \Phi_0/(2\pi\xi_0^2)$, yielding $\xi_0 \simeq 2.44 \times 10^{-8}$ m. Combining the Ginzburg Landau parameter with the coherence length, the London penetration depth can be obtained as $\lambda_L(T \rightarrow 0) \simeq 2.39 \times 10^{-7}$ m.

An estimation of the electron-phonon interaction strength λ_{ep} is possible in terms of the McMillan formula from Eqn. 2.50 [28]. Applying this model, and taking the repulsive screened Coulomb part $\mu^* \approx 0.13$, yields $\lambda_{ep} \approx 0.52$; this characterizes $\text{La}_3\text{Pd}_4\text{Si}_4$ as a SC in the weak coupling limit.

Similarly, an electron - phonon enhancement factor of about the same magnitude can be found if recent electronic structure calculations are considered [148], where the calculated density of states at the Fermi energy corresponds to a bare band value $\gamma_b = 19.8$ mJ/molK². A comparison with the experimentally derived Sommerfeld value $\gamma = 29$ mJ/molK² yields $\lambda_{ep} \approx 0.46$, supporting the weak coupling regime.

Based on the value of $l_{tr}/\xi \approx 0.75$ one can classify $\text{La}_3\text{Pd}_4\text{Si}_4$ as a weakly coupled superconductor in the dirty limit; the value of $\kappa_{GL} \approx 10$ refers to a type II superconductor.

7.3.2 $\text{Ce}_3\text{Pd}_4\text{Si}_4$

Intermetallic compounds based on Ce are known since long time for a variety of interesting ground states, primarily triggered by the Kondo effect as a result of distinct interactions between conduction electrons and the magnetic moment of the Ce ion. In the following,

results derived from resistivity, heat capacity and magnetization measurements will be used to obtain information on the ground state properties of $\text{Ce}_3\text{Pd}_4\text{Si}_4$.

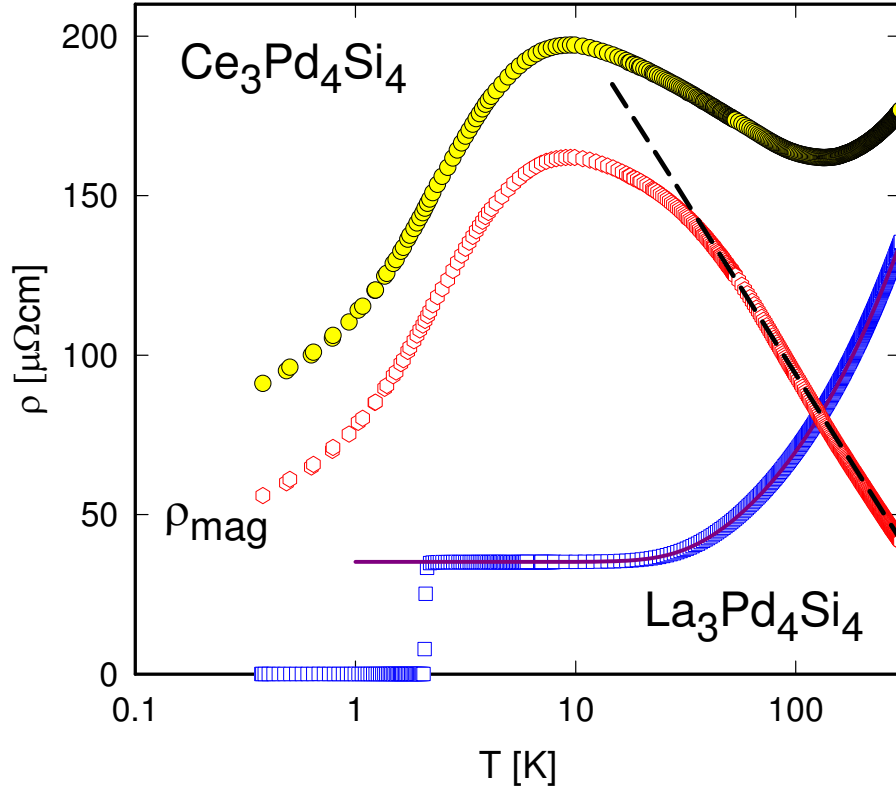


Figure 7.6: Temperature dependent resistivity ρ of $\text{La}_3\text{Pd}_4\text{Si}_4$ and $\text{Ce}_3\text{Pd}_4\text{Si}_4$ plotted on a logarithmic temperature scale. The magnetic contribution $\rho_{mag}(T)$ of $\text{Ce}_3\text{Pd}_4\text{Si}_4$ is also shown in this plot, where the dashed line should emphasize Kondo interaction; $\rho_{mag} \approx \rho(\text{Ce}_3\text{Pd}_4\text{Si}_4) - \rho(\text{La}_3\text{Pd}_4\text{Si}_4)$. The solid line is a least squares fit as explained in Fig. 7.3.1.

Shown in Fig. 7.6 are temperature dependent resistivity measurements of $\text{Ce}_3\text{Pd}_4\text{Si}_4$ and of $\text{La}_3\text{Pd}_4\text{Si}_4$; the latter compound serves as non-magnetic reference, representing the contribution to the electrical resistivity owing to the electron - phonon interaction. While $\rho(T)$ of $\text{La}_3\text{Pd}_4\text{Si}_4$ exhibits superconductivity below 2 K and a simple metallic behavior in the normal state region (see the previous section), $\rho(T)$ of $\text{Ce}_3\text{Pd}_4\text{Si}_4$ shows a much more complex temperature dependence as typical for Kondo lattice systems. The most dominant feature is a maximum in $\rho(T)$ around 8.5 K with $\rho(T)$ dropping above and below this temperature. Well above 100 K, a local minimum develops in $\rho(T)$. A comparison of the experimental data of $\text{Ce}_3\text{Pd}_4\text{Si}_4$ and $\text{La}_3\text{Pd}_4\text{Si}_4$ allows to derive the magnetic part, ρ_{mag} , if one assumes that the phonon contribution of both compounds is equal. $\rho_{mag}(T)$ of $\text{Ce}_3\text{Pd}_4\text{Si}_4$ is included in Fig. 7.6, too. The logarithmic temperature dependence of ρ_{mag} at elevated temperatures evidences Kondo interaction in the presence of crystalline electric field splitting. The drop of $\rho(T)$ at low temperatures results from the development

of a coherent state owing to the Kondo lattice properties of $\text{Ce}_3\text{Pd}_4\text{Si}_4$. In general, such a coherent state would be concomitant with Fermi liquid features, and a T^2 behavior of $\rho_{mag}(T)$ should become obvious. The present experimental data, however, reveal a distinctly different power law.

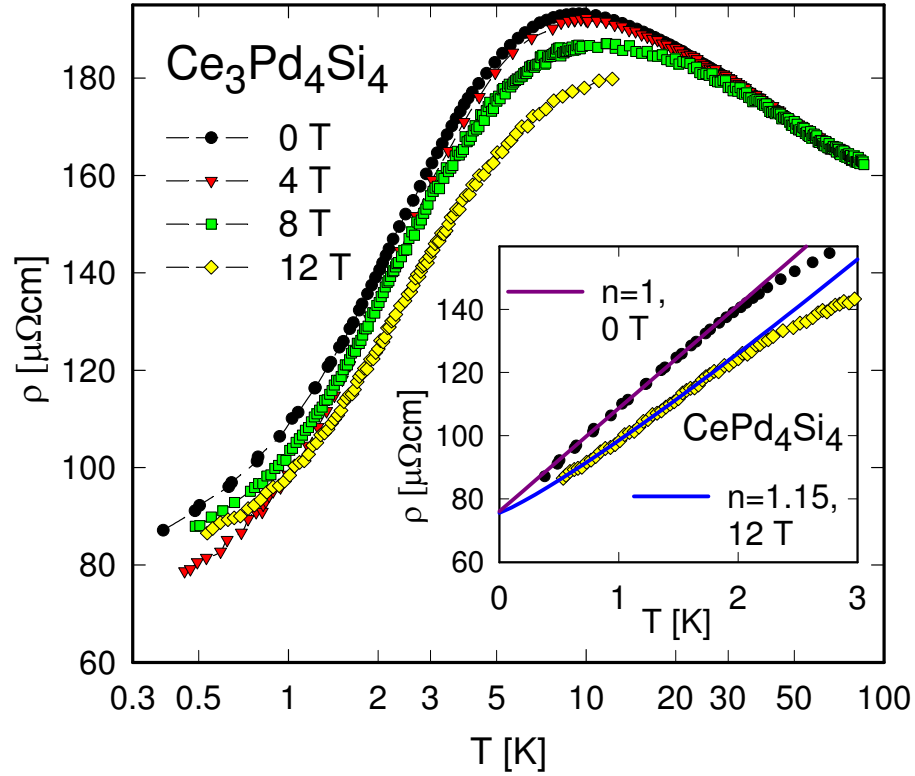


Figure 7.7: Low temperature electrical resistivity, ρ , measured at various externally applied magnetic fields. The inset shows resistivity details together with power law fits for the zero and 12 T run.

A closer inspection of the low temperature resistivity data is shown in Fig. 7.7, where measurements at various magnetic fields are added. The low temperature maximum in $\rho(T)$ is weakly field dependent and shifts from about 8.5 K at zero magnetic field to about 10.5 K at an externally applied field of 8 T. Such a field dependence of the electrical resistivity is typical for cerium and ytterbium based Kondo lattices. At the lowest temperatures of this study, Fermi liquid features are absent in $\rho(T)$. Rather, the zero field measurement can be accounted for by a simple power law, $\rho(T) = \rho_0 + AT^n$, where the exponent $n = 1$ reveals best agreement; in the case of the 12 T run, $n = 1.15$. These exponents are indicative of a non-Fermi liquid behavior, arising, most likely, from the proximity of a magnetic instability of the Ce ions.

A magnetic state of the Ce ions in $\text{Ce}_3\text{Pd}_4\text{Si}_4$, can be concluded from magnetic susceptibility measurements, $\chi(T)$, as shown in Fig. 7.8. Applying a modified Curie-Weiss law

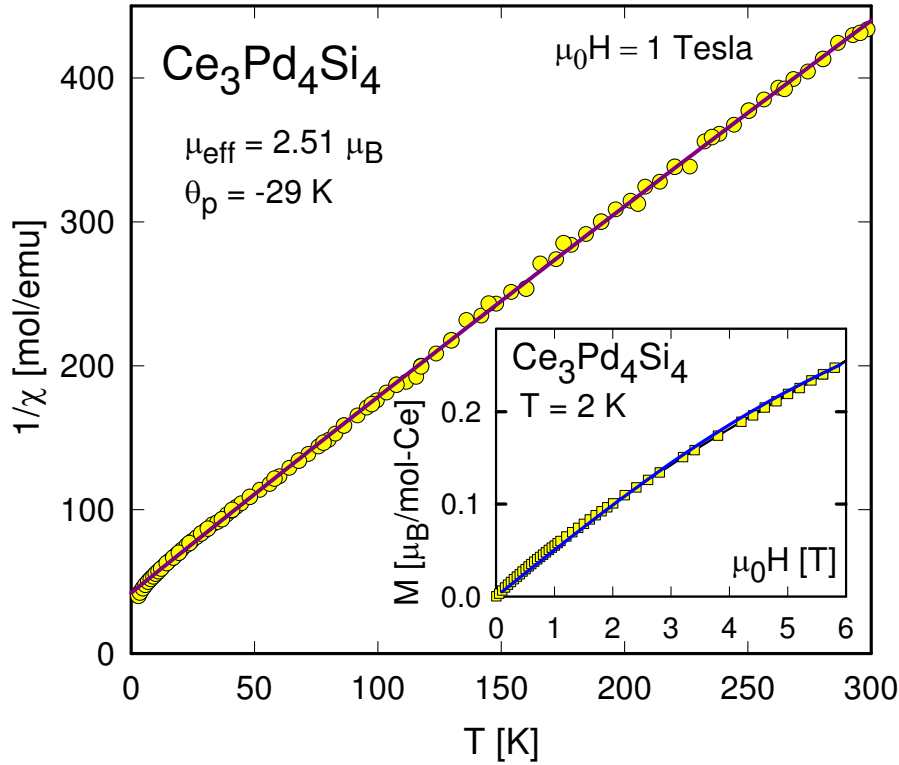


Figure 7.8: Temperature dependent magnetic susceptibility, χ of $\text{Ce}_3\text{Pd}_4\text{Si}_4$ plotted as $1/\chi$ vs. T . The solid line is a fit employing a modified Curie-Weiss law. The inset displays the isothermal magnetization ($T = 2 \text{ K}$) of $\text{Ce}_3\text{Pd}_4\text{Si}_4$; the solid line is the magnetization of an effective spin 1/2 system with a Landè factor $g_{\text{eff}} = 0.775$.

to the experimental data, i.e. Eqn. 4.12, yields information concerning a temperature independent Pauli contribution χ_0 , the effective magnetic moment μ_{eff} (deduced from the Curie constant C) and the paramagnetic Curie temperature θ_p . Results of a least squares fit ($T > 50 \text{ K}$) according to the Eq. (4.12) are shown as solid line in Fig. 7.8, revealing an effective magnetic moment $\mu_{\text{eff}} = 2.51 \mu_B$ close to that of the $\text{Ce-}4f^1$ electronic configuration [$\mu_{\text{eff}}(\text{Ce}^{3+}) = 2.54 \mu_B$] and a paramagnetic Curie temperature $\theta_p = -29 \text{ K}$. The latter refers to antiferromagnetic interactions among the Ce ions. $\chi(T)$ at low temperatures does not show any characteristic anomaly being typical for long range magnetic order. This is in line with isothermal magnetization data taken at $T = 2 \text{ K}$ (inset, Fig. 7.8). A smooth, slightly curvilinear $M(H)$ dependence is observed with relatively small magnetization values at 6 T. A description of these data can be done calculating the field dependent magnetization of an effective spin 1/2 system at $T = 2 \text{ K}$, employing a Landè factor $g_{\text{eff}} = 0.775$. Fairly good agreement is obtained in this way, except for the low field range, where the disagreement between the model and the experimental data appears to be in line with the Curie-like bending of the magnetic susceptibility at low temperatures.

CEF effects are the primary cause for the appearance of only small magnetization values, well below $g_j j = 2.14 \mu_B$, associated with the total angular momentum of the free Ce^{3+} ion. A comparison with magnetization data of $\text{Ce}_3\text{Pd}_4\text{Ge}_4$ at $T = 2$ K [149] shows for the latter a clear indication for a metamagnetic phase transition around 4 T, thus referring to an antiferromagnetic ground state.

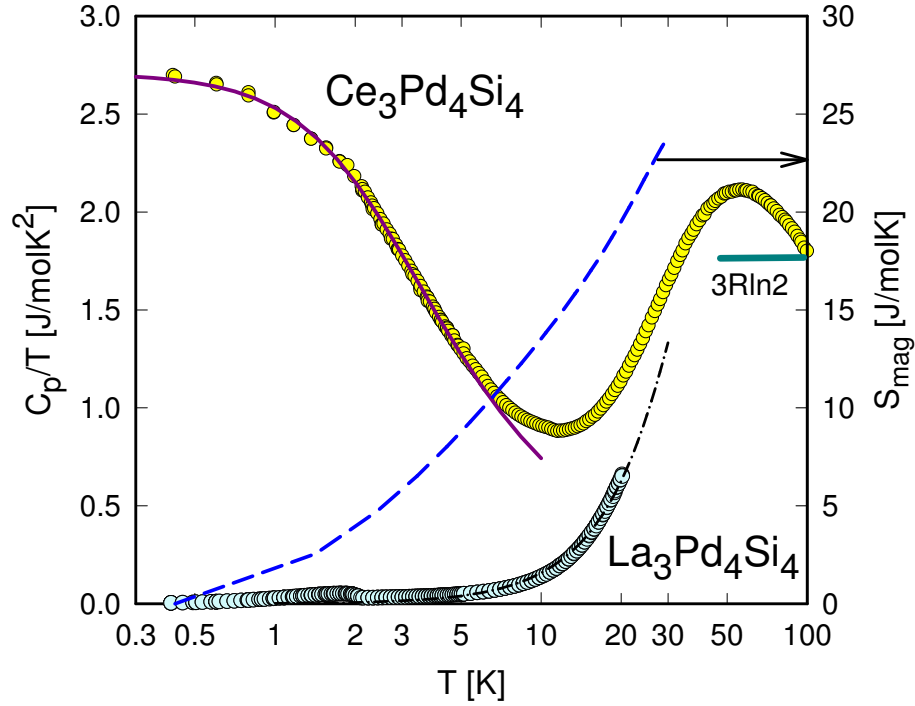


Figure 7.9: Temperature dependent specific heat C_p of $\text{Ce}_3\text{Pd}_4\text{Si}_4$ plotted as C_p/T vs. $\ln T$. For purpose of comparison, C_p/T of $\text{La}_3\text{Pd}_4\text{Si}_4$ is added, too. The solid line represents the heat capacity of a spin fluctuation model according to Eqn. 2 near to the quantum critical point and the dashed-dotted line is a smooth extrapolation of heat capacity data using the Debye model with $\theta_D = 280$ K. The dashed line is the calculated magnetic entropy S_{mag} of $\text{Ce}_3\text{Pd}_4\text{Si}_4$, referring to the right axis.

To further prove the ground state of $\text{Ce}_3\text{Pd}_4\text{Si}_4$, heat capacity measurements, C_p , have been performed down to 400 mK. Results are displayed in Fig. 7.9 as C_p/T vs. T , together with those of $\text{La}_3\text{Pd}_4\text{Si}_4$. The most prominent feature is an almost logarithmic contribution in the range of a few Kelvin, followed by a smooth saturation of C_p/T towards zero with very large values of about 2.7 J/molK^2 , corresponding to $\gamma = 0.9 \text{ J/molK}^2$ per cerium ion. Considering renormalization group calculations by Oliveira and Wilkins [150], the Kondo temperature T_K follows from $T_K = 0.68 \cdot R/\gamma = 6.2 \text{ K}$ if a doublet is considered as ground state.

Assuming that the phonon contribution to the heat capacity of $\text{Ce}_3\text{Pd}_4\text{Si}_4$ can be represented by the specific heat of $\text{La}_3\text{Pd}_4\text{Si}_4$, the magnetic entropy S_{mag} can be derived by

integrating C_{mag}/T . Results of this evaluation are plotted in Fig. 7.9 as dashed line, referring to the right axis. An entropy of $3 \cdot R \ln 2$ is reached around 18 K. The slow rate of the recovery of magnetic entropy in $\text{Ce}_3\text{Pd}_4\text{Si}_4$ is a consequence of the Kondo effect present in this compound. $S_{mag}(T)$ also allows to estimate the Kondo temperature independently from $T_K = T(S_{mag} \approx 0.45 \cdot R \ln 2) \approx 4.4$ K [151], in very good agreement with the estimation obtained from the Sommerfeld value. Kondo type interaction is also supposed to be responsible for the suppression of long range magnetic order, absent in $\text{Ce}_3\text{Pd}_4\text{Si}_4$ at least down to 400 mK.

The further increase of S_{mag} at higher temperatures indicates that the excited crystalline electric field levels are not well separated from the ground state; hence some hybridization between CEF levels might appear. This is seen from some deformation of the maximum of the magnetic contribution to the electrical resistivity, too.

In order to test whether or not $\text{Ce}_3\text{Pd}_4\text{Si}_4$ is at or near the quantum critical point, the self-consistent renormalisation (SCR) model of Moriya and Takimoto [136] can be taken into account:

$$\begin{aligned}
C_m &= 9N_0 \int_0^{x_0} dx x^2 \left\{ \left[u^2 - 2u \frac{dy}{dt} + \left(\frac{dy}{dt} \right)^2 \right] \times \right. \\
&\times \left[-\frac{1}{u} - \frac{1}{2u^2} + \psi'(u) \right] - \\
&\left. - t \frac{d^2 y}{dt^2} \left[\ln u - \frac{1}{2u} - \psi(u) \right] \right\} \quad (7.3)
\end{aligned}$$

where $x^2 = u \cdot t - y$, $u = u(y)$ and $y = y(y_1, y_0)$ is the reduced staggered susceptibility and $t = T/T_0$. T_0 is some characteristic temperature, scaling a temperature dependent physical quantity; y_1 is a constant. The parameter y_0 measures the distance of the system to the magnetic instability and provides a measure of the inverse correlation length [152]. As y_0 approaches zero, the system approaches the quantum critical point.

An adjustment of Eqn. 7.3 to the experimental data is displayed in Fig. 7.9 as solid line, revealing excellent agreement between the data and the model for $T_0 = 3.5$ K, $y_0 = 1.5$ and $y_1 = 15$. The model reveals a constant for $T \rightarrow 0$ followed by a $T^{-1/2}$ dependence; finally, at higher temperatures, a logarithmic decrease of C_p/T occurs, in accord with the experimental findings. The finite - although small - value of y_0 indicates that $\text{Ce}_3\text{Pd}_4\text{Si}_4$ is not directly at the QCP; nevertheless it proves that this sample is next to a phase transition at $T = 0$.

A more stable magnetic state, however, was observed for $\text{Ce}_3\text{Pd}_4\text{Ge}_4$ [149], where due to the increase of the unit cell volume owing to the Si/Ge substitution, a decrement of hybridization takes place; as a consequence, magnetic order occurs and the system has

moved away from quantum criticality.

Chapter 8

Summary

Non-centrosymmetric superconductors were found in different materials, crystallizing in various non-centrosymmetric point groups, with a clear indication of strong influences or dominance of unconventional pairing being absent. All of the explored superconducting materials exhibit the phase transition to the superconducting state at low, below 4 K.

Bulk properties like the temperature dependent electrical resistivity, specific heat, or magnetization evidence superconductivity in LaPtSi below $T_c = 3.35$ K. A thorough analysis of the experimental data reveals a fully gapped *s*-wave superconducting state. Examining $l_{tr}/\xi \approx 0.92$, we classify LaPtSi as a weakly coupled superconductor in the dirty limit. The value of $\kappa_{GL} \approx 8.7$ refers to a type II superconductor. DFT calculations derived both the electronic structure and phonon properties of LaPtSi. The absence of inversion symmetry in the crystal structure is responsible for a lifting of the two-fold degeneracy of the electronic bands, except in the Γ - Z direction. Superconductivity originates predominantly from Pt and La electronic states since Pt-*d* and La-*d* states dominate the electronic DOS at the Fermi energy. Specific \vec{q} -vectors, associated with a softening of phonons in various directions in the reciprocal space (e.g., Γ - Z' , Γ - Z) are supposed to mediate superconductivity via $\vec{k}_F + \vec{q} = -\vec{k}_F$. Although there is a rather large spin-orbit splitting in LaPtSi, the topology of the Fermi surface enforces predominantly spin-singlet pairing. This seems to explain why unconventional superconductivity has not been observed experimentally for LaPtSi.

Physical property measurements of the EpTX₃ materials show superconducting behavior prevailing in the compositions BaPtSi₃, BaPdSi₃, SrNiSi₃, SrPdSi₃, SrPdGe₃, SrPtSi₃ and SrPdGe₃ for different physical properties. The transition temperatures, going from 1 K to a maximum of 3 K, and the relevant superconducting lengths (ξ_{GL} in the range of 44 nm to 105 nm, λ_L from 131 nm to 307 nm) are listed in Tab. 5.1. DFT calculations of the band structure indicate that a tuning effect due to the Z^2 dependency of the spin-orbit

interaction is possible. The behavior of the heat capacity measurements as well as the μ SR measurements do not show any peculiarities or a violation of the time reversal symmetry. Therefore, the EpTX_3 compounds ($\text{Ep} = \text{Sr, Ba}$; $\text{T} = \text{Ni, Pd, Pt, Cu, Ag, Au}$; $\text{X} = \text{Si, Ge, Sn}$) can be classified as dirty type II superconductors with an s -gap symmetry and a conventional BCS behavior.

LaIrSi , however, could not be confirmed to be a bulk superconductor. Measurements of the specific heat and the electrical resistivity bolster up this conclusion. However, small kinks in the C_p data and a drop of around 50 % in the ρ data were visible. Percolation theory explains, how just a small foreign phase can give such results. A certain foreign phase, holding responsible for this feature, was not identified. Rather small values of the Sommerfeld value of $\gamma = 2.8$ mJ/mol K were obtained. The resulting small value of the electronic density of states at the Fermi surface is, in general, detrimental to the formation of a superconducting phase.

Non centrosymmetric superconductivity in single crystals of HfRhGe was proven by specific heat measurements as a bulk property and electrical resistivity measurements as a transport property. The transition temperatures are 1.66 K and 1.69 K for C_p and ρ , respectively. Small cracks inside the sample might be responsible for an improper high electrical resistivity. Obtaining $\mu_0 H_{cth}$ from specific heat measurements allows to identify HfRhGe as a dirty type II superconductor with a κ_{GL} of 17.1 in the intermediate coupling regime. The London penetration depth λ_L and the GL coherence length ξ_{GL} were calculated to be 159.54 nm and 9.31 nm, respectively. Even for single crystals of HfRhGe , strong deviations of the upper critical field derived from heat capacity measurements ($\mu_0 H_{c2}$) and ρ measurements ($\mu_0 H_{c2}^{\text{res}}$) persist. Superconductivity as a bulk property in the specific heat measurements is suppressed at 380 mT, whereas the electrical resistivity data exhibit signs of superconductivity even at 2 T.

CeIrSi is a magnetic material influenced by the cubical symmetric CEF with a doublet ground state Γ_7 and AFM below 1.2 K. The excited state is a quartet state which is expected to be at significant higher temperature, as the entropy due to the magnetic ground state appears to stagnate at $R \ln 2$ and then increases smoothly without reaching the full entropy level of $R \ln 6$ at 80 K. The effective magnetic moment was derived from the CW law as $\mu_{\text{eff}} = 2.63 \mu_B$ which is slightly enhanced over the respective value of a Ce^{3+} ion. The magnetic moment of the ground state was calculated as $0.71 \mu_B$, which is also slightly below the value obtained from experiment. Both of these effects might be explained by the Ir $5d$ -contribution. Further features, like an initial magnetization and a ferromagnetic transition at around 11 K might be explained in terms of a $\text{CeSi}_{1.7}$ foreign phase.

Bulk properties of $\text{RE}_3\text{Pd}_4\text{Si}_4$ with $\text{RE} = \text{La}$ and Ce both with the $\text{U}_3\text{Ni}_4\text{Si}_4$ -type structure

were investigated by means of resistivity, specific heat and magnetic susceptibility measurements. Nonmagnetic $\text{La}_3\text{Pd}_4\text{Si}_4$ is characterized by superconductivity below about 2 K. Disagreement from a simple, fully gapped s -wave BCS superconductor are obvious from different physical measurements. First, the deviations of the temperature dependent specific heat, from the positive curvature of the upper critical field $\mu_0 H_{c2}$. Second, the smaller jump height of the specific heat although the superconducting phase makes up at least 98 % of the bulk volume. Third, the strong broadening of the transition width electrical resistivity measurements while exposed to external magnetic fields. A two band and two gap model developed by Padamsee, reasonably well describes the heat capacity data in the superconducting state if $\alpha_1 = \frac{2\Delta_1(0)}{k_B T_c} = 1.95$ and $\alpha_2 = \frac{2\Delta_2(0)}{k_B T_c} = 1.1$.

The isostructural Ce-based compound behaves as a Kondo lattice, exhibiting a pronounced maximum in the temperature dependent electrical resistivity as well as an extended logarithmic temperature range as a result of the Kondo effect in presence of crystalline electric field effects. At low temperatures, distinct deviations from a Fermi liquid ground state are evident in both resistivity and heat capacity data, provoked from the proximity of a phase transition at $T = 0$.

Appendices

Appendix A

Programs and drafts

This chapter deals with the programs developed and the drafts for the FRITZ measurement setup. The programs were either written in C++ or Mathematica. At first, the C++ program for calculating the specific heat capacity C_p from the raw data of the PPMS data file is discussed. The program has two distinct folders, input and output. The user has to put the raw data in the input folder, execute the program and insert the mass of the sample (in μmol) and the mass of the N grease in μg . The program does not distinguish between different magnetic fields. For measurements in high magnetic fields and to higher temperatures, the program should be adapted and extended.

Second, the Mathematica tool for analyzing the heat capacity data is provided. It can be used for superconductors but also for magnetic transitions with minor amends. Before the program can be used, the data files must be analyzed by a spline functions. The program needs the ZF data and the data where superconductivity is completely suppressed to calculate the respective entropy. It further calculates the κ value as well as the GL coherence length ξ_{GL} and the London penetration depth λ_L .

Third, the Mathematica program for simulating the influence of percolation theory is sketched. By changing the parameter FProb, one can adjust the density of the percolation areas and see the influence on the electrical conductivity.

Fourth, the drafts of the FRITZ sample holder are provided.

Listing A.1: C++ Code Addenda Berechnung

```
#include <stdio.h>
#include <stdlib.h>
#include <string>
#include <string.h>
#include <vector>
#include <iostream>
```

```
#include <fstream>
#include <sstream>
#include <tchar.h>
#include <windows.h>

using namespace std;

int matrizenlesen(ifstream &name, string dateiname, long double **matrix)
{
    matrix = new long double*[1000];
};

int apiezon (ifstream &name, string dateiname, long double **matrix, float mass);

long double interpol (int k, long double temperatur, long double value, long double **traeger);

int main (/*int y, char **argument*/)
{
    int j, k, l, m, durchlaeufe;
    float masse, mol;
    bool Filescount = true;
    k=0;
    l=0;
    m=0;
    durchlaeufe=0;

    masse = 0;
    mol = 0;

    string traeger_name = "addenda";
    string total_name;
    string sample_name;

    ifstream traeger, total;
    fstream sample;

    WIN32_FIND_DATA FindFileData;
    HANDLE hFind;
    TCHAR *FileScan;
    FileScan = (TCHAR *) ".\\Input\\*.*";

    long double **fl_matrix_traeger=new long double*[1000];
```

```
long double **fl_matrix_total=new long double*[1000];
long double **fl_matrix_sample=new long double*[1000];

for( j=0; j<1000; j++)
{
    fl_matrix_traeger[j] = new long double[2];
    fl_matrix_total[j] = new long double[2];
    fl_matrix_sample[j] = new long double[2];
}

while (masse==0 || masse>1000)
{
    printf ("Enter the amount of apiezon in %cg:\n",230);
    scanf ("%f",&masse);
    if (masse<=0 || masse>1000)
    {
        printf ("Mass must be greater than 0 %cg and less than 1000 %cg↵
                ", 230, 230);
    }
}

while (mol==0 || mol>1000)
{
    printf ("Enter the mol in %cmol:\n",230);
    scanf ("%f",&mol);
    if (mol<=0)
    {
        printf ("Mol must be greater than 0 %cmol", 230);
    }
}

hFind = FindFirstFile(FileScan , &FindFileData);
Filescount = FindNextFile(hFind , &FindFileData);
k=apiezon(traeger , traeger_name , fl_matrix_traeger , masse);

while (hFind != INVALID_HANDLE_VALUE && Filescount == true)
{
    Filescount = FindNextFile(hFind , &FindFileData);
    total_name = "./Input/";
    total_name += FindFileData.cFileName;
    sample_name = "./Output/";
    sample_name += FindFileData.cFileName;
    sample_name += "_result.dat";
    l=matrizenlesen(total , total_name , fl_matrix_total);
```



```

{
    size_t scansize=0;
    while (zeilentext.find ( ",", scansize+1, 1 )<zeilentext.length←
        ())
    {
        scansize=zeilentext.find ( ",", scansize+1, 1 );
        zeilentext.replace ( scansize, 1, "␣" );
    }
    istringstream istr(zeilentext);
    if (istr >> fl_matrix_total_raw[i][0] >> fl_matrix_total_raw[i]←
        ][1] >> fl_matrix_total_raw[i][2] >> fl_matrix_total_raw[i]←
        ][3] >> fl_matrix_total_raw[i][4] >> fl_matrix_total_raw[i]←
        ][5] >> fl_matrix_total_raw[i][6] >> fl_matrix_total_raw[i]←
        ][7] >> fl_matrix_total_raw[i][8] >> fl_matrix_total_raw[i]←
        ][9] >> fl_matrix_total_raw[i][10] >> fl_matrix_total_raw[i]←
        ][11] >> fl_matrix_total_raw[i][12])
    {
        matrix[i][0] = fl_matrix_total_raw[i][6];
        matrix[i][1] = fl_matrix_total_raw[i][12];
    } else
    {
    }
    i++;
}
}
else
{
    cout << "Datei␣" << dateiname << "␣nicht␣im␣Verzeichnis␣gefunden"←
        ;
    return 0;
}
return i;
}

long double interpol (int k, long double temperatur, long double ←
    value, long double **traeger)
{
    int i=0;
    long double steig=0, ergeb=0;
    for (i=0; i<k-1; i++)
    {
        if (temperatur>traeger[i][0] && temperatur<traeger[i+1][0])
        {
            steig=(traeger[i+1][1]-traeger[i][1])/(traeger[i+1][0]-traeger[i]←

```

```

        i][0]);
    ergeb=-traeger[i][0]*steig+traeger[i][1]+steig*temperatur;
    ergeb=value-ergeb;
    return ergeb;
}
}
return 0;
}

int apiezon (ifstream &name, string dateiname, long double **matrix, ←
    float mass)
{
    int i=0;
    int j=0;
    long double **fl_matrix_traeger_raw=new long double*[1000];
    float **fl_matrix_traeger_raw_2=new float*[1000];
    for( j=0; j<1000; j++)
    {
        fl_matrix_traeger_raw[j] = new long double[3];
        fl_matrix_traeger_raw_2[j] = new float[3];
    }
    name.open(dateiname.c_str());
    if (name)
    {
        string zeilentext;
        while (getline(name, zeilentext))
        {
            istringstream istr(zeilentext);
            istr >> fl_matrix_traeger_raw_2[i][0] >> ←
                fl_matrix_traeger_raw_2[i][1] >> fl_matrix_traeger_raw_2[i]←
                ][2];
            if (istr >> fl_matrix_traeger_raw[i][0] >> ←
                fl_matrix_traeger_raw[i][1] >> fl_matrix_traeger_raw[i][2])
            {

            } else
            {
            }

            printf ("Temperatur: %Lf; Traeger: %Lf\n", ←
                fl_matrix_traeger_raw[i][0], fl_matrix_traeger_raw[i][2]);
            printf ("<-->Temperatur: %f; Traeger: %f\n\n", ←
                fl_matrix_traeger_raw_2[i][0], fl_matrix_traeger_raw_2[i]←
                ][2]);

```

```
matrix[i][0] = fl_matrix_traeger_raw[i][0];
matrix[i][1] = fl_matrix_traeger_raw[i][1]+↵
    fl_matrix_traeger_raw[i][2]*mass;
    i++;
}
}
else
{
    cout << "Datei_" << dateiname << "_nicht_im_Verzeichnis_gefunden"↵
        ;
    return 0;
}
return i;
}
```

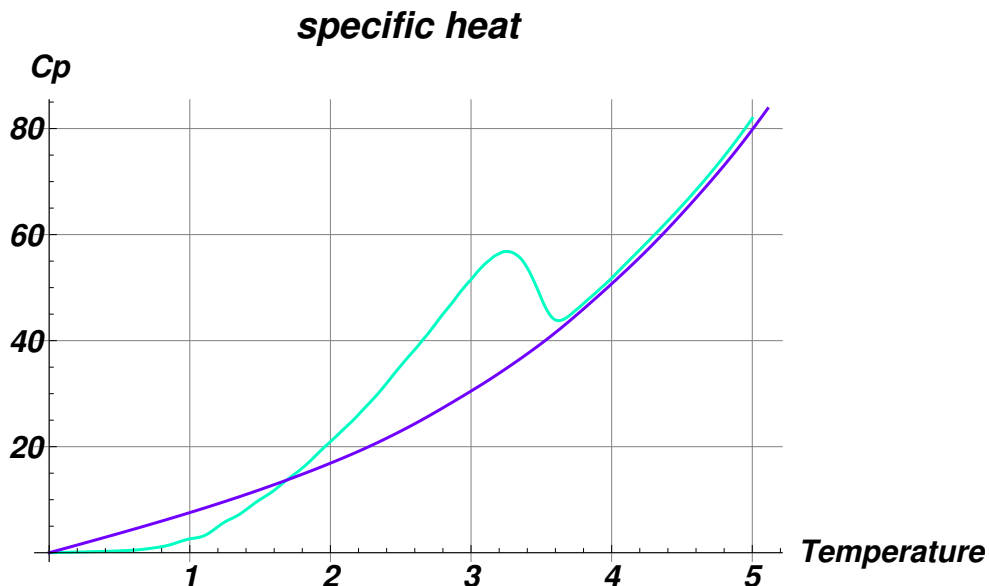


```
"Splines must be of equal distance and borders";
messungNC = OpenRead[
  "c:\\Users\\Friedrich\\Dropbox\\Diss\\Dissertation\\Proben\\
  Auflistung\\LaPtSi\\LaPtSiCp_0T5_spline.prn"];
messungSC = OpenRead[
  "C:\\Users\\Friedrich\\Dropbox\\Diss\\Dissertation\\Proben\\
  Auflistung\\LaPtSi\\LaPtSiCp_0T_spline.prn"];
```

```
title = Read[messungSC, String]; subtitle = Read[messungSC, String];
cp = ReadList[messungSC, {Number, Number}];
```

```
title = Read[messungSC, String]; subtitle = Read[messungSC, String];
cpNC = ReadList[messungNC, {Number, Number}];
```

```
bild = ListPlot[{cp, cpNC}, Joined → True,
  AxesOrigin → {0, 0}, AxesLabel → {"Temperature", "Cp"},
  PlotLabel → "specific heat", GridLines → Automatic,
  Background → GrayLevel[1],
  PlotStyle → {{Hue[0.46], PointSize[0.005],
    Thickness[0.004]}, {Hue[0.74], PointSize[0.005],
    Thickness[0.004]}}},
  BaseStyle → {FontSlant → "Italic", FontSize → 16,
  FontFamily → "Trebuchet", FontWeight → "Bold"}]
```



```
total = Length[cp] (*calculates the number of x,  
  y value of the file, returning "total"*);  
n = 1; (*start value of temperature t*)  
m = 2000; (*endvalue of temperature t*)  
in = 2; (*incremental value delta_t*)  
endtemp = 20;  
Samplevolume = 1.54 * 10 ^ (-3);  
SprungT = 3.4;  
Hc2 = 4000;  
(*in Gauss*)  
GammaSommerfeld = 7.2;  
(*in mJ/mole K^2*)  
BetaSommerfeld = 0.4;  
(*in mJ/mole K^4*)
```

```

MS = OpenRead[
  "c:\\Users\\Friedrich\\Dropbox\\Diss\\Dissertation\\Tools\\Muehlschlegel\\
  Muehlschlegel1959_new.TXT"];
MSval = ReadList[MS, {Number, Number}];
Muehlschlegel = Table[0, {Length[MSval] - 1}, {2}];

For [ii = 1, ii < Length[MSval] - 1, ii++,
  Muehlschlegel[[ii, 1]] = MSval[[ii, 1]] * SprungT;
  Muehlschlegel[[ii, 2]] = MSval[[ii, 2]] * GammaSommerfeld / MSval[[ii, 1]] +
  BetaSommerfeld * Muehlschlegel[[ii, 1]]^2];

TableForm[Muehlschlegel];

Muehlschlegelout = OpenWrite[
  "c:\\Users\\Friedrich\\Dropbox\\Diss\\Dissertation\\Proben\\Auflistung\\
  Muehlschlegel_LaPtSi_cp_new.dat", FormatType -> OutputForm];
Write[Muehlschlegelout, TableForm[Muehlschlegel]];
Close[Muehlschlegelout];

"Calculation of the area A below Cp"
Sum[(cp[[i, 2]] + cp[[i + 1, 2]]) / (cp[[i + 1, 1]] + cp[[i, 1]]) *
  (cp[[i + 1, 1]] - cp[[i, 1]]), {i, 2, total - 3}];

entropyf = Table[{(cp[[i, 1]] + cp[[i + 1, 1]]) / 2,
  Sum[(cp[[k, 2]] + cp[[k + 1, 2]]) / (cp[[k + 1, 1]] + cp[[k, 1]]) *
  Abs[(cp[[k + 1, 1]] - cp[[k, 1]])], {k, 1, i}}, {i, 1, total - 1}];
entropyNC = Table[{(cpNC[[i, 1]] + cpNC[[i + 1, 1]]) / 2,
  Sum[(cpNC[[k, 2]] + cpNC[[k + 1, 2]]) / (cpNC[[k + 1, 1]] + cpNC[[k, 1]]) *
  Abs[(cpNC[[k + 1, 1]] - cpNC[[k, 1]])], {k, 1, i}}, {i, 1, total - 1}];

deltaentropy =
  Table[{(entropyf[[i, 1]]), (entropyNC[[i, 2]] - entropyf[[i, 2]])}, {i, 1, total - 1}];
index = 1;
While [deltaentropy[[index, 1]] < SprungT, index++];
"Thermodynamical critical field in Gauss:"
Hctherm = Sqrt[2 * Sum[Abs[(deltaentropy[[k, 2]] + deltaentropy[[k + 1, 2]])] / 2 *
  Abs[(deltaentropy[[k + 1, 1]] - deltaentropy[[k, 1]])], {k, 1, index}] /
  (4 * Pi * Samplevolume)] * 4 * Pi

"Kappa Ginzburg Landau Parameter:"
Kappa = 1 / Sqrt[2] * Hc2 / Hctherm

```

Calculation of the area A below Cp

Thermodynamical critical field in Gauss:

526.402

Kappa Ginzburg Landau Parameter:

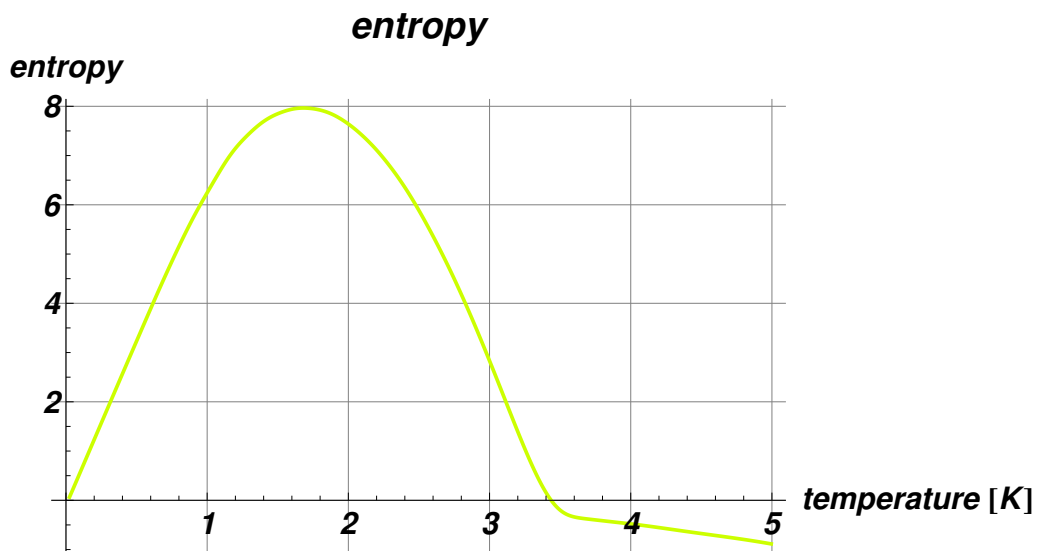
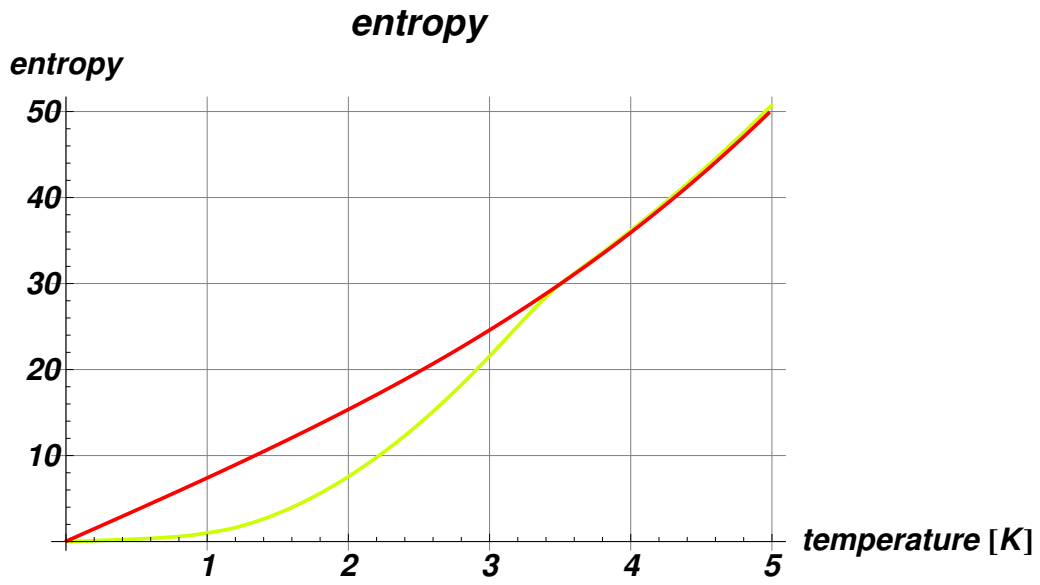
5.37313

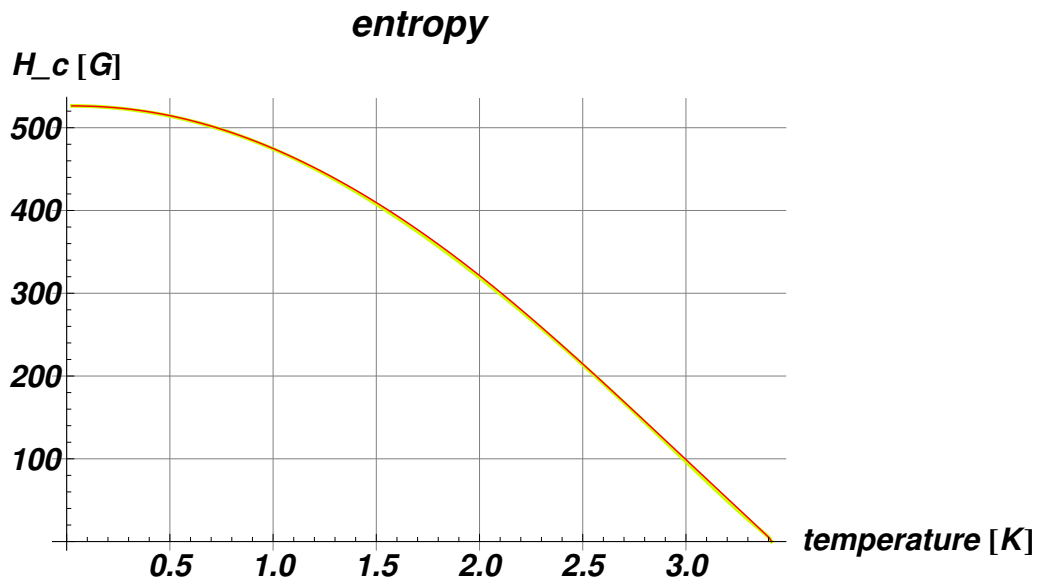
```

hfeld = Table[{(deltaentropy[[index + 1 - i, 1]]),
  Sqrt[2 * Sum[(deltaentropy[[k, 2]] + deltaentropy[[k + 1, 2]]) / 2 *
    Abs[(deltaentropy[[k + 1, 1]] - deltaentropy[[k, 1]])], {k, index -
    i + 1, index}] / (4 * Pi * Samplevolume)] * 4 * Pi}, {i, 0, index}];
hfeldold = Table[{(deltaentropy[[index + 1 - i, 1]]),
  Sqrt[2 * Sum[(deltaentropy[[k, 2]] + deltaentropy[[k + 1, 2]]) / 2 *
    Abs[(deltaentropy[[k + 1, 1]] - deltaentropy[[k, 1]])], {k, 1, i}] /
    (4 * Pi * Samplevolume)] * 4 * Pi}, {i, 0, index}];
ergebnisHctherm = OpenWrite[
  "c:\\Users\\Friedrich\\Dropbox\\Diss\\Dissertation\\Proben\\Auflistung\\LaPtSi\\
  LaPtSi3_Hctherm_cp.dat", FormatType -> OutputForm];
Write[ergebnisHctherm,
  TableForm[N[Table[{hfeld[[i, 2]], hfeld[[i, 1]]}, {i, 1, index}]]]];
Close[ergebnisHctherm];

ListPlot[{entropyf, entropyNC},
  AxesLabel -> {"temperature [K]", "entropy"},
  AxesOrigin -> {0, 0}, Joined -> True, PlotLabel -> "entropy",
  GridLines -> Automatic, Background -> GrayLevel[1],
  PlotStyle -> {{Hue[1.2], Thickness[0.005]}, {Hue[1.0], Thickness[0.005]}},
  BaseStyle -> {FontSlant -> "Italic", FontSize -> 16,
  FontFamily -> "Trebuchet", FontWeight -> "Bold"}]
ListPlot[{deltaentropy}, AxesLabel -> {"temperature [K]", "entropy"},
  AxesOrigin -> {0, 0}, Joined -> True, PlotLabel -> "entropy",
  GridLines -> Automatic, Background -> GrayLevel[1],
  PlotStyle -> {{Hue[1.2], Thickness[0.005]}, {Hue[1.0], Thickness[0.005]}},
  BaseStyle -> {FontSlant -> "Italic", FontSize -> 16,
  FontFamily -> "Trebuchet", FontWeight -> "Bold"}]
ListPlot[{hfeld, hfeldold}, AxesLabel -> {"temperature [K]", "H_c [G]"},
  AxesOrigin -> {0, 0}, Joined -> True, PlotLabel -> "entropy",
  GridLines -> Automatic, Background -> GrayLevel[1],
  PlotStyle -> {{Hue[1.2], Thickness[0.005]}, {Hue[1.0], Thickness[0.002]}},
  BaseStyle -> {FontSlant -> "Italic", FontSize -> 16,
  FontFamily -> "Trebuchet", FontWeight -> "Bold"}]
Close[messungSC];
Close[messungNC];

```





```

FeG = 50;
FProb = 5;
Peend = Table[{0, 0}, {i, FeG}, {j, FeG}];
Peborder = Table[{0, 0}, {i, FeG}, {j, FeG}];
MatrixForm[%];
Pebase = Table[{i, j, RandomInteger[{1, 100}]}, {i, FeG}, {j, FeG}];
MatrixForm[%];
For [ii = 1, ii < FeG + 1, ii++, For [jj = 1, jj < FeG + 1, jj++,
  If [Pebase [ii, jj, 3] < (FProb + 1),
    Peend [ii, jj, 1] = ii; Peend [ii, jj, 2] = jj,]]]
For [ii = 2, ii < FeG, ii++, For [jj = 2, jj < FeG, jj++,
  If [(Peend [ii + 1, jj - 1, 1] ≠ 0 || Peend [ii + 1, jj, 1] ≠ 0 ||
    Peend [ii + 1, jj + 1, 1] ≠ 0) && Peend [ii, jj, 1] ≠ 0,
    Peborder [ii, jj, 1] = ii; Peborder [ii, jj, 2] = jj,]]]
p1 = ListPlot [Peend, PlotStyle → RGBColor [0.6, 0.6, 1],
  ImageSize → {500, 500}, AspectRatio → 1, PlotMarkers -> {■, 899 / FeG},
  PlotRange → {{0, FeG + 5 / FeG}, {0, FeG + 5 / FeG}}]
p2 = ListPlot [Peborder, PlotStyle → Directive [Blue],
  ImageSize → {500, 500}, AspectRatio → 1, PlotMarkers -> {■, 899 / FeG},
  PlotRange → {{0, FeG + 5 / FeG}, {0, FeG + 5 / FeG}}]
Show [
  p1,
  p2]

```

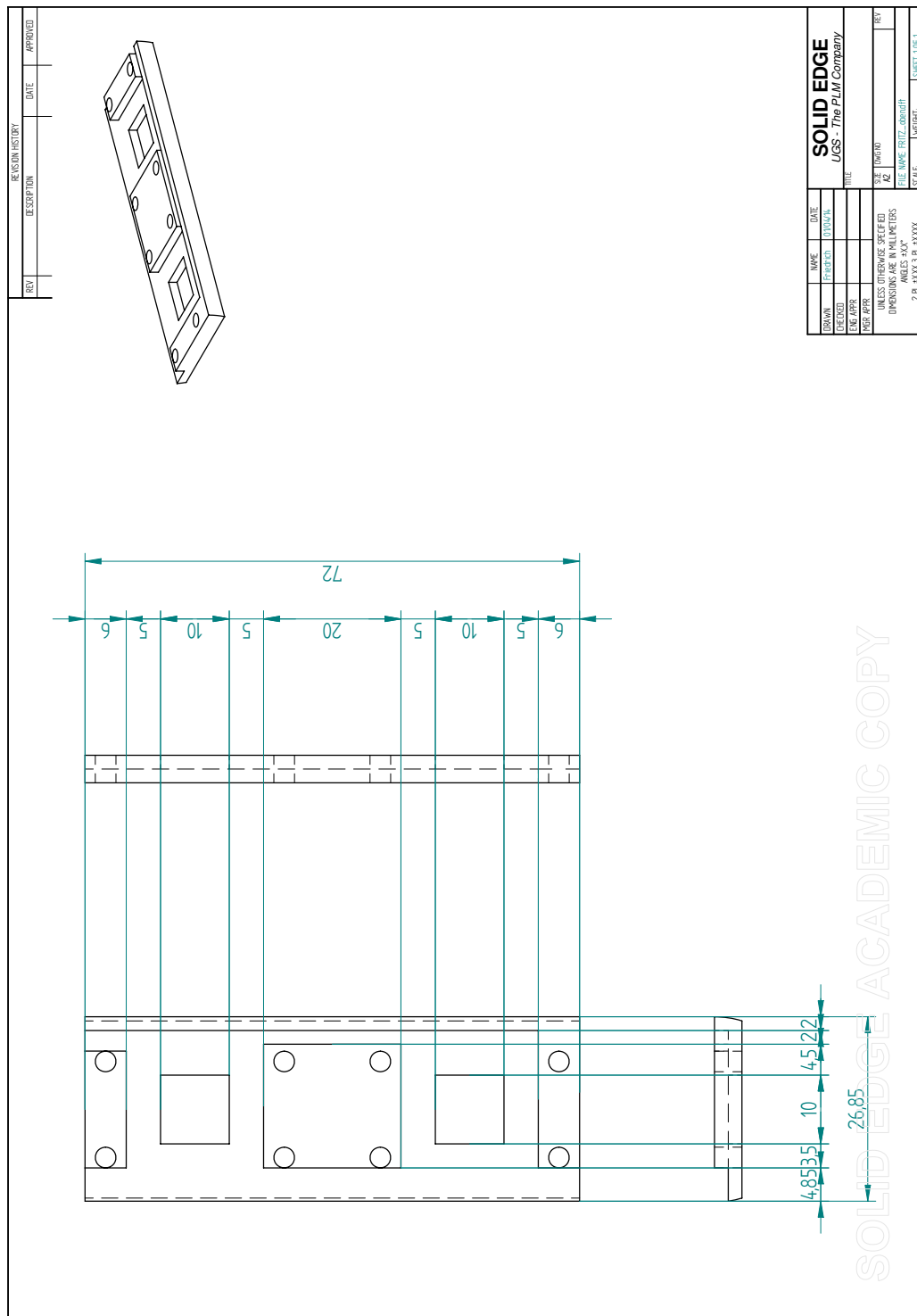
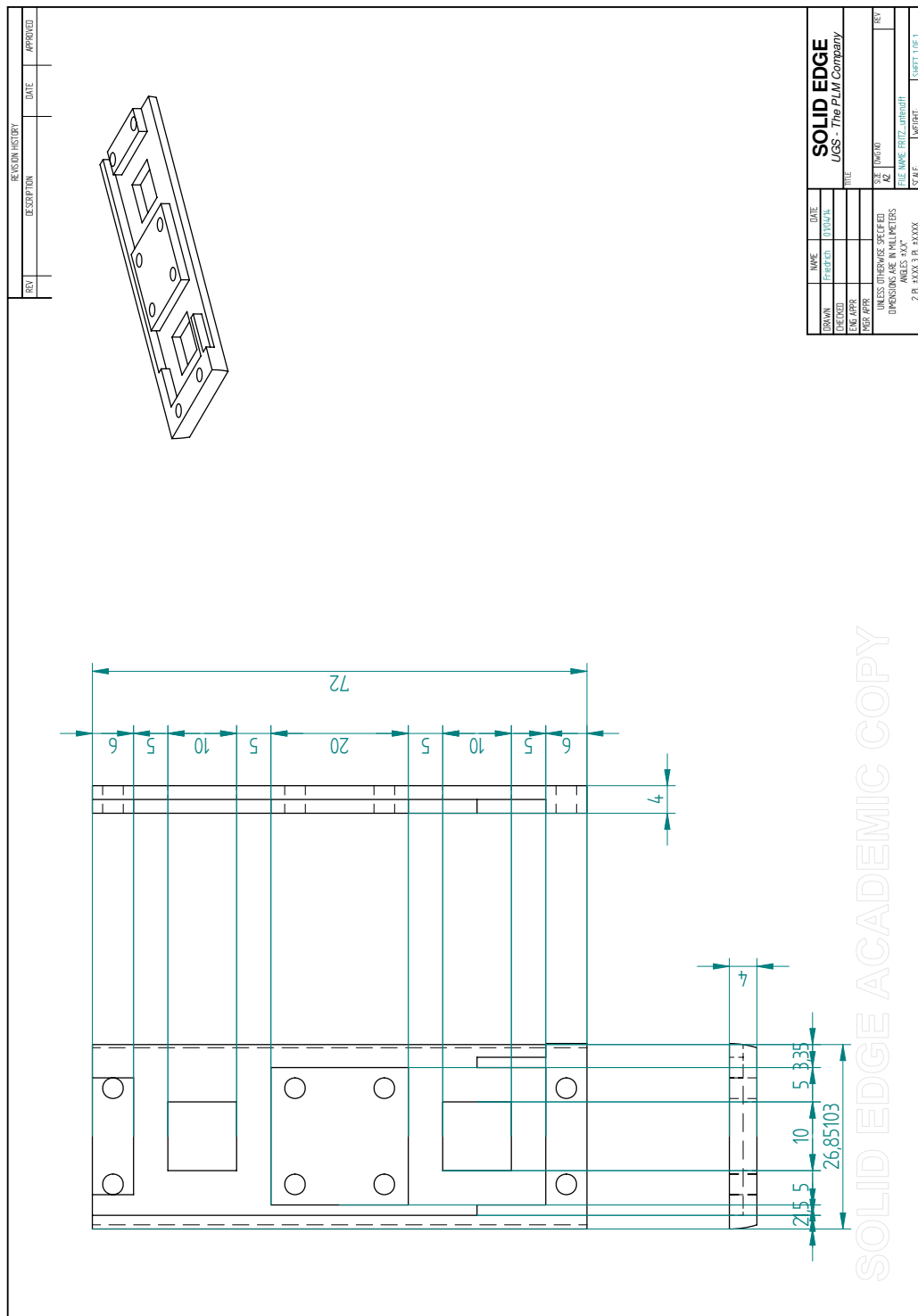


Figure A.1: Drafts of the FRITZ sample holder (Top view).



REVISION HISTORY		
REV	DESCRIPTION	DATE

APPROVED

NAME	DATE	TITLE
DESIGN		
ENGINEER		
ENG APPR		
MGR APPR		
UNLESS OTHERWISE SPECIFIED DIMENSIONS ARE IN MILLIMETERS ANGLES IN DEG		
FILE NAME	FRITZ_solidedge	
SCALE		
WEIGHT		
SHEET 01 OF 1		

SOLID EDGE
UGS - The PLM Company

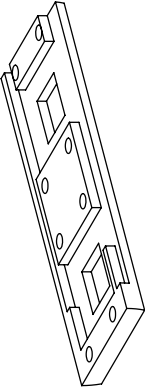


Figure A.2: Drafts of the FRITZ sample holder (Bottom view).

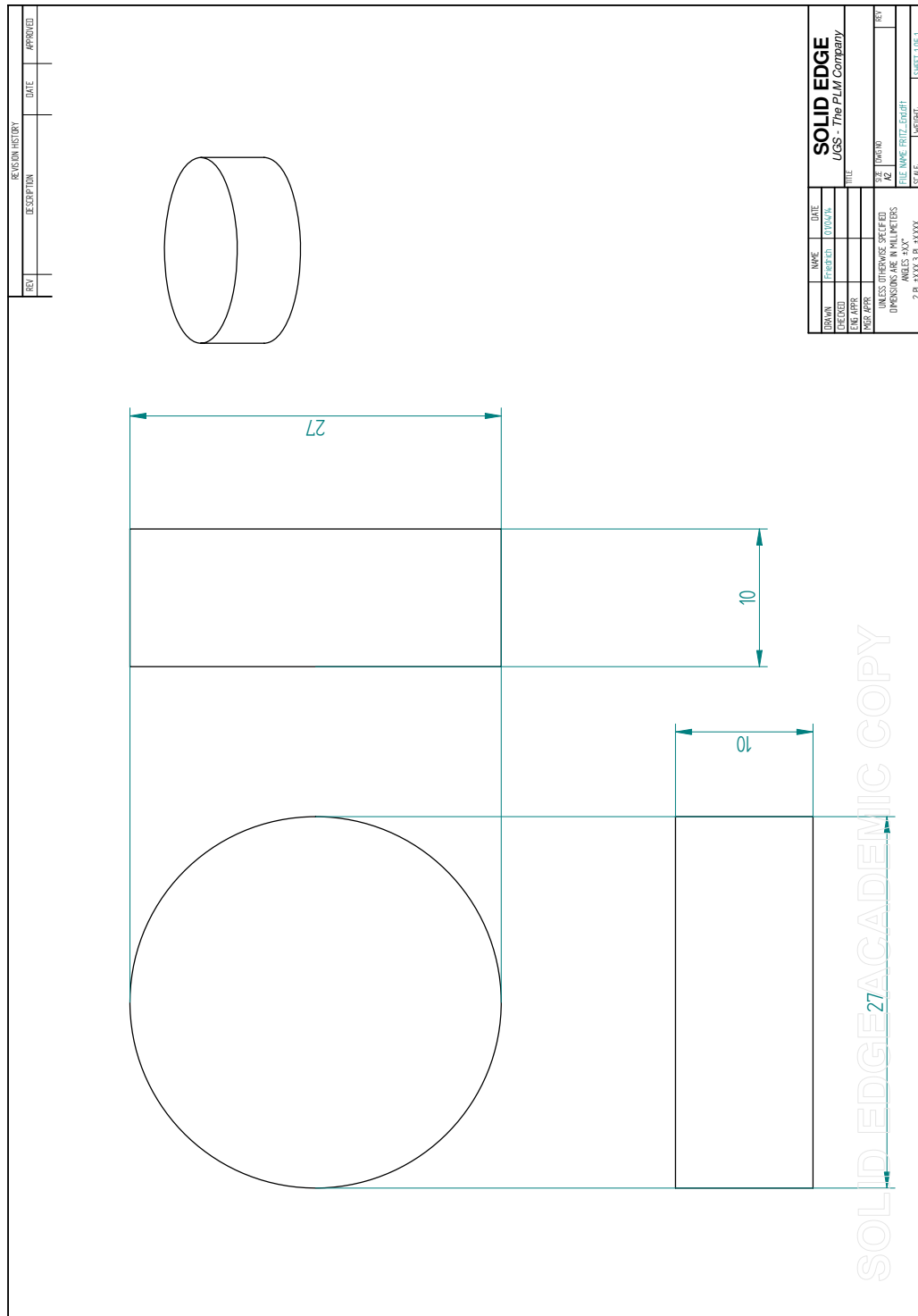


Figure A.3: Drafts of the FRITZ sample holder (Lower part).

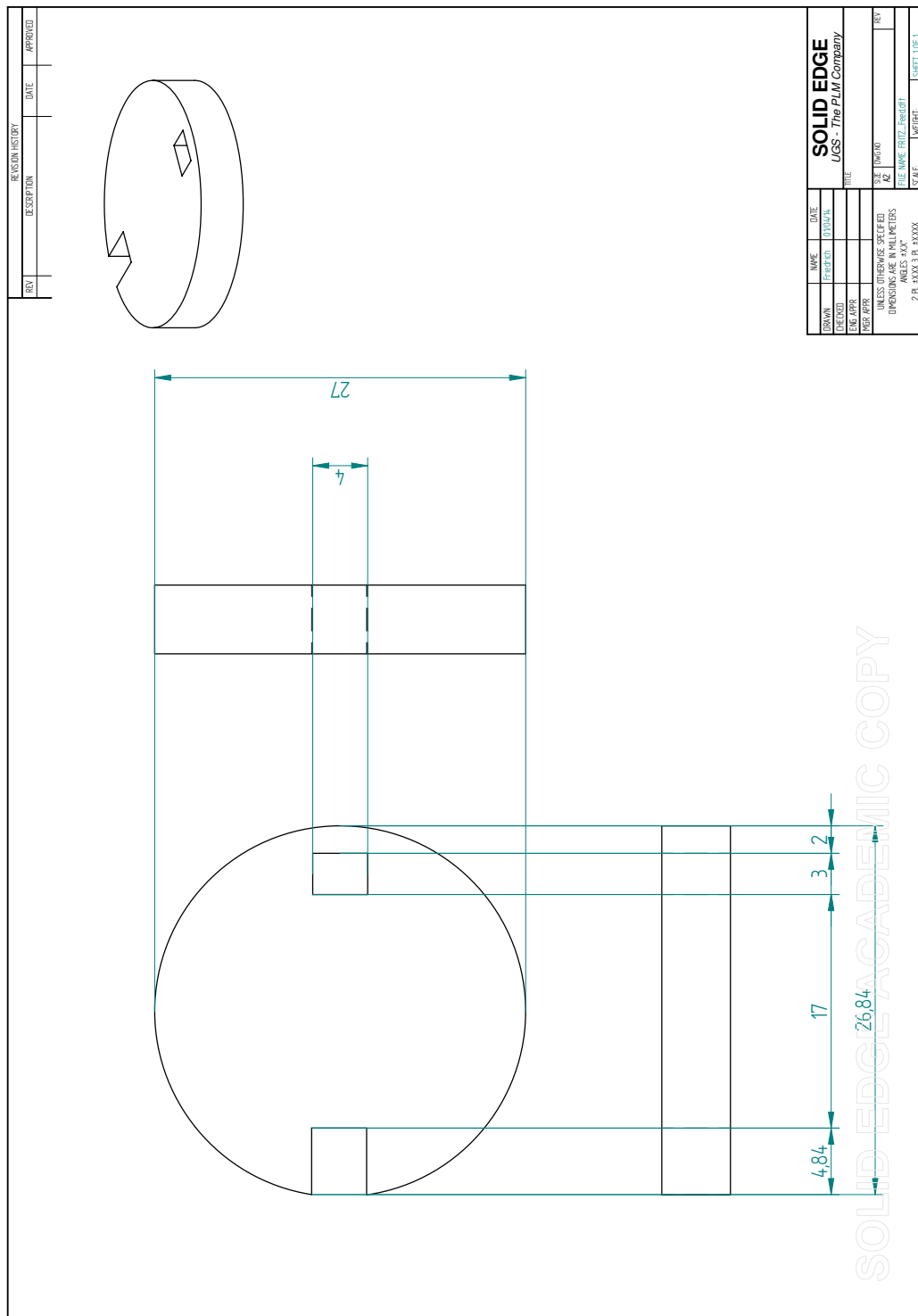


Figure A.4: Drafts of the FRITZ sample holder (Feed through).

Appendix B

1-1-3 tables

Tables in this appendix provide a detailed listing of the BaAl_4 derivative structures like the 1-2-2 (see Tab. B) and the 1-1-3 (see Tab. B), regarding their structural properties. Theoretical band structure calculations were performed for the class of the NCS with the BaNiSn_3 -type crystal structure (see Tab. B). This allows a comparison of theoretical and experimental results. The impact of ASOC on the NCS SC was theoretically calculated and depicted in Tab. B.5.

Table B.1: X-Ray single crystal data for $\text{SrAu}_{1.6}\text{Ge}_{2.4}$ at RT, standardized with program Structure Tidy (MoK α -radiation; $2^\circ \leq 2\theta \leq 70^\circ$; ω -scans, scan width 2° ; 150 sec/frame; Anisotropic displacement parameters in [102nm^2])

Parameter/compound	
Space Group	P4/nmm
Composition from EPMA	SrAu _{1.5} Ge _{2.5}
Formula from refinement	SrAu _{1.6} Ge _{2.4}
a, c [nm]	0.44796(2), 1.06315(5)
μ_{abs} [mm^{-1}]	94.65
V (nm^3)	0.2133
ρ_x (gcm^{-3})	9.76
Reflections in refinement	$274^3 4s(\text{Fo})$ of 324
Number of variables	21
$R_F = \sum F_0 - F_c / \sum F_0$	0.028
R_{Int}	0.059
wR2	0.084
GOF	1.207
Extinction (Zachariasen)	0.0015(1)
Residual density e-/ \AA^3 ; max; min	2.07; -2.98
Atom parameters	
Sr1 in $2c(1/4,1/4,z)$; occ.	1.04(2)

z		0.74895(9)			
$U_1 1= U_2 2; U_3 3$		0.0128(4); 0.0168(6)			
M1 in $2c(1/4, 1/4, z)$; occ.		0.709(7) Au + 0.291 Ge			
z		0.13122(5)			
$U_1 1= U_2 2; U_3 3$		0.0151(2); 0.0169(3)			
M2 in $2c(1/4, 1/4, z)$; occ.		0.252(5) Au + 0.748 Ge			
z		0.36823(8)			
$U_1 1= U_2 2; U_3 3$		0.0142(4); 0.0157(5)			
M3 in $2b(3/4, 1/4, 1/2)$; occ.		0.49(1) Au + 0.51 Ge			
$U_1 1= U_2 2; U_3 3$		0.0174(3); 0.0171(3)			
M4 in $2a(3/4, 1/4, 0)$; occ.		0.103(9) Au + 0.897 Ge			
$U_1 1= U_2 2; U_3 3$		0.0160(5); 0.0153(6)			
Interatomic distances [nm] with standard deviation ≤ 0.0001					
Sr1 -	4M2	0.3404		-4M3	0.2642
	-4M1	0.3414		-4Sr1	0.3404
	-4M3	0.3467	M3 -	4M2	0.2642
	-4M4	0.3484		-4M3	0.3168
M1 -	1M2	0.252		-4Sr1	0.3467
	-4M4	0.2639	M4 -	-4M1	0.2639
	-4Sr1	0.3414		-4M4	0.3168
M2 -	1M1	0.252		-4Sr1	0.3484

Table B.2: Crystallographic data of all $EpTX_3$ compounds ($Ep = Sr, Ba$; $T = Ni, Pd, Pt, Cu, Ag, Au$; $X = Si, Ge, Sn$; $BaNiSn_3$ type; Space group $I4mm$; Ep in $2a(0,0,z)$, T in $2a(0,0,z)$, X in $2a(0,0,z)$, X in $4b(0, 0.5, z)$ Part I

Comp.	Lattice Param. (nm)	Ep in $2a; z$	T in $2a; z$	X in $2a; z$	X in $4b; z$	Method	Ref.
$BaNiSi_3$	-					XPD	*
$BaNiGe_3$	-					XPD	*
$BaNiSn_3$	$a = 0.482(1)$ $c = 1.093(2)$	0.5759	0.2313	0	0.3253	XSCD	[90]
$SrNiSi_3$	$a = 0.41958(3)$ $c = 0.97915(7)$	0.5984	0.2413	0	0.353	XPD	[95]
	$a = 0.4193(1)$ $c = 0.9791(3)$	0.596	0.242	0	0.352	XPD	*
$SrNiGe_3$	$a = 0.44677(4)$ $c = 1.0286(1)$	0.59	0.241	0	0.34	XPD	*
$SrNiSn_3$	$a = 0.474(1)$ $c = 1.088(2)$	0.571	0.23	0	0.321	XSCD	[90]
	$a = 0.4717(3)$ $c = 1.0966(2)$	0.544	0.23	0	0.302	XPD	*
$BaPdSi_3$	$a = 0.43963(3)$ $c = 1.0186(2)$	0.6156	0.2607	0	0.3702	XPD	[95]
$BaPdGe_3$	$a = 0.45508(2)$	0.6048	0.2499	0	0.3568	XSCD	[95]

	c = 1.0365(1)						
BaPdSn ₃	a = 0.487(1) c = 1.117(2)	0.587	0.236	0	0.337	XSCD	[153]
	a = 0.48789(2) c = 1.1174(2)	0.5901	0.2391	0	0.3385	XPD	*
SrPdSi ₃	a = 0.4296(3) c = 1.0029(3)	0.6072	0.2477	0	0.3667	XPD	*
SrPdGe ₃	a = 0.44623(2) c = 1.02737(7)	0.6006	0.2425	0	0.3538	XSCD	[91]
	a = 0.44677(4) c = 1.0286(1)	0.6	0.2419	0	0.355	XPD	*
SrPdSn ₃	a = 0.479(1) c = 1.123(2)	0.591	0.233	0	0.336	XSCD	[153]
	a = 0.47928(7) c = 1.1252(2)	0.585	0.227	0	0.333	XPD	*
SrPtSi ₃	a = 0.43132(3) c = 0.98893(9)	0.605	0.25	0	0.365	XPD	*
SrPtGe ₃	a = 0.4478(2) c = 1.01366(9)	0.5988	0.2436	0	0.3558	XSCD	[91]
	a = 0.44859(3) c = 1.01364(8)	0.6	0.245	0	0.357	XPD	*
SrPtSn ₃	-					XPD	*
BaPtSi ₃	a = 0.44094(2) c = 1.0013(2)	0.6022	0.2502	0	0.3608	XPD	[94]
	a = 0.44079(2) c = 1.0017(2)	0.5991	0.2477	0	0.356	XSCD	[95]
BaPtGe ₃	a = 0.45636(2) c = 1.02341(6)	0.6065	0.2475	0	0.3533	XSCD	[97]
	a = 0.45636(2) c = 1.02341(6)	0.5999	0.2469	0	0.3532	XSCD	[95]
BaPtSn ₃	a = 0.485(1) c = 1.107(2)	0.5778	0.2313	0	0.3253	XSCD	[90]
BaCuSi ₃	-					XPD	[154]
BaCuGe ₃	-					XPD	[155]
BaCuSn ₃	-					XPD	*
SrCuSi ₃	-					XPD	*
SrCuGe ₃	-					XPD	*
SrCuSn ₃	-					XPD	*
BaAgSi ₃	-					XPD	[156]
BaAgGe ₃	-					XPD	[107]
BaAgSn ₃	-					XPD	*
SrAgSi ₃	-					XPD	*
SrAgGe ₃	-					XPD	*
SrAgSn ₃	-					XPD	*
BaAuSi ₃	-					XPD	[156]
BaAu _{1.1} Ge _{2.9}	a = 0.4615(2) c = 1.0492(5)	0.6312	0.2512	0	0.387	XPD	[98]

SrAuSi ₃	-					XPD	*
SrAuGe ₃	-					XSCD	*
SrAuSn ₃	-					XSCD	[99]

Table B.3: EpT_xX_{4-x} phases in the ternary systems Ep-T-X (Ep = Sr, Ba; T = Ni, Pd, Pt, Cu, Ag, Au; X = Si, Ge, Sn) with a BaAl₄ derivative structure type

Compound	Lattice Parameter (nm)	Space group	Structure type	Method	Ref.
BaNi ₂ Si ₂	a = 0.650(1) b = 0.535(1) c = 1.133(2)	<i>Cmcm</i>	BaNi ₂ Si ₂	XSCD	[114]
HT-BaNi ₂ Ge ₂	a = 0.42665(1) c = 1.12545(3)	<i>I4/mmm</i>	ThCr ₂ Si ₂	XPD	[111]
LT-BaNi ₂ Ge ₂	a = 0.84693(4) b = 1.13503(5) c = 0.43212(2)	<i>Pnma</i>	BaNi ₂ Ge ₂	XSCD	[111]
SrNi ₂ Ge ₂	a = 0.417(1) c = 1.025(2)	<i>I4/mmm</i>	ThCr ₂ Si ₂	XSCD	[157]
SrPd ₂ Si ₂	a = 0.4310 c = 0.9876	<i>I4/mmm</i>	ThCr ₂ Si ₂	XPD	[158]
SrPd ₂ Ge ₂	a = 0.44088(2) c = 1.01270(8)	<i>I4/mmm</i>	ThCr ₂ Si ₂	XSCD	[159]
SrPt ₂ Si ₂	a = 0.427 c = 0.9895	<i>I4/mmm</i>	ThCr ₂ Si ₂	XPD	[160]
	a = 0.42914(7) c = 0.9904(2)	<i>P4/nmm</i>	CaBe ₂ Ge ₂	XSCD	[161]
SrCu ₂ Si ₂	a = 0.42 c = 1.0	<i>I4/mmm</i>	ThCr ₂ Si ₂	XSCD	[162]
SrCu _{1.7} Si _{2.3}	a = 0.41881(5) c = 1.00267(8)	<i>I4/mmm</i>	ThCr ₂ Si ₂	XPD	[95]
SrCu ₂ Ge ₂	a = 0.428(1) c = 1.031(2)	<i>I4/mmm</i>	ThCr ₂ Si ₂	XSCD	[157]
SrCu ₂ Sn ₂	a = 1.1197(4) b = 0.4322(2) c = 0.4859(1) b = 108.41(1)	<i>C2/m</i>	CaCu ₂ Sn ₂	XSCD	[112]
BaAg ₂ Ge ₂	a = 0.458 c = 1.069	<i>I4/mmm</i>	ThCr ₂ Si ₂	XSCD	[162]
BaAg _{1.3} Ge _{2.7}	a = 0.4652(9) c = 1.0606(2)	<i>I4/mmm</i>	ThCr ₂ Si ₂	XPD	[107]
BaAg ₂ Sn ₂	a = 0.481(2) c = 1.135(2)	<i>I4/mmm</i>	ThCr ₂ Si ₂	XSCD	[163]
SrAg ₂ Si ₂	a = 0.438(2) c = 1.048(2)	<i>I4/mmm</i>	ThCr ₂ Si ₂	XSCD	[163]
	a = 0.43835(6)			XPD	*

	$c = 1.0464(2)$				
SrAg_2Ge_2	$a = 0.445$ $c = 1.085$	$I4/mmm$	ThCr_2Si_2	XSCD	[162]
SrAg_2Sn_2	$a = 0.467(1)$ $c = 1.173(2)$	$I4/mmm$	ThCr_2Si_2	XSCD	[157]
BaAu_2Ge_2	$a = 0.4577(2)$ $b = 0.5656(2)$ $c = 1.0558(5)$	$Immm$	$\text{Ce}(\text{Ni},\text{Sb})_4$	XSCD	[98]
SrAu_2Si_2	$a = 0.437(1)$ $c = 1.014(2)$	$I4/mmm$	ThCr_2Si_2	XSCD	[157]
$\text{SrAu}_{1.6}\text{Ge}_{2.4}$	$a = 0.44796(2)$ $c = 1.06315(5)$	$P4/nmm$	CaBe_2Ge_2	XSCD	*
$\text{SrAu}_{1.9}\text{Ge}_{2.1}$	$a = 0.44866(2)$ $c = 3.1808(2)$	$I4/mmm$	BaCu_2Sb_2	XSCD	*
SrAu_2Ge_2	$a = 0.451(2)$ $c = 1.035(2)$	$I4/mmm$	ThCr_2Si_2	XSCD	[163]
$\text{SrAu}_{1.4}\text{Sn}_{2.6}$	$a = 0.46447(7)$ $c = 1.1403(2)$	$I4/mmm$	ThCr_2Si_2	XSCD	[110]

Table B.4: Structural parameters as calculated by DFT for the EpTX_3 compounds in the body-centered tetragonal BaNiSn_3 -structure-type, space group $I4mm$, with Wyckoff positions: Ep in 2a $(0,0,z \cdot c)$, T in 2a $(0,0,z \cdot c)$, X in 2a $(0,0,z \cdot c)$, and X in 4b $(0, \frac{1}{2} \cdot a, z \cdot c)$ and $(\frac{1}{2} \cdot a, 0, z \cdot c)$.

EpTX_3 compound	a [nm]	c [nm]	c/a	volume [nm ³]
SrNiSi_3	0.41236	0.96076	2.330	0.08169
SrPdSi_3	0.42505	0.98521	2.318	0.08900
SrPtSi_3	0.42798	0.97861	2.287	0.08962
SrNiGe_3	0.42948	0.97864	2.279	0.09026
SrPdGe_3	0.44262	1.00791	2.277	0.09873
SrPtGe_3	0.44468	0.99950	2.248	0.09882
BaNiSi_3	0.42388	0.98368	2.321	0.08837
BaPdSi_3	0.43622	1.00284	2.299	0.09541
BaPtSi_3	0.43825	0.99354	2.267	0.09541
EpTX_3 compound	Ep in 2a z	T in 2a z	X in 2a z	X in 4b z
SrNiSi_3	0.5934	0.2399	0	0.3447

SrPdSi ₃	0.6043	0.2460	0	0.3613
SrPtSi ₃	0.6016	0.2462	0	0.3598
SrNiGe ₃	0.5848	0.2365	0	0.3359
SrPdGe ₃	0.5990	0.2429	0	0.3539
SrPtGe ₃	0.5982	0.2439	0	0.3543
BaNiSi ₃	0.6011	0.2506	0	0.3508
BaPdSi ₃	0.6097	0.2551	0	0.3644
BaPtSi ₃	0.6055	0.2532	0	0.3614

Table B.6: Computational settings used with the atomic potentials involved: Here # gives the number of valence states that are taken into account for the DFT calculations and that are specified under the entry valence states. RWIGS is the Wigner-Seitz radius used in evaluating the *spd*- and site-projected wave function character of each band to give a local partial density of states (DOS). For each compound the maximum value of ENCUT = $1.25 \times \text{ENMAX}$ involved is used as an energy cutoff to define the size of the basis set.

Atom	#	valence states	RWIGS [nm]	ENMAX [eV]	ENCUT [eV]
Sr	10	$4s^2 4p^6 5s^2$	0.2138	226.327	-
Ba	10	$5s^2 5p^6 6s^2$	0.1979	186.981	-
Ni	16	$3p^6 3d^8 4s^2$	0.1058	367.726	459.7
Pd	16	$4p^6 4d^9 5s^1$	0.1217	270.984	338.7
Pt	10	$5d^9 6s^1$	0.1455	230.228	-
Si	4	$3s^2 3p^2$	0.1312	245.704	307.1
Ge	14	$3d^{10} 4s^2 4p^2$	0.1217	287.700	359.6

Appendix C

Cleaning procedure of the ^3He PPMS inset

This chapter provides an overview of the cleaning procedure for the ^3He PPMS inset. It can be seen as a rough guideline and should not be done without precautions. In general, a conventional cleaning procedure with the external LN_2 trap must have been performed before. For questions of any kind, contact Prof. Ernst Bauer, Prof. Herwig Michor, Prof. Michael Reissner or Prof. André Strydom.

Purpose: To unplug He3 impedance when LN2 Cryoclean and PPMS Cryoclean do not work. The concept is to bake (340K) the moisture out of the capillary while pulling on both ends of the capillary. Note: You will need a pump stand with a turbo pump on it.

1. Quick secure the He3 gas using the He3 Gasmon wizards.
2. Place the He3 probe into the chamber and purge and seal.
3. Connect the pump stand to the He3 fill port and start to pump.
4. Set PPMS temperature to 340K.
5. When the external pump has reached good vacuum conditions, open the FILL valve.
6. Using He3 Gasmon, go to options and select allows valve control and allow pump control.
7. Using He3 Gasmon, set turbo pump to 75Krpm, close bypass valve and open supply valve. NOTE: To toggle valve (after allowing valve control), place mouse cursor over valve and double click. This will toggle the valve open and close. To set

turbo RPM, double click over the RPM dialogue box. Click the red or green light to power up and down the turbo.

8. Pump on He3 impedance overnight; 14 hours.
9. When “bake-out” period is complete, power down turbo and close gasmon.
10. While the external pump is still pumping, close the FILL valve. This will leave the system under vacuum.
11. Power down and remove external pump.
12. Set cryostat to 300K and then remove insert and place back on He3 cart.
13. Release He3 gas back into the refrigerator by opening the manual TANK valve.
14. Run a LN2 cryoclean and run a performance test.

Bibliography

- [1] F. Steglich, J. Aarts, C. D. Bredl, W. Lieke, D. Meschede, W. Franz, H. Schäfer. *Physical Review Letters* **43**, 25, p. 1892 (1979)
- [2] J. G. Bednorz, K. A. Müller. *Zeitschrift für Physik B Condensed Matter* **64**, 2, pp. 189–193 (1986)
- [3] Y. Maeno, H. Hashimoto, K. Yoshida, S. Nishizaki, T. Fujita, J. G. Bednorz, F. Lichtenberg. *Nature* **372**, 6506, pp. 532–534. ISSN 0028-0836 (1994)
- [4] E. Bauer, G. Hilscher, H. Michor, C. Paul, E. W. Scheidt, A. Griбанov, Y. Seropegin, H. Noël, M. Sigrist, P. Rogl. *Phys. Rev. Lett.* **92**, p. 027003 (2004)
- [5] E. Bauer, M. Sigrist. *Non-Centrosymmetric Superconductors*, volume 847 of *Lecture Notes in Physics*. Springer (2012)
- [6] H. Yuan, D. Agterberg, N. Hayashi, P. Badica, D. Vandervelde, K. Togano, M. Sigrist, M. Salamon. *Physical Review Letters* **97**, 1. ISSN 0031-9007, 1079-7114 (2006)
- [7] S. M. Shamsuzzaman, Y. Inada, S. Sasano, S. Harada, Z. Guo-qing. *Journal of Physics: Conference Series* **200**, 1, p. 012183. ISSN 1742-6596 (2010)
- [8] E. Bauer, G. Rogl, X.-Q. Chen, R. Khan, H. Michor, G. Hilscher, E. Royanian, K. Kumagai, D. Li, Y. Li, R. Podloucky, P. Rogl **82**, 6. ISSN 1098-0121, 1550-235X (2010)
- [9] P. G. de Gennes, R. Alben. *Physics Today* **28**, 6, p. 54. ISSN 00319228 (1975)
- [10] D. Shechtman, I. Blech, D. Gratias, J. W. Cahn. *Physical Review Letters* **53**, 20, p. 1951–1953 (1984)
- [11] N. W. Ashcroft, D. N. Mermin. *Solid State Physics*. Cengage Learning (1976)
- [12] W. Borchardt-Ott. *Kristallographie: Eine Einführung für Naturwissenschaftler*. Springer, München, 6 edition (2008)
- [13] F. Bloch. *Zeitschrift für Physik* **52**, 7-8, pp. 555–600
- [14] Y. A. Bychkov, E. i. Rashba. *Pis'ma Zh. Eksp. Teor. Fiz.* **39**, 2, pp. 66–69 (1984)
- [15] A. Junod, T. Jarlborg, J. Muller. *Physical Review B* **27**, 3, p. 1568 (1983)

- [16] L. Gupta, M. Multani. *Selected Topics in Magnetism*. World Scientific Publishing Co. Pte. Ltd., Singapore 9128, New Jersey, London (1993)
- [17] C. Poole, H. J. Farach, R. J. Creswick, R. Prozorov. *Superconductivity*. Academic Press, 2 edition (2007)
- [18] W. Buckel. *Supraleitung*. Wiley-VCH, 6 edition (2004)
- [19] K. H. Bennemann, J. B. Ketterson. *Superconductivity*, volume 1. Springer (2008)
- [20] W. Meißner and R. Ochsenfeld. *Naturwissenschaften* **V21**, p. 787 (1933)
- [21] V.L. Ginzburg and L.D. Landau. *Zh. Eksp. Teor. Fiz.* **20**, **1064** (1950)
- [22] H. Fröhlich. *Physical Review* **79**, 5, pp. 845–856 (1950)
- [23] B. Serin, C. A. Reynolds, C. Lohman. *Phys. Rev.* **86**, 2, pp. 162–164 (1952)
- [24] B. T. Matthias, T. H. Geballe, V. B. Compton. *Rev. Mod. Phys.* **35**, 1, pp. 1–22 (1963)
- [25] L. N. Cooper. *Physical Review* **104**, 4, pp. 1189–1190 (1956)
- [26] J. Bardeen, L. N. Cooper, J. R. Schrieffer. *Physical Review* **108**, 5, p. 1175 (1957)
- [27] G. M. Eliashberg. *Z. Eksp. Teor. Fiz* **38**, 966 (1960)
- [28] W. L. McMillan. *Phys. Rev.* **167**, p. 331 (1968)
- [29] B. D. Josephson. *Physics Letters* **1**, 7, pp. 251–253 (1962)
- [30] A. P. Mackenzie, Y. Maeno. *Reviews of Modern Physics* **75**, 2, p. 657 (2003)
- [31] G. R. Stewart, Z. Fisk, J. O. Willis, J. L. Smith. In *Ten Years of Superconductivity: 1980–1990*, p. 85–88. Springer (1993), URL http://link.springer.com/chapter/10.1007/978-94-011-1622-0_8
- [32] G. R. Stewart. *Reviews of Modern Physics* **56**, 4, p. 755 (1984)
- [33] R. A. Fisher, S. Kim, B. F. Woodfield, N. E. Phillips, L. Taillefer, K. Hasselbach, J. Flouquet, A. L. Giorgi, J. L. Smith. *Physical review letters* **62**, 12, p. 1411 (1989)
- [34] E. Chashechkina, P. Chaikin. *Physical Review B* **65**, 1. ISSN 0163-1829, 1095-3795 (2001)
- [35] B. Mühlischlegel. *Z. f. Physik* **155**, 313 (1959)
- [36] J. C. Philips. *Phys. Rev. Lett.* **10**, 3, pp. 96–98 (1963)
- [37] S. Kirkpatrick. *Reviews of modern physics* **45**, 4, p. 574 (1973)
- [38] D. B. Gingold, C. J. Lobb **42**, 13, p. 8220 (1990)
- [39] K. Maki. *Physical Review* **148**, 1, p. 362 (1966)

- [40] N. R. Werthamer, E. Helfand, P. C. Hohenberg **147**, 1, p. 295 (1966)
- [41] G. Deutscher, I. Grave, S. Alexander. Phys. Rev. Lett. **48**, 21, pp. 1497–1500 (1982)
- [42] G. Eguchi, D. Peets, M. Kriener, Y. Maeno, E. Nishibori, Y. Kumazawa, K. Banno, S. Maki, H. Sawa **83**, 2. ISSN 1098-0121, 1550-235X (2011)
- [43] L. J. Van der Pauw. Philips Research Reports **13**, 1, pp. 1–9 (1958)
- [44] Khan, Rao Tahir Ali. *Pressure and field response of strongly correlated electron systems*. Ph.D. thesis, Technische Universität Wien (2010)
- [45] Ackerl, Norbert. *High Pressure Studies on Quantum Criticality of Ce-based Kondo Lattices*. Diploma thesis, Technische Universität Wien (2013)
- [46] R. S. Hayano, Y. J. Uemura, J. Imazato, N. Nishida, T. Yamazaki, R. Kubo. Physical Review B **20**, 3, p. 850 (1979)
- [47] URL <http://www.stfc.ac.uk/home.aspx>
- [48] URL <http://www.isis.stfc.ac.uk/>
- [49] F. Kneidinger, H. Michor, A. Sidorenko, E. Bauer, I. Zeiringer, P. Rogl, C. Blaas-Schenner, D. Reith, R. Podloucky. Physical Review B **88**, 10. ISSN 1098-0121, 1550-235X (2013)
- [50] K. Klepp, E. Parthé. Acta Crystallographica Section B: Structural Crystallography and Crystal Chemistry **38**, 5, p. 1541–1544 (1982)
- [51] J. Evers, G. Oehlinger, A. Weiss, C. Probst. Solid State Communications **50,1**, pp. 61–62 (1984)
- [52] S. Ramakrishnan, K. Ghos, A. D. Chinchure, V. R. Marathe, G. Chandra. Physical Review B **52,9**, pp. 6784–6795 (1995)
- [53] W. H. Lee, R. N. Shelton. Physical Review B **35,10**, pp. 5369–5371 (1987)
- [54] I. Zeiringer, A. Grytsiv, P. Brož, P. Rogl. J. of Solid State Chemistry (2012)
- [55] G. Kresse, J. Furthmüller. Phys. Rev. B **54**, pp. 11169–11186 (1996)
- [56] G. Kresse, D. Joubert. Phys. Rev. B **59**, pp. 1758–1775 (1999)
- [57] P. E. Blöchl. Phys. Rev. B **50**, p. 17953 (1994)
- [58] D. M. Ceperley, B. J. Alder. Phys. Rev. Lett. **45**, pp. 566–569 (1980)
- [59] H. Monkhorst, J. Pack. Phys. Rev. B **13**, pp. 5188–5192 (1976)
- [60] D. Alfè. Comp. Phys. Commun. **180**, pp. 2622–2633 (2009)
- [61] H. Bärnighausen. Commun. Math. **9**, p. 139 (1980)

- [62] H. Bärnighausen, U. Müller. Symmetriebeziehungen zwischen den Raumgruppen als Hilfsmittel zur straffen Darstellung von Strukturzusammenhängen in der Kristallchemie, University of Karlsruhe and University GH Kassel (1996)
- [63] J. Y. Chen, H. H. Sung, K. J. Syu, W. H. Lee. *Physica C* **470**, pp. 772–773 (2010)
- [64] A. Wilson. *Proc. Roy. Soc. A* **167**, 580 (1938)
- [65] N. F. Mott. *Philosophical Magazine* **26**, 6 (1972)
- [66] K. Togano, P. Badica, Y. Nakamori, S. Orimo, H. Takeya, K. Hirata **93**, 24. ISSN 0031-9007, 1079-7114 (2004)
- [67] T. Klimczuk, Q. Xu, E. Morosan, J. Thompson, H. Zandbergen, R. Cava. *Physical Review B* **74**, 22. ISSN 1098-0121, 1550-235X (2006)
- [68] E. Bauer, R. T. Khan, H. Michor, E. Royanian, A. Grytsiv, N. Melnychenko-Koblyuk, P. Rogl, D. Reith, R. Podloucky, E.-W. Scheidt, W. Wolf, M. Marsman. *Phys. Rev. B* **80**, p. 064504 (2009)
- [69] A. P. Pikul, D. Gnida. *Solid State Communications* **151**, 10, pp. 778–780. ISSN 00381098 (2011)
- [70] A. M. Clogston. *Phys. Rev. Lett.* **9**, 6, pp. 266–267 (1962)
- [71] K. Hummer, A. Grüneis, G. Kresse. *Physical Review B* **75**, 19. ISSN 1098-0121, 1550-235X (2007)
- [72] M. Weinert, E. Wimmer, A. J. Freeman. *Phys. Rev. B* **26**, p. 4571 (1982)
- [73] M. Weinert, G. Schneider, R. Podloucky, J. Redinger. *J. Phys.: Condens. Matter* **21**, p. 084201 (2009)
- [74] D. Reith, C. Blaas-Schenner, R. Podloucky. *Physical Review B* **86**, 10. ISSN 1098-0121, 1550-235X (2012)
- [75] J. Callaway. *Energy Band Theory*, chapter 1. Academic Press, New York and London (1964)
- [76] L. P. Gor'kov, E. I. Rashba. *Phys. Rev. Lett.* **87**, p. 037004 (2001)
- [77] A. Junod, D. Bichsel, J. Muller. *Helv. Phys. Acta* **52**, 580 (1979)
- [78] C.-J. Kang, K.-H. Ahn, K.-W. Lee, B. I. Min. *J. Phys. Soc. Jpn.* **82** (2013)
- [79] B. Chevalier, P. Lejoy, A. Cole, M. Vlasse, J. Etourneau. *Solid State Communications* **41**, 11, pp. 801–804 (1982)
- [80] L. M. Gelato, E. Parthé. *Journal of applied crystallography* **20**, 2, p. 139–143 (1987)
- [81] E. Bauer, S. Bühler-Paschen. *Strongly correlated electron systems* (2012)
- [82] P. Coleman, P. W. Anderson, T. V. Ramakrishnan. *Physical review letters* **55**, 4, p. 414 (1985)

- [83] P. G. De Gennes, J. Friedel. *Journal of Physics and Chemistry of Solids* **4**, 1-2, pp. 71–77 (1958)
- [84] E. Belin-Ferré. *Properties and Applications of Complex Intermetallics*. Number 2 in Book Series on Complex Metallic Alloys, World Scientific Publishing Co. Pte. Ltd., Singapore. ISBN 13 978-981-4261-63-0 (2010)
- [85] K. W. H. Stevens. *Proceedings of the Physical Society. Section A* **65**, 3, p. 209 (1952)
- [86] A. Arrott. *Physical Review* **108**, 6, p. 1394 (1957)
- [87] H. Yashima, N. Sato, H. Mori, T. Satoh. *Solid State Communications* **43**, 8, pp. 595–599 (1982)
- [88] N. Sato, H. Mori, T. Satoh, T. Miura, H. Takei. *J. Phys. Soc. Jpn.* **57**, pp. 1384–1394 (1988)
- [89] D. Kußmann, R. Pöttgen, U. C. Rodewald, C. Rosenhahn, B. D. Mosel, G. Kotzyba, B. Künnen. *Z. Naturforsch.* **54b**, 1155-1164 (1999)
- [90] W. Dörrscheidt, H. Schäfer. *Journal of the Less Common Metals* **58**, 209-216 (1978)
- [91] H. Fujii, A. Sato. *Journal of Alloys and Compounds* **508**, 338–341 (2010)
- [92] K. Miliyanchuk, F. Kneidinger, C. Blaas-Schenner, D. Reith, R. Podloucky, P. Rogl, T. Khan, L. Salamakha, G. Hilscher, H. Michor, E. Bauer, A. D. Hillier. *Journal of Physics: Conference Series* **273**, p. 012078. ISSN 1742-6596 (2011)
- [93] N. Melnychenko-Koblyuk, A. Grytsiv, P. Rogl, E. Bauer, R. Lackner, E. Royanian, M. Rotter, G. Giester. *J. Phys. Soc. Jpn.* **77**, Supplement A, 54 (2008)
- [94] E. Bauer, R. Khan, H. Michor, E. Royanian, A. Grytsiv, N. Melnychenko-Koblyuk, P. Rogl, D. Reith, R. Podloucky, E.-W. Scheidt, W. Wolf, M. Marsman. *Physical Review B* **80**, 6. ISSN 1098-0121, 1550-235X (2009)
- [95] N. Nasir, N. Melnychenko-Koblyuk, A. Grytsiv, P. Rogl, J. Wosik, G. E. Nauer, G. Giester. *J. of Solid State Chemistry* **183**, 565-574 (2010)
- [96] N. Melnychenko-Koblyuk, A. Grytsiv, P. Rogl, M. Rotter, E. Bauer, G. Durand, H. Kaldarar, R. Lackner, H. Michor, E. Royanian, M. Koza, G. Giester. *Physical Review B* **76**, 144118 (2007)
- [97] R. Demchyna, Yu. Prots, W. Schnelle, U. Burkhardt, U. Schwarz. *Z. Kristallogr. NCS* **221**, 109-111 (2006)
- [98] I. Zeiringer, N. Melnychenko-Koblyuk, A. Grytsiv, E. Bauer, G. Giester, P. Rogl. *Journal of Phase Equilibria and Diffusion* **32**, 2, 115 (2011)
- [99] A. Tkachuk, A. Mar. *Journal of Solid State Chemistry* **180**, 2298–2304 (2007)
- [100] I. Zeiringer, A. Grytsiv, P. Broz, P. Rogl. *Journal of Solid State Chemistry* **196**, 125-131 (2012)

- [101] E. Bauer, S. Berger, C. Paul, M. D. Mea, G. Hilscher, H. Michor, M. Reissner, W. Steiner, A. Grytsiv, P. Rogl. *Phys. Rev. B* **66**, 214421 (2002)
- [102] V. Babizheztksyy, R. Guerin, O. Isnard, K. Hiebl. *J. of Solid State Chem.* **172**, 265-276 (2003)
- [103] D. Gout, T. J. Barker, O. Gourdon, G. J. Miller. *Chem. Mater.* **17**, 3661-3667 (2005)
- [104] L. Bin, J. D. Corbett. *J. of Inorganic Chem.* **46(21)**, 8812-8818 (2007)
- [105] L. Frik, D. Johrendt, A. Mewis. *Anorg. Allg. Chem.* **632**, 1514 (2006)
- [106] Z. Ban, M. Sikirica. *Acta Crystallogr.* **18**, 594-599 (1965)
- [107] I. Zeiringer, M. X. Chen, I. Bednar, E. Royanian, E. Bauer, R. Podloucky, A. Grytsiv, P. Rogl, H. Effenberger. *Acta. Mater.* **59**, 2368-2384 (2011)
- [108] B. Eisenmann, N. May, W. Müller, H. Schäfer. *Z. Naturforsch. B* **27**, 1155-1157 (1972)
- [109] J. Dünner, A. Mewis, M. Roepke, G. Michels. *Zeitschrift für anorganische und allgemeine Chemie* **621**, 9, pp. 1523–1530. ISSN 0044-2313, 1521-3749 (1995)
- [110] A. Hellmann, A. Löhken, A. Wurth, A. Mewis. *Z. Naturforsch.* **62b**, 155-161 (2007)
- [111] V. Hlukhyy, A. Senyshyn, D. Trots, T. Fässler. *HASYLAB Annual Report* **1021** (2007)
- [112] M. Pani, M. Fornasari, P. Manfrinetti, F. Merlo. *Intermetallics* **19**, 957 (2011)
- [113] M. Pani, F. Merlo, M. Fornasari. *Z. Anorg. Allg. Chem.* **633**, 1581-1586 (2007)
- [114] W. Dörrscheidt, H. Schäfer. *Zeitschrift fuer Naturforschung, Teil B. Anorganische Chemie* **35**, 297-299 (1980)
- [115] R. Settai, T. Takeuchi, Y. nuki. *Journal of the Physical Society of Japan* **76**, 5, p. 051003. ISSN 0031-9015 (2007)
- [116] N. Kimura, K. Ito, K. Saitoh, Y. Umeda, H. Aoki, T. Terashima. *Physical Review Letters* **95**, 24. ISSN 0031-9007, 1079-7114 (2005)
- [117] L. D. Jennings, C. A. Swenson. *Physical Review* **112**, 1, p. 31 (1958)
- [118] N. N. Bogoljubov, V. V. Tolmachov, D. V. Širkov. *Fortschritte der Physik* **6**, 11-12, pp. 605–682. ISSN 00158208, 15213979 (1958)
- [119] C. W. Chu, P. H. Hor, R. L. Meng, L. Gao, Z. J. Huang, Y. Q. Wang. *Physical Review Letters* **58**, 4 (1987)
- [120] T. P. Orlando, E. J. McNiff Jr, S. Foner, M. R. Beasley **19**, 9, p. 4545 (1979)
- [121] T. F. Smith, H. L. Luo. *J. Phys. Chem. Solids* **28**, 569 (1967)
- [122] F. Kneidinger, H. Michor, E. Bauer, A. Griбанov, A. Lipatov, Y. Seropegin, J. Sereni, P. Rogl. *Physical Review B* **88**, 2. ISSN 1098-0121, 1550-235X (2013)

- [123] E. Wawrzynska, S. Baran, J. Leciejewicz, W. Sikora, N. Stüsser, A. Szytula. *J. Phys.: Cond. Mat.* **15**, p. 803 (2003)
- [124] E. Wawrzynska, J. Hernandez-Velasco, B. Penc, W. Sikora, A. Szytula, A. Zygmunt. *J. Phys.: Cond. Mat.* **15**, p. 5279 (2003)
- [125] G. Bocelli, O. Sologub, P. Salamakha. *J. Alloys and Compounds* **360** (2003)
- [126] E. Wawrzynska, J. Hernandez-Velasco, B. Penc, A. Szytula. *J. Phys.: Cond. Mat.* **16** (2004)
- [127] E. Wawrzynska, J. Hernandez-Velasco, B. Penc, A. Szytula. *J. Magn. Magn. Mater.* **288**, p. 111 (2005)
- [128] H. Fujii, T. Mochiku, H. Takeya, A. Sato. *Phys. Rev. B.* **72**, p. 214520 (2005)
- [129] H. Fujii. *J. Phys.: Condens. Matter* **18**, p. 8037 (2006)
- [130] T. Mochiku, H. Fujii, H. Takeya, T. Wuernisha, K. Mori, T. Ishigaki, T. Kamiyama, K. Hirata. *Physica C* **182**, pp. 463–465 (2007)
- [131] S. Kasahara, H. Fujii, H. Takeya, T. Mochiku, A. D. Thakur, K. Hirata. *J. Phys.: Condens. Matter* **20**, p. 385204 (2008)
- [132] S. Kasahara, H. Fujii, T. Mochiku, H. Takeya, K. Hirata. *Physica B* **403**, p. 1119 (2008)
- [133] P. Rogl, B. Chevalier, J. Etourneau. *J. Solid State Chem.* **88**, 429 (1990)
- [134] A. Lipatov, A. Griбанov, A. Grytsiv, P. Rogl, E. Murashova, Y. Seropegin, G. Giester, K. Kalmykov. *Journal of Solid State Chemistry* **182**, 2497 (2009)
- [135] E. Parthe, L. Gelato, B. Chabot, M. Penzo, K. Cenzual, R. Gladyshevskii. *Handbook of Inorganic and Organometallic Chemistry: Typix Standardized Data and Crystal Chemical Characterization of Inorganic Structure Types: Vol 8.* Springer Verlag, Berlin, Heidelberg (1994)
- [136] T. Moriya, T. Takimoto. *J. Phys. Soc. Japan* **64**, 960 (1995)
- [137] T. Roisnel, J. Rodriguez-Carvajal. *Mater. Sci. Forum* **118**, 378 (2001)
- [138] T. Roisnel, J. Rodriguez-Carvajal. *Materials Science Forum, Proceedings of the European Powder Diffraction Conference EPDIC7*, **118**, 378 (2000)
- [139] Stoe & Cie GmbH. *STOE WINXPOW*, version 1.06 edition (1999)
- [140] J. C. H. Chiu. *Phys. Rev. B* **13**, 31507 (1976)
- [141] H. Padamsee, J. E. Neighbor, C. A. Shiffman. *J. Low Temp. Phys.* **12**, 387 (1973)
- [142] F. Bouquet, R. A. Fisher, N. E. Phillips, D. G. Hinks, J. D. Jorgensen. *Phys. Rev. Lett.* **87**, 047001 (2001)
- [143] C. L. Huang, J.-Y. Lin, C. P. Sun, T. K. Lee, J. D. Kim, E. M. Choi, S. I. Lee, H. D. Yang. *Phys. Rev. B* **73**, 012502 (2006)

- [144] Y. Nakajima, T. Nakagawa, T. Tamegai, H. Harima. *Phys. Rev. Lett.* **100**, 157001 (2008)
- [145] S. V. Shulga, S.-L. Drechsler, G. Fuchs, K.-H. Müller, K. Winzer, M. Heinecke, K. Krug. *Phys. Rev. Lett.* **80**, 1730 (1998)
- [146] S. Manalo, H. Michor, M. El-Hagary, G. Hilscher, E. Schachinger. *Phys. Rev. B* **63**, 104508 (2001)
- [147] K.-H. Müller, G. Fuchs, A. Handstein, K. N. 1, V. Narozhnyi, D. Eckert, M. Wolf. *Physica C* **372–376**, 1251 (2002)
- [148] M. J. Winiarski, M. Samsel-Czekala. *J. Alloys and Compounds* **546**, 124 (2013)
- [149] H. J. Im, Y. S. Kwon, M. H. Jung. *Phys. Rev. B* **124**, 181 (2002)
- [150] L. N. Oliveira, J. Wilkins. *Phys. Rev. Lett.* **47**, 1553 (1981)
- [151] H.-U. Desgranges, K. Schotte. *Phys. Lett.* **91**, A, 240 (1982)
- [152] E. D. Bauer, V. A. Sidorov, S. Bobev, D. J. Mixson, J. D. Thompson, J. L. Sarrao, M. F. Hundley. *Phys. Rev. B* **71**, 014419 (2005)
- [153] W. Dörrscheidt, H. Schäfer. *Journal of the Less-Common Metals* **70**, P1 – P10 (1980)
- [154] X. Yan, G. Giester, E. Bauer, P. Rogl, S. Paschen. *Journal of ELECTRONIC MATERIALS* **Vol. 39**, No. 9 (2010)
- [155] N. Melnychenko-Koblyuk, A. Grytsiv, P. Rogl, H. Schmid, G. Giester. *Journal of Solid State Chemistry* **182**, 1754–1760 (2009)
- [156] I. Zeiringer, M. Chen, A. Grytsiv, E. Bauer, H. Effenberger, R. Podloucky, P. Rogl. *Acta. Mater.* **60(5)**, 2324-2336 (2012)
- [157] W. Dörrscheidt, H. Schäfer, N. Niess. *Zeitschrift fuer Naturforschung, Teil B. Anorganische Chemie* **31**, 890-891 (1976)
- [158] A. Palenzona, S. Cirafici, F. Canepa. *Journal of the Less-Common Metals* **135**, 185-194 (1987)
- [159] H. Fujii, A. Sato. *Physical Review, Serie 3. B* **79**, 224522-1 (2009)
- [160] I. Mayer, P. Yetor. *Journal of the Less-Common Metals* **55**, 171-176 (1977)
- [161] H. A. Fischer. PhD Thesis: Ternäre Silicide der schweren Erdalkali-Elemente mit Palladium und Platin **University Köln** (2000)
- [162] B. Eisenmann, N. May, W. Müller, H. Schäfer, A. Weiss, J. Winter, G. Ziegler. *Zeitschrift fuer Naturforschung, Teil B* **25**, 1350-1352 (1970)
- [163] N. May, H. Schäfer. *Zeitschrift fuer Naturforschung, Teil B* **27**, 864-865 (1972)

Acknowledgement

I would like to thank my thesis supervisor Professor Ernst Bauer for giving me the chance to work in his group, his constant support and his mentoring advices.

Furthermore, I want to thank Professor Peter Rogl as well as Professor Raimund Podloucky for the fruitful collaboration and discussions on non-centrosymmetric materials

Many thanks to my external coworkers Isolde Zeiringer, David Reith and Claudia Blaas-Schenner for the outstanding cooperation, their support and the exchange on different topics of superconductivity, solid state physics and physical chemistry.

I have to thank Professor Herwig Michor, Professor Michael Reissner and Professor André Strydom for theoretical discussions and the support on different measurement devices.

I want to thank my now and former co-workers in the group of Professor Bauer: Norbert Ackerl, Gaku Eguchi, Patrick Heinrich, Tahir Khan, Esmaeil Royanian, Leonid Salamakha and Alexander Zavarsky for the technical and scientific discussions as well as the company either in the basement laboratory or in the office.

With gratitude to my colleagues I want to specially thank Diana Geiger, Jonathan Hänel, Matthias Ikeda, Stefan Laumann, Karl-Anton Lorenzer, Andrey Sidorenko and Petr Tomes for our rich discussions, for their support in the laboratory and our friendships.

I want to mention and thank the members of the workshop: Andreas Lahner and Friedrich Faszt, Jürgen Gindl and Josef Sicherl.

Moreover, I want to thank all the members of the Institute of Solid State Physics for the good working environment, which makes it hard to say goodbye.

I am very thankful for my parents and my sister for their special support, their kindness and our strong company.

Many thanks to Lucy Win for reviewing the script in the sense of proper wording.

Finally, I want to express my deepest gratitude to the FWF Project 22295 for their financial support, making this project possible.

Many thanks to all of you.
Friedrich

Journal Publication List

F. Kneidinger, H. Michor, E. Bauer, A. Griбанov, L. Lipatov, Y. Seropegin, J.G. Sereni, P. Rogl: "Superconductivity and non-Fermi-liquid behavior of $\text{La}_3\text{Pd}_4\text{Si}_4$ and $\text{Ce}_3\text{Pd}_4\text{Si}_4$ "; *Physical Review B*, **88** (2013), 024423; S. 1 - 7.

F. Kneidinger, H. Michor, A. Sidorenko, E. Bauer, I. Zeiringer, P. Rogl, C. Blaas-Schenner, D. Reith, R. Podloucky: "Synthesis, characterization, electronic structure, and phonon properties of the noncentrosymmetric superconductor LaPtSi "; *Physical Review B*, **88** (2013), 104508; S. 1 - 9.

F. Kneidinger, L. Salamakha, A. Sidorenko, E. Bauer, I. Zeiringer, K. Miliyanchuk, N. Melnychenko-Koblyuk, A. Grytsiv, P. Rogl, C. Blaas-Schenner, D. Reith, R. Podloucky: "The Ternary $\text{EpT}_x\text{X}_{4-x}$ Compounds: Crystal Structures and Physical Properties"; to be published

V. Babizhetskyy, B. Kotur, S. Oryshchyn, C. Zheng, F. Kneidinger, L. Leber, C. Simson, E. Bauer, H. Michor: "Crystal and electronic structure and physical properties of Ni_5P_4 "; *Solid State Commun.*, **164** (2013), S. 1 - 5.

G. Eguchi, F. Kneidinger, L. Salamakha, S. Yonezawa, Y. Maeno, E. Bauer: "Pressure study of the noncentrosymmetric 5d-electron superconductors CaMSi_3 ($\text{M} = \text{Ir}, \text{Pt}$)"; *Journal of the Physical Society of Japan*, **81** (2012), 074711; S. 1 - 4.

M. Falmbigl, F. Kneidinger, M. Chen, A. Grytsiv, H. Michor, E. Royanian, E. Bauer, H. Effenberger, R. Podloucky, P. Rogl: "Cage-Forming Compounds in the Ba-Rh-Ge System: From Thermoelectrics to Superconductivity"; *Inorganic Chemistry*, **52** (2013), S. 931 - 943.

M. Falmbigl, F. Kneidinger, A. Grytsiv, H. Michor, H. Müller, P. Rogl, E. Bauer, G. Hilscher, G. Giester: "Crystal structure, and physical properties of the novel compounds EuRh_3Ge_7 and EuIr_3Ge_7 "; *Intermetallics*, **42** (2013), S. 45 - 51.

B. Kotur, V. Babizhetskyy, E. Bauer, F. Kneidinger, A. Danner, L. Leber, H. Michor: "Metal site doping in the narrow-gap semiconductor FeGa_3 "; *Materials Science*, **49** (2013), S. 211 - 219.

B. Kotur, V. Babizhetskyy, E. Bauer, F. Kneidinger, A. Danner, L. Leber, H. Michor: "Metal Site Doping in the Narrow-Gap Semiconductor FeGa_3 "; *Physicochemical Mechanics of Materials*, **2** (2013), S. 69 - 75.

Z. Malik, F. Kneidinger, H. Michor, S. Puchegger, E. Bauer, G. Giester, P. Rogl: "Physical properties of non-centrosymmetric $\text{Ni}_2\text{Zn}_{11}$ "; *Intermetallics*, **38** (2013), S. 88 - 91.

K. Miliyanchuk, F. Kneidinger, C. Blaas-Schenner, D. Reith, R. Podloucky, P. Rogl, T. Khan, L. Salamakha, G. Hilscher, H. Michor, E. Bauer, A.D. Hillier: "Platinum metal silicides and germanides: superconductivity in non-centrosymmetric intermetallics"; *Journal of Physics: Conference Series*, **273** (2011), 012078; S. 1 - 4.

M. Kriegisch, R. Grössinger, C. Grijalva, A. Muhammad, F. Kneidinger, N. Mehboob, F. Kubel and R. Sato-Turtelli: "Magnetic properties of highly textured Fe₈₅Ga₁₅"; *IEEE Transactions on Magnetics*, **PP 99** (2014)

Erklärung

Hiermit versichere ich, dass ich die vorliegende Arbeit ohne unzulässige Hilfe Dritter und ohne Benutzung anderer als der angegebenen Hilfsmittel angefertigt habe. Die aus fremden Quellen direkt oder indirekt übernommenen Gedanken sind als solche kenntlich gemacht. Die Arbeit wurde bisher weder im Inland noch im Ausland in gleicher oder ähnlicher Form einer anderen Prüfungsbehörde vorgelegt.

Die vorliegende Dissertation wurde am Institut für Festkörperphysik der Technischen Universität Wien unter der wissenschaftlichen Betreuung von Ao.Univ.Prof. Univ.Prof. Dipl.-Ing. Dr.techn. Ernst Bauer angefertigt.

Ich erkenne die Promotionsordnung der Technischen Universität Wien an.

Wien, 10. Februar 2014

Curriculum Vitae

Persönliche Daten

Dipl.-Ing. Friedrich Kneidinger, BSc (WU)

Hardeggasse 55/6/24, 1220 Vienna

Born on 27th of June 1985

Ausbildung

1991 – 1995 Volksschule Traun/ Oedt, Traun

1995 – 2003 BRG Traun, Traun

2004 – 2009 Diplomstudium der Technischen Physik, Technische Universität Wien

2009 – 2014 Doktoratsstudium der technischen Wissenschaften, Technische Universität Wien

2010 – 2013 Bachelorstudium Betriebswirtschaftslehre, Wirtschaftsuniversität Wien

Berufserfahrung

2003 – 2004 Österreichisches Bundesheer

2008 – 2009 Areva NP GmbH

2009 – 2013 Projektassistent (FWF), Technische Universität Wien

Weitere Aktivitäten

2012-2013 Teilnahme Vienna City Marathon